Control of Voltage Source Converter Based Multi Terminal DC and Hybrid AC/DC Systems

by

Aram Kirakosyan

A thesis
presented to the University Of Waterloo
in fulfillment of the
thesis requirement for the degree of
Doctor of Philosophy
in
Electrical and Computer Engineering

Waterloo, Ontario, Canada, 2020

Examining Committee Membership

The following served on the Examining Committee for this thesis. The decision of the Examining Committee is by majority vote.

External Examiner	MARTIN ORDONEZ Professor
Supervisor	MAGDY SALAMA Professor
Supervisor	EHAB F. EL-SAADANY Professor
Internal Member	CLAUDIO A. CANIZARES Professor
Internal Member	MEHRDAD KAZERANI Professor
Internal-external Member	GORDON SAVAGE Professor

Author's Declaration

I hereby declare that I am the sole author of this thesis. This is a true copy of the thesis, including any required final revisions, as accepted by my examiners.

I understand that my thesis may be made electronically available to the public.

Abstract

The journey of power systems started with the development of the dc technology pioneered by Thomas Edison in the late 19_{th} century. Meanwhile, Nicola Tesla led the investigation of ac technology, which soon surmounted the dc paradigm in the "War of Currents", driven by the urge to favor higher-efficiency systems. For about a century, ac was the preferred choice in all sections of power systems, including generation, transmission, and distribution. However, with recent advances in power electronic technology, such as Voltage Source Converters (VSC), the conversion between ac and dc has become more practical, leading to the development of dc and hybrid ac/dc grids. These grids have been formed in both transmission and distribution systems. Specifically, on the transmission side, the advancement of the Multi-Terminal High Voltage Direct Current (MT-HVDC) grids enabled the formation of dc grids covering large geographical areas and integrating bulk renewable energy sources such as offshore wind. On the distribution side, on the other hand, the development of Multi-Terminal Direct Current MicroGrids (MT-DCμGrid) became an attractive solution for interconnecting increasingly popular dc generation sources with dc loads.

The control of the converters interfacing with those dc grids is one of the challenges for the future expansion of such systems and is the subject matter of the current Ph.D. thesis. The conventional droop control of VSCs has been the widely accepted solution for both MT-HVDC and MT-DCμGrid applications as it allows several converters to simultaneously regulate the dc grid voltage and share power imbalance in the system. However, droop-controllers have several application-specific challenges. This thesis investigates those challenges and proposes new control structures to overcome them. Specifically, the effect of the converters' control on the regulation of dc network-related parameters, that is, on dc voltage regulation and ratio-based power-sharing between converters, is investigated for both MT-HVDC systems and MT-DCμGrids and new control approaches are proposed. Furthermore, the effect of the converters' control on the interaction of MT-HVDC systems with neighboring ac grids is investigated, and advanced solutions are developed for enabling enhanced mutual frequency support of the ac systems interconnected through MT-HVDC systems. The developed strategies are applicable to general structure grids, do not require additional hardware and can be seamlessly integrated into the existing control solutions. The developed control strategies aim to assist systems operators in enhancing the performance of hybrid ac/dc systems. Comprehensive time-domain and modal analysis are conducted to compare the proposed strategies with relevant studies available in the recent literature, validating the advantage of the developed methods.

Acknowledgements

Foremost, I would like to express my sincere gratitude to my Ph.D. advisors Prof. Ehab El-Saadany and Prof. Magdy Salama for their valuable guidance, scholarly inputs and consistent encouragement throughout my doctoral studies. Despite their busy schedules, they were always able to dedicate time to me when I needed it. Prof. Ehab believed in me at the beginning and throughout my Ph.D. studies and he never limited my actions while simultaneously providing the necessary guidelines to succeed. I am also ever-thankful to Prof. Salama: After each meeting with him I always got more inspired, motivated, and confident about my abilities. I am honored that this dissertation has been examined by Prof. Martin Ordonez, Prof. Claudio Canizares, Prof. Mehrdad Kazerani, and Prof. Gordon Savage. I owe respect and thanks to them for their time and insight. My success with doctoral studies was also due to the continuous guidance of Prof. Mohamed El Moursi, my M.Sc. supervisor, and Ph.D. collaborator. To me Prof. El Moursi is a true example of a real leader. I will always be grateful to Prof. El Moursi for his support and kindness. I owe a lot to my parents Robert and Karine, who encouraged and helped me at every stage of my personal and academic life, and longed to see this achievement come true. Special thanks to my sister Anahit and my brother Armen, for whom my success was always their success. No matter how difficult it was for them, my family always wanted me to continue the path I have chosen, and I am sure that I would not have achieved anything without them. I want to thank my friends in Canada who made my life more enjoyable here. I would like to thank my friends from UAE and, most notably, my friends and relatives from Armenia, who were always there for me, at least virtually. I would like to extend my gratitude to Canada, a country where I never felt like an outsider and to which I owe a lot; to UAE: a hospitable country which enabled my first international experience; and finally to Armenia: a country of my origin and where a big portion of my heart is, especially during the current difficult days for my country. Last but not least, I want to thank my wife Amalya, whose support was the biggest motivation throughout my Ph.D. studies, whose purposefulness was educative to me, and who gave birth to our lovely son Robert just several days before I earned to be called Dr. Aram.

Table of Contents

List of Figures

List of Tables

List of Abbreviations

A-VSG	Adaptive Virtual Synchronous Generator.
ac	Alternating Current.
ADC	Adaptive Droop Control.
AF	Assistance Factor.
AGC	Automatic Generation Control.
AVS	Average Voltage Sharing.
AVSC	Average Voltage Sharing Based Controller.
C-FD	Conventional Frequency Droop.
dc	Direct Current.
DG	Distributed Generation.
dq	Direct-Quadrature.
FC	Frequency Cooperativeness.
FD	Frequency Droop.
FLL	Frequency Locked Loop.
GHG	Green House Gases.
HIL	Hardware In the Loop .
HMG	Hybrid Microgrid.
HVDC	High Voltage DC.
I-V	Current-Voltage.
IC	Interlinking Converter.
ICC	Inner Current Controller.
IEEE	The Institute of Electrical and Electronics Engineers.
IGBT	Insulated Gate Bipolar Transistor.
kV	Kilo Volt.
kVAR,MVAR	Kilo and Mega Volt-Ampere Reactive.
kW, MW	Kilo and Mega Watt.
LCC	Line Commutated Converter.
LED	Light Emitting Diode.
LPF	Low Pass Filter.
LV, MV	Low Voltage and Medium Voltage.
MMC	Modular Multilevel Converter.
MPPT	Maximum Power Point Tracker.
MT-DCμGrid	Multi-Terminal DC MicroGrid.

MT-HVDC	Multi-Terminal HVDC.
ODCVC	Outer DC Voltage Controller.
OSG	Orthogonal Signal Generator.
P-V	Power-Voltage.
PCC	Point of Common Coupling.
PI	Proportional Integral.
PLL	Phase Locked Loop.
PMSG	Permanent Magnet Synchronous Generator.
PQ	Active and Reactive Power.
PR	Proportional Resonant.
PSI	Power Sharing Index.
PSIC	Power Sharing Index Based Controller.
PV	Photovoltaic.
PVD	Pilot Voltage Droop.
PWM	Pulse Wide Modulation.
QSS	Quasi Steady State.
RCP	Rapid Control Prototyping.
RES	Renewable Energy Sources.
ROCOF	Rate of Change of Frequency.
RTS	Real-Time Simulation.
SBDC	Synchroconverter Based Droop Control.
SCR	Short Circuit Ratio.
SOGI	Second Order Generalized Integrator.
SRF	Synchronous Reference Frame.
TDS	Time Domain Simulation.
UC	Unit Commitment.
VSC	Voltage Source Converter.
WPP	Wind Power Plants.
WT	Wind Turbine.

Chapter 1

Introduction

1.1 History of ac and dc electricity: "The War of Currents"

It is difficult to imagine modern life without electricity, as it is used in practically every aspect of life: we use it in our homes for lighting and heating and for operating domestic appliances; we use it in our factories for producing essential goods such as clothes, paper, food; we also use it for transportation, telecommunication, computing. This list, in fact, includes almost every aspect of modern human life. According to recent reports, 87% of the world's population has access to electric energy [1]. Such wide use of electric energy is motivated by the fact it is the most versatile and easily controlled form of energy [2]. Specifically, electricity is weightless, has relatively little losses in conversion and distribution, and is easy to use.

Human interest to understand and use the electricity phenomena can perhaps be dated back to the 17th century; by that time, scientists were able to generate very short, nearly instantaneous, current flows. It was only after the invention of the voltaic cell by Italian science-pioneer Alessandro Volta in about 1800 that relatively long-lasting electric power sources become available. The power produced by Volta's source relied on chemical reactions and was for short use only. The practical usage of electricity dates back to 1808, when Cornish chemist Humphry Davy developed the electric carbon-arc lamp [3]. Around two decades later after Davy's discoveries, the British scientist Michael Faraday made another major breakthrough by unfolding the principles of electricity generation without relying on chemical reactions [4]. Faraday observed that electricity can be induced by moving magnets inside coils of copper wire. However, it was only in the 1870s that the introduction of reliable and long-lasting incandescent light bulbs by Tomas Edison made electrical power available for the larger public. Edison founded the Edison Illuminating Company aiming at the development of a low-voltage direct current (dc) system and supplying power for domestic and industrial lighting. The use of dc technology, which features unidirectional current flow, was a natural and uncomplicated solution for electricity usage at that time, as the contemporary electric sources such as batteries were also based on that technology.

A young Serbian inventor named Nicola Tesla was by then working for Edison's company and had a task of developing dc generators. After successfully accomplishing the task, Tesla left the company over financial arguments, after which he joined other inventors in an attempt to lead the world's adoption of large-scale electrification. Tesla started to work on his own projects, developing an inductor motor and transformer (the Tesla Coil) that operates on alternating current (ac), the latter being a technology where the current reverses direction a certain number of times per second (e.g., 60 times in North American 60 Hz system). After the successful introduction of Tesla's inductor motor to the engineering community in 1888, an entrepreneur and engineer, George Westinghouse, became interested in financing Tesla's endeavors to promote ac based technologies. Tesla was hired by Westinghouse Electric & Manufacturing Company's Pittsburgh labs and started his intensive effort to develop ac based power technology.

Not wanting to lose his dominance in the electrification market, Edison started denigrating Tesla's ac technology, stating that it is more dangerous than its dc counterpart. This rivalry gave rise to the so called "War of Currents", which was a competition over whether the emerging electric power grids should be based on dc or ac technology [5]. In 1893, at the height of the "battle", Edison's company, named Edison General Electric, and Westinghouse's company competed in a bid on electrifying the Chicago World's Fair – also known as the World's Columbian Exposition. Edison bid to electrify the fair with direct current for $ 554,000, but lost to George Westinghouse, who claimed he could electrify the fair for only $ 399,000 using Tesla's ac technology [6]. After this defeat, Edison's dc technology yielded its place to the ac phenomena in the years ahead. Specifically, Westinghouse ensured a contract for Tesla to use the latter's polyphase ac induction motor patent to build a generating station by Niagara Falls. The energy generated was enough to power Buffalo, New York and other parts of the Eastern United States. At this stage, Edison was dismissed from the board of directors of his own company, whose name was changed to simply General Electric, and the company shifted to the use of ac technology as well.

After its win in the "War of Currents", ac technology dominated power generation, transmission, distribution and usage for over a century. Several factors facilitated the acceptance of ac technology and its dominance over the dc alternative: with ac technology voltages are easily converted from one level to another, and conversion from mechanical to electrical power and vise versa is relatively straightforward. For that reason, ac power was more economical for transfer over long distances because stepping-up voltages to higher levels with the help of power transformers resulted in less system losses. This conversion with the dc technology did not become equally uncomplicated for over a century.

Over the past few decades, the development of advanced semiconductor switches have facilitated the conversion between ac and dc power as well as between different dc voltage

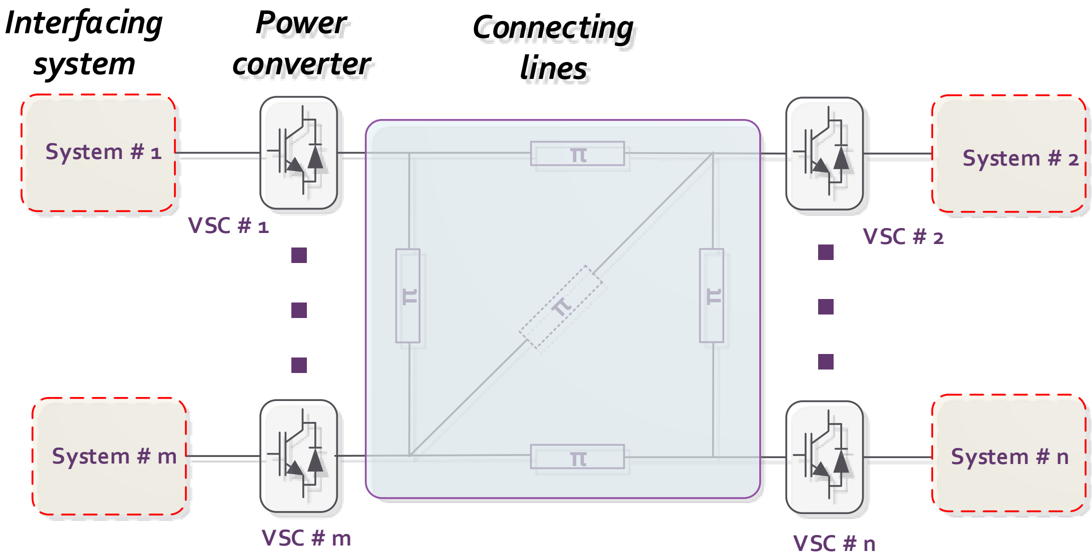

Figure 1.1. General structure of multi-terminal dc grids

levels. Such power transformation is done with devices called converters, which contain semiconductor switches. Apart from the increasing availability of power electronics semiconductor switches with higher power handling capability and faster switching rates, the advancement of dc/ac or dc/dc converters became possible due to the development of real-time computer controllers that make the implementation of advanced control algorithms possible. Meanwhile, increasing concerns about global warming have been one of the forces driving the call for change in the conventional power industry. In an effort to reduce CO2 and greenhouse gas (GHG) emissions, and to meet the ever-increasing load demand, several countries have adopted policies promoting the integration of power from renewable energy sources (RESs) such as wind and solar. The adaptation of energy from RESs has changed the nature of how power is generated (e.g., dc generation in the case of solar), where the power should be transmitted from (e.g., transfer from sea in case of offshore wind). The above-described technological developments and the necessity to modify conventional power industries have brought dc technology back as a potential alternative for several applications, reviving the century long "War of Currents".

In fact, in several applications, dc technology has already proved to be the preferred option. Specifically, dc provides more-economical transmission of bulk power over long distances using high voltage dc (HVDC) technology, which is especially applicable for the integration of certain RESs such as remote hydro resources or offshore wind. This developments has brought the notion of multi-terminal HVDC (MT-HVDC) transmission grids, with several parallel-connected converters forming a dc grid on the transmission level. On the other hand, in low voltage power systems, certain types of generation and new loads use dc technology. Therefore, their direct integration through dc multi-bus microgirds, namely multi-terminal dc microgrids (MT-DCμGrid) have proved to be more practical. The general topology of dc grids, including MT-HVDC and MT-DCμGrid systems, is shown in Fig. 1.1, where a dc grid is connected with neighboring systems through power converters. It is worth noting that the most-accepted converter topology for the formation of dc systems are Voltage Source Converters (VSC). A more-detailed description of the these converters, plus their comparative advantages and operation principles, is given next. Also, the development history of VSC based dc grids will be talked through in the next sections. The design of advanced controllers of those VSCs, which is crucial for proper functioning of dc grids, will be the main theme of this thesis.

1.2 The development history of multi-terminal high voltage dc systems

Dc systems have already been in use during recent decades for the transmission of large amounts of electric power between networks. In such transmission, at the sending grid, the first converter modifies the ac power to dc, transfers the power through dc lines to the second converter, and then the dc power is transformed back to ac and supplied to the receiving grid. This approach, in which only two converters form the dc system, is called point-to-point dc transmission. The first commercial point-to-point dc transmission project, the Gotland 1 HVDC link commissioned back in 1954, utilized mercury-arc valve based converters for realizing the ac to dc conversion [7]. Starting from the late 1960s, after the development of semi-controlled solid-state switches, thyristor based HVDC technology became dominant over its counterpart that used mercury-arc valves. The first point-to-point HVDC system using thyristor valves was the Eel River project in Canada, which was built by General Electric and put into operation in 1972 [8]. However, thyrsitor based switches can only be turned on in a controlled manner, whereas their turn-off is determined by the circuit that the switches are connected to. This limitation causes several operational challenges, such as the high harmonic distortion injected into the grids the converters are connected to, and a high short-circuit-ratio (SCR) requirement that those grids must meet. Typically, thyristor based converters could be connected to grids with an SCR of more than two [9].

Another breakthrough in the conversion and transmission of dc power happened in the late 1990s with the introduction of high-power VSCs. The first point-to-point VSC based HVDC system, the Hellsjon-Grangesberg project in Sweden, was commissioned in 1997 [10]. Compared to LCC based HVDC grids, VSC based HVDC systems have several advantages, including their capability of regulating reactive power, the option of connecting them to weak ac systems, and their need of a smaller converter area. Among the limitations of LCC based HVDC systems is their restricted capability of forming dc grids by the parallel connection of more than two converts on their dc sides. The reason behind this limitation is that LCCs have unidirectional current flow on their dc sides, and the dc power reversal is achieved by changing the dc voltage polarity of the other converters, which in turn modifies the dc system voltage. Therefore, power reversal between two converters would directly affect the power flow in the other converters connected to the same dc system. Although there are a few existing LCC-HVDC systems that have more than two converter stations, such as the Quebec-New England three-terminal system in Canada, the feasibility of expanding such systems to include more converter stations is limited. With VSC based HVDC systems, on the other hand, the dc voltage is unipolar and is controlled in a tight range. This feature allows a large number of converters to be paralleled on the dc side, which achieves the desired power regulation with relatively simpler controls and protection schemes. As a result, the usage of VSC in HVDC applications facilitate the formation of MT-HVDC systems.

What is more, the constant polarity of the voltage allows usage of advanced cable technology, e.g., XLPE cables [11]. The latter cables are considered technology of the future, as their light weight characteristics make them easy to transport, their homogeneous extruded insulation system provides the possibility of dynamic moving installations and rapid manufacturing of the cables, and the absence of oil leaks makes these cables environmentally friendly. The above-mentioned characteristics make them suitable for undersea applications, and they are specifically useful for the integration of large offshore wind sources. The smaller converter area of VSCs further facilitates the VSC-HVDC connection of offshore resources, and supports the formation of offshore MT-HVDC systems.

MT-HVDC grids, that is, transmission systems with more than two VSC stations, are now available for the connection of several ac areas and wind farms. a number of MT-HVDC projects around the world are already in operation or to be constructed in the near future. China has commissioned three-terminal (the Nan'ao project), four-terminal (the Zhangbei project) and five-terminal (the Zhoushan project) MT-HVDC systems [12–14]. The Zhangbei project was put into operation in 2019 to provide around 4.5 GW of wind power to Beijing. MT-HVDC grids are expected to further empower efficient

Figure 1.2. Potential connection routes of European MT-HVDC Supergrid.

socio-economic operation of the power networks of different countries and facilitate large integration of RES, cross-border power market trading, exchanges of power reserves, etc. The Atlantic Wind Connection, a prospective MT-HVDC system to be built on the East Coast of the United States, will integrate local offshore wind resources [15]. The connection of the Nordic pool with continental Europe is yet another major upcoming MT-HVDC project [16]. What is more, Europe plans to construct a Supergird to interconnect several countries and grid operators and to integrate massive renewable energy sources such as the solar power available in the north of Africa and wind energy from the North Sea, as shown in Fig. 1.2 [17, 18].

1.3 The development history of multi-terminal dc microgrids

Apart from increasingly receiving acceptance for use in transmission networks, dc technology is also regaining its role in low voltage systems. Many RES (photovoltaic systems, fuel cells, etc.) output power in dc form. Small-scale wind generation, on the other hand, produces power in the ac form, but uses a dc conversion stage to avoid synchronization requirements when connecting to the main ac grid. Battery storage systems and electric vehicles, technologies that are also dc in nature, have seen a rapid increase in popularity in recent years. What is more, certain types of recently emerged loads, such as light-emitting diode (LED) lightbulbs, notebook computers, elevators, are inherently dc in nature. Therefore, an ac/dc conversion is required to connect those units to conventional ac microgrids or distribution networks. Thus, the dc grid architecture became a potential alternative to ac systems because it reduces the number of power conversion stages, leading to a simpler system structure with lower cost and higher efficiency [19]. Furthermore, the use of such microgrids avoids problems such as the need for frequency synchronization, and reactive power flow during steady-state operation. It also alleviates problems such as those related to power quality. In certain instances, the installation of such MT-DCμGrids is also cheaper compared to that of their ac equivalents [20]. Such developments are bringing Edison′s century-old vision of distributing power in the dc form closer to reality.

In fact, several MT-DCμGrids have already been implemented in the world. One of the first commercial implementations of such systems is the MT-DCμGrids in Xiamen University in China [21]. The reported projects vary from relatively small-scale for dc ceiling-grids to larger-scale behind the meter dc connections between residential houses [22]. Among the notable applications of such systems is the Sendai Microgrid, implemented in Japan between 2005 and 2008. This microgrid was able to continue its proper operation during the tsunami and earthquake that shocked Japan in 2011, achieving a milestone in microgrid implementation [23]. It is worth noting that the dc power supplied to data racks and control rooms prevented disturbance propagation in the Sendai Microgrid system. Several other MT-DCμGrids projects have been suggested for residential buildings, including the EPARC dc building project in Taiwan, Fukuoka Smart House project in Japan, and the Green Homes venture in Korea, shown in Fig. 1.3 [24]. With companies like Walmart and Amazon installing more PV panels on their buildings, the development of such small-scale dc systems is becoming even more popular [25].

1.4 Challenges for dc grid development

Despite the obvious prospects for developing VSC based multi-terminal dc systems, these grids can still be considered to be in their infancy. Technical challenges associated with their formation and operation are one of the key factors restricting the wider popularity of dc grids. Among the challenges are the requirement for the design of new converter typologies, protection of dc grids, control of converters, etc. For example, new configurations of multilevel VSCs are becoming attractive solutions for MT-HVDC applications as they result in less harmonic distortion and thus need less filtering. One of the main challenges in

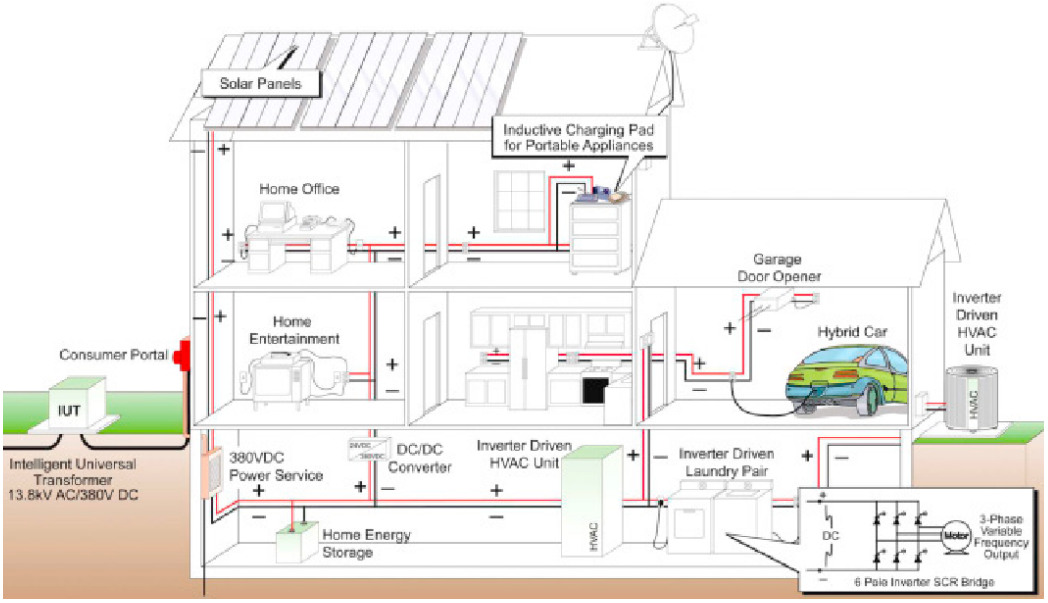

Figure 1.3. Architecture of Green Homes MT-DCμGrids.

the protection of such grids is in breaking of the dc circuit, which is complicated by the fact that the dc current has no natural zero-crossing point. Finally, the development of advanced control strategies for converters interfacing with dc grids is of prime importance for the proper operation of dc systems and for bringing them into widespread use. The latter point is the subject of this thesis.

1.5 Objectives of the thesis

The main objective of this thesis is to facilitate the formation of multi-terminal dc grids by developing enhanced control strategies for VSCs interfacing with those grids. The research described in this thesis considers the control of dc side variables and the management of interactions with the systems neighboring those dc grids. The detailed objectives of the thesis are as follows:

- To develop a control algorithm for droop-controlled VSCs in MT-HVDC systems that will ensure proper regulation of dc system parameters. Specifically, strategies should be developed to ensure enhanced dc voltage regulation and power-sharing between droop-controlled converters. The developed strategy should be general, i.e. it should not rely on the information of the system topology and parameters. Furthermore, the designed method should ensure continuous system operation even in the presence of large delays in the communication network it uses.

- To further enhance the control strategies of MT-HVDC systems and so ensure the desired interaction with neighboring ac systems. In particular, by redirecting active power within the MT-HVDC grid, precise and selective mutual frequency support should be achieved between MT-HVDC interconnected ac systems.
- To design a decentralized control approach for MT-DCμGrids for ensuring proper load distribution between droop-controlled dc energy resources. The approach should not rely on the prior information of system parameters or topology, and should enhance steady state operation without sacrificing the dynamic performance of dc grids.

1.6 Outline of the thesis

Chapter 2 introduces the structure and models of the main components of MT-HVDC and MT-DCμGrids considered in this study. The basic control strategies of those converters are also demonstrated. Consideration is given to the components that have major affect on the controller operation of the converters interfacing with dc grids. Relevant literature on advanced controllers for those converters is then reviewed in Chapter 3, and the drawbacks of recently reported strategies are revealed. Chapter 4 presents the converter controllers proposed for voltage regulation and power sharing in MT-HVDC systems. Chapter 5 continues the previous chapter by proposing a controller that ensures enhanced interaction of MT-HVDC systems with neighboring ac grids. A decentralized controller that ensures proper load distribution in MT-DCμGrids is proposed in Chapter 6. Finally, Chapter 7 concludes the thesis and presents possible directions for the future research.

Chapter 2

System Modelling and Base Control

This chapter introduces the main components considered in MT-HVDC systems and MT-DCμGrids, and approaches used for modelling those components. The presentation of those models helps understanding the general system operation, and the base-level controllers of the converters. Additionally, the models shown in this chapter are later used for conducting the time-domain and stability analysis of the systems combining the proposed controllers and the existing networks.

The components of MT-HVDC grids are presented in Section 2.1. The model of three-phase ac/dc VSC connected to the grid though a filter is introduced first, followed by the model of dc network. The grid synchronization technique for three-phase ac/dc converters is then presented followed by the description of lower-level control of those converters. The model of the systems interfacing to MT-HVDC grids is then discussed, including the model of conventional ac grids and that of WPPs. Furthermore, the modeling of MT-DCμGrids is shown in Section 2.2, which includes the modeling of dc/dc converters. As it will be discussed later, the controller proposed for MT-DCμGrids relies on single-phase frequency detection. Therefore, the structure of grid synchronization technique for single-phase application is also presented in Section 2.2.

As will be shown in the later chapters (Chapter 4-Chapter 6), the control approaches proposed in this thesis modify the outer-level loops of the existing control methods. Therefore, the converter models presented in this chapter are based on average-value based modeling technique, which is an accepted technique in the literature for investigating new outer-layer control approaches of VSCs [26–31]. These models allow maintaining dynamics presenting the interaction of the controllers and power system with reduced computational burden, which is of more use when investigating control of VSCs in relatively large systems consisting of several converters. Such average models, on the other hand, do not consider the high-frequency harmonics, do not reveal possible resonances associated with the switching and other high-frequency phenomena, which are out of the scope of this thesis.

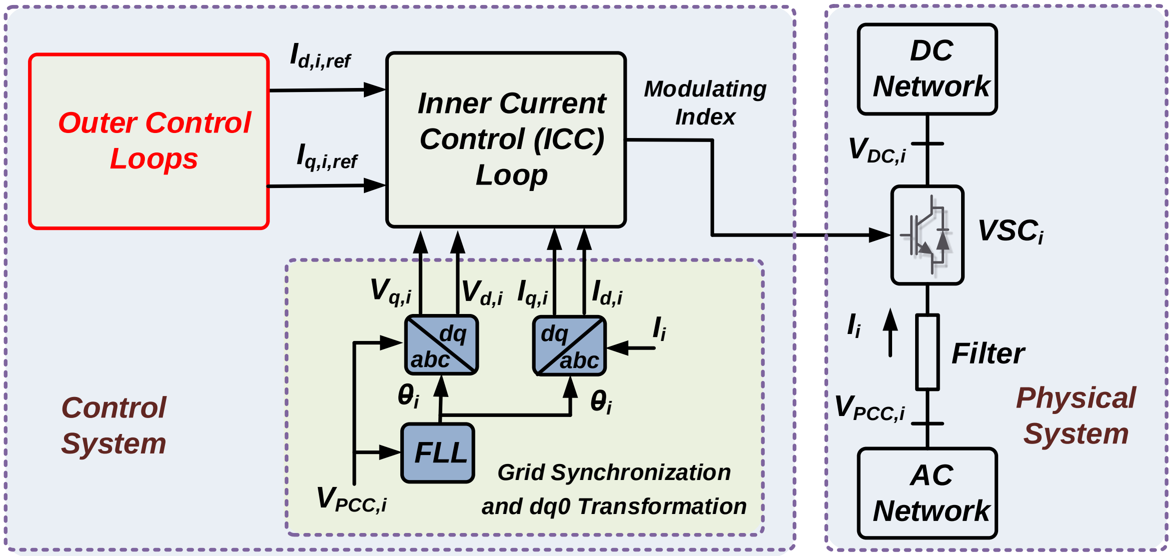

Figure 2.1. General structure of VSC integrated in the MT-HVDC system, the converter's control loops and its grid synchronization part.

2.1 Modelling and base control of the three phase VSC based MT-HVDC system

The general structure of the VSC integrated in the MT-HVDC system, the converter's control loops and its grid synchronization part are shown in Fig. 2.1. The control system generates the modulating index (control signal) which is provided to the VSC as a reference for shaping the latter's output voltage. Elaboration on each of the components is provided below, whereas the strategies developed in this thesis constitute the highlighted outer control loops of VSCs as will be shown in the latter chapters.

2.1.1 Modeling of the MT-HVDC VSCs

Three-phase ac/dc VSCs are one of the main components of MT-HVDC systems. A simple structure of a two-level three-phase VSC connected to the grid through a transformer/phase reactor is shown in Fig. 2.2a. Six IGBT switches are shown in the figure to represent the converter valves. In practice each valve consists of several series and parallel connected

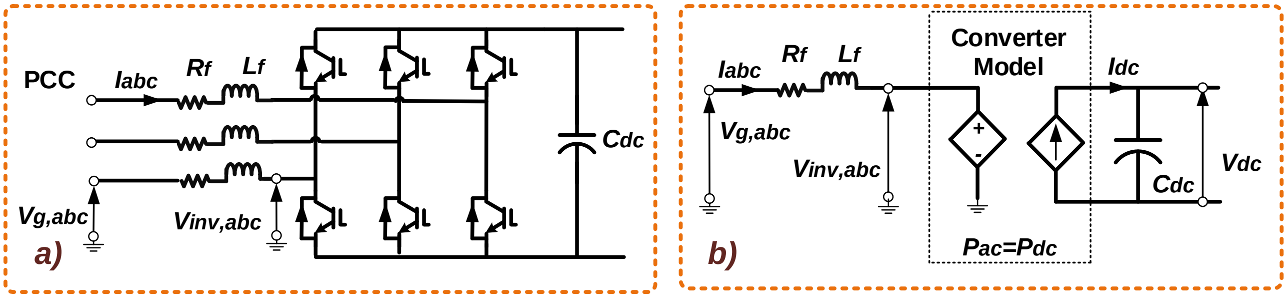

Figure 2.2. a) The topology of a two-level three phase VSC connected to the grid through filter and b) the corresponding equivalent circuit.

IGBTs to allow the converter to have higher voltage and current withstand capabilities compared to the rating of an individual switch. Anti-parallel diodes are added to each IGBT to allow the four-quadrant operation of the converter. The average value model of the three-phase ac/dc VSC shown in Fig. 2.2b is constructed based on the following assumptions [32]:

- As depicted in Fig. 2.2b, the dc side of the VSC is considered to be an ideal current source connected to the dc bus in parallel with a dc capacitor.
- The ac side of the VSC is assumed to be an ideal and fully controllable ac voltage source, and the value of the ac source voltages are determined by the modulation indexes provided by the control loop. The ac side voltage sources are connected to the PCC via a filter reactor L_f and R_f. In practice, the inductive element is used for filtering high frequency harmonics and providing means of control. The resistive element is used to represent the losses occurring in the converter such as caused by the switching and resistive parts of the filters.
- The dc and ac sides are interlinked by the active power balance between the two sides of the converter.

Applying Kirchhoff's law to the ac side of the VSC, the following s-domain three-phase equation is derived for the i_{th} converter:

$$V_{g,abc,i} = R_{f,i} I_{abc,i} + L_{f,i} s I_{abc,i} + V_{abc,i} \qquad (2.1)$$

where $V_{g,abc,i}$ and $V_{inv,abc,i} = V_{abc,i}$ are the three phase voltages at the PCC and inverter terminals, respectively, and the $I_{abc,i}$ is the three phase current passing though the filter reactor. The voltage $V_{inv,abc,i}$ is proportional to the three phase modulation voltage provided by the controller.

The ac quantities of equation 2.1 are then transferred to the synchronous $dq0$ reference frame by using Park transformation, which results in equation (2.2). Such transformation reduces each three-phase ac quantity (e.g., voltages, currents) into its two dc components, with the zero-sequence component being zero for balanced systems. This transformation facilitates the control of the currents and voltages as simple Proportional Integer (PI) controllers achieve zero steady-state error for dc quantities. Also, this transformation allows development of controllers that are able to regulate the converters active and reactive power injections independently. Detailed description of $abc - dq0$ transformation is provided in the Appendix.

$$\begin{cases} V_{g,d,i} = R_{f,i} I_{d,i} + L_{f,i} s I_{d,i} + V_{d,i} - \omega L_{f,i} I_{q,i} \\ \\ V_{g,q,i} = R_{f,i} I_{q,i} + L_{f,i} s I_{q,i} + V_{q,i} + \omega L_{f,i} I_{d,i} \end{cases} \tag{2.2}$$

In equation (2.2), $I_{d,i}$, $I_{q,i}$, $V_{g,d,i}$, $V_{g,q,i}$, $V_{d,i}$ and $V_{q,i}$ are the d and q axis components of the inverter current, the filter voltage and the inverter voltage of the i_{th} converter, respectively. ω is the angular frequency of the ac grid, which is present in the speed term $L_{f,i} \omega I_{d,i}$.

As the VSC is assumed to be an ideal voltage source, the voltage generated at the converter terminals is determined as

$$\begin{cases} V_{d,i} = \dfrac{m_d * V_{dc}}{2} \\ \\ V_{q,i} = \dfrac{m_q * V_{dc}}{2} \end{cases} \tag{2.3}$$

where m_d and m_q are the modulation indexes of the converter provided by the controller as will be later discussed. The power on the ac side of the VSC can be calculated as per

$$P_{ac,i} = V_{d,i} I_{d,i} + V_{q,i} I_{q,i} \tag{2.4}$$

Considering the power balance on the ac and dc sides of the VSC, the current injected to the dc grid before the capacitor is

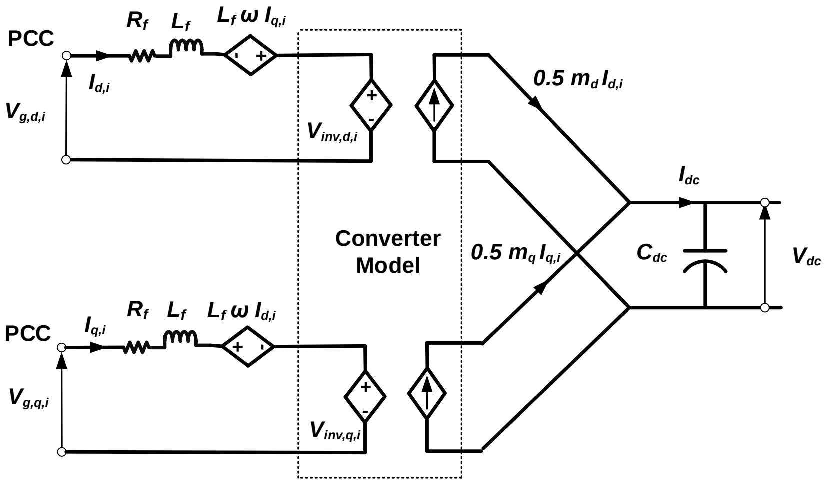

Figure 2.3. Equivalent circuit of three-phase ac/dc VSC in $dq0$ reference frame.

$$I_{dc,i} = \frac{P_{dc,i}}{V_{dc,i}} \approx \frac{P_{ac,i}}{V_{dc,i}} = \frac{V_{d,i}I_{d,i} + V_{q,i}I_{q,i}}{V_{dc,i}} \tag{2.5}$$

The combination of (2.3) and (2.5) yields to

$$I_{dc,i} = \frac{V_{dc,i}m_dI_{d,i} + V_{dc,i}m_qI_{q,i}}{2V_{dc,i}} = \frac{m_dI_{d,i} + m_qI_{q,i}}{2} \tag{2.6}$$

The equivalent circuit of the converter can therefore be represented in dq reference frame as shown in Fig. 2.3.

2.1.2 Modeling of the dc network

Similar to many other studies designing new controllers for VSCs interfacing to dc grids [27, 28, 30, 31, 33], this thesis uses π section model of dc lines. It is worth mentioning that the dynamics associated with higher frequency transients (e.g., lightning transients) can be captured by using more-advanced line models, which is out of the scope of this thesis. The respective equivalent circuit is shown in Fig. 2.4, where L_{ij} and R_{ij} are the inductance

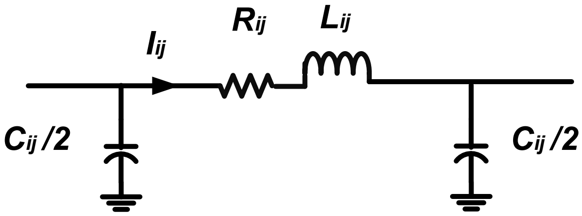

Figure 2.4. π equivalent circuit of the line.

and resistance of the line between i_{th} and j_{th} nodes, C_{ij} is the respective capacitance of the line, distributed at two ends of the line.

At each converter station, the capacitances of the VSCs and lines are in parallel. The equivalent capacitance seen at each converter is therefore given by

$$C_{eq,i} = C_{dc,i} + \sum_{j=1,j\neq i}^{n} \frac{C_{ij}}{2} \tag{2.7}$$

where $C_{eq,i}$ is the aggregated capacitance at i_{th} station, $C_{dc,i}$ is the capacitance of the VSC capacitor bank and C_{ij} is the capacitance of the dc line between i_{th} and j_{th} converter stations, n is the number of converter stations. The same approach can be used in case if intermediate junctions are present in the dc system, while in the systems under thesis the latter is absent.

The imbalance between input and output powers of dc capacitor causes dc voltage variations. The dynamic behavior of dc voltage at the i_{th} converter station is determined by the equation (2.8),

$$V_{dc,i} = \frac{1}{sC_{eq,i}}(I_{dc,i} + \sum_{j=1,j\neq i}^{n} I_{ji}) = \frac{1}{sC_{eq,i}}(I_{dc,i} + \sum_{j=1,j\neq i}^{n} \frac{V_{dc,j} - V_{dc,i}}{2(R_{ij} + L_{ij}s)}) \tag{2.8}$$

where I_{ji} is the current flowing from j_{th} to i_{th} node, $V_{dc,j}$ is the voltage of the neighboring j_{th} converter, $I_{dc,i}$ is the injected current from the ac system, which is determined as per equation (2.5). Finally, the block diagram model of the ac and dc sides of the VSC can be presented together as shown in Fig. 2.5.

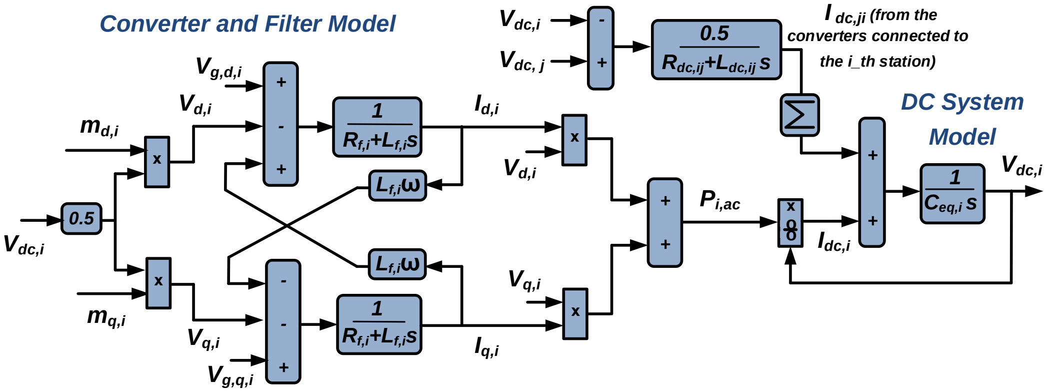

Figure 2.5. Block-diagram models of both the ac and dc sides of the considered three-phase ac/dc VSC at the i_{th} converter station without its control.

2.1.3 The base case controller of three phase ac/dc VSC

Hierarchical control strategy with a fast inner current controller (ICC) and the slower outer loops is commonly used for the VSCs of the MT-HVDC system. This strategy is developed based on the converter+filter model presented in Subsection 2.1.1. As shown in Fig. 2.6, the decoupled current control is realized in the d and q axes for the inner loop of the cascaded control structure, where the dq reference frame is aligned with PCC voltage. Such alignment is achieved with the help of FLL that will be introduced in Subsection 2.1.4. The decoupling effect between d and q axes currents is realized by providing voltage compensation for the speed voltage term and feedforward compensation of the ac grid voltage. The current controller loop generates the modulation indexes m_d and m_q, which are used to shape the fundamental component of the inverter output voltage. The tuning of the ICC's parameters is discussed in the Appendix.

The outer control loops generate the current references based on the pre-specified tasks. The d -xis reference current is usually determined based on the active power/dc bus voltage control loops to respectively regulate either the converter output active power magnitude or the dc voltage at the converter terminals. This thesis aims an identification of suitable control strategies for the calculation of active current reference and the subsequent management of the active power flow through the VSCs considering several objectives related to the operation of dc grids. The q-axis reference current, on the other hand, is used to either regulate the PCC voltage on the ac side of the VSC or the latter's reactive power

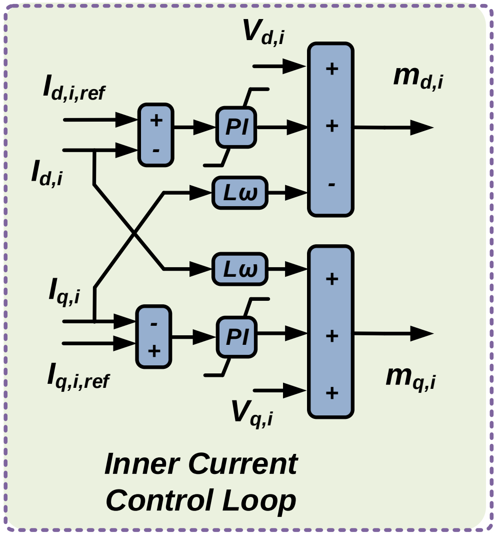

Figure 2.6. Structure of the inner current control loop of three-phase ac/dc VSC.

output.

2.1.4 Three-phase frequency detection technique for MT-HVDC application

An accurate estimation of the grid frequency and phase angle are challenging tasks and prerequisite for the proper operation of the grid connected VSC based systems [34,35]. The detection of those parameters allows performing the Park transformation and acquiring d, q voltage and current components used in the previously presented models. It is usual practice to align the d, q reference frame with the d axis of the PCC voltage. To achieve this alignment, Synchronous Reference Frame Phased Locked Loops (SRF-PLL) are widely used in the literature [32, 36].

In this thesis, instead of SRF-PLL, the recently proposed FLL [37] is used to align the dq synchronous reference frame with the PCC voltage of the respective VSC. Although conventional SRF-PLL has a simple structure and fast dynamics during ideal grid voltage conditions, they suffer from poor disturbance rejection when grid voltage is unbalanced and distorted. To overcome this issue, several advanced SRF-PLLs, with filtering stage for the rejection of dominant disturbances, have been recently presented in the literature.

However, as it is shown in [38], advanced SRF-PLLs can achieve enhanced disturbance rejection only at the expense of settling time not less than two cycles [39, 40]. Having the aim to achieve similar characteristics as conventional type 2 SRF-PLL (zero steady state error in the detected phase during the step change in frequency), FLL has been recently proposed in [37]. The advantage of the FLL is that unlike SRF-PLL, the phase angle with FLL is detected outside of the closed-loop feedback control system. That is, for the type 2 SRF-PLL two integrators are used in the closed loop system for the phase angle detection: one in the Loop Filter (PI controller) and the other in the Voltage Controlled Oscillator (integrator). While for the FLL only one integrator is used in the phase detection loop. Therefore, the FLL achieves faster detection of the phase angle than SRF-PLL. The operational principle of FLL can be better visualized when the grid voltage is purely sinusoidal with unity magnitude. The Clarke transformation of this ideal three-phase voltage is as follows

$$\frac{2}{3}\begin{bmatrix} 1 & \frac{-1}{2} & \frac{-1}{2} \\ 0 & \frac{\sqrt{3}}{2} & \frac{-\sqrt{3}}{2} \\ \frac{1}{2} & \frac{1}{2} & \frac{1}{2} \end{bmatrix} \begin{bmatrix} sin(\omega t+\theta) \\ sin(\omega t+\theta-\frac{2pi}{3}) \\ sin(\omega t+\theta+\frac{2pi}{3}) \end{bmatrix} = \begin{bmatrix} sin(\omega t+\theta) \\ -cos(\omega t+\theta) \\ 0 \end{bmatrix} \tag{2.9}$$

The derivatives of the α, β components computed in 2.9 will be as follows

$$\begin{bmatrix} V_\alpha(t)' \\ V_\beta(t)' \end{bmatrix} = \begin{bmatrix} (sin(\omega t+\theta))' \\ (-cos(\omega t+\theta))' \end{bmatrix} = \begin{bmatrix} \omega cos(\omega t+\theta) \\ \omega sin(\omega t+\theta) \end{bmatrix} \tag{2.10}$$

Taking into account that $sin(\alpha)^2 + cos(\alpha)^2 = 1$, the grid frequency can be determined as per

$$\sqrt{V_\alpha(t)'^2 + V_\beta(t)'^2} = \sqrt{\omega^2(cos^2(\omega t+\theta) + sin^2(\omega t+\theta))} = \omega \tag{2.11}$$

The voltage phase angle can be extracted by integrating the grid frequency acquired in (2.11). In the case of non-ideal grid voltage, the FLL implementation is shown in Fig. 2.7. The prefilters are used to eliminate the dominant harmonics present in the d, q components of the grid voltage, after which each of those components is divided by the instantaneous

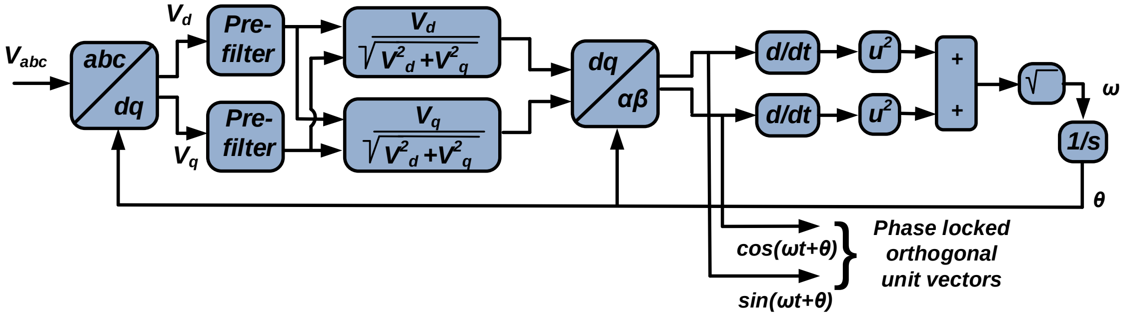

Figure 2.7. FLL for the acquisition of the orthogonal unit vectors.

magnitude of the grid voltage to get the unity magnitude voltage to be transformed to α, β frame. The orthogonal unit vectors $cos\theta$ and $sin\theta$ shown in Fig. 2.7 are directly utilized in the controller of the respective converter for the d, q transformation of the voltages and currents.

2.1.5 Modeling of Modular Multilevel Converter

The controllers developed for MT-HVDC systems, which will be presented in Chapter 4 and Chapter 5, are also validated considering Modular Multilevel Converter (MMC) based systems. To this end, an aggregated model of the half-bridge MMC was developed according to Fig. 2.8 [41–43]. In this model, the control signal is the number of inserted and blocked modules, $N_{inserted}$ and $N_{blocked}$, respectively. The capacitor voltage V_{cap} is the main output of the block, which presents the average value of MMC capacitor modules. Although the model is developed based on the assumption that the voltages of capacitor modules are well-balanced, it is still suitable for investigating the control system dynamics [44].

2.1.6 Modelling of the systems interfacing to MT-HVDC grids

This subsection presents the modeling of the systems connected to the ac sides of ac/dc converters in MT-HVDC grids. As the ac and dc sides of the VSC are connected through an active power balance, the components responsible for the active power management in those ac systems are elaborated upon. Concentration on the specific components is motivated by their relevance and impact on the performance of converters' controllers developed later

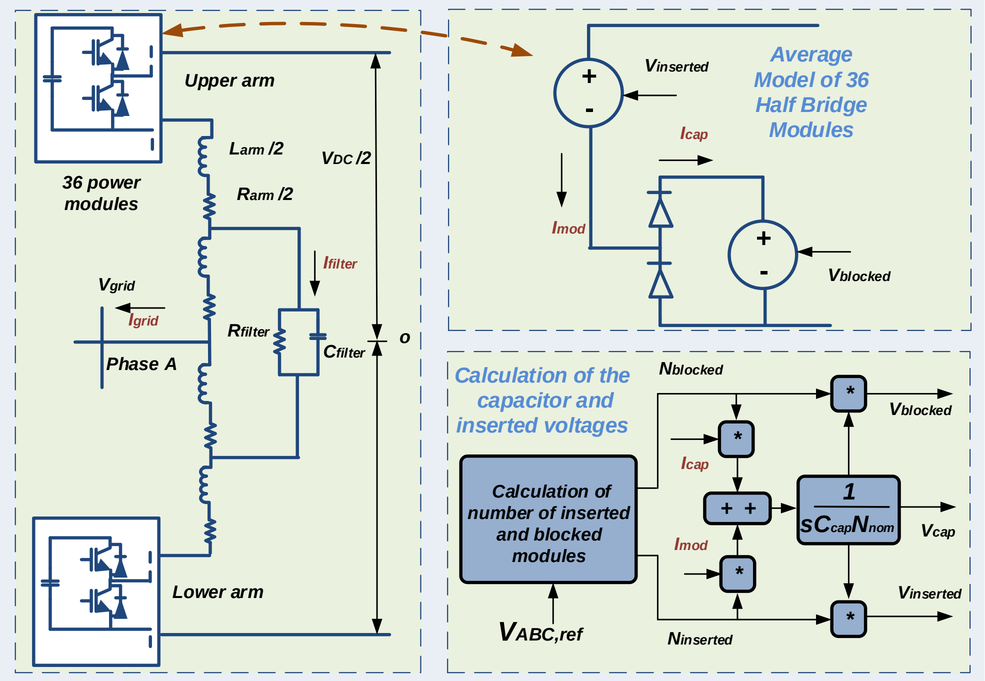

Figure 2.8. The implemented average model of the Half Bridge Modular Multilevel Converter (MMC) and the calculation of the inserted and module capacitor voltages.

in this thesis. Particularly, Chapter 5 demonstrates how the active power can be re-routed between the converter stations of MT-HVDC systems for ensuring enhanced frequency characteristics of each ac grids connected to individual converter. Thus, the ac components that have a major impact on frequency response are elaborated.

2.1.6.1 Modelling of the ac systems interfacing to MT-HVDC grids

An aggregated representation of ac generators together with frequency-dependent loads is used for the modeling the frequency dynamics of ac systems [45], therefore the frequency dynamics of the i_{th} ac grid can be expressed as follows

$$f_i - f_{nom,i} = \frac{P_{m,i} - P_{l,i} - P_{VSC,i}}{2H_i s + D_i} \tag{2.12}$$

where f_i and $f_{nom,i}$ are the measured and nominal frequencies of the system, $P_{m,i}$ and $P_{l,i}$ are the mechanical power provided to the generator and the load demand at the system, H_i and D_i are the equivalent inertia constant of the ac system and its load damping constant, respectively. The selection of the frequency dependent load models is done to present the possible impacts of the loads on the proposed frequency regulation technique.

The mechanical power $P_{m,i}$ is provided by the corresponding turbine-governor model. Three different energy sources, namely thermal, gas and hydro, are considered in this thesis. Thus, the corresponding turbine-governor models are implemented below. Please note that the selection of the ac systems' models does not affect the development of the proposed strategies. The selection of the below-described turbine-governor models aims to present large variety in frequency responses of ac systems, thus serve as a more challenging scenario for the verification of the proposed algorithms presented later in this thesis. IEEEG1 turbine-governor model, which is depicted in Fig. 2.9, is used to represent steam power plants as recommended by [46]. The parameters of the model are taken from [47]. The gas-fired plants are represented with the GAST turbine-governor model of Fig. 2.10 with the parameters acquired from [48]. Hydraulic turbines used in hydro power stations are modeled according to [49, 50], and the respective block-diagram based model is shown in Fig. 2.11. The parameters of the above-presented models can be found in the Appendix.

2.1.6.2 Modelling of the WPPs interfacing to MT-HVDC grids

MT-HVDC systems are becoming a popular for integration wind energy, especially when offshore wind generation is considered. Therefore, in the considered MT-HVDC systems

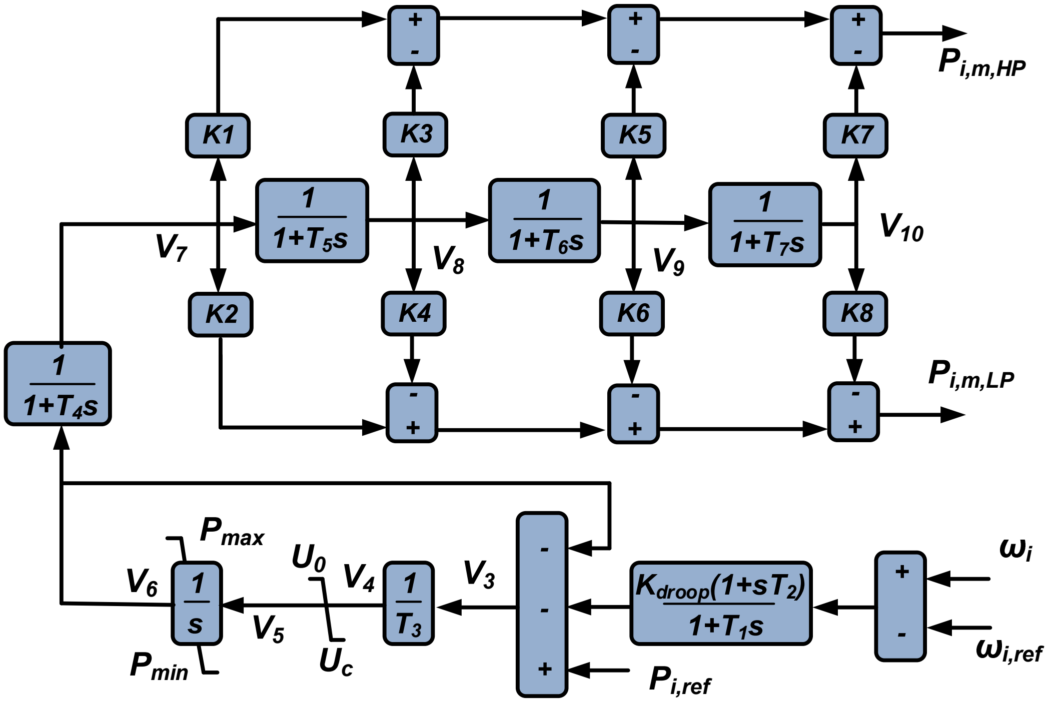

Figure 2.9. IEEEG1 model used to represent steam turbine-governors in this thesis.

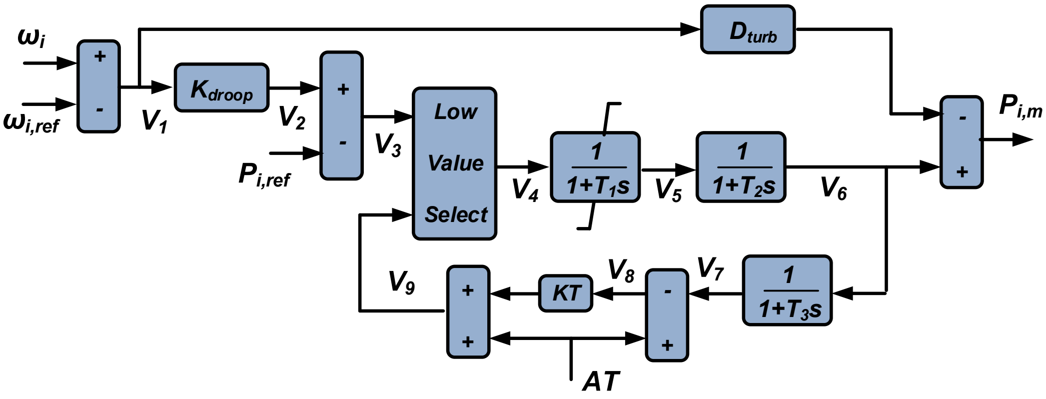

Figure 2.10. GAST model diagram used to represent gas turbine-governors in this thesis.

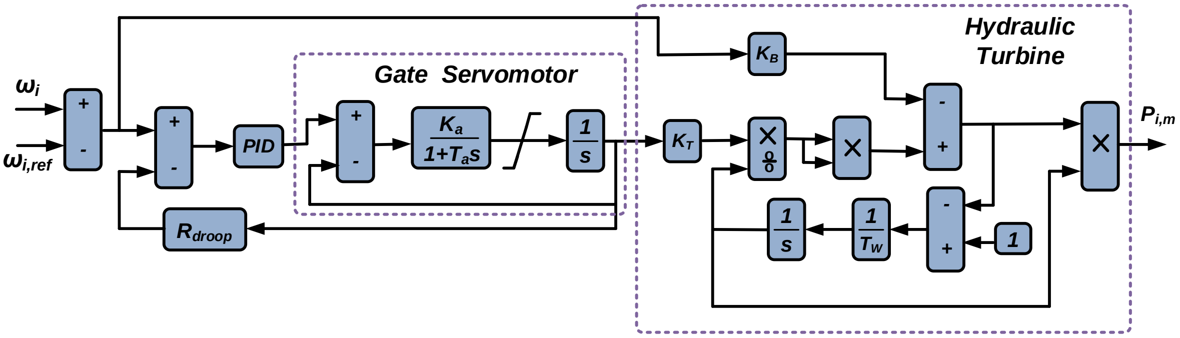

Figure 2.11. Hydraulic turbine and governor model used in this thesis.

wind turbines are interfaced to at least one of the converter stations of MT-HVDC systems. Type-4 variable speed wind turbines with Permanent Magnet Synchronous Generators (PMSG-WT) are considered in this thesis with the dynamics of the i_{th} turbine given by

$$\begin{cases} w_{r,i} - w_{r,nom,i} = \dfrac{1}{sJ_{WT}}(\dfrac{N_p}{2}(T_{m,i} - T_{e,i}) - Dw_{r,i}) \\[2ex] T_{(m/e),i} = \dfrac{P_{(m/e),i}}{w_{r,i}} \\[2ex] P_{m,i} = \dfrac{1}{2}\pi\rho r^2 v_{wind}^3 C_p(\beta_i\lambda_i) \end{cases} \tag{2.13}$$

where $T_{m,i}$ and $T_{e,i}$ are the mechanical and electrical torque of the wind turbine, respectively, $P_{m,i}$ and $P_{e,i}$ are the mechanical and electrical power of the wind turbine, respectively, N_p is the number of pole pairs, D is the damping, $w_{r,i}$ is the turbine speed, ρ is the air density, r is the turbine blade radius, v_{wind} is the wind speed, J_{WT} is the combined moment of inertia of the generator and turbine blades. The power coefficient C_p is a function of the tip speed ratio λ_i and pitch angle β_i as per equation (2.14) [51].

$$\begin{cases} C_p = (0.44 - 0.0167 * \beta_i) * sin(\pi * (\lambda_i - 3)/15 - 0.3 * \beta_i) - 0.00184 * (\lambda_i - 3) * \beta_i \\[2ex] \lambda = \dfrac{w_{r,i}R}{v_{wind}} \end{cases} \tag{2.14}$$

The electrical power $P_{e,i}$ extracted from the turbine is given by

$$\begin{cases} P_{e,i} = P_{MPPT,i} - \Delta P_{del.,WT,i} \\ P_{MPPT,i} = w_{r,i}^3 k_{MPPT} \\ \Delta P_{del.,WT,i} = P_{del.,WT,max,i} - P_{del.,WT,i} \end{cases} \tag{2.15}$$

where $P_{MPPT,i}$ is the power acquired from Maximum Power Point Tracking (MPPT) algorithm as per (2.15). Please notice that the turbines might operate at off-MPPT point by $\Delta P_{del.,WT,i}$ reduced power as the deloaded operation enables WTs to provide sustainable frequency support capability [52, 53]. 10% maximum delaoding level for WTs ($P_{del.,WT,max} = 0.9 P_{MPPT}$) is considered in this thesis [54]. $P_{del.,WT,i}$ is the actual deloading power, which is a function of frequency deviations and is generated by the centralized controller as will be explained in Chapter 5. From the WPP owners' perspective the above-described sub-optimal operation of wind turbines might not be desired. However, several TSOs have already put or are planning to place requirements on wind farms to participate in system frequency responses, even if the service would be achieved at the expense of reduced power output during normal operation [55, 56]. For example, the European Network of Transmission System Operators (ENTSO-E) has already put a requirement on WPPs to participate in frequency support with the details provided in the updated grid code titled Requirements for Generators (RfG) [56, 57]. Specifically, the RfG requires large wind farms to participate in both over-frequency and under-frequency events, demanding those farms to operate below available capacity to achieve the mentioned goal [56]. The participation of wind farms in frequency regulation might also be viewed as an ancillary service with additional financial benefits provided for that service [56], and this participation can also improve the system flexibility [58].

2.2 Modelling and base control of dc/dc converter based MT-DCμGrids

2.2.1 Modelling of dc/dc converters

In MT-DCμGrid applications, dc/dc converters are usually used to interface energy sources and loads to dc grid. The dc/dc converter considered in this thesis is of boost type, and its topology is shown in Fig. 2.12a. The converter consists of two semiconductor devices; a transistor and a diode, and of two energy storage devices; inductor L_f and capacitor C_{dc}.

Fig. 2.12b depicts the equivalent average-value based circuit of the boost converter. The converter is modelled as a variable current source behind the capacitor on the higher voltage side, which is also the dc grid side. On the low voltage side the converter is represented as a variable voltage source connected to the energy source through L_f- R_f impedance. The power balance is used to connect the two sides (voltage source side and current source side) of the converter in the developed model. The Kirchhoff's voltage law across L_f, R_f of the i_{th} converter is given by

$$V_{dc,source} = R_{f,i} I_{inner,i} + L_{f,i} s I_{inner,i} + V_{dc,low,i} \tag{2.16}$$

where $V_{dc,source}$ and $V_{dc,low,i}$ are the voltages across the energy course and variable voltage source, respectively, and $I_{inner,i}$ is the current flowing through an inductor L_f. As the focus of this thesis is the modification of the outer loop controller, the source is modeled as an ideal voltage source [59]. The inductor current is therefore given by

$$I_{inner,i} = \frac{V_{dc,source} - V_{dc,low,i}}{R_{f,i} + L_{f,i} s} \tag{2.17}$$

The magnitude of current I_i injected by the current source is then determined based on the power balance equation as per

$$I_i = \frac{I_{inner,i} V_{dc,low,i}}{V_{dc,i}} \tag{2.18}$$

The voltage $V_{dc,low,i}$ is determined as per (2.19) as a function of the duty ratio D_i supplied by the control system.

$$\begin{cases} V_{dc,low,i} = m_i \dfrac{V_{dc,i}}{2} + \dfrac{V_{dc,i}}{2} \\ m_i = ((1-D) - 0.5) * 2 \end{cases} \tag{2.19}$$

In (2.19), m_i is the modulation index scaled from [-1 to 1]. Finally, the voltage across the output capacitor is determined as a function of the input current I_i and output current $I_{out,i}$

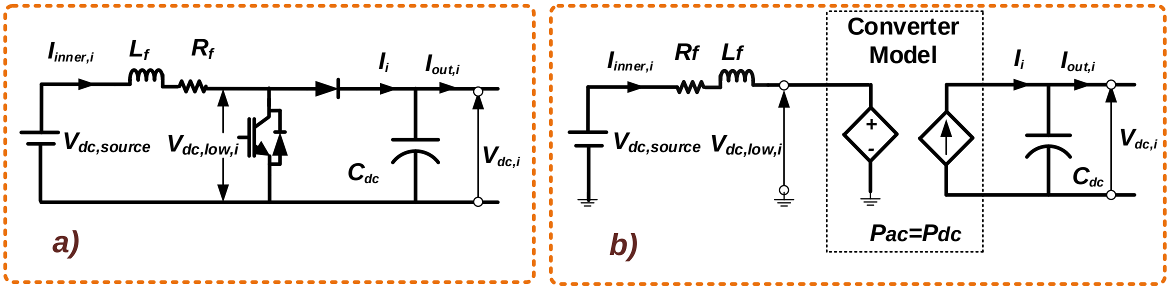

Figure 2.12. a) The topology of a dc/dc boost converter and b) its equivalent circuit.

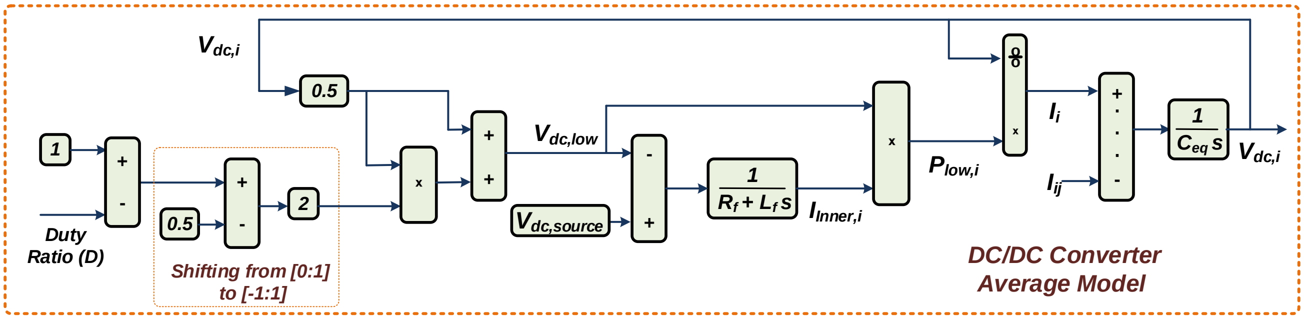

Figure 2.13. The mathematical model of the dc/dc boost converter.

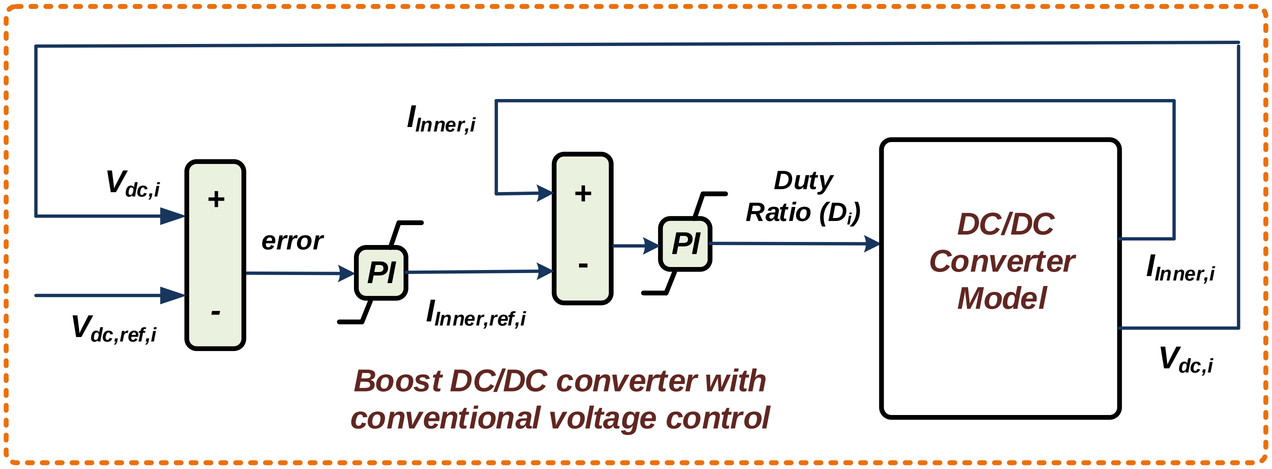

Figure 2.14. Conventional voltage control of dc/dc converter.

$$\begin{cases} V_{dc,i} = (I_i - \sum_{j=1}^{n} I_{ij}) \dfrac{1}{sC_{eq,i}} \\ I_{out,i} = \sum_{j=1}^{n} I_{ij} \\ C_{eq,i} = C_{dc,i} + \sum_{j=1, j\neq i}^{n} \dfrac{C_{ij}}{2} \end{cases} \tag{2.20}$$

where $I_{out,i}$ is determined as a sum of all currents I_{ij} flowing from the i_{th} converter towards any other j_{th} converter connected to the former converter. The equivalent capacitance $C_{eq,i}$ is determined as a sum of converter capacitance $C_{dc,i}$ and capacitances C_{ij} of the π modeled lines connected to the i_{th} converter. The mathematical model of the converter based on equation (2.16)-(2.20) is shown in Fig. 2.13.

The dc/dc converters are connected in parallel to form the MT-DCμGrid. Cascaded controller is implemented for these dc/dc converters as shown in Fig. 2.14. The inner loop determines the duty ratio of the converter by controlling the inductor current I_{inner}, and the reference for the latter parameter is determined in the outer voltage control loop. This cascaded control structure ensures the reference current and voltage tracking, providing current limiting capability and increasing the system bandwidth.

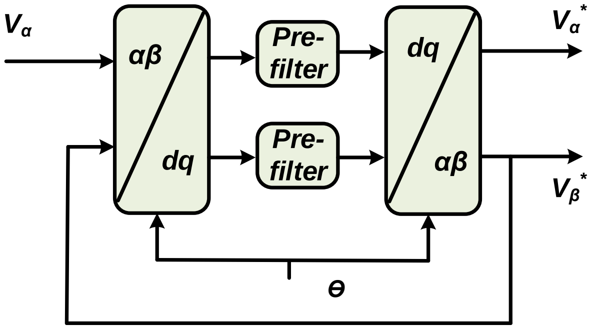

Figure 2.15. Inverse-Park transformation-based OSG block.

2.2.2 Single-phase frequency detection technique for MT-DCμGrid application

In this thesis, a new control solution is developed for MT-DCμGrids and presented in Chapter 6. An important component of the proposed algorithm is the proper detection of the frequency of a single-phase ac signals, which is going to be superimposed on dc grid voltage. Therefore, in this subsection the model of the frequency detection technique is presented. Recently reported single phase frequency detection algorithm, namely Type-1 single-phase Frequency Locked Loop (FLL), is used in the current work [60].

Like in three-phase frequency detection algorithms, the synchronous reference frame (SRF) technique can be also applied for single-phase frequency detection applications. However, in single-phase applications the Park transformation can not be directly applied as there is only one input signal: that is, there is only α component input to the frequency detection algorithm in single-phase use instead of $\alpha - \beta$ components naturally available in three-phase application. An orthogonal signal generation (OSG) method is therefore used to generate fictitious β component, which is orthogonal to the initial single-phase input α component. The implemented OGS for single-phase systems is depicted in Fig. 2.15, where the as pre-filters are low pass filters [61].

After generating the orthogonal signals $\alpha^* - \beta^*$ in OSG, these components are then supplied to SRF based frequency detection algorithm. The latter algorithm is identical to the portion of FLL presented in the previous section for three-phase system application. Fig.2.16 depicts the diagram of the complete structure of single-phase FLL. In Fig.2.16, after OSG operation, the selective elimination of the dominant harmonics and the amplitude

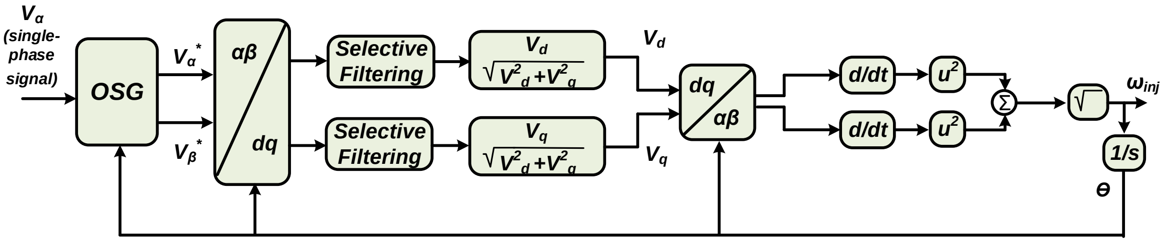

Figure 2.16. The block diagram of the implemented structure of the frequency estimation part in the implemented FLL

normalization allow generation of the unity voltages with negligible harmonic content. Those voltages are the inputs required to be provided to the frequency detection loop, where the Clark Transformation is used to generate the α, β orthogonal and filtered unit vectors, and the grid voltage is simply estimated as

$$\sqrt{V_\alpha(t)'^2 + V_\beta(t)'^2} = \sqrt{\omega^2(cos^2(\omega t + \theta) + sin^2(\omega t + \theta))} = \omega \tag{2.21}$$

The implemented algorithm achieves enhanced performance with zero steady-state error even when the input single-phase voltage is not purely sinusoidal or when the input experiences changes in magnitude, frequency or phase angle. Therefore, the implemented frequency detection algorithm allows proper operation of the controller proposed in Chapter 6.

2.3 Modal Analysis

The MT-HVDC and MT-DCμGrid systems considered in this studies are formed by combining the respective models of different components described above. Before conducting the time-domain simulations of the considered test systems and the developed control approaches, the respective models are used for conducting modal analysis and evaluating the system's stability. To these end, the linearization of the respective models around an operating point is performed using the Simulink linearization toolbox [62]. Please note that with this technique a linear state-space model is computed by linearizing each block in a model individually. The combined block-diagram model of the VSC based MT-HVDC

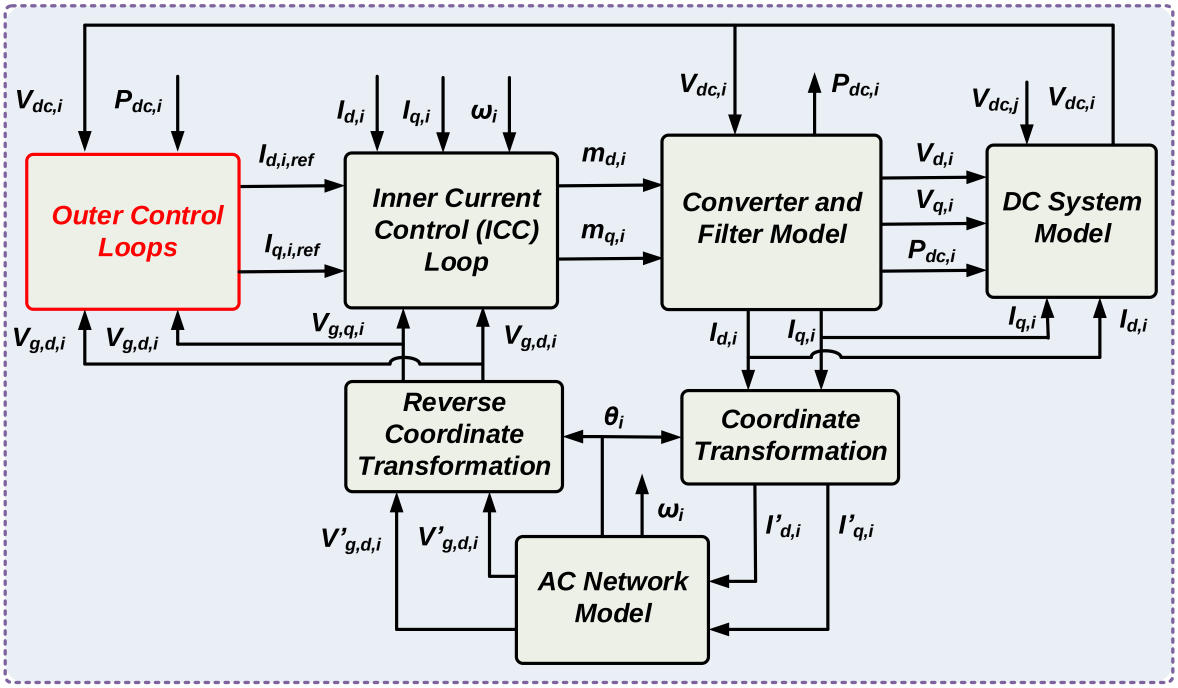

Figure 2.17. The combined block diagram of the VSC based MT-HVDC system used for the stability analysis.

system used for the linearization is shown in Fig. 2.17. The variables of the converter's model and the ac network's model are interfaced by applying coordinate transformation on the variables of the respective models (e.g. converter currents, grid voltages). The details about the coordinate transformation are provided in the Appendix. Similarly, the combined block-diagram model of the VSC based MT-DCμGrid is shown in Fig. 2.18. After linearizing the respective models, the acquired state-space models have the form of (2.22)

$$\Delta \dot{x} = A\Delta x + B\Delta u \tag{2.22}$$

where Δx and Δu represent the state and input vectors, A and B represent the state and input matrix, respectively. Afterwards, the system eigenvalues are acquired from the state matrix A under varying parameters as discussed later. The acquired modes are used to investigate the effect of the parameter variation on the movement of the eigenvalues.

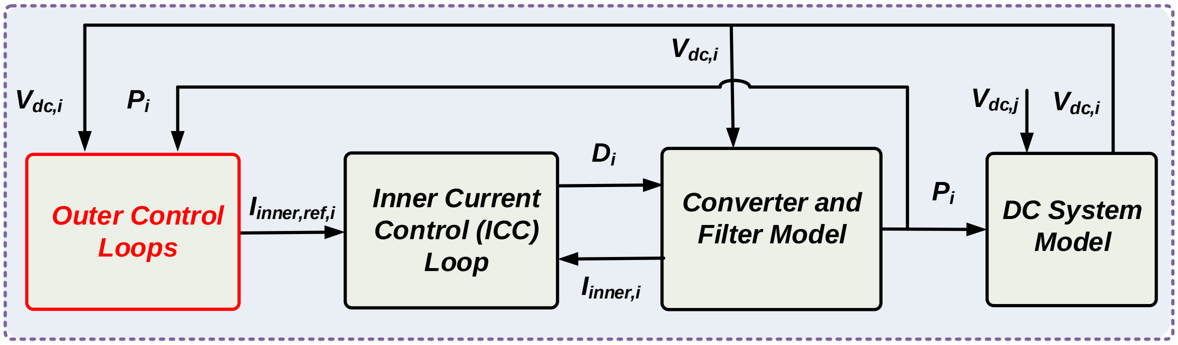

Figure 2.18. The combined block diagram of the MT-DCμGrid used for the stability analysis.

Please note that when considering the effect of the variation of a certain parameter on the eigenvalue movement, the operating point is not change throughout variation of the considered parameter. Furthermore, the participation factor analysis was conducted to illustrate the relative significance of a specific state to the mode of interest. Therefore, for any eigenvalue λ_i, the right eigenvector ϕ_i (column vector) and left eigenvector ψ_i (row vector) are calculated so that they satisfy the equations (2.23) and (2.24), respectively [45].

$$A * \phi_i = \lambda_i * \phi_i \tag{2.23}$$

$$\psi_i * A = \lambda_i * \psi_i \tag{2.24}$$

where λ_i is the i_{th} eigenvalue. The participation factor matrix is then constructed based on the definition of [63, 64] as per

$$P_{k,i} = \frac{|\phi_{i,k}||\psi_{k,i}|}{\sum_{k=1}^{n} |\phi_{i,k}||\psi_{k,i}|} \tag{2.25}$$

The participation factor $P_{k,i}$ indicates the relative participation of the k_{th} state variable on the i_{th} eigenvalue, which can be helpful, especially for understanding the root cause of the dominant poles. The above definition of participation factor resolves the issue of imaginary parts of the participation factor that would result from direct element-wise multiplication of right and left eigenvectors when complex eigenvalues are present in the system.

2.4 Discussion

This chapter elaborated on some of the components of the dc and hybird ac/dc systems. The respective circuit-based and mathematical models were then developed for those components. Main attention was given to the components that have relatively more influence on the converters' control interfacing to those dc systems. After presenting the implemented models for MT-HVDC and MT-DCμGrid systems, the base-case controllers for each system was detailed. The control strategies examined in the Literature Review chapter (Chapter 3) and the control approaches proposed later in this thesis (Chapter 4-Chapter 6) use the controllers of this chapter in their lower-level structure. Finally, the approach for evaluating the stability of the proposed controllers is discussed.

Chapter 3

Literature Review

The parallel operation of the converters in dc grids is a widely accepted practice due to advantages such as reliability and ease of expansion. Therefore, regulation of the dc system voltage is important for stable and continuous operation of the dc grid as the voltage is a direct indicator of the power balance in the network. As such, the dc voltage behaves similar to an ac frequency in the ac system [65]: the active-power mismatch in an ac system leads to the frequency deviation, where as that in a VSC based dc grid leads to the dc voltage deviation. What is more, the surplus of active power in a dc system increases dc system voltage, similar to what happens in ac grids, where excess active power causes frequency increase. The identical trend exists for the lack of active power, with reduced dc voltage and ac frequency in dc and ac systems, respectively.

However, unlike ac frequency, dc voltage is not a global parameter across the entire dc system and might vary significantly at different terminals in the dc network, increasing the complexity of controlling dc voltage and power flow. Moreover, little standardization is present for dc networks. Nevertheless, dc voltage is considered to be the best indicator of the stable and continuous operation of dc grids, in both MT-HVDC and MT-DCμGrid applications. Therefore, the control of dc voltage is of vital importance for dc systems. What is more, proper rerouting of the active power in dc grids is critical for achieving various control objectives, for example, ratio-based power sharing between converters. These goals can be realized by developing proper control algorithms for VSCs interfacing with dc grids.

This chapter reviews the relevant literature on existing control approaches for the outer loops of ac/dc VSCs employed in MT-HVDC systems and dc/dc converters employed in MT-DCμGrids. An introduction to the basic alternatives to the outer loop control for both applications is provided. The voltage-power/current droop controller is emphasized as this approach is widely used for both MT-HVDC and MT-DCμGrids applications.

3.1 Droop control in MT-HVDC systems

MT-HVDC systems have been the subject of many recent scientific works, including studies on the development of modelling approaches [36, 66] for such systems, combined ac-dc power flow algorithms [67–70], dc and ac fault ride-through strategies [71–74], enhancement of the transient stability of MT-HVDC based systems [31, 75, 76], the development of oscillation damping strategies [77, 78], dc voltage control [79–83] and mutual frequency support [79, 84–90] algorithms. From the dc grid perspective, dc link voltage control, and sharing of the power mismatch in dc grids between VSCs are of prime importance, whereas from the ac perspective, it is important to achieve proper mutual frequency support between MT-HVDC interconnected ac systems.

3.1.1 Main control approaches

The dc grid voltage control approaches are divided into three main categories: (1) master-slave control, (2) voltage-margin control and (3) voltage-droop control [71]. The first approach relies on a single converter to control the dc grid voltage, while other converters operate under constant power/current control modes. This approach achieves precise dc voltage control at the master converter and accurate power regulation at the converters other then the master converter, assuming that the master converter is able to accommodate any power imbalance in the dc grid [91]. However, this approach requires significant power headroom in the master converter to accommodate power imbalances and might result in high stresses on the grid/unit connected at the master converter. What is more, the system voltage control can be lost if the master converter is disconnected or when this converter reaches its power limits. To increase system reliability, decentralized control approaches such as voltage-margin and voltage-droop ones have been developed. Similar to the master-slave approach, at any operating point, the voltage-margin relies on a single converter to regulate the dc voltage while the other converters adopt constant power control. However, unlike the former controller, the voltage-margin controller continues reliable operation after the failure of the master converter as another converter picks up on the task of regulating the dc voltage. The updated master converter regulates the grid voltage at a different voltage level to allow autonomous transition between the voltage regulating converters. The transition between these two reference voltages might cause high stress on the converters and other system components [71]. Furthermore, the difference between the two voltage references in voltage-margin control should be large enough to avoid transition during normal system operation, as such transition might cause poor dc voltage regulation.

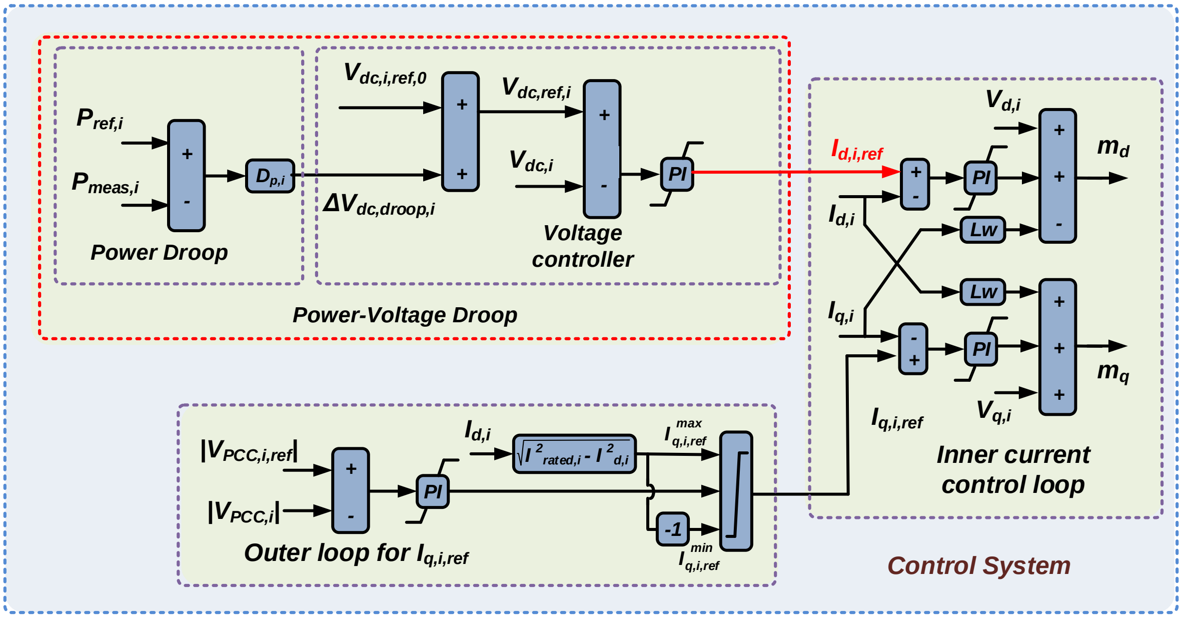

Figure 3.1. The power-voltage droop control structure for three-phase ac/dc converter in MT-HVDC applications.

Originated from the power-frequency droop control of ac systems, dc power-voltage droop approach is commonly used for the control of VSC based MT-HVDC systems [31, 36, 66–90, 92–97]. Conventional power-voltage droop control is shown in Fig. 3.1, where the dc voltage reference is linearly altered with any change in the converter power mismatch (the difference between reference and measured active power injections). This control strategy aims to achieve power/current sharing and dc voltage regulation simultaneously using several converters based on their respective droop coefficient. Droop control has an advantage over master-slave control in terms of distributed voltage regulation and reduced stress on individual ac grids, whereas the advantage of droop control over voltage-margin control is reduced system oscillations.

However, the difference between the conventional dc power-voltage droop control and the ac power-frequency droop control is the lack of a common signal in the dc grid and much faster dynamics associated with dc voltage control [98]. The combined result is poor reference tracking for the converters, which brings additional challenges to controller implementation. In addition, the load sharing is not exclusively dependent on the droop parameters but is also determined based on the line parameters and system topology of a dc grid, making it difficult to plan the exact power sharing.

Fig. 3.1 also shows one of the possible implementations of the loop responsible for generating the reactive current reference $I_{q,i,ref}$. In this figure, the voltage magnitude at the PCC is compared with its reference value and the error is minimized by feeding it to the respective controller. The control of the magnitude of the immediate output voltage of the converter results in reactive power injection/absorption to/from the grid. Thus, the $I_{q,i,ref}$ can be generated for accurately controlling the reactive power output of the converter or for regulation of the ac side voltage to its nominal value. If the latter is the control objective, then in Fig. 3.1 the voltage magnitude error should be replaced with the reactive power injection error (difference between the desired reactive power reference and the measured reactive power). It is, however, worth noting that the reactive power is bound to ac grids only: it does not propagate to multi-terminal dc systems and is generated locally at each converter. Therefore, detailed evaluation of reactive power control is not provided in this study.

3.1.2 Existing droop-based voltage regulation approaches

As can be seen from Fig. 3.1, in the droop control concept the initial voltage reference of the i_{th} converter the $V_{dc,ref,i,0}$ is necessarily penalized by the $\Delta V_{dc,droop,i}$ if the measured power is not equal to the reference power. The latter situation leads to the dc voltage profile deviation once there is a change in the dc system power [36, 99, 100]. Considering the stochastic nature of renewable energy sources, which are typically connected to MT-HVDC systems, the power injection to the dc grid is expected to fluctuate most of the times. This power variation would subsequently result in frequent voltage deviations from their reference values, which might cause insulation damage or even lead to the malfunction of the dc protection in case the voltages exceed the allowed limits [33].

Several studies tried to address the voltage regulation in the droop-controlled MT-HVDC systems. In [99, 100], the scaling of all droop gains in the system is proposed to reduce the dc link voltage deviations, concluding that the limited scaling headroom is available to achieve proper power distribution. Further, in [101] it is shown that for the droop control approach one of the main considerations for the droop gain selection is the tradeoff between the settling time and the steady state dc link voltage deviation from its nominal value. In [102], a limiter scheme is implemented in the power-voltage loop to locally restrict the dc voltage reference so that it does not exceed the allowed value. However, this tactic may cause an addition of different voltage deviation terms to the dc references at each converter, which may result in the change of the desired power flow between converter stations.

Alternative method reported to achieve an enhanced voltage profile is to select a suitable operating point or droop gain based on the power flow calculation. [65] presented Model Predictive Controller to enhance the dc voltage regulation and avoid the transition between the control modes when converters operate at the capacity limits. The paper claims the regulation of dc voltages to their steady state values after the disturbance. However, the approaches which are based on the calculation of the power flow require the complete system model, have the drawback of longer computation time and inability to react to fast changes in the system. The Generalized Droop Control approach initially proposed in [94] is used in [71] for overcoming the dc voltage regulation issue specifically during the ac side faults. This approach, however, requires disabling the VSCs during the ac faults, which might cause harsh transients on the system. [103] proposed an adaptive modification of the droop gains considering the current operational point of the droop-controlled converters. By monitoring both voltage and power deviations continuously, the authors claim to maintain the voltage within its limits during large disturbances, simultaneously ensuring enhanced power sharing capability. However, the steady-state performance with the originally prespecified droop gains is not matching the performance acquired with the adaptive gains. Therefore, as can be observed from the results presented in [103], the converters with higher rating might transfer less power than the converters with lower rating, contradicting to the commonly accepted droop control philosophy. Moreover, some of the mentioned studies make a questionable assumption of lossless MT-HVDC system and consider flat dc voltage profile across the system.

3.1.3 Existing power mismatch sharing approaches

The conventional droop controller of Fig. 3.1, which rely on the local voltage feedback $V_{dc,i}$, does not provide accurate power sharing due to the fact that the dc voltages may be different at each converter station (as a result of different voltage drops at different lines [100,101,104,105]). Therefore, the power mismatch sharing after a system disturbance is not only determined by the droop constants $D_{p,i}$ but is also affected by the dc system configuration and line resistances [26,106]. Furthermore, it is shown in [104] that in the case of the conventional controller implemented based on the local dc voltage measurements, the power flow solution might be non-unique. The results in [104] illustrate that dc side disturbance may cause unacceptable drift in the converter active power injections with local dc voltage control. References [65, 107] proposed an Optimal Power Flow based droop control strategy to achieve an accurate power sharing. However, similar to the issue of power-flow based voltage regulation strategies, the power sharing precision is affected by the fast nature of the changes in the injected wind power and relatively longer time periods for the update of the setpoints.

An adaptive modifications of droop gains based on the operating condition of the grid is proposed in [108, 109]. However, the implementation of the latter controllers requires exact knowledge of the network configuration, parameters and the input power to the dc system. For basic MT-HVDC system structure, several studies proposed an addition of compensating terms (equal to the product of the converter output current and the line resistance) to the voltage references to mitigate the issue of inaccurate power sharing [110, 111]. The application of this approach to more general grid structures (e.g. meshed grid) is challenging as it may be difficult to find suitable compensation constants to coordinate the voltage controls. Additionally, there is a tradeoff between large and small virtual impedance values as the former will limit the power output capacity of converters and the latter will degrade the precision of current sharing [112].

To achieve an accurate power mismatch sharing between droop-controlled VSC in MT-HVDC grids, a Pilot Voltage Droop (PVD) control approach was patented by a team from ABB [113]. This strategy was then used in several other studies including [26, 79, 101, 104, 114]. For example, PVD based adaptive droop controller proposed in [104] dynamically changes the droop gains to ensure power mismatch sharing according to the currently available headroom of each converter station. The operating principle of the PVD control approach is as follows: a single dc link voltage $V_{dc,pilot}$ is measured at any point of the dc grid and communicated to all converter stations through fiber optic communication links is used as a feedback signal as depicted in Fig 3.2. The error to the PI controller of the d axis current loop is zero in steady state, therefore the following can be written

$$(P_{i,ref} - P_i)D_{P,i} = V_{dc,pilot} - V_{dc,pilot,ref} \tag{3.1}$$

where $P_{i,ref}$ and P_i are the reference and measured active power values of the ith converter, respectively, and $D_{P,i}$ is the droop constant of the respective converter, $V_{dc,pilot,ref}$ is the reference dc voltage. Therefore, for each PVD controlled converter the power deviation will be precisely determined based on the droop gain $D_{P,i}$ as the right-hand side of the (4.4) is identical for all of the converters. This eliminates the sensitivity of the power sharing on the dc system resistances, therefore PVD control approach is selected as a backbone for the proposed voltage-regulation controller in Chapter 4.

However, it should be noted that the dc link capacitors are usually designed to be charged in about one cycle given the transfer of the converter rated power through them.

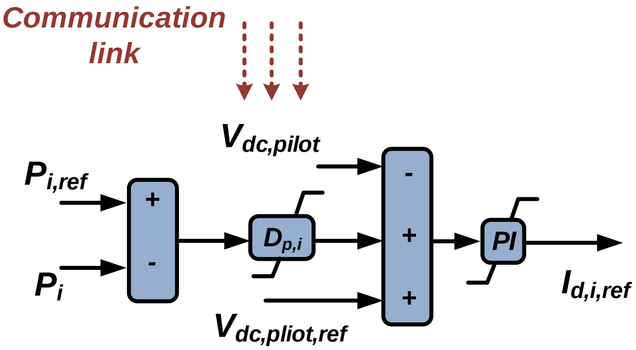

Figure 3.2. The outer loop of the PVD controlled converter for determining the d axis current reference $I_{d,ref}$

Therefore, the dynamics associated with the dc link voltages are very fast, exposing a requirement of high bandwidth communication if those voltages are to be transferred to other converters as in PVD. Thus, large latencies in the communication might affect the normal operation of the PVD control structure. However, most of the PVD based papers did not considere the possibility of the presence of excessive latencies in the communication for the transfer of the pilot voltage information. Only [102] considers communication time delay on the performance of the MT-HVDC operation when PVD controller is employed. However, the requirement for the detection of the exact communication delay and the availability of the clock with the same global time reference for all converter stations are drawbacks of the approach presented in [102]. Furthermore, although modal analysis of the PVD based controller is performed in [26, 104], no specific consideration is given to the effect of the communication delay. Finally, in many communication-based MT-HVDC controllers optimistic time delays in the order of 1-10 ms are considered [115], whereas several studies reported a possibility of larger communication delays for the MT-HVDC systems [116, 117]. Finally, as can be seen from equation (4.4), PVD controller uses identical dc voltage references for all converters, which might not be desired from the system operators' perspective.

The detailed demonstration of the drawbacks of PVD controlled converters during large latencies in the communication network is provided in Chapter 4. What is more, a new controller relaying on the communication between neighbouring converters is developed in the same chapter. As it will be shown later in Chapter 4, the proposed controller overcomes the mentioned drawbacks of the existing controllers by achieving an accurate power-sharing between converters of a general structure MT-HVDC system even when there are large disturbances in the communication network.

3.1.4 Frequency support with MT-HVDC systems

Sudden disturbances in ac systems (e.g., connection/disconnection of large loads/ generators, large change of wind warm injected power) or in dc grid (e.g., converter/line loss) causes deviation of frequency in the ac system connected to the MT-HVDC grid. The control of the active power through the converters of MT-HVDC system can have a significant impact on ac system frequency response. The investigation of the interaction of MT-HVDC systems with their neighboring ac systems is therefore important for understanding the issues created by such interaction and to seize the opportunities provided by such an interaction for achieving enhanced system operation.

The general characteristic of the ac frequency response is elaborated first and can be visualized in Fig. 3.3 [118, 119]. In the latter figure, five distinct frequency regulation stages can be highlighted in terms of their time scales: arrest period (inertial response), rebound and stabilizing periods (the first three periods majorly constitute primary frequency response), recovery period (majorly constitutes the secondary frequency response) and tertiary frequency response stages. The severity of the variation of the system frequency depends on the system characteristics (ac generator droop settings, system inertia, governor characteristics, etc.) and the extent of the change in the ac system active power. The total inertia of the system highly determines the initial fall of the frequency in the inertial response period. Therefore, predicting the initial ROCOF of system based on the inertia is relatively straightforward and is given by

$$\frac{df}{dt} = \frac{\Delta P}{2H} \tag{3.2}$$

where f is the frequency of the system, H is the total inertia of the system, and ΔP is the change of the active power in the system. Afterward, the controller commands the turbine-governor for increased power output, therefore the fall of the frequency is being arrested after several seconds of the event initiation. After the nadir point–the point where the frequency experiences the largest deviation–the frequency is brought back to the quasi-steady-state condition in the primary frequency response period. The secondary control takes over after around the first 20-30 seconds of disturbance to restore the system

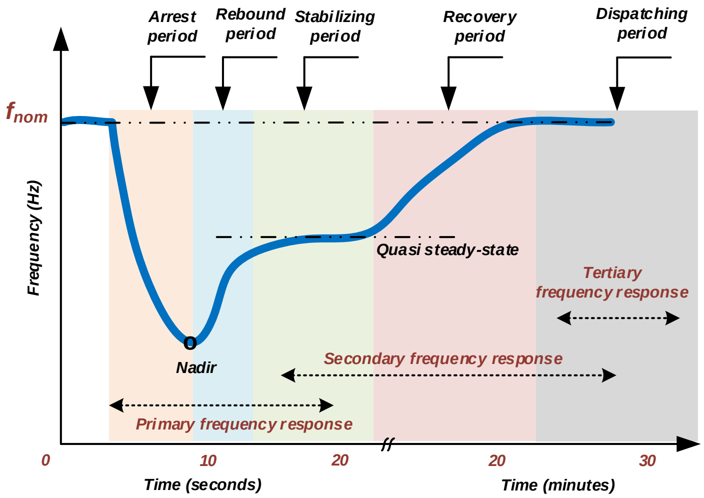

Figure 3.3. General characteristics of ac system's frequency response.

frequency to the nominal value by Automatic Generator Control (AGC) [120]. Afterward, operators dispatch the generators in the tertiary control timeline.

With the recent increase in the renewable generation penetration in ac systems, the transfer of bulk active power to those ac grids might reduce the ac system inertia if it replaces the conventional synchronous generation capacity. Thus, the system frequency response would get deteriorated, and larger ROCOFs and frequency nadirs can be observed in t Delivering additional power from MT-HVDC to the affected ac grids can be useful for improving the latter system's frequency response. Such service is especially useful in the primary frequency response timescale, as the converters have an ability of fast control of the active power, thus they can quickly redirect active power to the affected ac systems and enhance their frequency characteristics. To this end, several control strategies for VSCs in MT-HVDC systems have been introduced in the recent literature.

The virtual inertia of the VSCs could be simulated by utilizing the energy stored in the capacitors of the converters [29]. However, as the power required to provide the necessary frequency support might be significant, large capacitor would have been required, significantly increasing the overall cost of the system. Thus, inertia emulation and frequency support from wind warms, and autonomous power redistribution of the active power between the converter terminals, thus between ac systems connected to those converters, are considered to be more effective alternatives to provide frequency support [88].

There are two main approaches for provision of fast frequency response from wind farms.

In the first method, the kinetic energy of the wind turbines' rotating masses is transferred to the ac grids [29, 115]. This approach results in deceleration of the wind turbines and might initiate significant second frequency drop during turbine speed recovery stage [121]. The second approach suggests operation of the turbines in a de-loaded mode unlike the conventionally accepted MPPT mode. This allows to have an available power headroom for the turbines to be used for frequency support purposes [54, 122]. Significant deloading of WPPs might not be desired by the latters' owners as it might reduce their revenues.

With the previously discussed power-voltage droop controllers, the dc grid disunites ac networks, effectively buffering disturbance propagation from one ac system to the others. This decoupling also results in no mutual frequency support between asynchronous ac systems; therefore, each ac system overcomes its disturbance by the local power reserves only. However, if a proper control structure is adapted, then by means of active power rerouting in dc system and the possible utilization of the energy stored in the MT-HVDC systems, the stress on individual ac network can be reduced. Therefore, the frequency support to the neighboring ac grids through MT-HVDC systems has been another popular topic in the recent literature [26, 28, 29, 54, 65, 88, 97, 115, 121–125].

Frequency droop (FD) technique for MT-HVDC systems, originally introduced in [96], has been used in several studies, including [26, 27, 90, 115, 124, 126], to achieve power reserve sharing and frequency provision between MT-HVDC interconnected asynchronous ac systems. The FD approach applied to the converters of MT-HVDC systems is similar to the droop control applied to the conventional generators. Like the generators in a single area share the burden of a disturbance with the conventional droop control, asynchronous ac systems would try to share the burden of a disturbance with FD equipped converters in MT-HVDC system. As a typical example of FD controller, the approach proposed in [26] for VSC based MT-HVDC system is demonstrated in Fig.3.4. The power reference of the respective converter is modified based on the local frequency error. The PVD controller is also implemented in the outer control loop of the hierarchical control structure to generate the reference active current $I_{d,i,ref}$. To enhance the FD performance, an adaptive $V-I-f$ droop control is proposed in [97], in which the frequency droop gain is adjusted for power sharing and frequency support purposes. PVD based $P-V-f$ controller is proposed in [26, 124] to enable MT-HVDC participation in the frequency support of its surrounding ac areas and to achieve an exact power sharing simultaneously. A similar approach is also adopted by exploiting a $V-f$ droop in [127].

Similar to the power-droop concept, where the power is shared between the converters according to the droop gains, the FD loop has an objective to share the burden of the frequency support between the droop-controlled systems connected through MT-HVDC grid. However, unlike power droop control, where the exact power sharing can be established

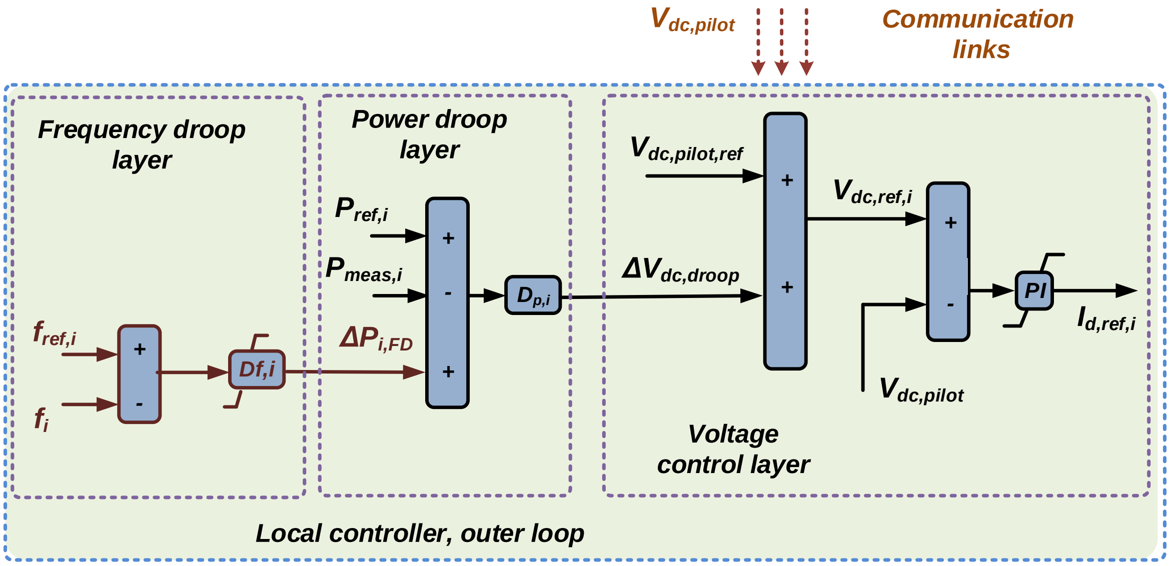

Figure 3.4. Frequency droop control implemented on the PVD controlled VSC in MT-HVDC applications.

by the droop gain selection, the frequency deviation sharing through FD is not exact. It is important to note that the time the nadir point occurs (Fig. 3.3) and the deviation of frequency at the nadir point, are complex function of the power system parameters. Among those parameters system inertia and turbine-governor characteristics play major role. Unlike the ROCOF, which could be readily expressed by (3.2) for any given disturbance, the calculation of frequency deviation at nadir point is not as direct. Studies like [128] attempted to come up with relatively simple equations for calculating the nadir frequency. However, as shown in [128], such calculation requires significant simplifications of the actual model of the system, demands certain assumptions and might not provide very accurate estimation of the frequency at nadir point. This fact restricts analytical calculation of the frequency deviation according to the active power injected to ac system, complicating selection of the droop gains for achieving the desired mutual frequency support between MT-HVDC interconnected ac systems. This limitation is also confirmed by the frequency evaluation in the results of the former presented FD based papers and the fact that no paper discussed the accuracy of the frequency deviation sharing.

Enhancement of the original FD control was attempted in [126] within the unit commitment framework. This study concluded that the extent of support between asynchronous ac systems is highly dependent on droop-coefficient selection. [129] attempted to give an analytical formulation of the ac system frequency behavior in response to various system disturbances when the control structure of [26] is employed. However, while expressing the system frequency deviation as a function of a given disturbance, [129] only considers the network quasi-steady state frequency deviation. However, the maximum frequency deviation (frequency nadir) and ROCOF, important parameters for the primary frequency response, are not considered in [129]. [27, 124] suggested the addition of a distress signal to transmit information about the ac side disturbance in MT-HVDC systems, activate the FD loop, and to achieve ratio-based reserve sharing. Based on the simplified mathematical models of the whole system, [27, 124] attempted the design and parameter setting of FD controllers, e.g., droop-coefficient selection. However, those design procedures require prior knowledge of system topology and parameters and do not consider the complete system dynamics (e.g., important dynamics associated with the turbine-governor action of ac generators are usually neglected). Therefore, accurate ratio-based frequency deviations might not be achieved during the entire period of a frequency event, especially during the maximum frequency deviation (nadir) point, as the latter is a complex function of system parameters [128]. Moreover, many of these parameters having a major impact on the frequency dynamics (e.g. system inertia) might experience significant variation in a relatively short period [130], hindering achievement of the desired mutual frequency support during the primary frequency response.

References [97] and [131] proposed an adaptive modification of the droop gains based on the local frequency error to provide a more reasonable allocation of the unbalanced power between ac systems. [97] uses the conventional cascaded control structure of VSCs, whereas [131] is based on the virtual synchronous generator concept. However, similar to the previous strategies, and verified by the results presented in [97, 131], the latter approaches do not have a mechanism to achieve precise frequency deviation ratios between ac grids.The main deficiency of the frequency-droop control strategies, including adaptive droop approaches, is their inability to accurately achieve desired ratio of frequency deviations of ac systems. This deficiency results from the lack of a mechanism (e.g., integral action) in frequency droop approaches for nullifying the error in ratio-based difference of the frequency deviations. By adaptively modifying the droop gains, this error could be minimized (but not nullified) at the expense of larger variation of the dc voltages, the latter being caused by a more 'aggressive' response of the proportional droop controller. Relatively large variation of droop gains might even cause a violation of the dc voltage limits.

The reference [114] proposed an integral-action based coordinated control structure for MT-HVDC systems, and this approach was later extended in [79] in the developed controller for enhancing frequency support characteristics of master-slave controlled MT-HVDC system. However, as it was previously discussed, the master-slave concept may fail to regulate the dc link voltage and might cause larger stresses on the grid connected to the master station compared to the other grids. A unified control structure proposed in [84] applied an integral action on the local frequency error of the droop-controlled converters of MT-HVDC systems. As this action tries to nullify the frequency error in each grid at the expense of other ac systems, it might eventually result in controller fighting due to the limited spare active power reserves available in the interconnected system. To overcome the presented issues with the frequency support, an enhanced control approach is developed in this thesis and presented in Chapter 5. The proposed control architecture allows equalizing the effect of the disturbance between MT-HVDC interconnected asynchronous ac systems considering the allowed frequency variation of those girds. Furthermore, the developed control strategy is augmented to allow fair mutual frequency support based on the operational condition of each participating ac grid.

3.2 Droop control in MT-DCμGrids

Similar to MT-HVDC systems, the parallel operation of the converters in MT-DCμGrids is a widely accepted practice due to advantages such as reliability and ease of expansion. The main approaches used for the voltage control in MT-DCμGrids are master-slave control [132, 133] and voltage droop control [134–145]. Similar to the converter control in MT-HVDC systems, the droop control method is preferred choice in MT-DCμGrid applications. The droop control aims regulation of the dc system voltage simultaneously by several converters, as well as achievement of the current sharing between several converters based on the desired portions. The latter feature being of more importance in dc mirogrids considering limited capacities of the power sources in those grids.

Fig. 3.5 demonstrates the current-voltage (I-V) droop control integrated in the outer control loop of the dc/dc converter connected to the dc grid on one side and to the constant voltage source on the other side. The current $I_{i,j}$ flows from the j_{th} converter to the terminal of the i_{th} converter. In such droop control approach, the voltage reference is linearly reduced with an increase of the converter output current. Considering the action of the droop control loop, the current reference provided by the voltage control loop is given by (3.3)

$$\begin{aligned} I_{inner,i,ref} &= (V_{dc,ref} - V_{dc,i} - I_{out,i} * k_{droop,i}) * G_{PI}(s) \\ &= error * G_{PI}(s) \end{aligned} \tag{3.3}$$

where $V_{i,ref}$ is the reference dc voltage of the i_{th} converter, $k_{droop,i}$ is its droop gain and $G_{PI}(s)$ is used to represent the PI controller. The quantity $(V_{dc,ref} - V_i - I_{out,i} * k_{droop}) = error$ represents the error term. Due to the controller action, the steady state error input to the PI controller is zero. Therefore, the following can be written

$$I_{out,i} = \frac{V_{dc,ref} - V_{dc,i}}{k_{droop,i}} \tag{3.4}$$

By assuming that the difference $(V_{dc,ref} - V_{dc,i})$ is close for different droop-controlled converters, the relative magnitude of $k_{droop,i}$ with respect to the droop gains of other converters determines the participation of i_{th} converter in delivering the load demand. However, due to the difference in the local dc voltages at the terminal of each converter, the currents of the droop-controlled converters might not be solely determined by the droop constants.

3.2.1 Existing droop control approaches in MT-DCμGrids

Several centralized, decentralized and distributed control strategies proposed in the literature aim to achieve enhanced and prolonged operation of the dc microgrids. In this

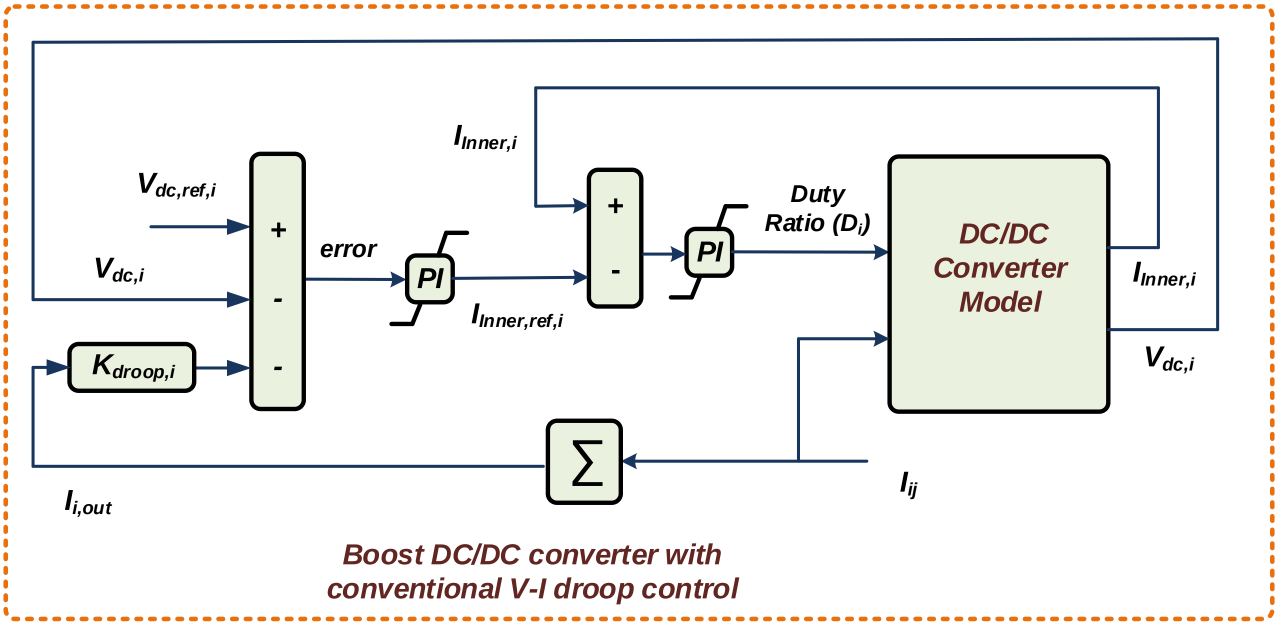

Figure 3.5. Conventional droop control of dc/dc converter.

aspect, an inaccurate current sharing due to the mismatched line impedances in the droop controlled converters is one of the most discussed issues in the literature [134–152].

Some papers consider the usage of the communication network to ensure accurate current sharing between droop controlled converters in MT-DCμGrids. Those communicated values are used to adjust reference signals provided to the primary controller [134–145]. In [138], average current and droop coefficient controllers have been employed to enhance the current sharing accuracy. An algorithm with noise cancellation capability is proposed in [143], where the information of the neighboring converters is used to enhance load sharing accuracy. Adaptive modification of the droop gains proposed in [142,144,145] relies on the update of the droop gains based on the information communicated by the neighboring converters. However, unlike MT-HVDC grids, where the cables have embedded fiber-optic communication links [153], the high-bandwidth communication infrastructure might not be available MT-DCμGrids. Also, the cost of the power components in MT-HVDC systems is significantly higher than the costs associated with the communication infrastructure, which is not the case with MT-DCμGrids. Therefore, several recent studies tried to design decentralized control strategies for MT-DCμGrids, that is, controller that do not employ communication.

Communication-free control approaches designed for MT-DCμGrids based on the availability of information of the grid topology and impedances are reported in [147–149]. The inaccuracies in the existing information and the changing system configuration (e.g. location of the DGs and loads) are the downsides of those approaches. Alternatively, an estimation of the line resistances of the parallel connected converters and the consequent improvement in the current sharing accuracy is proposed in [148,149]. The reference [148] uses an additional hardware to estimate this resistance. In [149], on the other hand, pulse injection is used to estimate the line resistances of the parallel-connected converters in a single bus dc microgrid. The estimated values are used to form the compensating terms (virtual resistances) to overcome the inaccurate current-sharing caused by the differences in the resistances of the lines connecting the converters to the single dc bus. However, no methodology is provided for finding suitable compensation constants for general structure dc microgrids, that is, MT-DCμGrids. Therefore, like other studies which use the virtual resistance concept, the strategy of [149] has limited application for meshed dc systems [108]. If the voltage of the common bus of the dc grid is available, it can be used to simplify the estimation of the line impedances as reported in [146, 150]. The concept of the virtual capacitor is used in [150], where the rate of change of the dc voltage is used to overcome the adverse effect of the mismatched line resistances on current sharing. However, the improvement in the current sharing is achieved at the cost of system dynamic response. The dynamics of the droop control converters are enhanced in [154] by modifying the PI controller structure.

3.2.2 Signal injection-based droop control approaches in MT-DCμGrids

The technique of superimposing a small ac voltage on the dc grid voltage by all droop controlled converters is the backbone of another group of papers [144,151,152]. All strategies in this group achieve enhanced control of general structure MT-DCμGrids in a decentralized manner. Unlike many other strategies, the controllers in this group of papers do not rely on the prior information of system topology and parameters, therefore they are attractive from the perspective of ensuring plug-and-play feature of converters in MT-DCμGrids. Considering the mentioned advantages, a new controller is developed in Chapter 6 of this thesis using similar philosophy. However, the proposed strategy has several advantages over the existing strategies, to understand which first the operation of the existing strategies is explained in details below.

The small active flow between converters, which is resulted from the difference of the phase angles of the superimposed ac signals, is used to adjust output voltages in [151].

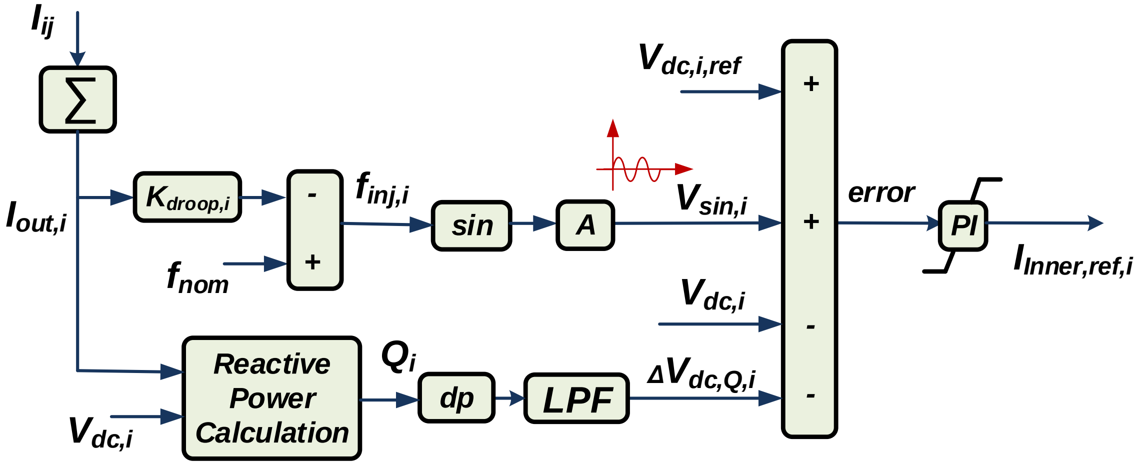

Figure 3.6. SBDC of the converters in MT-DCμGrid applications

Whereas references [144, 152] proposed so called synchroconverter based droop control (SBDC) approach. The latter strategies rely on the reactive power flow between dc/dc converters caused by mismatched phase angles of the superimposed ac signals. The structure of SBDC controller is shown in Fig. 3.6 and its description is provided below.

In SBDC approach, at every i_{th} droop-controlled converter a small ac voltage $V_{sin,i}$ is added on the original dc voltage reference $V_{sin,i}$. The controllers track the added sin reference and a small dc signal is being superimposed on dc grid voltage. The magnitude of the signal is determined by the gain A, selected as 2% of the nominal dc voltage. The determination of the frequency of the injected signal, $f_{inj,i}$, is of prime importance for the operation of SBDC approach. This frequency is determined as a function of the converter output current $I_{out,i}$ as per

$$f_{inj,i} = f_{nom} - I_{out,i}k_{droop,i} \tag{3.5}$$

where f_{nom} is the nominal frequency of the injected signal and $k_{droop,i}$ is the droop gain of the i_{th} converter. Like any other droop control approach, the SBDC strives to equalize the product $I_{out,i}k_{droop,i}$ for all droop-controlled converters so their output current is proportional to their droop gains. To achieve the latter goal, the frequencies of the injected small ac voltages at all converters should be synchronized. The process of the synchronization of the SBDC of [144, 152] is detailed below.

Assume that at a certain operation instant the product $I_{out}k_{droop}$ of the i_{th} converter is higher than the identical product of any other j_{th} droop-controlled converter that uses SBDC approach. In this situation, the frequency of the injected signal at the i_{th} converter, $f_{inj,i}$, will be lower than the frequency of the injected signal at the j_{th} converter, $f_{inj,j}$. The difference in the frequencies results in the difference of phase angles of the injected small ac signals. Assuming mostly resistive network in dc microgrids (very low X/R ratio), the larger phase angle of the superimposed signal at the j_{th} converter results in a small reactive power flow from j_{th} to i_{th} converter. The resultant reactive power is locally calculated at the i_{th} converter as show in Fig. 3.6. The positive reactive power flowing to the i_{th} converter, or the negative reactive power flow Q_i form the converter, is used for generating the $\Delta V_{dc,Q,i}$ term as per

$$\Delta V_{dc,Q,i} = Q_i d_p G_{LPF}(s) \tag{3.6}$$

where d_p is a controller parameter and $G_{LPF}(s)$ is the transfer function of the low pass filter, the latter being used for minimizing components of Q_i other than its dc value. The voltage $\Delta V_{dc,Q,i}$ is then substructed from the the local dc voltage reference. With the negative reactive power flow from the i_{th} converter as in the previously described scenario, the local dc voltage reference $V_{dc,ref,i}$, and thus the measured dc voltage $V_{dc,i}$, increases. This increase in the terminal voltage results in a reduction of the converter output current I_{out}, which in turn reduces $I_{out,i}k_{droop,i}$. This alteration of $I_{out}k_{droop}$ product continues until the frequencies of the injection signals at two converters are synchronized, in turn equalizing the produces $I_{out}k_{droop}$ of the two considered converters using SBDC approach, thus achieving a proper droop operation.

As can be seen in Fig. 3.6, the SBDC approach largely modifies the conventional I-V droop control of Fig. 2.14. The latter strategy directly adds $I_{out}k_{droop}$ term to the local voltage reference, and has a drawback of inaccurate current sharing between droop-controlled converter. The SBDC approach tries achieving the accurate current sharing indirectly by adding a sin term $V_{sin,i}$ and voltage changing terms $\Delta V_{dc,Q,i}$ to the voltage control loop. As it have explained, the SBDC approach relies on the assumption that the frequencies of the superimposed signals are eventually getting synchronized. It is worth noting that in case if those frequencies fail to synchronize, the controller would not only result in a inaccuracy in the current sharing, but might only jeopardize the stable system operation. In fact, the system might fail to synchronize in case if the inductive impedance of the considered lines is not negligible compared to the resistance of those lines. In the latter case, the assumption that the difference in the frequencies results only reactive power exchange is inaccurate, affecting the explained logic of the controller operation. What is more, connection of a single converter simultaneously to several converters might result in a simultaneous change of the small reactive power with those converters, which again might negatively impact the describes synchronization process. The strategy proposed in this thesis, on the other, achieves accurate current-sharing without large modifications of the the conventional droop-control structure and does not rely on synchronization procedure like the one described above. Therefore, as will be shown in Chapter 6, the proposed strategy achieves enhanced control of droop-controlled converters in MT-DCμGrids.

3.3 Discussion

This chapter provided a literature review on the controllers for the converters forming dc systems. Several recently reported control approaches for the control of VSCs in MT-HVDC systems and MT-DCμGrids were presented and their operations were elaborated. The drawbacks of some of the advanced control strategies were discussed, as those gaps in the literature will be used to form a basis for the development of the proposed controllers in Chapter 4-Chapter 6.

Chapter 4

DC Voltage Regulation and Power-Sharing in MT-HVDC Systems

This chapter of the thesis presents the first part of the developed controllers for the VSCs used in MT-HVDC applications. Specifically, the control of MT-HVDC's dc side variables is discussed in this chapter.

The voltage regulation issue of the droop-controlled converters is addressed in the first section of this chapter. The developed technique ensures that the average dc voltage of the system is regulated to the nominal value without changing the current flow between the VSCs, which allows to achieve fast and precise power regulation without the risk of large steady state deviations in dc system voltages. Without losing the generality, the developed solution is applied to enhance the operation of PVD controlled VSCs, as the latter solution achieves accurate power-sharing for general structure MT-HVDC systems. To further enhance the speed of the power regulation, the FLL is applied for the grid synchronization, which is shown to enable enhanced power regulation of the MT-HVDC system during ac grid disturbances.

Furthermore, the second section of the chapter addresses the power-sharing issue between VSCs in MT-HVDC systems. Firstly, it is demonstrated that the PVD-based control approaches might get affected in case there are large latencies in the communication network. Therefore, an alternative control structure is designed instead of the existing approach for ensuring accurate power sharing between the droop controlled converter stations. By communicating the Power Sharing Index (PSI) between neighboring converters, the proposed solution achieves exact droop control operation independent of the dc system topology and line parameters.

Finally, the third section demonstrates the combined performance of the control structures developed in the first two sections of this chapter.

Nonlinear time-domain simulations are conducted in the Matlab/Simulink environment considering different MT-HVDC test systems to better demonstrate the capability of the proposed controllers in achieving the control objectives in various operational conditions. Modal analysis is carried out to reveal the sensitivity of the system's eigenvalues to the changes in control parameters and the latencies in the communication. It is demonstrated that the proposed strategies remains in the stable operation even when excessive latencies are encountered in the communication. The first part of this chapter's work has been published in the IEEE Transactions on Power Delivery [155], and the second part is published in IEEE Transactions on Power Systems [156].

4.1 The voltage regulation strategy for droop-controlled VSCs in MT-HVDC systems

This section presents the voltage regulation controller developed for MT-HVDC systems, explains its operation principle and verifies it's performance by detailed time-domain simulation study.

4.1.1 The development of the voltage regulation strategy

As it was discussed in the the Literature Review chapter, when there is a sudden change in the active power flow in the dc system, the droop-control action makes the participating converters to experience different deviations from their reference dc voltages. This difference in the voltage deviation aims at evacuating the excess power in the dc system based on the converters' pre-set droop coefficients. Therefore, the droop-controlled converters necessarily experience voltage deviation from the nominal value during the operation of the droop loop. The drawbacks of the existing voltage-regulation approaches have also been detailed in Chapter 3.

Also, as it has been previously described, the power-sharing between the droop-controlled converters with conventional droop approach might be affected by the dc system topology and parameters. Therefore, in this section the voltage regulation issue is demonstrated using the PVD control approach, as the latter solution is able to achieve an accurate power-sharing independent of the system structure and parameters. Detailed explanation of the dc voltage regulation problem as well as PVD operation was provided in Chapter 3.

As with the other droop-controlled approaches, the extent of voltage deviation in PVD controlled dc systems depends on the amount of active power change in those systems as well as on pre-specified droop gains. As per [101], the dc voltage deviation for the PVD controlled converter is defined according to (4.1)

$$\begin{cases} \Delta V_{pilot} = D_{P,i} T_i \Delta P_{system} \\ \\ \sum_{i=1}^{n} T_i = 1 \end{cases} \tag{4.1}$$

where ΔV_{pilot} is the voltage deviation at pilot voltage bus (generally 5-10 % max), $D_{P,i}$ is the power droop gain of the i_{th} droop controlled converter, ΔP_{system} is the total power mismatch in the dc system, n is the total number of the droop-controlled converters. T_i is the power sharing coefficient of that converter, determining the portion of the total mismatch power that the i_{th} converter should accommodate. As it can be seen from equation (4.1), and as it will be verified in the simulation studies, higher droop gains tend to increase converter dc link voltage deviations from their nominal value. The same trend holds for the conventional power-voltage droop controllers as well, with the identical relationship depending on the system parameters as well. However, increasing the power droop gains improves the transient response of the system and provides better system stability [101].

Fig. 4.1 illustrates a typical effect of the change of power droop gains on the system pole movement, which is acquired from the conducted modal analysis on the test system depicted in Fig. 4.2. The detailed description of the latter test system is provided in the simulation study section, whereas its parameters can be found in Table 1 in the Appendix. It can be clearly seen from Fig. 4.1 that with very small droop gains the system might even be in the unstable region (right side of the imaginary axis). With an increase in droop gains the dominant poles move to the left side of the imaginary axis. Therefore, from the stability point of view, it is desired to select higher droop gains. What is more, the higher droop gains result in faster regulation of converter active power injection as it results in a faster change of the converters terminal voltage for a given disturbance. The latter point will be also demonstrated by the conducted time-domain simulations.

To overcome dc voltage deviation issue in droop-controlled MT-HVDC system and simultaneously achieve increased system stability and enhanced transient response, an average voltage regulation algorithm is developed for those systems. An equal voltage shifting terms ΔV_{avg} are added to the reference voltages of all droop controlled converters, which have the aim to regulate the average dc voltage to the nominal value specified by the system operator. Important to notice that the current flow between the converter stations does not alter with the addition of equal voltage shifting terms as this flow is dependent on the difference between the converter terminal voltages and not on the absolute values of those voltages. The calculation of the ΔV_{avg} and the realization of the proposed scheme

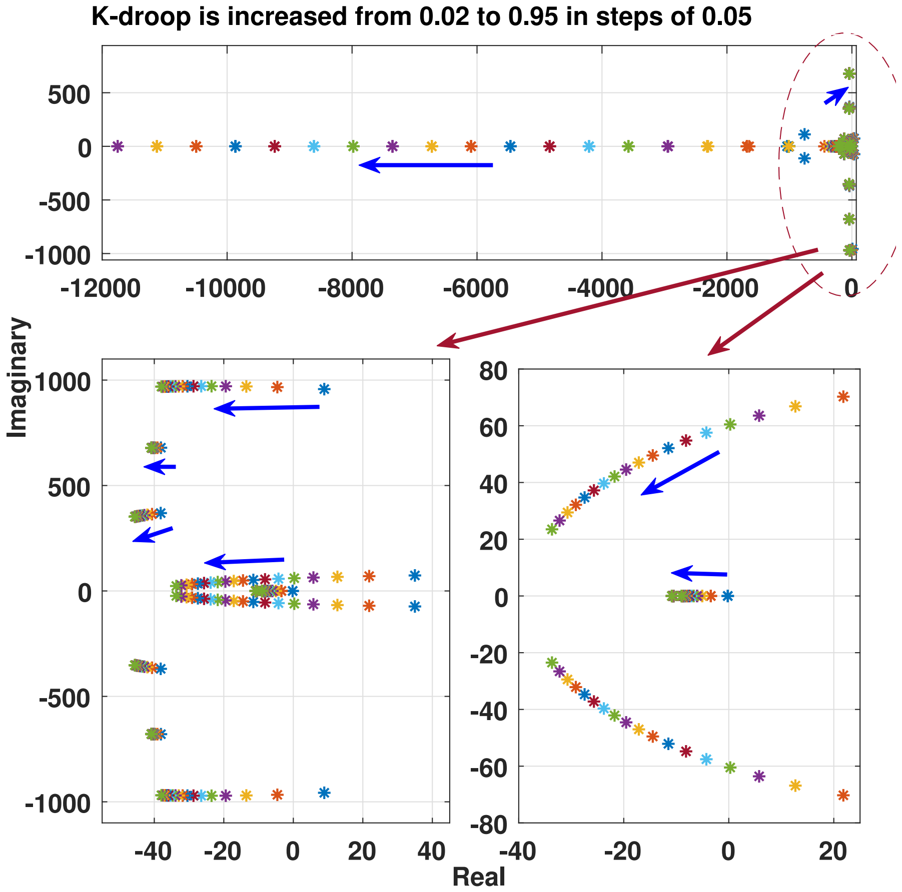

Figure 4.1. Movement of the system eigenvalues with PVD control when droop gain is increased from 0.02 to 0.95 in steps of 0.05.

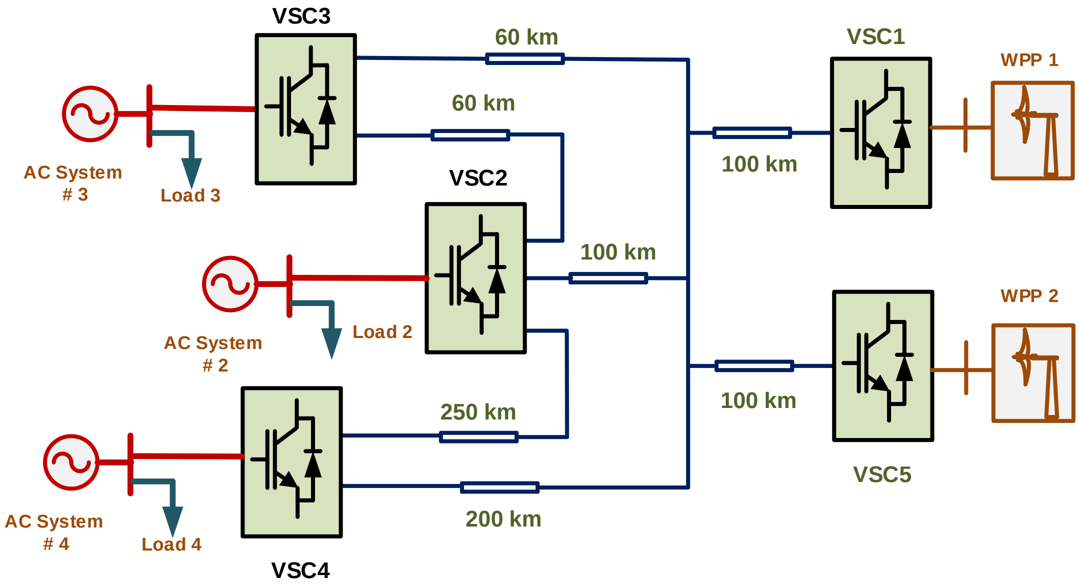

Figure 4.2. The five terminal MT-HVDC system under study.

is depicted in Fig. 4.3, where the measured dc link voltages at all converter stations are communicated to the centralized controller. Please note that both droop-controlled and other converters (e.g., constant power controlled converters connected to WPPs) send their terminal voltage information to the central controller as the proper regulation of the dc voltage at all converters is of importance. The average dc link voltage of the system is then calculated as per

$$V_{dc,avg} = \sum_{i=1}^{n} \frac{V_{dc,i}}{n} \tag{4.2}$$

where $V_{dc,i}$ is the measured voltage at the i_{th} converter, with total of n such converters in the system, including those that are not droop-controlled. It should be noted that the $V_{dc,i}$ is a per-unit value which allows the controller to function even if various voltage levels present in the dc system (e.g. due to the presence of dc/dc converters). Afterwards, the difference between the nominal voltage and the average voltage is fed to the centralized PI controller which generates the voltage shifting term ΔV_{avg}. The latter term is communicated back to all droop-controlled converters and is added to their reference dc voltages.

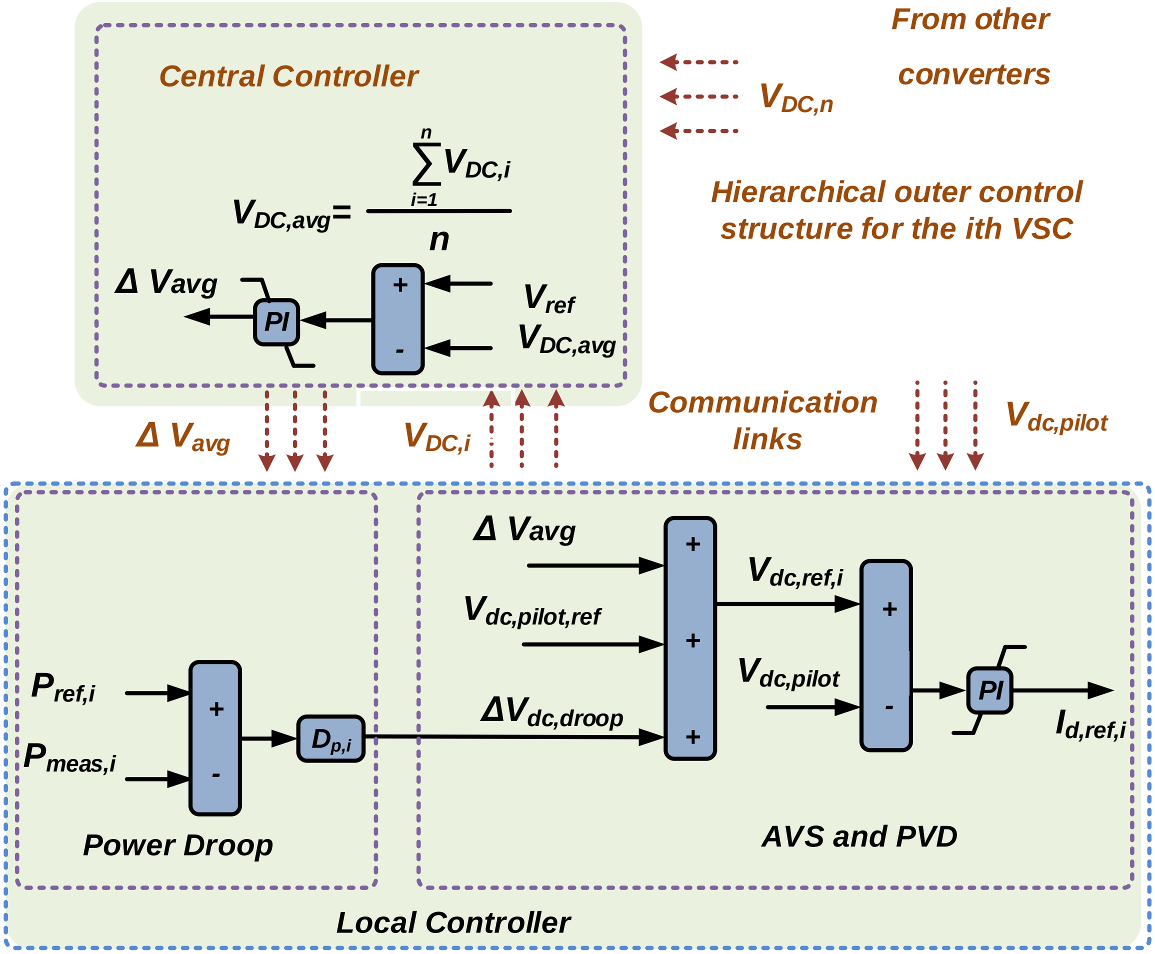

Figure 4.3. The proposed outer control loop for active current reference $i_{d,i}$ calculation and the FLL for the grid synchronization.

Considering the power droop control loop together with AVS loop, the reference dc link voltage at the i_{th}, converter which is operating under PVD control, will be determined as per

$$\begin{cases} \Delta V_{avg} = (V_{ref} - V_{dc,avg})(k_{p,AVS} + \dfrac{k_{i,AVS}}{s}) \\ V_{dc,i,ref} = V_{dc,common,ref} + \Delta V_{avg} + (P_{i,ref} - P_i)D_{P,i} \end{cases} \tag{4.3}$$

where $V_{dc,i,ref}$ is the final reference voltage for the i_{th} converter, V_{ref} is the nominal dc voltage, which is set equal to the common reference voltage $V_{dc,common,ref}$, $k_{p,AVS}$ and $k_{i,AVS}$ are the proportional and integral gains of the implemented controller. As it was previously mentioned, the PVD loop is responsible for achieving accurate power-sharing and is not connected for the implementation of the proposed controller. Thus, the proposed controller can be seamlessly integrated to other droop control structures as well (e.g. conventional local voltage based droop controller).

Assuming that the converter operates within the allowed current rating, the PI controller, which generates the current reference $i_{d,i,ref}$ (Fig. 4.3), ensures that the error input to it is zero. Therefore, for steady state operation, the following can be written

$$(P_i - P_{i,ref})D_{P,i} = V_{dc,common,ref} + \Delta V_{avg} - V_{dc,common} \tag{4.4}$$

Because on the right side of the (4.4) all the three terms are the same for each PVD controlled converter, the power sharing between the converters will be precisely determined based on the droop gains. This eliminates the dependency of the power sharing on the MT-HVDC system configuration and the line lengths. If the above-described voltage regulation strategy is applied to any other controller (e.g. conventional power-voltage droop control), then the similar power-sharing will be achieved with and without the voltage regulation loop, whereas the presence of that loop would still ensure accurate control of the dc system's average voltage. The developed voltage-regulation algorithm is named average voltage sharing (AVS) control. Please note that the AVS controller uses communication for transferring the voltage information to the central controller and receiving back the correction voltage. However, the initial fast dynamic operation of the controller in Fig. 4.3 is ensured by the usage of the locally measured variables. Therefore, as it will be shown in the latter sections, even in the presence of relatively large delays in the communication, the usage of AVS controller results in stable system operation and proper voltage regulation.

What is more, (4.4) could employ half of the squared values of initial voltage reference $V_{dc,common,ref}$ and the respective feedback $V_{dc,common}$ signals. Such controllers have been used in several papers including [30, 104, 124] as it is claimed to enhance the system dynamic response. In the case of using the latter-mentioned approach, the correction term ΔV_{avg} would not be required to get squared. In fact, squaring the correction term would mean squaring the output of the PI controller in Fig. 4.3. This situation would result in only positive voltage correction term ΔV_{avg}, which would continuously increase the system average voltage and result in tripping of the system. Therefore, to regulate the average dc system voltage, the voltage correction term should always be added to the initial reference dc voltage independent of the structure of original power-voltage droop loop.

4.1.2 Verification of the voltage regulation strategy

To demonstrate the problems with the existing approaches more clearly, and to better understand the operation of the proposed voltage regulation approach and verify its effectiveness, the time-domain simulation study is conducted in the MATLAB/ Simulink environment considering different operational scenarios.

4.1.2.1 System under study

The single line representation of the system under study is shown in Fig. 4.2, where three ac areas and two WPP are connected through MT-HVDC network. Both converters #3 and #4 operate in the inverter mode, whereas the converters #1, #2 and #5 operate in the rectifier mode under normal operation. The WPPs, which are connected to VSC #1 and #5, are operating in the constant power control mode.

In the initial steady state, each of the wind turbines delivers 150 MW. The VSC2 acts as a rectifier with reference power of -300 MW, whereas reference for both inverters VSC3 and VSC4 is 300 MW. The system base power, which is used in the controller implementation and in the representation of the results, is 900 MW. The pilot bus is chosen at VSC5. Although the recent industrial applications of VSC-HVDC systems mostly consider MMC based VSCs, it is worthy to point out that MMC and the two-level converters have similar controller design in the outer control layers [157, 158]. Therefore, two level VSC is used as a base-case for the investigation of the proposed controller [29, 108, 159], while the results are also verified for the MMC based MT-HVDC systems in the end of the study. The dc grid voltage is 300 kV and the cable parameters are taken from [160], [161]. All the droop controlled converter stations are equally rated (450 MVA) and have the same droop gains

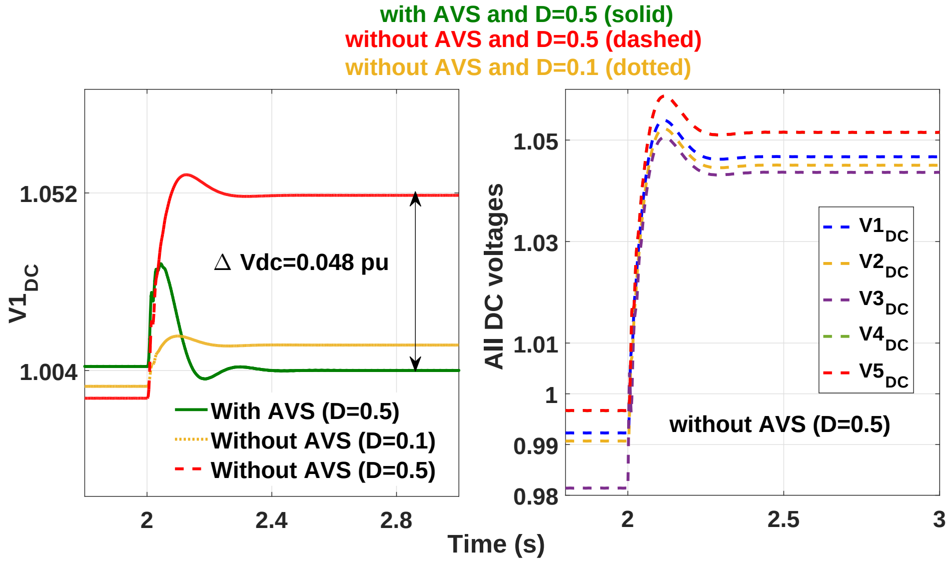

Figure 4.4. System response when the reference power at VSC 4 is decreased. dc voltage at the VSC1 with AVS vs conventional droop with different power droop gains (left) and dc voltages at all five stations without AVS and 0.5pu power droop gain (right).

to make the analysis of power sharing more clear. Further, the rating of each WPP is 200 MVA. The system parameters are detailed in Table A7.

4.1.2.2 Power reference decrease in the VSC4

In this scenario, the power reference in the inverter VSC4 is decreased from 0.33 pu to 0 pu at time t=2s. The delays for the communication of both AVS shifting term and the common dc link voltage are considered to be 2.5 ms [72], whereas the effects of larger delays will be investigated in Section 4.2 and Section 4.3. In the left side of Fig. 4.4, the profile of the dc voltage at VSC1 is shown for the cases with smaller power droop gain (D=0.1) and without AVS, and with larger droop gain (D=0.5) with and without AVS. While on the right side, the dc link voltages for all converter stations are shown for the case with D=0.5 and without AVS to clearly illustrate how the dc link voltage profile increases with power increase in the dc grid. As it can be seen from Fig. 4.4, without AVS the dc link voltage deviation with D=0.1 is much smaller than in the case of D=0.5. This is in line with equation (4.1), where the dc link voltage deviation is proportional to the droop gain. However, the smaller power droop results in slower reference tracking and may not provide enough sensitivity for the exact power sharing (the latter problem is avoided by utilizing

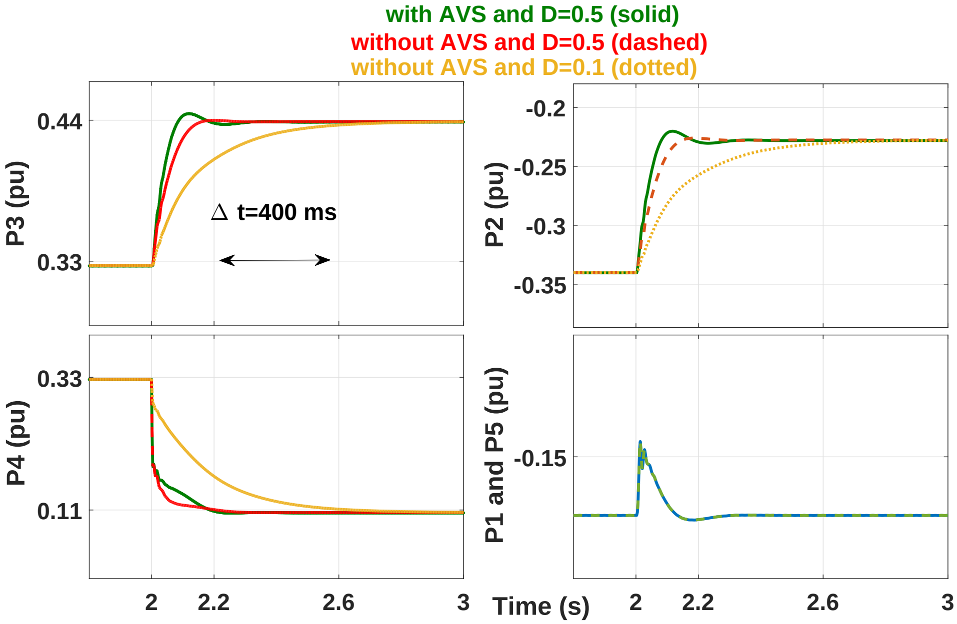

Figure 4.5. Converter power injections when the reference power at VSC 4 is decreased. AVS vs the conventional droop with different power droop gains.

PVD control). This point can be validated from Fig. 4.5, where the power traces of all VSCs are shown for the above mentioned three different scenarios. It can be observed from Fig. 4.5 that with the power droop gain D=0.5, both with and without AVS the settling time of the converter's power is around 200 ms (with the slightly less overshoot when AVS is not included). Whereas with the droop gain of D=0.1 the power settling time increases to 600 ms, which may violate grid codes related to active power injection dynamics. Therefore, the droop gain of D=0.5 is chosen for all other considered scenarios. It can be concluded from Fig. 4.4 and Fig. 4.5 that the inclusion of the AVS control loop enables steady-state dc voltage regulation around the nominal value without having noticeable impact on the system dynamic performance.

4.1.2.3 The sudden power reduction from WPPs

Considered as one of the worst case scenarios, in this case both WPPs deliver rated 200 MW power each when at time t=2s the WPP's power is reduced to 0 (shown in Fig. 4.6 $P1$ and $P5$). The decrease of the dc system active power causes a decrease in the system dc link voltage profile. As it can be observed from Fig. 4.6, the dc link voltage is less

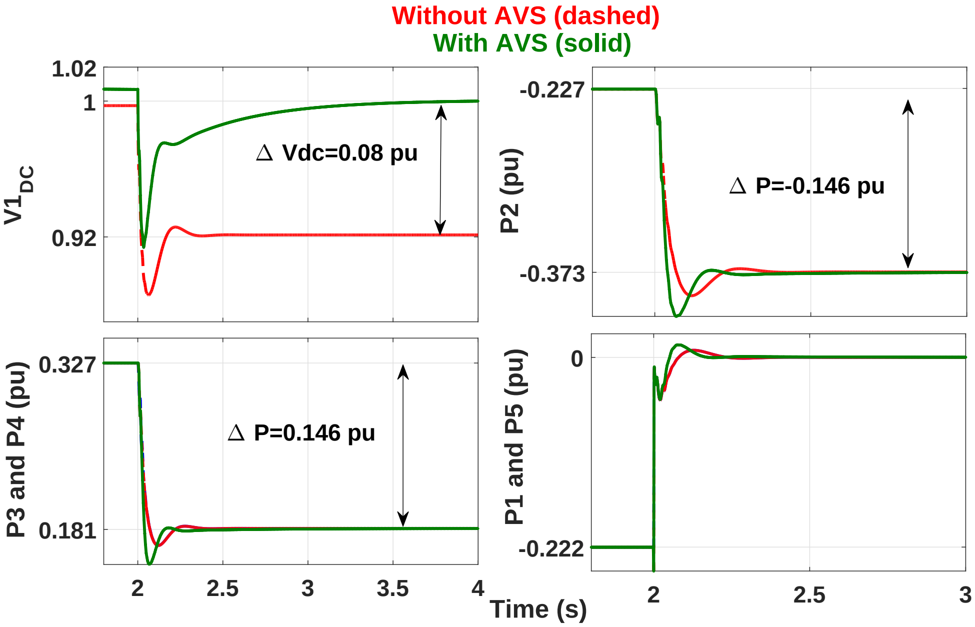

Figure 4.6. System response during an outage of WPPs. AVS vs the conventional droop.

than 0.92 pu when the conventional PVD is used. This may cause undervoltage protection activation and trip of the converters, especially if further reduction of the dc power causes additional decrease in the voltage. Whereas with the implementation of the AVS scheme the dc link voltage profile is regulated around its nominal value. While the system response in terms of active power transient is similar with both control structures with the proposed one having slightly more overshoot and faster settling time as can be observed from the traces of $P2, P3$ and $P4$ in Fig. 4.6.

Another important observation from Fig. 4.6 is that all the converters share the system power change equally ($\Delta P = 0.146pu$ for the PVD controlled converters). For the case of comparison, the same scenario is investigated when instead of PVD the conventional control structure (based on local dc voltage measurements) equipped with AVS loop control is used. It can be clearly visualized from Fig. 4.7 that the local droop suffers from poor reference tracking and unequal power sharing between converters. E.g., both inverters VSC3 and VSC4 have identical active power references and droop gains. Therefore, their active power magnitudes should be ideally equal. As it can be seen from Fig. 4.6, with the PVD+AVS control the traces of the P3 and P4 do follow each other before as well as after the disturbance.

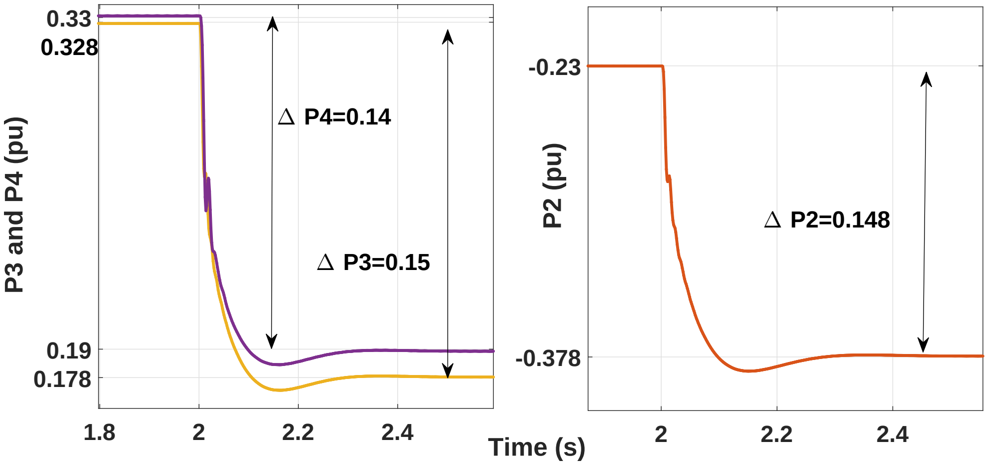

Figure 4.7. Power traces at the droop controlled converters during an outage of WPPs when instead of PVD the local voltage based controller is used.

To also demonstrate the issue of inaccurate power sharing with the conventional controller, the developed AVS loop is integrated to the local voltage based conventional controller instead of PVD controller and identical disturbance is initiated in the system. In Fig. 4.7, the active power traces even before the disturbance are determined by the dc grid topology and line resistances, making unequal initial operating conditions for comparison between the two cases. Following the disturbance, the converters continue to experience undesired difference in their ratio-based power injections.

4.1.2.4 System performance enhancement with FLL during ac side faults

In this scenario, the voltage sag in Grid 3 makes the modulus of the $V_{PCC,3}$ voltage to reach 0.73 pu and experience 60° phase angle jump. To illustrate the system transient response enhancement with FLL, the comparison with conventional PLL is carried out for this case. As it can be observed from the upper plot in Fig. 4.8, before the sag is initiated at time t=2s, the A phase of $V_{PCC,3}$ voltage is perfectly aligned with the $sin\theta$ component of the θ synchronization angle detected with both FLL and PLL. As the phase angle jumps by 60° at time t=2s, it takes about one cycle for FLL to ensure synchronization with grid voltage. This can be observed from the zero crossing points. While for the PLL it takes more than two cycles to synchronize with grid voltage. As a result, less overshoots and faster settling time can be noticed for the active and reactive power traces at VSC3 with FLL in comparison with PLL (lower part of Fig. 4.8).

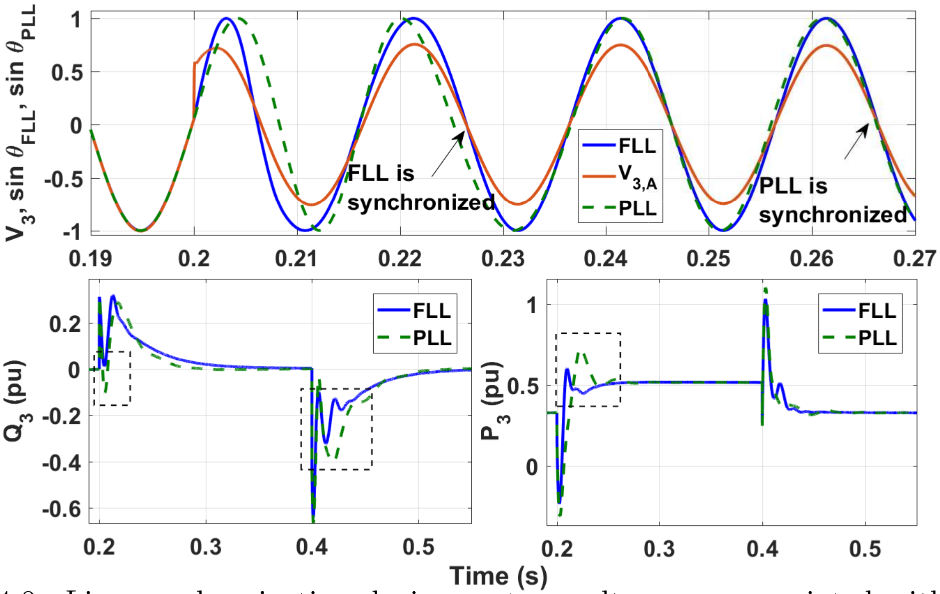

Figure 4.8. Line synchronization during system voltage sag associated with phase angle jump. The phase A grid voltage, $sin(\theta)$ of the positive sequence phase angle θ detected with FLL and conventional PLL.

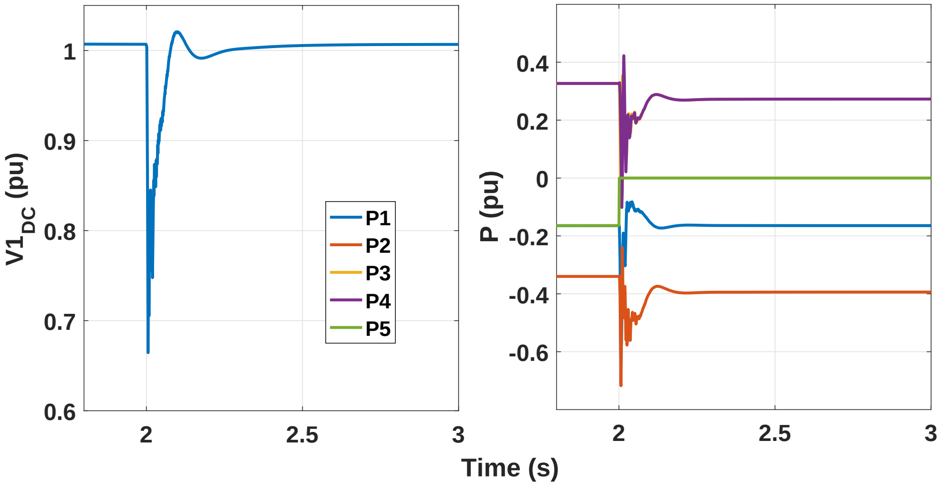

Figure 4.9. dc link voltage at VSC1 and the system power traces when dc fault occurs near the pilot bus (VB5).

4.1.2.5 System performance during dc side faults

As a worst case scenario, the dc fault is applied on the cable connecting the pilot voltage bus at VSC5 to the system. Once the fault is detected, the pilot bus is switched from VSC5 to VSC1. The fault occurs at time t=2s. The detection of the fault and isolation of the faulty cable takes 5 ms. As the faulted line is quickly cleared, the power transactions between the faulted lines continue. As can be seen on the left side of Fig. 4.9, the dc link voltage profile at VSC1 experiences a dip for 5 ms before the fault is detected and cleared. It can be seen that the voltage is smoothly restored to its nominal value soon after the fault is cleared. Whereas in the right side of Fig. 4.9 the power traces at all five VSCs are depicted to illustrate the transient power response as well as the steady state power sharing between converters. As the wind power from VSC5 stopped to be delivered to dc grid, both P3, P4 decreases equally while the P2 increases in the same amount.

4.1.2.6 Effect of the AVS scheme on the system current profile

In the droop controlled MT-HVDC system, the set of dc link voltage and active power references are usually calculated by the tertiary loops. The proposed AVS scheme adds

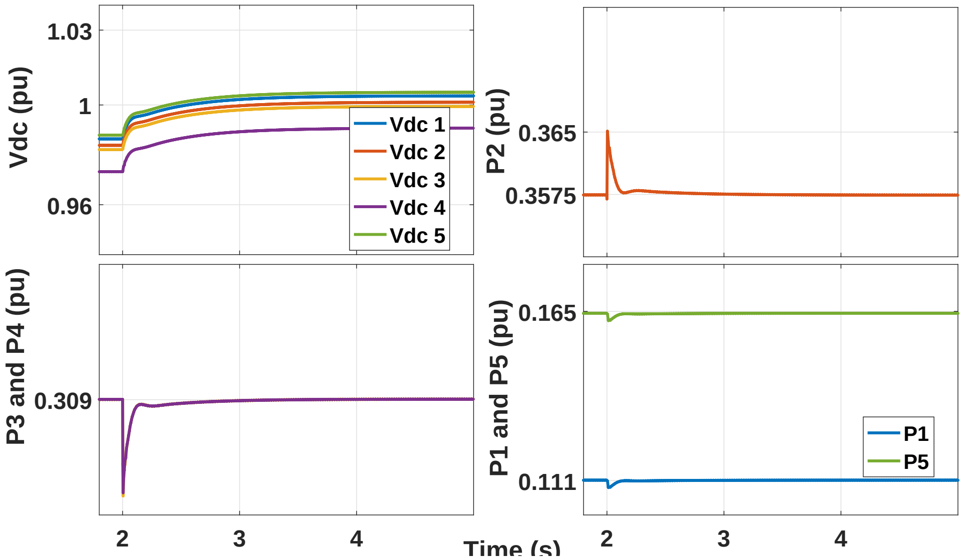

Figure 4.10. The activation of the AVS scheme results in regulation of the average dc link voltage and does not noticeably change the steady state active power flows.

equal voltage shifting term to the dc voltage references of all droop controlled converter stations, so as to regulate the average dc voltage to the required value (e.g., 1 pu). As the added term is equal for each station, the relative difference between the dc voltage references of droop controlled converters remains the same with AVS as it was without AVS. Therefore, the AVS scheme does not result in a change of current flows between converters. To illustrate the latter point, Fig.4.10 shows the case when the AVS scheme is initially disabled and is activated at time t=2s. It can be observed from Fig.4.10 that the activation of the AVS causes the average dc link voltage to be regulated to the nominal value. There is also no noticeable difference in the converter steady-state power injections before and after activation of the AVS scheme, which is a result of unaltered converters' current injections. Therefore, the AVS scheme can be enabled without affecting the operation of the power-regulating loops.

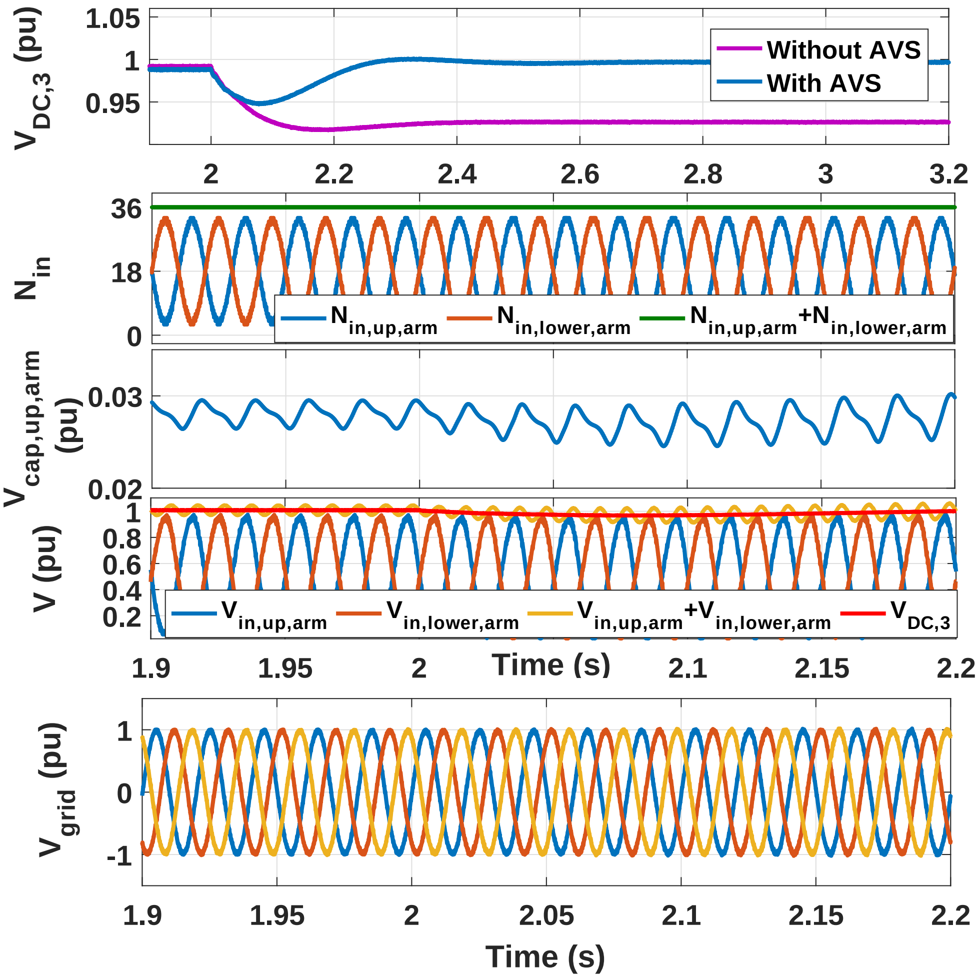

Figure 4.11. Shown for the Converter 3, dynamics with MMC based MT-HVDC system during wind power decrease. From top to bottom-the dc voltages with AVS and without, the number of the inserted modules in the upper and lower arms of phase A, the capacitor voltage at an individual module, the inserted voltages in the upper and the lower arms of phase A and the ac side voltage.

4.1.2.7 Performance evaluation with the Modular Multilevel Converter based MT-HVDC system

In this section, it is validated that if the MT-HVDC converter stations are based on Modular Multilevel Converter (MMC), then the internal dynamics of the MMC does not affect the proper functioning of the proposed control strategy. Special attention is paid to the relatively fast dynamics such as dc link voltage regulation [162]. The simulation scenario with the fast reduction of the wind power is repeated below. It can be observed from the top subfigure of the Fig. 4.11 that without implementing the proposed AVS control loop, the dc link voltage (shown for the Converter 3) experiences a large deviation from nominal value. In contrary, the same subfigure depicts that the inclusion of the AVS loop regulates the average dc link voltage to the nominal value. The second from the top subfigure of the Fig. 4.11 depicts the number of the inserted modules in the upper and lower arms of the phase A of the Station 3. It is worthy to notice that the summation of the inserted modules in the upper and lower arms of the same phase is always equal to the total number of modules per arm side (36 in this case). The third from the top subfigure of the Fig. 4.11 shows the calculated capacitor voltage per MMC submodule. Please note some of the subfigures are presented in the shorter time scale (1.9-2.2s) to provide better visibility of the dynamics in spite of the fact that at time 2.2 s the steady state is not yet reached (see the top subfigure). The multiplication of the module capacitor voltage with the number of inserted modules results in the inserted voltage in the upper and lower arms of phase A (Fig.4.11). The last subfigure of Fig. 4.11 shows that the ac side MMC voltages are balanced and well regulated.

4.2 Power sharing controller considering large delays in the communication network

This section elaborates on the negative effect that the communication delay might have on the operation of MT-HVDC systems. A new control structure is then developed to ensure proper operation of MT-HVDC system and accurate power sharing between converter stations even when realistically large communication delays are considered. Modal and time-domain analysis are considered to demonstrate the severity of the existing problem and to validate the effectiveness of the proposed solution.

4.2.1 Lantencies in the communication

The MT-HVDC system control structure is underpinned by a communication system based on either a fiber optic, radio, power line communication, or a combination of those approaches. The amount of the communication delay depends on the technology used, on the distance between the converter stations, etc. The reference [115] claimed that delays up to 10ms are usual with the fiber optic communication, while 38ms delay for the same technology for one-way communication is reported in the Bonneville Power Administration system [116]. The latencies associated with modems via microwave are reported to be 80ms [116,163]. Larger delays in the order of 150ms are reported for communication of the grid frequency to the offshore wind farms [117]. It can be thus observed that large range of communication delays is encountered in the literature. As shown in the next sections, the effect of the communication delays on the operation of MT-HVDC systems is investigated by conducting modal analysis and time domain simulations for the encountered range of delays. Transport delays are introduced in the respective models to represent the communication delays present in the actual systems.

The consideration of the latencies is especially important with PVD control approach, where the communicated voltage signal is used as a feedback in the control architecture. The dc link capacitors are usually designed to be charged in about one cycle given the transfer of the converter rated power through them. Therefore, the dynamics associated with the dc link voltages are relatively fast, exposing a requirement of high bandwidth communication if those voltages are to be communicated to other converters as in PVD. To illustrate the effect of the communication latencies on the PVD control performance, Fig. 4.12 shows the pole movement when the communication delay is increased from 15 ms to 52 ms. It can be observed that the system poles move towards the unstable region and around 40 ms they appear in the right side of the imaginary axis. Therefore, the conventional PVD approach is limited for the applications where large delays are encountered.

4.2.2 Proposed Control Strategy

Having an aim to achieve exact power sharing between VSCs, a new control structure is developed for a general structure MT-HVDC system. Fig. 4.13 shows the outer loop of the cascaded controller of VSC, where the proposed modifications are implemented. Unlike an alternative PVD controller, the implemented controller relies on local dc voltage feedback. Unlike other controllers using local voltage feedback, the proposed control strategy relies on the communication of the Power Sharing Index (PSI) between pair of converters to ensure accurate power sharing between converters. Selection of the converter pairs can be done

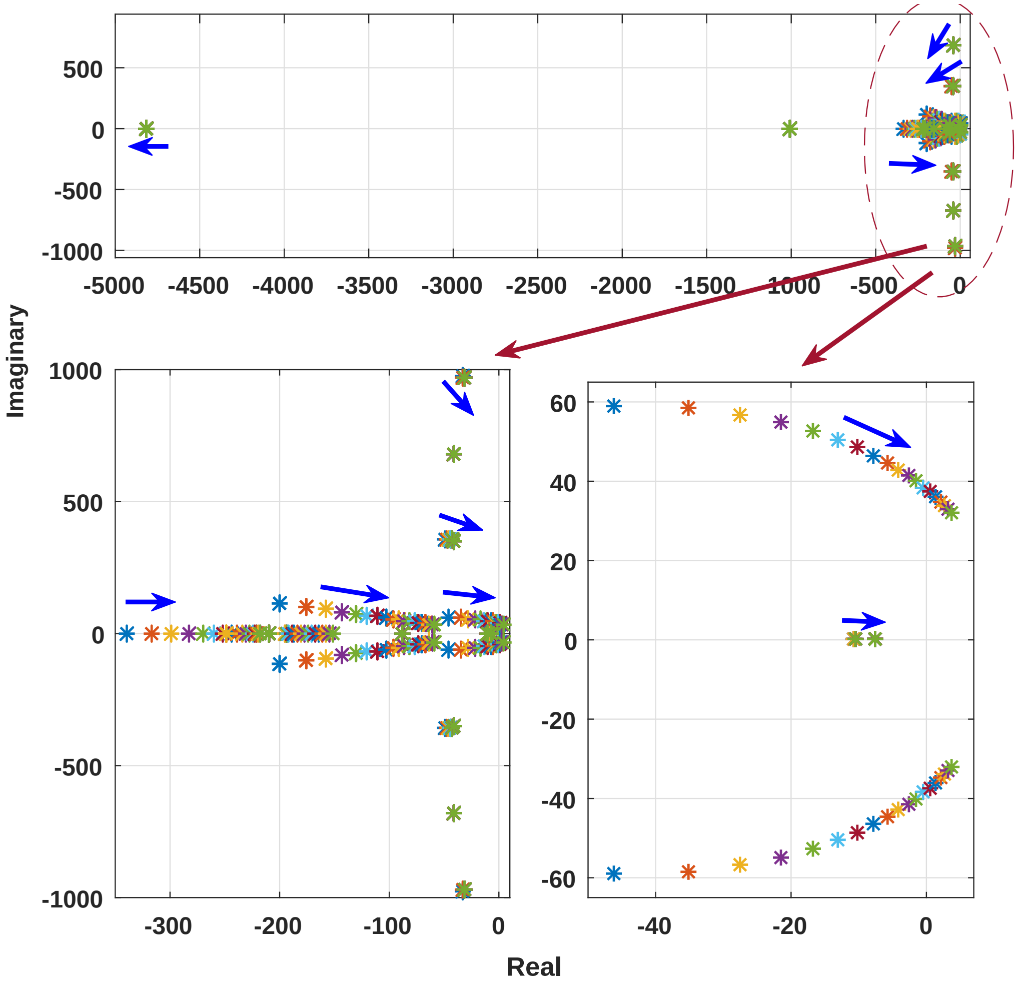

Figure 4.12. The movement of the system eigenvalues with PVD control when the communication delay is increased from 15 ms to 52 ms in steps of 2ms.

by system operators based on the network topology and specific operation considerations. The PSI is determined as per (4.5) and is shown in Fig. 4.13. Here the dc link reference voltage at i_{th} converter station is modified as per

$$\begin{cases} PSI_i = (P_{ref,i} - P_i)D_i \\ V_{dc,ref,i} = V_{dc,ref,i,0} + (PSI_i - \\ -PSI_j e^{-T_d s})(K_{P,PSI,i} + \frac{K_{I,PSI,i}}{s}) + PSI_i \end{cases} \tag{4.5}$$

where the i_{th} converter variables $V_{dc,ref,i,0}$ and $V_{dc,ref,i}$ are the initial and the modified dc link voltage references, respectively, P_i and $P_{ref,i}$ are the measured and reference power, respectively, D_i is the power droop constant. The term $e^{-T_d s}$ is used to represent the communication delay associated with the transfer of the PSI of the j_{th} converter to the i_{th} converter, where T_d is the amount of the delay in seconds. The error between PSIs is sent to the PI controller to generate the correction term $\Delta V_{dc,PSI}$ for the dc link voltage reference. The proportional $K_{P,PSI,i}$ and integral $K_{I,PSI,i}$ gains are tuned based on the modal analysis elaborated in the next section. Finally, the dc voltage reference of the i_{th} station is computed according to (4.5), and the local dc voltage at the i_{th} controller is used as a feedback signal (Fig. 4.13).

The PSI of the i_{th} station, in its turn, is sent to its pair k_{th} station different for the j_{th} station, ensuring accurate power sharing between all droop controlled converters. The advantage of the proposed control strategy over PVD is that the tuning of the PI controller allows adjusting the dynamics associated with the correction term, enabling stable system operation when even large latencies are encountered in the communication. Additionally, the proposed controller utilizes the PSI measurement of the nearby VSC station, unlike its alternative that communicates the measured voltage information throughout the whole dc system. Therefore, the communication delays for transferring PSIs are likely to be smaller than those associated with PVD controller. Finally, the proposed strategy does not need a global dc voltage reference, therefore, unlike with the PVD controller, the operator-specified reference values can be tracked during normal operation.

As with any other power-voltage droop control, the strategy of Fig. 4.13 would inevitably experience deviation of the dc voltages from the nominal values, determined by the $\Delta V_{dc,droop,i}$ and $\Delta V_{dc,PSI,i}$. This issue is solved by combining the proposed power-sharing controller with the voltage regulation controller discussed in the previous section.

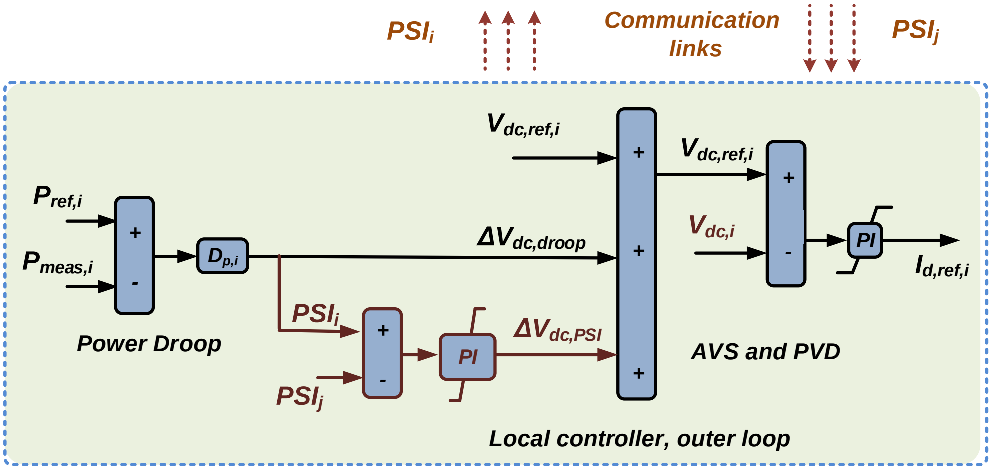

Figure 4.13. The proposed power-sharing control structure.

This section, however, elaborates on the operation of the controller of Fig. 4.13, whereas the operation of the combined controller will be discussed in Section 4.3.

The proposed approach is also general enough be integrated with different adaptive droop approaches. An example is an adaptive droop control proposed in [104], where the droop gains are dynamically changed to ensure power mismatch sharing according to the available headroom of each converter station. The work in [104] uses PVD as a tool to ensure accurate power sharing based on the updated droop gains. Similarly, the proposed approach can be integrated with the controller proposed in [104], where the change of the droop gain would change the PSI of the respective converter and accurate power sharing can be established based on the updated PSIes. It is worth noting that for the case of bipolar dc system, there would be two separate PSIes for positive and negative pole controls. Those indexes are sent their paired converters and the accurate power-sharing is achieved in both pole networks.

Furthermore, to avoid transients associated with the saturation of the PI-based controller in Fig. 4.13, the latter is equipped with an anti-windup loop. The current study uses Integrator Clamping technique to avoid windup effect, which is shown in Fig. 4.14. The error input to the respective PI controller is set to zero for the following conditions

- the error is positive, and the PI output is greater than the upper saturation limit
- the error is negative, and the PI output is lower than the lower saturation limit.

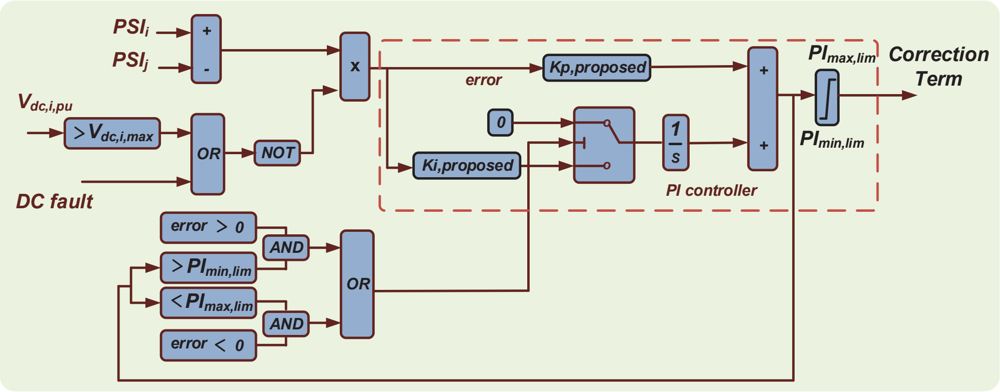

Figure 4.14. T he handling of the PI controller during transients considering anti-windup loop.

Otherwise, the error is fed directly to the PI controller.

It is important to evaluate the performance of the proposed controller during ac and dc faults as well. Faults in the ac grids may restrict the amount of the active power which can be transferred from the converter to the faulty grid. This is the result of the reduction of the grid voltage and the limited current carrying capability of the converter station, which can be mathematically expressed as

$$P_{max,fault,i} = V_{d,fault,i} I_{d,limit,i} \tag{4.6}$$

where $P_{max,fault,i}$ is the maximum active power possible to inject (or absorb) to the i_{th} system during fault, $V_{d,fault,i}$ is the magnitude of the PCC voltage during fault and the $I_{d,limit,i}$ is the maximum converter current restricted by the current limiter. Therefore, the accurate power sharing may not be possible to achieve in this case. It is therefore advised to deactivate the proposed controller during ac faults as shown in Fig. 4.14. It should be noticed that ac fault can be detected locally at any converter station by monitoring the dc voltage. Similarly, because during dc faults the power control ability of the converters may be lost, it is also recommended to deactivate the proposed controller during dc fault duration. The latter type of fault can be detected locally at any station within 1-2 ms [72].

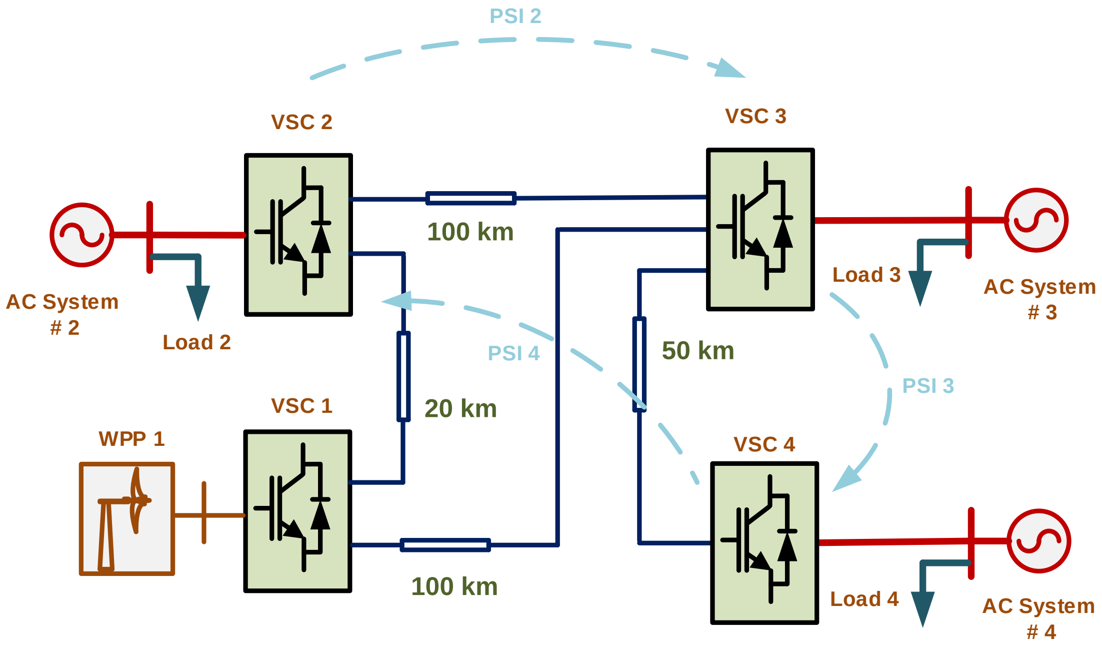

Figure 4.15. The four-terminal MT-HVDC system under study.

4.2.3 Modal analysis of the proposed controller

In this subsection, the effect of the controller parameter variation, and more importantly the effect of the communication delay on the stability of the system adopting the proposed PSI-based controller is evaluated through modal analysis. The test system used for modal analysis and for part of time-domain simulations used in this section is shown in Fig. 4.15, where three ac areas and Wind Power Plant (WPP) are connected through four terminal symmetrical monopole 300 kV MT-HVDC network. During the normal operation, the converters #1 and #4 operate in the rectifier mode, whereas the converters #2, #3 operate in the inverter mode. The linearization is done around nominal operating condition considering 0.3pu power droop constant (similar to the case with PVD). It is worthy to notice that the time delays are represented by rational transfer function for the linearization of the system. The second-order Pade approximation is used for this representation as per

$$e^{-T_d s} \approx \frac{\frac{T_d^2}{12}s^2 - \frac{T_d}{2}s + 1}{\frac{T_d^2}{12}s^2 + \frac{T_d}{2}s + 1} \tag{4.7}$$

As shown in Fig. 4.16 and Fig. 4.17, the proposed controller ensures stable system operation even considering large variation of controller parameters. While keeping the integral gain of the proposed controller $K_{I,PSI}$ equal to 10pu, the proportional gain is varied from 0.5pu to 10pu by steps of 0.5pu. As shown in Fig. 4.16, some of the dominant poles initially move to the left. When the gain is around 2pu, those poles start fast movement to the right. Therefore the proportional gain of 2pu is chosen for the proposed controller. Afterwords, the integral gain is changed from 5pu to 105pu. It can be seen from Fig.4.17 that different dominant pole clusters show opposite movement with an increase of the integral gain. Thus, an integral gain of 30pu is selected considering this trade off.

One of the main advantages of the proposed controller is the stable operation when large latencies are present in the communication. To validate this point, Fig. 4.18 illustrates the system root locus when the time delay is increased from 10ms to 150ms by step of 10ms. It can be observed that with an increase in the delay the poles move towards the right side of the s-plane, deteriorating the system stability. However, even with the considered large delays the system poles stay in the left half plane, determining the stable system operation.

The participation factor analysis of the proposed controller is also illustrated in the Fig. 4.18. The analysis reveals that the fastest poles located on the far left of the s-plane are mainly associated with the d, q axis currents in the phase reactor (Fig. 4.18

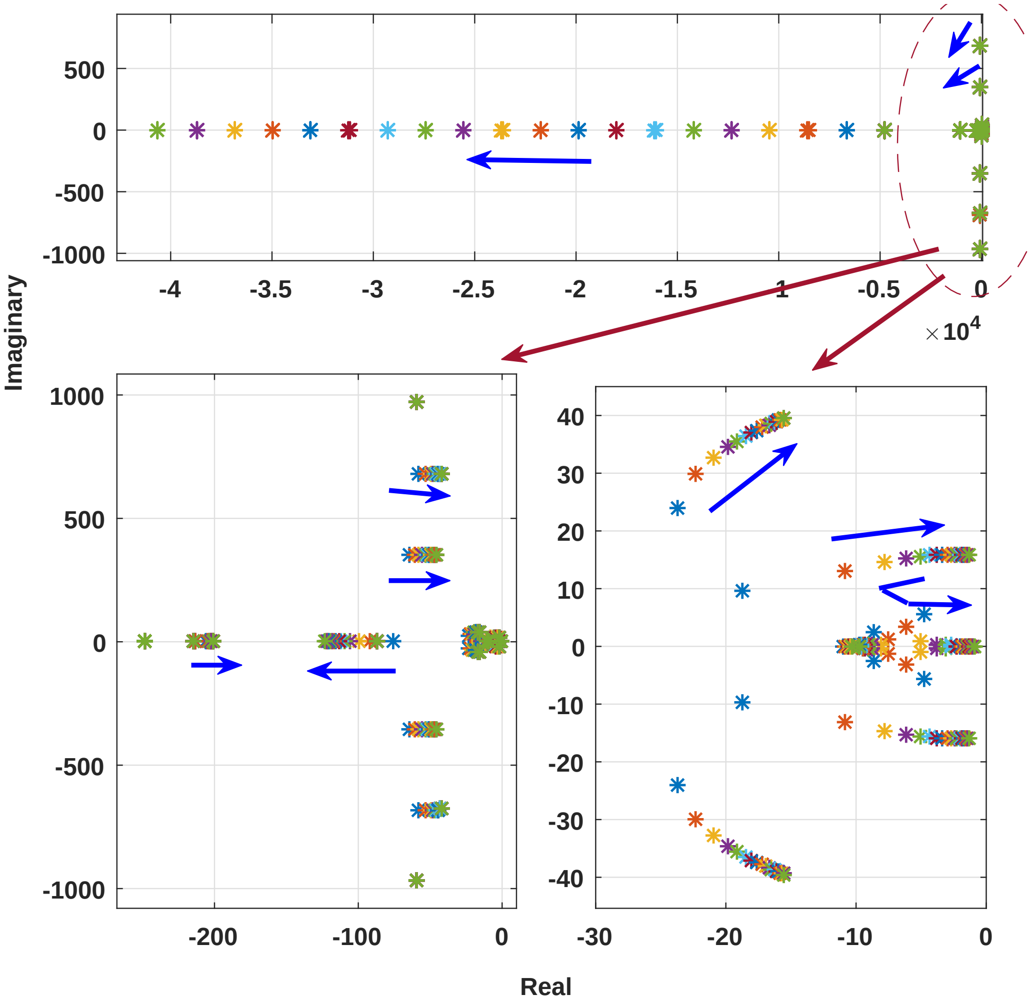

Figure 4.16. The movement of the system eigenvalues when the proportional gain of the proposed controller is increased from 0.5pu to 10pu in steps of 0.5pu (communication delay of 25 ms is considered).

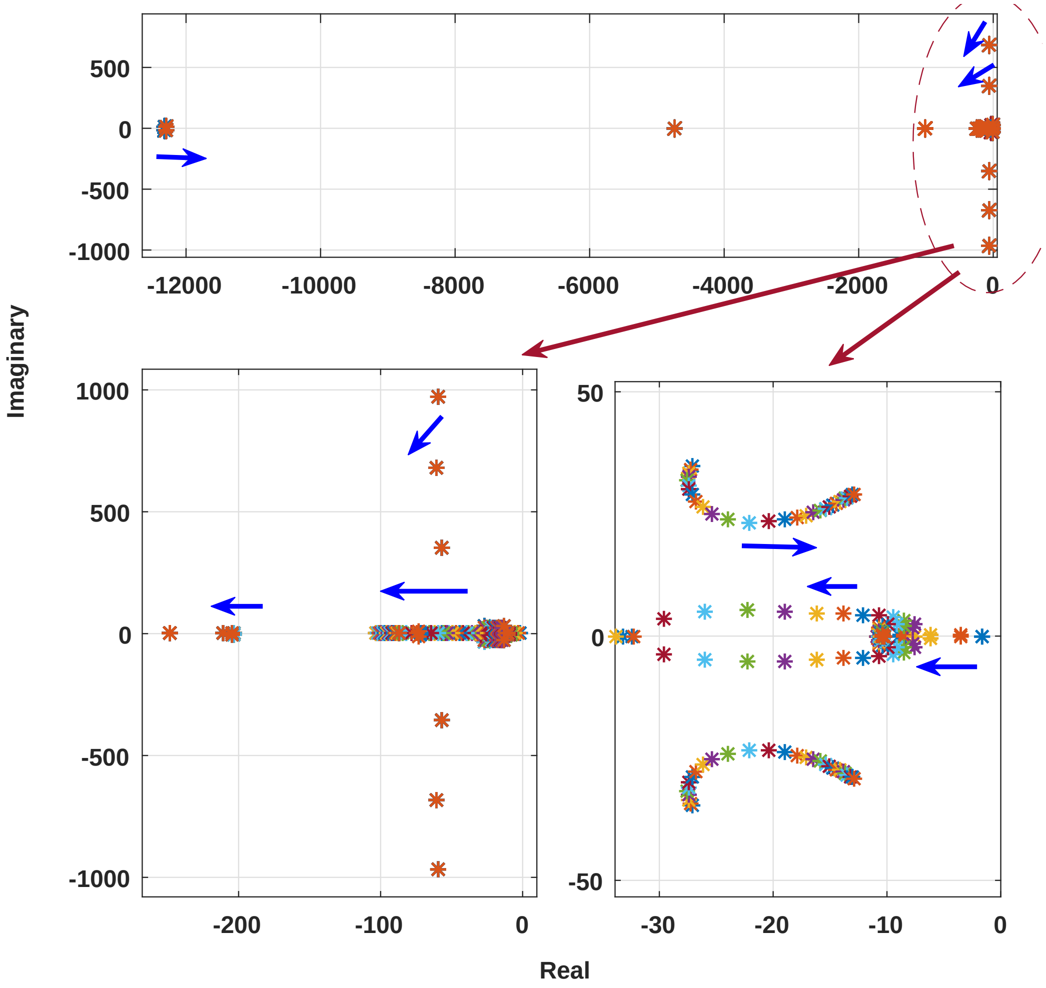

Figure 4.17. The movement of system eigenvalues when the integral gain of the proposed controller is increased from 5pu to 150pu in steps of 5pu (communication delay of 25 ms is considered).

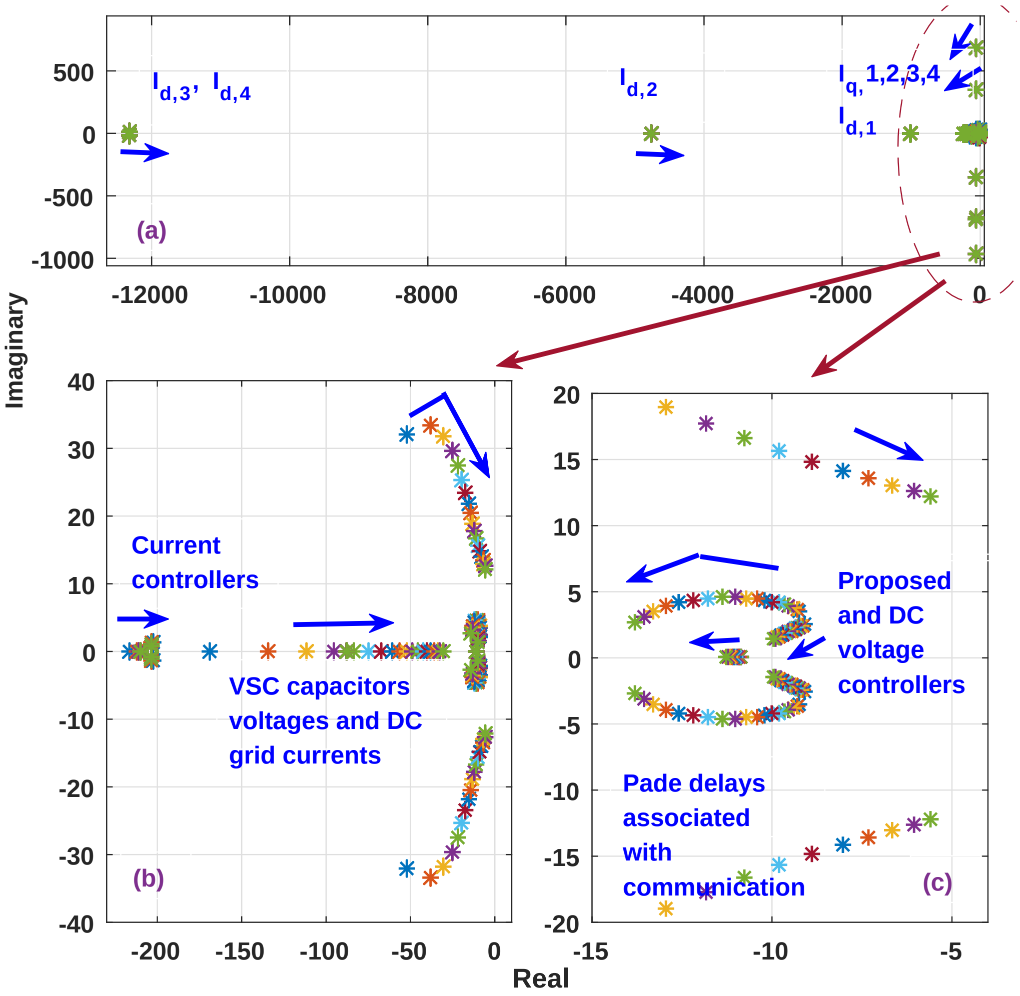

Figure 4.18. The movement of system eigenvalues with the proposed control strategy when the time delay is increased from 10 ms to 150 ms in steps of 10 ms. Also shown the participation of different states on the eigenvalues.

(a)). The movement of the eigenvalues associated with the inner current controller, dc grid capacitances and the currents in the pi sections can be clearly illustrated in Fig. 4.18 (b), where the movement of the system poles associated with dc voltage controller are also shown. It can be observed in Fig. 4.18 (a) that the eigenvalues associated with the Pade approximated time delays move fast to the right when the delay is increased. However, the poles associated with the proposed controller demonstrate a slow movement to the left and do not deteriorate system stability.

4.2.4 Time-domain simulations

A comprehensive simulation study is carried out in the MATLAB/Simulink environment to evaluate the performance of the proposed and existing control strategies during various operational scenarios. Several disturbances are simulated considering the four-terminal system shown in Fig. 4.15. In all cases the wind farms' converters are operating in a constant power controlled mode.

Initially equal active power references of -0.5 pu are set for the stations at the droop controlled inverters VSC2 and VSC3, and the reference for the droop controlled rectifier station VSC4 was set to 0.5 pu. The WPP plant injects 0.5 pu active power to the dc system. In all scenarios the droop gain is equal to 0.3 pu.

4.2.4.1 Performance of the proposed controller during step increase in wind power with 25ms communication delay

In the first scenario, 25ms communication delay is considered for the communication of the PSIs between the converter stations. The output wind power change from 0.5 pu to 0.7 pu is initiated at time t=2s. Fig.4.19 (a) illustrates the dc link voltages at all four converter stations, where it can be observed that the voltage profile increases with an increase of the power in the dc system. The PSIs for all stations are presented in the Fig. 4.19 (b). Here it can be clearly seen that before the disturbance and soon after the disturbance at time t=2s the PSIs are equal for all the converter stations as a result of the proposed controller action. The accurate power sharing can be also validated from the active power deviations shown in subfigure (c) and (d) of Fig. 4.19, where equal (0.065pu) active power sharing is achieved with the proposed control strategy.

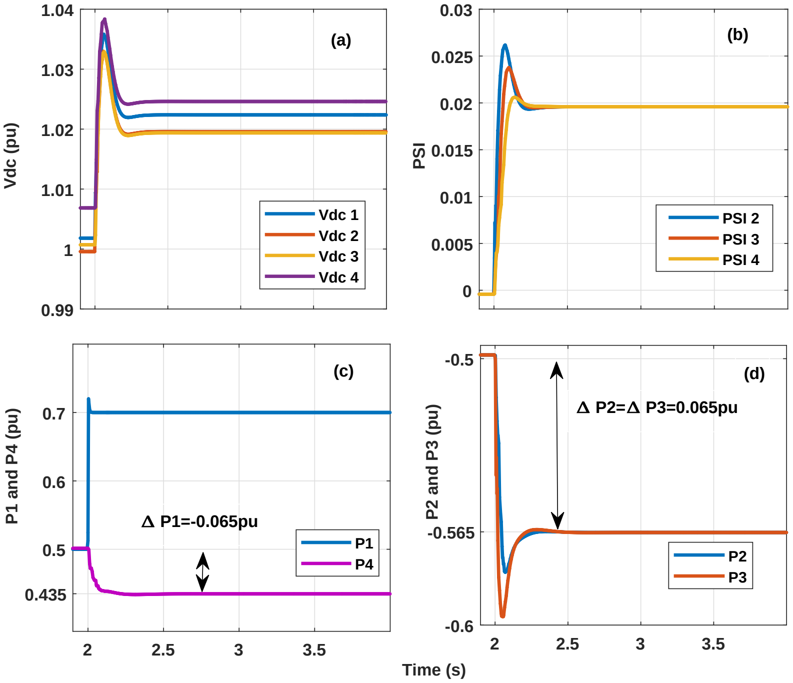

Figure 4.19. The system performance with proposed strategy during increase in wind power when communication delay is 25ms. dc link voltages (a) and PSIes (b) at all four converter stations, active power traces at rectifiers VSC1 and VSC4 in (c) and inverters VSC2 and VSC3 in (d).

4.2.4.2 Performance of the local voltage based droop controller during step increase in wind power

The same scenario of wind power increase from 0.5 pu to 0.7 pu is repeated with conventional local voltage based droop control strategy for a better illustration of the problem of inaccurate power sharing (Fig.4.20). When the wind power is increased at time t=2s, similar with the proposed control strategy, the dc voltage profile increases with conventional control strategy (subfigure (a) of Fig.4.20). The power mismatch sharing between droop controlled converters VSC 2, VSC 3 and VSC 4 are 0.07 pu, 0.065 pu and 0.06 pu, respectively (subfigures (c) and (d) of Fig. 4.20). It can be observed that the power sharing between converters differs slightly as opposed to the proposed controller. The resultant power sharing is dependent on the dc system parameters and topology. As a result, significant mismatch can be observed in the PSIes of the droop controlled converters shown in subfigure (b) of Fig.4.20.

4.2.4.3 Performance of the PVD controller during step increase in wind power with 25ms communication delay

The PVD controller performance under the same scenario of 25 ms and wind power change by 0.2 pu is depicted in Fig. 4.21. The accurate power sharing confirmed by the equal PSI can be validated from Fig. 4.21 (b), although at the expense of some transient oscillations. The same point can be validated by the equally shared power values seen in Fig. 4.21 (c) and (d).

4.2.4.4 Performance of the proposed and PVD controller during wind power change subject to higher communication delays

The identical step change in the wind power is initiated for the cases with larger time delays in the communication. As shown in the Fig. 4.22, the stability assessment is done by evaluating the dc grid voltage profiles. It can be seen from (a), (b) and (c) subplots of Fig. 4.22 that even with very large communication latencies like 150 ms, the proposed control approach results in stable system operation. In contrary, the PVD controlled system is unstable when latencies in the order of 50 ms are encountered for the communication of the pilot voltage. These scenario clearly demonstrates the advantage of the proposed controller of using local voltage feedback (unlike PVD strategy) during the dynamic operation to capture fast transients associates with the dc voltages. Thus, the

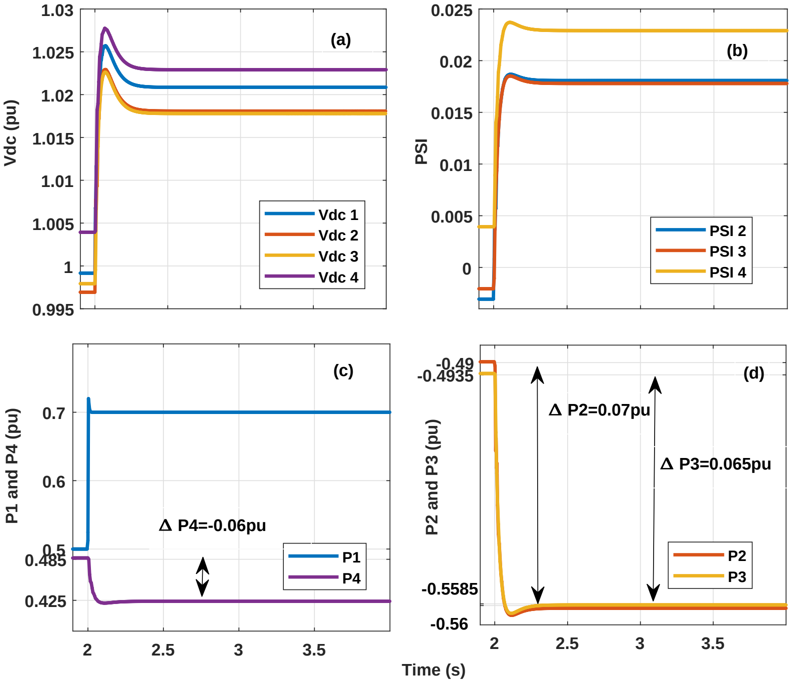

Figure 4.20. System performance with local voltage based droop control during increase in wind power. dc link voltages (a), PSIes (b) at all four converter stations, active power traces at rectifiers VSC1 and VSC4 in (c) and inverters VSC2 and VSC3 in (d).

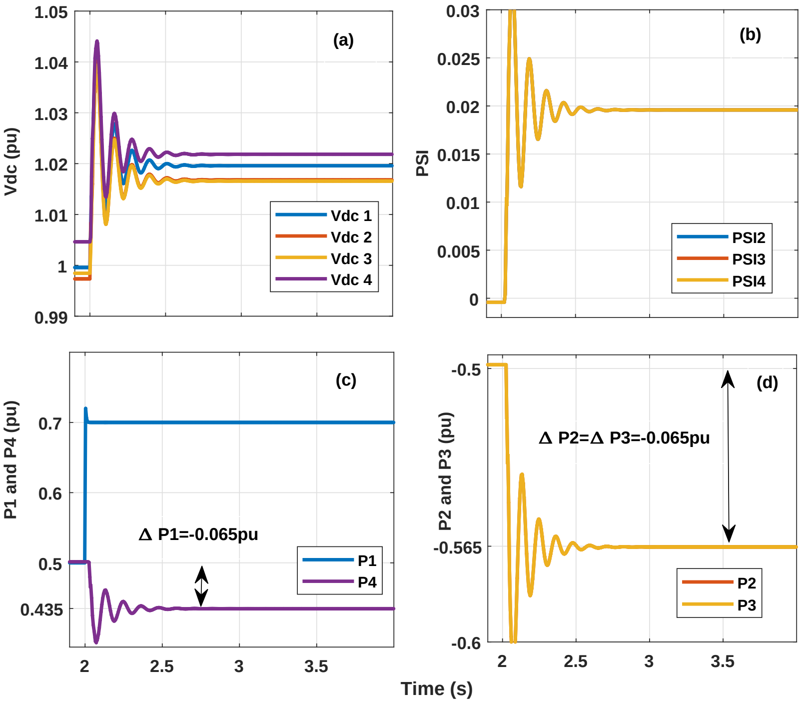

Figure 4.21. System performance with PVD during increase in wind power when communication delay is 25ms. dc link voltages (a), PSIes (b), active power trajectories at rectifiers VSC1 and VSC4 in (c) and inverters VSC2 and VSC3 shown in (d).

proposed strategy ensures a proper operation of the system when large delays are present in the communication of the signals.

4.2.4.5 Performance during large disturbance

To evaluate the system performance during large disturbances, in this scenario, three phase fault is applied in the system adjacent to VSC3. The three phase to ground fault causes reduction in the respective Point of Common Coupling voltage ($V_{PCC,3}$), which reaches to 0.2pu. As it was previously discussed, the power transfer from VSC3 reduces and reaches 0.2 pu (Fig. 4.23 part (a)), which is determined by the 1pu maximum current limit specified for the station. As a result of the action of the power droop, the power at the other rectifier station VSC2 increases, reaching almost 0.7 pu, while the power at the inverter station VSC1 decreases (shown in (a) and (b) subplots of the Fig. 4.23, respectively). This changes allow to avoid dc link overvoltage above the allowed limit (usually 10 %), which reaches 1.06 pu as can be seen in Fig. 4.23 (c). However, as can be observed from (d) part of Fig. 4.23, the PSI is not equal between VSC2 and VSC4, which is a consequence of the deactivation of the proposed controller.

4.3 Performance verification of the combined voltage regulation and power sharing approaches using the standard CIGRE B4 MT-HVDC test system

This section demonstrates the system performance when the previously developed voltage regulation and power-sharing strategies are combined together. The two developed loops have distinct control objectives, therefore, as it will be demonstrated in this section, the operation of one loop does not affect the proper operation of the other controller.

The CIGRE B4 benchmark test system is developed using SimPowerSystem toolbox of the MATLAB/Simulink environment for the complete validation of the integrated control strategy. The developed system is shown in Fig. 4.24, which is a five terminal bipolar grid with ±400 kV dc voltage. The line lengths are specified in the Fig. 4.24, while the other parameters of the system and the associated controller parameters are given in Table A8 [83, 164]. Both positive and negative pole lines, as well as the metallic return circuit, have the same RLC parameters [26]. During the initial steady state condition, all three droop controlled converters (VSC1, VSC2, VSC3) operate in the inverter mode and have

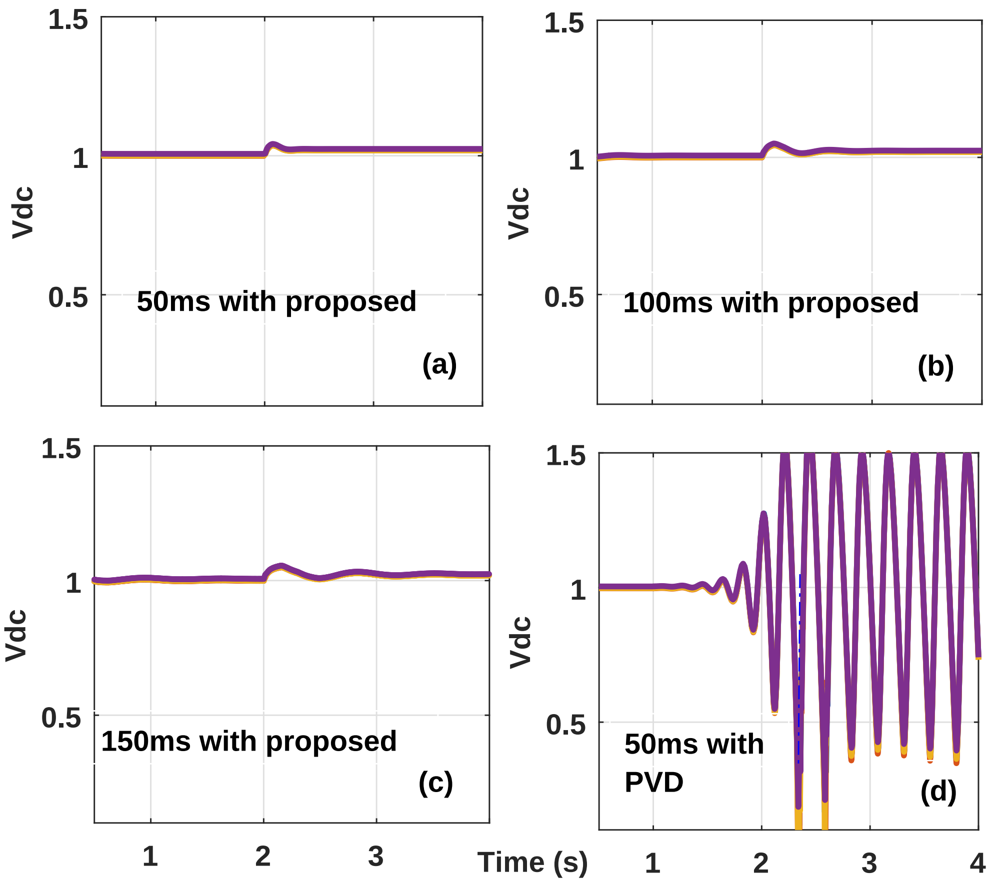

Figure 4.22. Comparison between PVD and proposed strategy when large latencies are encountered in the communication. dc link voltages with the proposed strategy for 50 ms(a), 100 ms (b) and 150 ms (c) and with the PVD for 50 ms (d) communication delay.

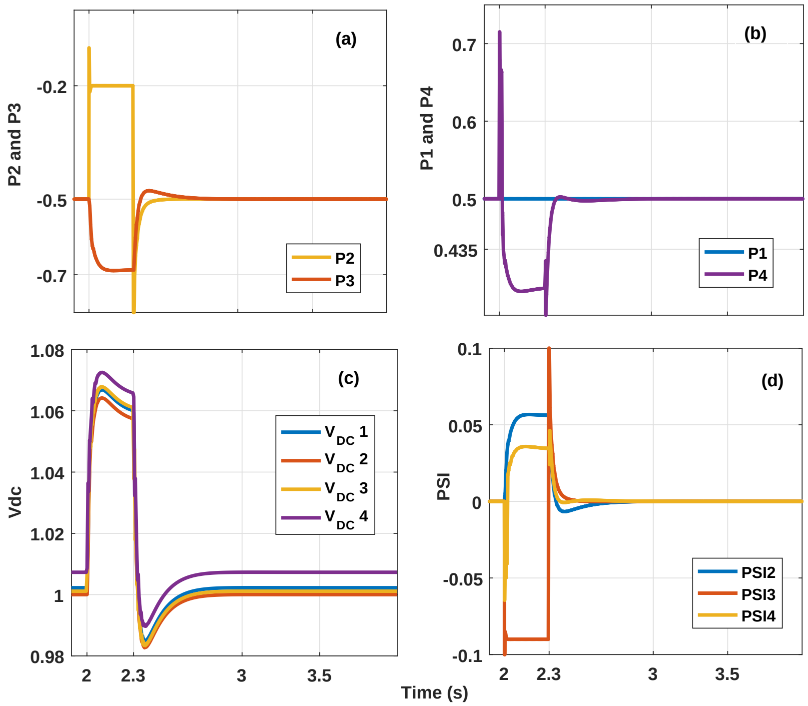

Figure 4.23. System performance with proposed strategy during three phase fault in the system near VSC3. active power injections at inverters VSC2 and VSC3 in (a) and rectifiers VSC1 and VSC4 in (b), dc link voltages (c) and PSIes (d) at all four converter stations.

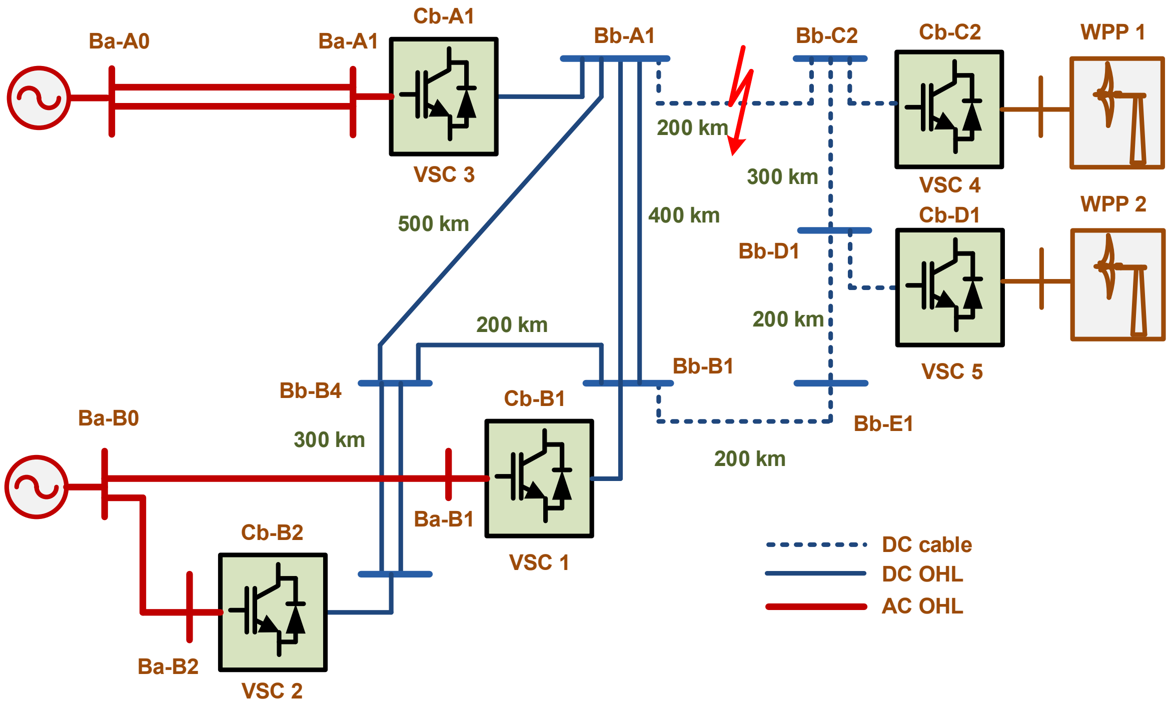

Figure 4.24. MT-HVDC test systems used in this study (part of CIGRE B4 benchmark system).

the power reference of 0.4 pu. For the clarity of the illustration, equal droop gains are selected for all three converters. The rectifier stations VSC4 and VSC5 deliver 0.45 pu and 0.95 pu wind power, respectively.

4.3.1 Time-domain verification of the combined controller

4.3.1.1 Performance evaluation during wind power increase

This case presents the effect of the power increase supplied by the wind station WPP 1. The communication delay associated with the transfer of PSI information is considered to be 50 ms (one way communication of PSIes), and the delay associated with the AVS term is accordingly considered to be as 100 ms (delay associated to sending the terminal voltage+delay associated with receiving the correction voltage term). The active power references at the droop controlled converters are equal to 0.4 pu, while the power references at the rectifier stations Cb-C2 and Cb- D1 are 0.45 pu and 0.95 pu, respectively.

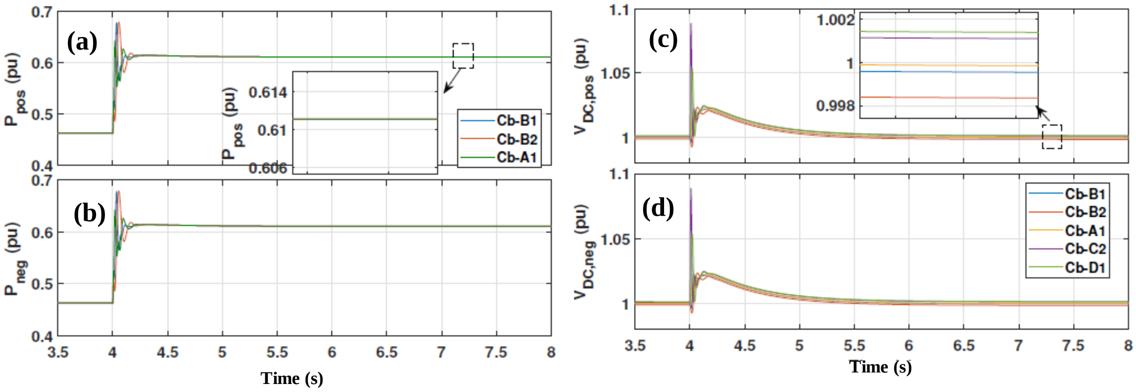

Figure 4.25. The active power injections of a) positive pole droop controlled converters and b) negative pole droop controlled converters, and the dc link voltages of c) positive and d) negative pole networks.

The implemented controller provides an equal power sharing capability to the droop controlled converters. As the identical droop gains are considered for all three droop controlled converters, the power mismatch should be shared equally between those converters. As it can be observed from Fig. 4.25a and Fig. 4.25b, during the initial steady state the power injections at all three converters are equal as a result of the action of the implemented controller. At the time t=4 s, the active power reference at the constant power-controlled rectifier station Cb-C2 is changed from 0.45 pu to 0.9 pu to imitate the sudden change in the wind power. The small transient in the Cb-D1 converter power injections is associated with the transients of the dc link voltages. The 0.45 pu wind power change is shared between three droop controlled inverter stations, resulting in about 0.15 pu power change in each converter (from 0.463 pu till 0.611 pu). The zoomed version of Fig. 4.25a verifies the precise power sharing between the designated converters.

Furthermore, Fig. 4.25c and Fig. 4.25d also depict the dc link voltages of the positive and negative pole network at all five converter stations, respectively. With an increase of the power injected to the dc system, the average profile of the dc voltage increases. Moreover, the profile of the dc voltage at the Cb-C2 converter increases relatively more to push more power to the dc grid. It should be pointed out that although the high communication delay results in relatively larger dc voltage transient, the 10% maximum voltage limit is not violated during whole operation. After an initial transient, the implementation of the AVS algorithm allows to bring the average dc voltage to the nominal value. The zoomed version of Fig. 4.25c verifies that while at steady state, the average dc voltage of positive pole is maintained at 1pu. This reduces the risk of the overvoltage in the dc system with the further changes in the system, specifically with an increase of the power injected to dc grid.

4.3.1.2 Performance evaluation during large communication delays

The implementation of the CIGRE B4 test-system further verified the advantage of the proposed control strategy over the existing approaches when large latencies are present in the system. To illustrate the robust nature of the integrated controller, Fig. 4.26 (a) illustrates the dc link voltage profiles when different values for the delays are considered for the proposed controller. Specifically, to make even a challenging case, the delay for the communication of the PSIes from VSC1 to VSC2 is 50 ms and the delay for the communication between VSC2 and VSC3 is 150 ms. It can be observed that soon after the disturbance (0.25 pu wind power increase) the system reaches steady state with the proposed controller. However, with the PVD controller, when the delay is around 50 ms, the system demonstrates oscillatory behavior even before the application of any disturbance (Fig. 4.26 (b)). The similar results were obtained for the four terminal MT-HVDC system (Fig. 4.15), and the standard CIGRE B4 system, which further confirms the advantage of the proposed system during large communication latencies.

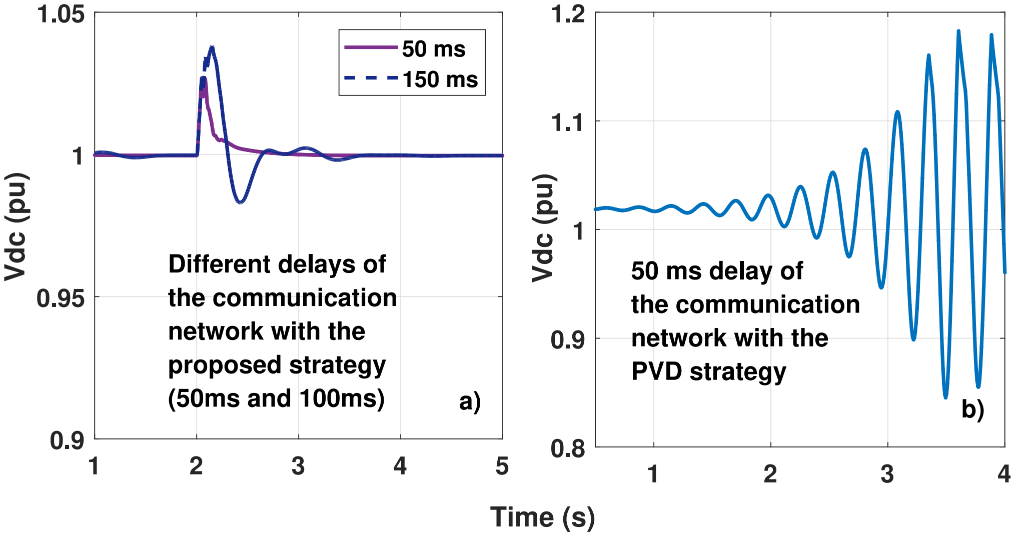

Figure 4.26. Comparison between PVD and proposed strategy when large latencies are encountered in the communication in the CIGRE B4 system. Dc link voltages with the proposed strategy for 50 ms and 150 ms communication delays (subfigure a) and dc link voltage with the PVD for 50 ms communication delay (subfigure b).

4.3.2 Real-time implementation of the proposed control structures

The performance of the CIGRE test-system considering the developed control structures is further tested in real-time implementation using OP5600-OPAL-RT simulator. Such real-time simulation (RTS) can execute powerful computations with high accuracy and low cost real-time execution. The usual applications of OPAL-RT to test the controllers are as follows [165, 166].

- Rapid control prototyping (RCP) where the RTS is used for the implementation of the physical controller, which is then connected to the physical system for testing. The realization of the controller through RTS provides flexibility and ease of debugging.
- Hardware in the Loop (HIL) where the physical controller is linked to the power components modeled using the RTS. A separate processor can be devoted for the implementation of the physical controller, which will result in creating an RCP or any DSP-based controller. The information exchange between the physical controller and the modeled plant is accomplished in real-time through I/O channels.

The latter application is adopted for testing the combined control approach. Such implementation allows to consider important features of practical implementations, including the delays existing in analog/digital conversions, and the noises that are present in the acquisitions of feedback signals. The SimPowerSystem model of the system shown in Fig. 4.24 is compiled using RT-LAB to convert the model to C-language. The compiled model is divided into master and slave subsystem which are loaded in two different cores of the OPAL-RT. The results of the real-time implementation will be discussed considering two separate case-studies presented below.

4.3.2.1 Real-time performance evaluation during dc side large disturbance

In this case, a pole-to-ground fault is applied to the system to illustrate the effects of the dc side large disturbances. The fault is applied in the middle of the line connecting the buses Bb-A1 and Bb-C2 by short circuiting the positive pole to the metallic return through a resistance of 0.0001 Ω. It can be observed from Fig. 4.27 (a) and (b) that once the fault is initiated, both positive and negative dc voltages experience transient, with relatively more voltage dips observed for the positive pole voltages. The fault is isolated within 5 ms [72] by disconnecting the positive pole cable between the buses Bb-A1 and Bb-C2. The fast disconnection and the consequent rerouting of the converter active power injections allows the system to return to the steady state within about 400 ms with the equally regulated active power injection profiles at the droop controlled converters (Fig. 4.27 (c) and (d)). It is worth noting that the dc voltages remain within 10% limit during the whole transient duration.

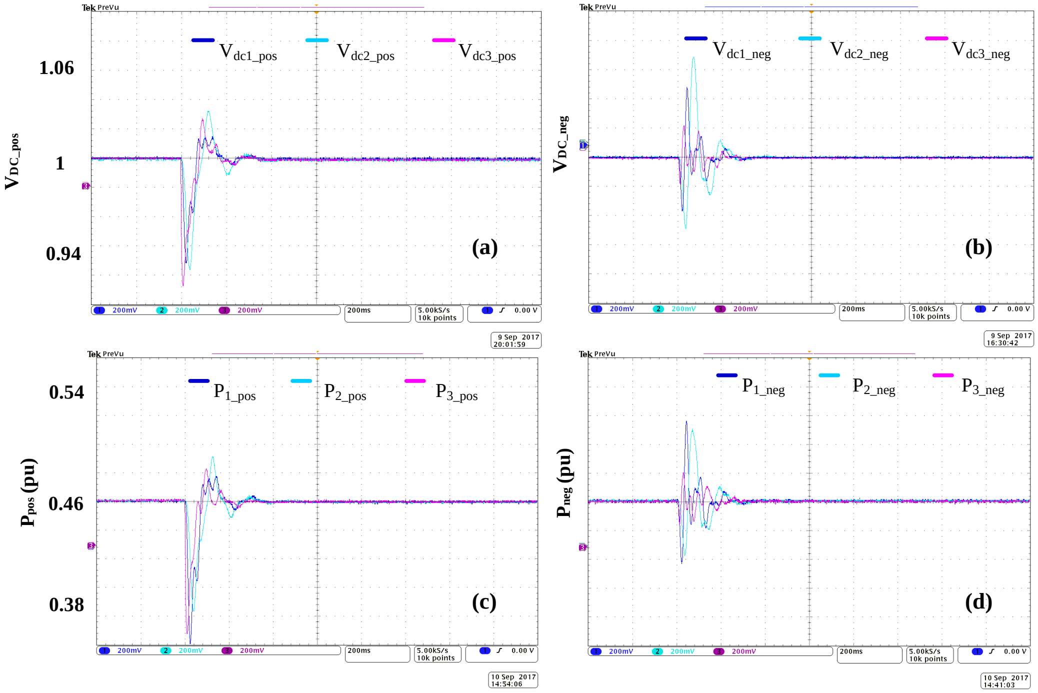

Figure 4.27. Dc link voltages (subfigures a to b) and active power injections (subfigures c and d) at the droop controlled converters when the pole to ground fault occurs in the middle of the line connecting buses Bb-A1 and Bb-C2 of the CIGRE B4 system.

4.3.2.2 Real-time performance evaluation during active power reference change in the droop controlled converter

In this scenario, the reference active power at the converter station VSC 2 of the CIGRE B4 test system is increased from 0.4 pu to 0.7 pu. The active power injections are shown in Fig.4.28 (a) and (b) for the positive and negative pole networks, respectively. The lower subfigures in Fig.4.28 (c) and (d) demonstrate the PSIes of the droop controlled stations. It is worthy to notice that soon after the transient is initiated, the PSIes at all droop controlled stations reach the same steady state value, indicating proper power mismatch sharing between those stations equipped with the proposed controller.

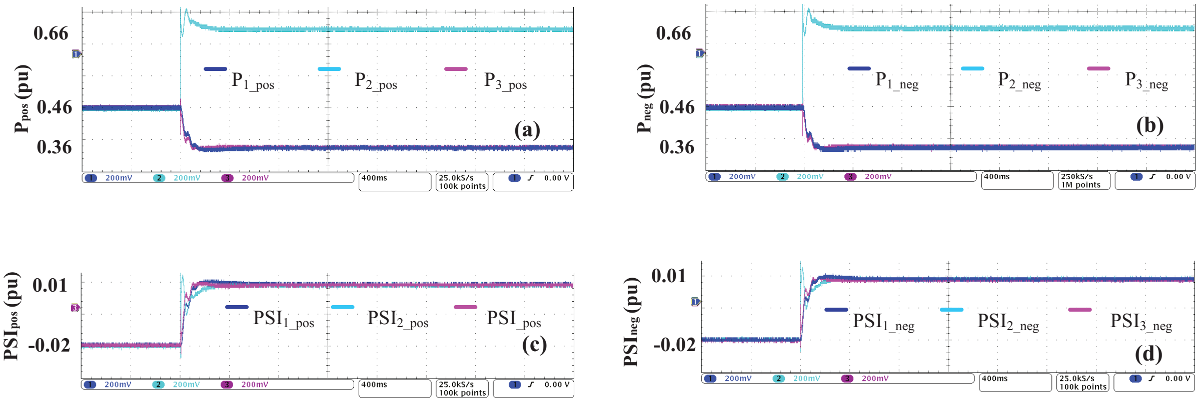

Figure 4.28. Active power injections (upper subfigures) and PSIes (lower subfigures) at the droop controlled converters of the CIGRE B4 system when the active power reference at VSC2 is changed from 0.4 pu to 0.7 pu.

4.4 Discussion

This chapter presented the first part of the developed control approach for MT-HVDC systems. Specifically, in the first section of this chapter, a voltage regulation algorithm was developed for MT-HVDC systems. The AVS loop ensures that the average dc voltage of the system is regulated to the nominal value, which allows achieving fast and precise power regulation without the risk of large steady state deviations in dc system voltages. To further enhance the speed of the power regulation, the FLL is applied for the grid synchronization, which is shown to enable enhanced power regulation of the MT-HVDC system during ac grid disturbances. The second section of the chapter focused on the power-sharing issue in MT-HVDC systems. It was shown that the proposed droop based control strategy has an advantage over conventional droop in terms of accurate power sharing which is determined solely by converter droop gains. The comparative analysis has been carried out between the proposed approach and alternative communication-based controller, namely Pilot Voltage Droop control. The analysis revealed that the proposed approach ensures enhanced system stability when even excessive latencies are encountered in the communication. Finally, the combined control solution was tested considering the benchmark CIGRE B4 test system. The modal analysis, time-domain and real-time simulations verified the capability of the proposed control approach in providing adequate system operation during normal operation and when subjected to large disturbances.

Chapter 5

Mutual Frequency Support Between MT-HVDC Interconnected AC Grids.

As it was discussed in the Literature Review chapter, the dc grid buffers disturbance propagation between ac systems connected through MT-HVDC systems, which results in an inability of ac grids to naturally support each other if any of those grids experiences a frequency event. It was discussed that the power-voltage droop strategies should be modified to create an artificial coupling between those ac systems and allow mutual frequency support.

In the first part of this chapter, the power-voltage droop strategy developed in Chapter 4 is augmented to enable mutual support between asynchronous ac grids interfacing to MT-HVDC systems. By properly redistributing the active power flow between the VSCs and thus between the ac grids those converters are connected to, the implemented controller achieves equalized disturbance distribution between MT-HVDC interconnected ac systems. The developed strategy provides superior performance compared to its counterparts discussed in the Literature Review chapter. Specifically, the disturbed grid experiences better frequency profile during the disturbance, e.g., less frequency nadir and reduced quasi steady-state frequency deviation.

In the second part of this chapter, the developed frequency support algorithm is further extended to consider operational states of each ac grid before determining the extent of the mutual frequency support. This modification allows distinguishing between the grids actually causing the disturbance and those grids assisting to overcome that disturbance; thus, the controller realizes more fair mutual frequency support. To this end, an algorithm is developed for continuously detecting the affected and supporting grids and achieve the desired ratio-based frequency deviations based on the pre-specified ratios. Modal analysis is conducted to elaborate on the stability of the developed controller, and time-domain simulations are conducted to demonstrate the comparative advantage of the proposed strategy. The work of this chapter has been published in the IEEE Transactions on Power Delivery [155] and IEEE Transactions on Power Systems [167].

5.1 Equalized mutual frequency support between MT-HVDC interconnected asynchronous ac systems

The Literature Review chapter have demonstrated the drawbacks of the existing frequency support strategies employed for the control of VSCs in MT-HVDC systems. The main deficiency of those strategies was the lack of mechanism that can distribute the relative affect of disturbances into the grids trying to overcome those disturbances in a predictable manner. Therefore, as it will also be demonstrated by the simulation results of this section, when the existing strategies are used, the relative frequency deviations of ac systems participating in mutual frequency support might not be according to pre-specified ratios. In fact, those deviations, and therefore the affect on each ac system, are highly dependent on the current operating point and selection of the controller parameters.

To achieve an enhanced frequency deviation sharing capability of the MT-HVDC network, an outer loop structure of the previously developed controller of VSCs is modified. Specifically an algorithm named frequency cooperativeness (FC) strategy, is integrated into the controller of Chapter 4. Unlike other frequency support algorithms, e.g. frequency droop (FD) control approach, the FC approach allows achieving prespecified frequency sharing, therefore reducing the maximum ROCOF, frequency deviations and quasi-steady state frequency after a sudden disturbance happen in the system. Also, the proposed approach allows consideration of the grid code requirements in the frequency support control approach of the MT-HVDC system. Therefore, the ac systems that has more strict grid code requirements (compared to other ac grids) will participate less in the mutual frequency support.

The structure of the developed control algorithm is shown in Fig. 5.1. After a system frequency deviation, the proposed controller dynamically changes the reference power of the i_{th} converter $P_{i,ref}$ by the power deviation term $\Delta P_{i,FC}$ according to the following equation

$$\Delta P_{i,FC} = \left(\sum_{k=1,k\neq i}^{m} \frac{\Delta f_k}{m-1} - \Delta f_i w_i\right)\left(k_{p,FC} + \frac{k_{i,FC}}{s}\right) \tag{5.1}$$

where m is the total number of the droop controlled converters, Δf_i and Δf_k are the frequency deviations from nominal values in the systems neighboring i_{th} converter and all other converters except the i_{th} converter, respectively. $k_{p,FC}$ and $k_{i,FC}$ are the

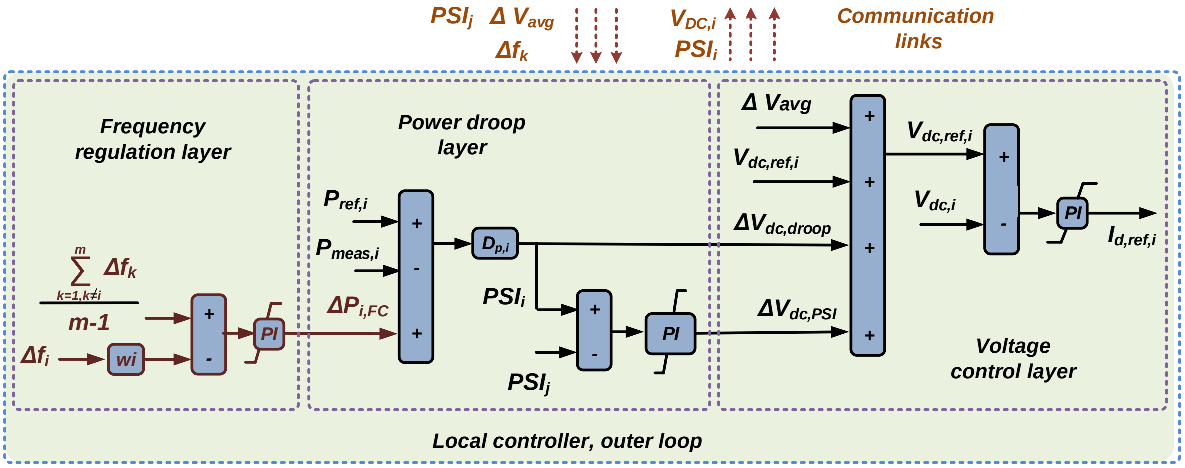

Figure 5.1. The structure of the designed algorithm for ensuring equalized mutual frequency support between MT-HVDC interconnected ac systems.

proportional and the integral gains of the PI controller applied on the respective frequency error, and w_i is the weight factor of the i_{th} converter and determines the relative frequency deviation sharing of the i_{th} system. For example, if all converters but one have the same weight factors, and for that one converter the weight factor is two times higher, then the frequency deviation of the latter system will be two times less in comparison with other systems given no limits are reached. The weight factor can be determined by the MT-HVDC system operator according to frequency requirements (maximum frequency nadir and ROCOF) specified by individual grid code [168, 169]. It is worth noting that the operation of the PSI based power-sharing between VSCs and FC based power-sharing between ac systems happens sequentially as the two control objectives might contradict each other. Therefore, whenever the frequency deviation exceeds the pre-specified limit at the any droop-controlled converter, the $\Delta V_{dc,PSI}$ term in Fig. 5.1 is sampled and hold for the duration of the frequency event.

Unlike the FD control, the integral action of FC algorithm allows sharing of the frequency deviations between ac systems in a predefined and controlled manner. It should be noted that the control strategy is also valid in the case when grids with various frequencies are interconnected to each other, as the pu frequencies are used for the control realization. As it will be shown in the next subsection, to achieve sufficient responsiveness for the fre-

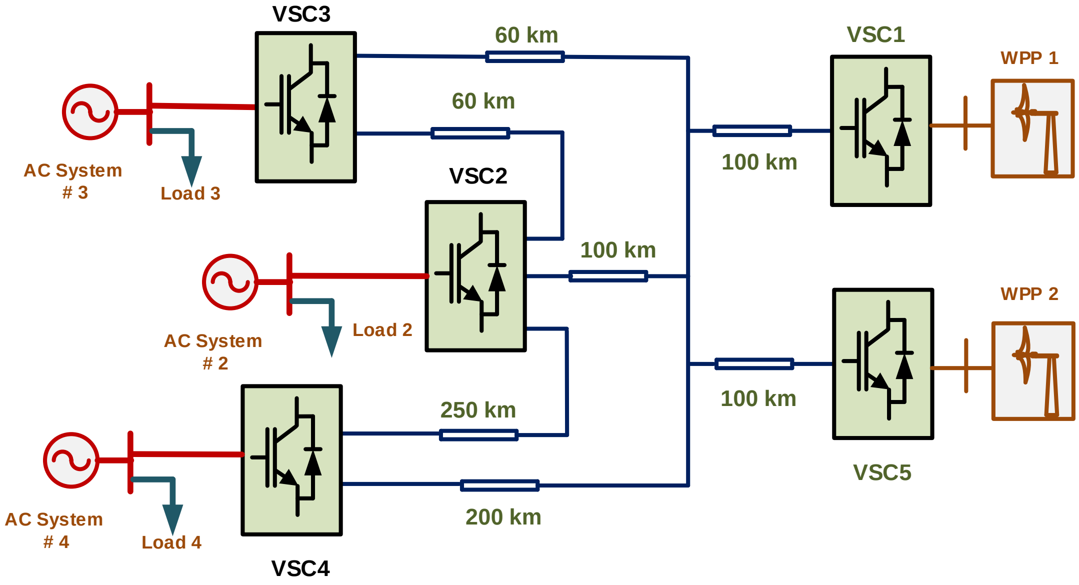

Figure 5.2. Five terminal MT-HVDC system under study.

quency regulation with FD algorithm high droop gains should be selected, which in turn causes severe deviations in the dc voltages during system transients. On the other hand, the integral action of the FC algorithm allows smooth variation of the dc voltage references, hence avoiding severe transient effects on the system voltage. It should be mentioned that the ac system frequency dynamics are much slower than that of the dc link voltages, which ensures the natural decoupling between the outer frequency regulation loop and the dc link voltage+power droop loop. The requirement to support the neighboring ac grid for the primary frequency response may cause a converter to reach its current limiting capability. Therefore, as it can be noted from Fig. 4.3, all PI controllers have limiter blocks associated with the current rating and maximum allowed change in the references of the converters. To avoid severe transients associated with the saturation and the integral action, the PI controllers should have an anti windup loop. Integrator Clamping technique is used to avoid windup effect.

5.1.1 Simulation study

To further demonstrate the drawbacks with the existing frequency support strategies, to better explain the operation of the proposed strategy and to verify the latter's effectiveness, a comprehensive simulation study is conducted in the MATLAB/ Simulink environment. The simulations conducted in this section use the five-terminal study system of Fig. 5.2, which is identical to the system depicted in Fig. 4.2 and is provided here for the readers reference. Please note that all three ac areas of the considered test system are dominated by hydro generation resources, thus the hydraulic turbine-governor model of Fig. 2.11 is employed for modeling those systems.

Several operational scenarios are considered. In the initial steady state, each of the wind turbines delivers 150 MW. The VSC2 acts as a rectifier with reference power of -300 MW, whereas reference for both inverters VSC3 and VSC4 is 300 MW. The system base power, which is used in the controller implementation and in the representation of the results, is 900 MW.

5.1.1.1 The primary frequency response during ac side disturbance

In this scenario, the ac side disturbance is implemented by increasing the load in Area 3 by 150 MW. If VSCs do not include frequency regulation loops, no change of power will be triggered in VSC3 or any other converter (left side of the Fig. 5.3). The frequency decrease in the Area 2 is tackled only by the governor action of generator G2 and therefore exceeds the allowed limit of most grid codes for the generators to stay connected to the grid [170].

The incorporation of both FD (gain of 0.1 pu) and FC loops in the control of VSCs allows the areas connected to the droop controlled converters to share the primary frequency reserves. The comparative performance between FC and FD is shown on Fig. 5.4, where the traces of the system frequencies shown in the right side of Fig. 5.4 indicate that with an implementation of the FC algorithm the frequencies in all three areas follow each other. While with the FD algorithm different ROCOF and frequency nadirs can be observed for three areas. This results in the minimum frequency for Area 2 to be 48.5 Hz with FC and 48.07 Hz with FD. The 430 mHz improvement of the frequency nadir in Area 3 may result in avoiding violation of the allowed maximum frequency nadir and the consequent tripping of generator G2. The steady state frequency deviation with FC is also reduced in comparison with FD as can be seen in Fig. 5.4. However, enhanced control of the VSCs (weather FC or FD) has more significance during the initial system transient as it utilizes fast power regulation capability of the VSCs. Meanwhile, the left side of the Fig. 5.4

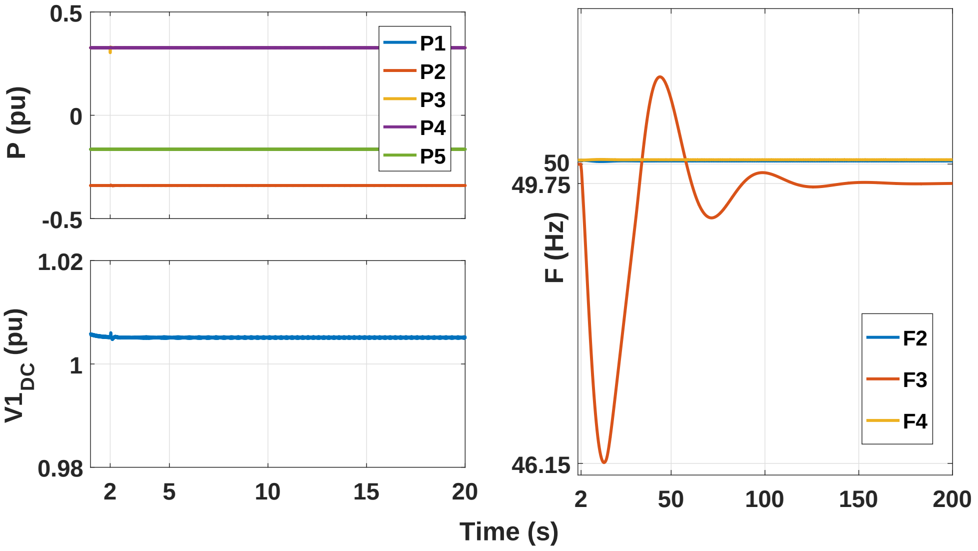

Figure 5.3. System dynamics when 150 MW load is increased in Gird 3 without any frequency response from VSCs.

illustrates the power trajectories at five areas as well as the dc link voltage at VSC1 with FD and with FC.

It is worth noting that the frequency nadir is significant in all of the previously shown cases. This trend is typical to the hydraulic turbine-governors used for the considered studies as those types of turbine-governors generally provide slower primary frequency response compared to other alternatives (steam or gas turbine-governors) [45]. The latter point is verified from much faster primary frequency response achieved with steam and gas turbine-governor systems presented in the next section (Section 5.2).

5.1.1.2 The primary frequency response during dc side disturbance

To illustrate the frequency deviation sharing performance during the dc side disturbance, the reference power change at the rectifier VSC2 from -300MW to -200MW is initiated at time t=2s. The opposite trends of the frequency deviations can be observed on the right side of Fig. 5.5 and Fig. 5.6. In the Area 2, the frequency is increasing as a result of a less power delivered to the dc grid from that area. In contrary, the frequencies in the Area 3 and Area 4 are decreasing as the total sum of the power injected to dc grid is decreased. However, it can be observed from the frequency traces shown in Fig. 5.5 that

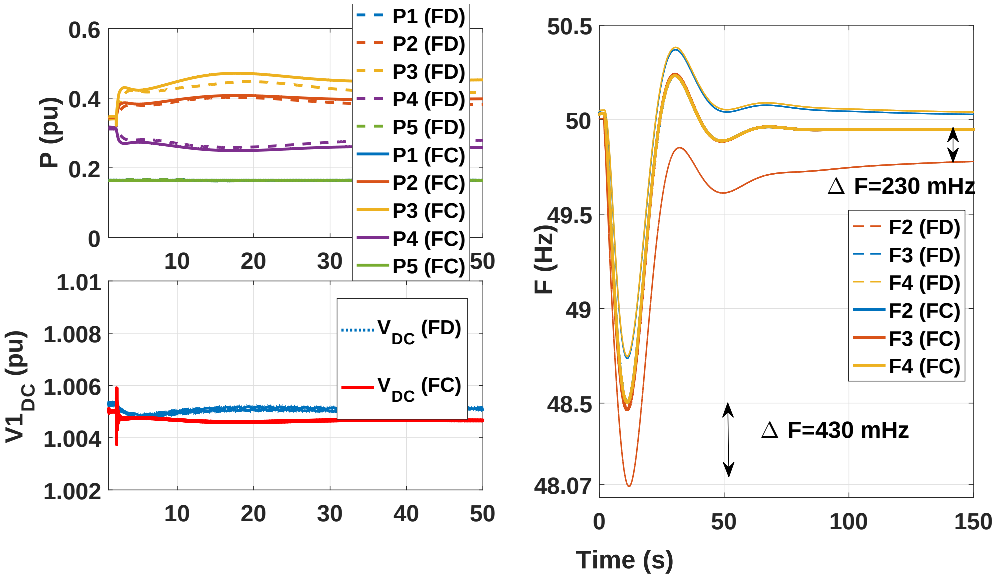

Figure 5.4. System dynamics when the 150 MW load is increased in Area 3 with FD and FC controllers. The power injections from the rectifier stations #1, #2 and #5 have sign reversed for better illustration.

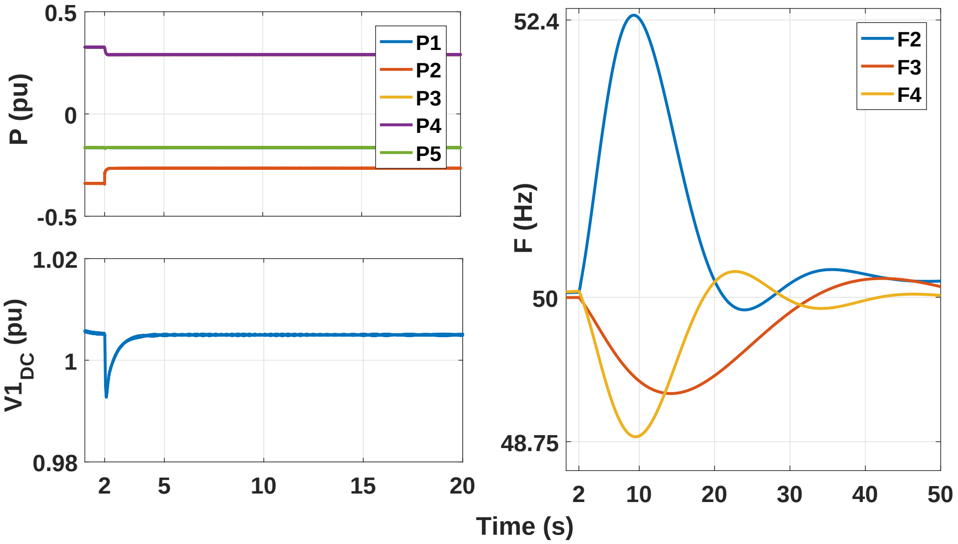

Figure 5.5. System dynamics when the Pref2 is changed from -300 to -200 without any frequency response from VSCs.

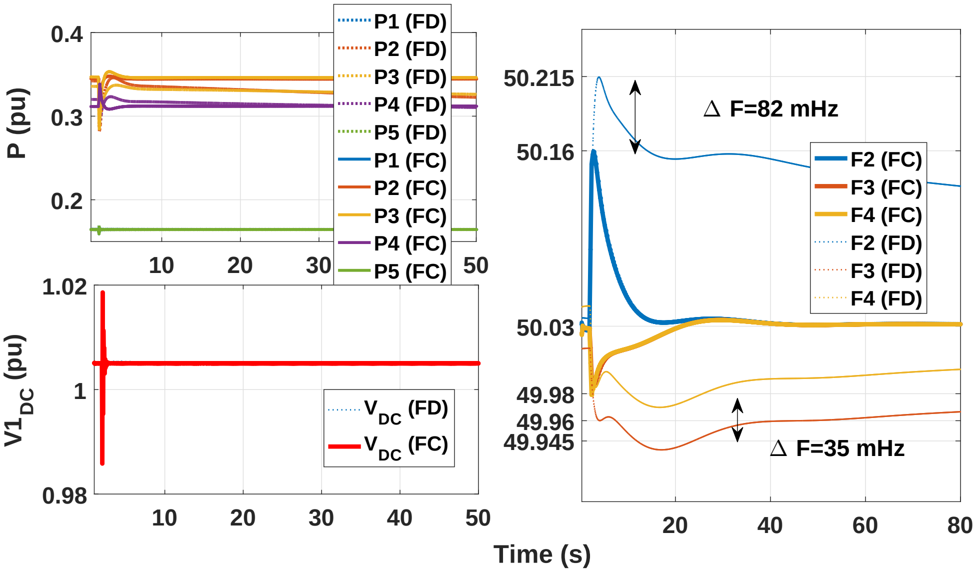

Figure 5.6. System dynamics when the Pref2 is changed from -300 to -200 with FD and FC controllers. The power injections from the rectifier stations #1, #2 and #5 have sign reversed for better illustration.

without any frequency regulation loop (power references at VSC3 and VSC4 are constant) the frequency of Area 2 increases to 52.4 Hz, which may violate some grid codes [170].

It can be observed that with FD and FC algorithms the frequencies of all three areas are improved significantly. The implementation of the FC algorithm allows to achieve less frequency deviation in Area 2 by 82 mHz, whereas the improvement of the same index in Area 3 and Area 4 are 35 mHz and 20 mHz, respectively. Furthermore, the FC loop facilitates faster regulation of all three frequencies to the steady state value.

5.1.1.3 Comparison of the control based on the local variables and the proposed strategy when system is subject to communication delays

In this scenario, comparison between FD and the proposed strategy is carried out. By incorporating 75ms communication delay in the system, this scenario is also used to illustrate the effect of the latencies on the proposed controller operation. In Fig.5.7, at time t=2s load decrease is initiated in the Area 4. The frequencies at all converter stations increase when both FD and FC are used. Fig. 5.7 (a) illustrates the comparison between the

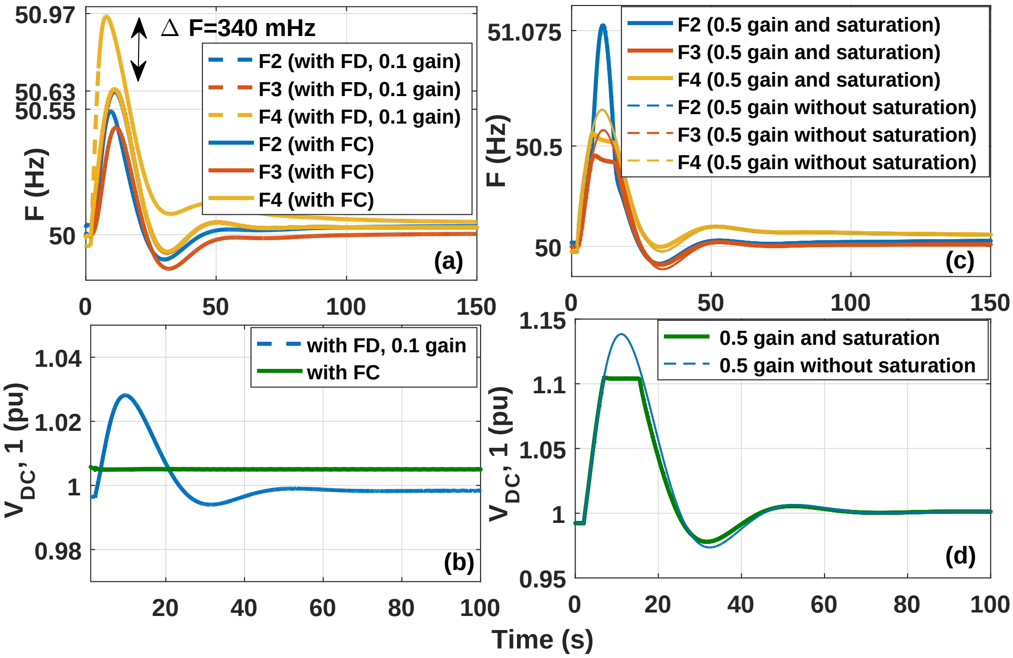

Figure 5.7. System dynamics when 150 MW load is decreased in Area 4. Left subfigures from top to bottom ((a) and (b))-the comparison of the system frequencies and dc link voltages when FC and FD (with 0.1 droop gain) are used. Right subfigures from top to bottom ((c) and (d))-the comparison of the system frequencies and dc link voltages when dc voltage saturation is enabled and without saturation (both cases consider FD of 0.5 droop gain).

response with FC (solid frequency traces) and with FD of 0.1 droop gain (dashed line). It can be observed from Fig. 5.7 (a) that the FC can overperform FD, achieving 340 mHz less frequency deviation for the Area 4. The dc link voltage at the VSC1 remains in the allowed limit for both scenarios (Fig. 5.7 (b)). To achieve higher sensitivity for the FD algorithm to the system frequency changes, the frequency droop gain should be increased. Fig. 5.7 (c) shows that with higher droop gain and no limitation on the dc link voltage reference, the frequency deviation sharing is enhanced (compared with lower frequency droop gain). However, as it can be seen from Fig. 5.7 (d) the higher droop gain causes more aggressive controller response in the form of higher dc link voltages, which in this case exceed the allowed 10 % overvoltage limit. The limitation of the dc link voltage references restricts the measured dc link voltages to the allowed limits (Fig. 5.7 (d)). Simultaneously, this saturation of dc voltage references causes deteriorated primary frequency response (Fig. 5.7 (c).) Therefore, it can be concluded that the proposed approach provides enhanced system response in comparison with the FD strategy. In addition, it can be noticed that the communication delays do not deteriorate the operation of the frequency loops. In fact, considering that the frequency dynamics are relatively slow in nature (as described in Chapter 3), even considered large delays do not affect the FC operation.

5.2 Selective frequency support of MT-HVDC systems

The mutual frequency support algorithm proposed in first section (Section 5.1) of this chapter was shown to enhance the primary frequency response of the asynchronous ac grids interconnected through MT-HVDC systems. It aimed equalizing the extent at which all the grids are affected in case of a disturbance in one of those grids. The existing controllers, including our latter-discussed approach, however, did not consider which grid is under the disturbance, so those strategies do not provide any selectivity during the frequency event. Accordingly, the system operators had no mechanism to predefine the relative amount of the frequency support provided by each area based on the latter's state (e.g. area under disturbance or area supporting the disturbed network). Also, the frequency support strategy presented in Section 5.1 of this chapter did not consider the frequency support from WPPs.

This section, therefore, extends on the work presented in Section 5.1 by proposing a new control approach to accurately achieve the desired extent of mutual frequency support between MT-HVDC interconnected asynchronous ac grids while considering the operational states of those grids. Specifically, each of the affected grids would receive frequency support from healthy systems based on the predefined ratios of frequency deviations between supporting ac systems and the affected ac grid. Therefore, the relative effect of the disturbance on the participating grids can be pre-defined, providing more fair allocation of the available power reserves. The developed detection technique continuously identifies the affected area, and the support algorithm is modified accordingly to accomplish the above-mentioned control objective. Thus, compared to the previous approaches, the controller proposed in this section adds an extra degree of freedom for controlling the amount of mutual frequency support between MT-HVDC interconnected asynchronous ac systems. Also, the controller discussed below takes into account scenarios when frequency response is extracted from WPPs as well. The proposed controller for the i_{th} converter station is shown in Fig. 5.8 and is elaborated below.

5.2.1 Implementation of the selective frequency support algorithm

Firstly, the implementation of the selective frequency support algorithm is presented. Specifically, the technique for continuously detecting the affected grid is explained, followed by elaboration on the required modifications of the frequency support algorithm, and finally the strategy implemented for achieving coordinated frequency support from WPPs is discussed.

5.2.1.1 Algorithm for detecting the affected grid

Proper detection of the grid where the disturbance actually happened is of prime importance for providing selectivity in mutual frequency support. It is worth noting that conventionally the frequency event is detected continuously based on the deviation of the frequency from the specified dead-band limits [126]. However, with any frequency support algorithm (FD,FC, etc.), the frequencies of all interconnected systems would likely exceed the dead-band limits as a result of the provided frequency support by each of the participating grids. This situation hinders from the identification of the area causing the disturbance. To overcome this issue, a method is developed to continuously identify the affected ac system.

If the disturbance occurring in the i_{th} area causes an active power shortage, the frequency support sharing algorithm would try to increase the active power flowing from MT-HVDC system to that area (positive $\Delta P_{i,FS}$ in Fig. 5.8). Therefore, independent of the operation mode of the i_{th} converter (inverter vs rectifier mode), the converter would experience a positive change in the power deviation (ΔP_i in Fig. 5.8). Meanwhile, the actual frequency deviation of that area Δf_i, defined as a difference of the nominal and

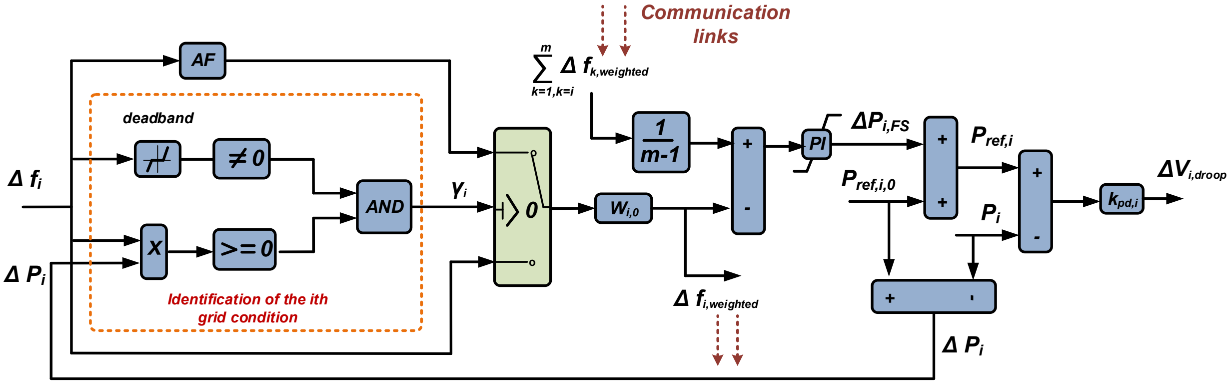

Figure 5.8. The proposed frequency regulation strategy for ac interfacing i_{th} converter.

measured frequencies as per (5.2), would also be a positive quantity due to the decreased system frequency.

$$\Delta f_i = f_{nom,i} - f_i \tag{5.2}$$

In contrary, the converter of the healthy j_{th} grid trying to provide frequency support to the affected i_{th} system would decrease its power reference (negative ΔP_j) and would experience frequency decline (positive Δf_j) due to the extra power it injects to the dc grid. Following the discussed logic, the trend of the power and frequency deviations during possible system disturbances is summarized in the below table. The considered disturbances are the ac power shortage or surplus (e.g. due to the ac generator/load connection or disconnection) and increase or decrease of the power injected to the dc grid by the converters except the droop-controlled ones (e.g., wind power increase or decrease).

	$\Delta P_{affect.}$	$\Delta f_{affect.}$	$\Delta P_{support.}$	$\Delta f_{support.}$
ac power shortage	pos.	pos.	neg.	pos.
ac power surplus	neg.	neg.	pos.	neg.
dc power increase	pos.	neg.	pos.	neg.
dc power decrease	neg.	pos.	neg.	pos.

As it can be clearly observed from the above table, if any of the ac grids causes the system disturbance, the product of its power deviation $\Delta P_{affect.}$ and frequency deviation $\Delta f_{affect.}$ would be a positive quantity. Opposite trend can be identified for the supporting healthy grids with the identical product being a negative quantity. In case if none of the ac grids are affected, and the frequency deviations are due to an external cause (e.g. change in the power injected by the WPP), all of the ac converters observe a negative product of the discussed quantities. Therefore, the sign of the $\Delta P_i \Delta f_i$ product serves as an indicator for the operational condition of the i_{th} ac grid. Shown in Fig. 5.8, once the frequencies exceed the minimum deadband and the discussed product is positive, the disturbance is detected at the i_{th} system. In case of the disturbed area the binary variable γ_i is positive, which is later used to modify the weight factors in the frequency support algorithm. The frequency deviation deadband has an aim to disable the supplementary operational loop during undesirable minor transients and is set to ± 0.05 Hz in this study.

5.2.1.2 Adaptive modification of the weight factors with the proposed approach

After an identification of the affected area, an accurate ratio-based frequency support sharing can be achieved. To this end, the original power reference of the i_{th} out of m droop-controlled converters $P_{ref,i,0}$ is modified as per (5.3)

$$\begin{cases} P_{ref,i} = P_{ref,i,0} + \Delta P_{i,FS} \\ \Delta P_{i,FS} = (\sum_{k=1,k\neq i}^{m} \dfrac{\Delta f_{k,weighted}}{m-1} - \Delta f_{i,weighted}) G_{PI,FS} \end{cases} \tag{5.3}$$

Due to the integral action of the controller $G_{PI,FS} = k_{P,FS} + k_{I,FS}/s$, the weighed frequency deviation of the i_{th} area $\Delta f_{i,weighted}$, which is given by (5.4), would be accurately regulated to the same quantity of the other participating grids.

$$\begin{cases} \Delta f_{i,weighted} = \Delta f_i w_i \\ w_i = \dfrac{w_{i,0} * AF_i}{100\%}; \gamma_i = 1 \\ w_i = w_{i,0}; \gamma_i = 0 \end{cases} \tag{5.4}$$

In (5.4), the original weight factor $w_{i,0}$ is determined based on the relative strictness of the frequency regulation in each of the participating ac grids. For example, if the MT-HVDC interconnected ac grids have similar grid codes on frequency regulation (e.g. same allowed maximum frequency deviation), then identical original weight factors could be set for all participating grids. In the proposed strategy, based on the disturbance index γ, the original weight factor of the affected area $w_{i,0}$ is multiplied by the assistance factor AF_i. The last parameter is pre-set by the system operator for the i_{th} ac system participating into mutual frequency support. AF_i determines the relative extent to which all other ac grids participate in providing frequency support in response to any disturbance happening in the i_{th} ac system. Specifically, by means of the power rerouting in dc grid, the proposed controller enables the supporting ac systems to experience the frequency deviation of AF_i percent of that of the i_{th} ac systems frequency deviation when the disturbance is caused by the latter system. Varying AF from 0 % to 100 % would allow the operators to precisely change the extent of mutual frequency support between asynchronous ac systems from 0 % to 100%. That being said, with AF_i=0 %, the i_{th} ac system would get no support from other grids in case if it experiences a disturbance. With an increase of AF_i, the frequency support provided to the i_{th} grid would increase accordingly. Selection of the particular value for the AFs would be under the discretion of system operators. Thus, the proposed approach provides an added degree of freedom that allows system operators to accurately determine the extent of mutual frequency support.

5.2.1.3 Coordinated Frequency Support Strategy from WPPs

To achieve frequency support from WPP during the main ac system disturbance, an ancillary frequency controller is implemented. The amount of the additional power is determined as a function of the onshore frequency deviations to reflect the severity of the ac disturbance and to extract the appropriate amount of extra power. The weighted average sum of the ac system frequencies is first calculated and then supplied to the controller to determine the total additional wind power $P_{del.,WPP,total}$ injected to the dc grid as per

$$\begin{cases} P_{WPP,total} = (\sum_{i=1}^{m} v_i \Delta f_i) G_{PD} \\ \sum_{i=1}^{m} v_i = 1 \end{cases} \tag{5.5}$$

where the v_i is the weight factor determining the extent each ac grid would have contribution on the frequency support provided by WPP, m is the total number of ac grids connected to the droop-controlled converters, G_{PD} is the transfer function of the proportional-derivative controller. Please notice that similar weighted frequency based control approach have been previously presented in [115] to reflect onshore frequency changes on the frequency of offshore wind farms. The maximum power headroom $P_{del.,WPP,max,i}$ at each WPP, which is the sum of headrooms of all WTs belonging to that plant, is then used for determining the relevant portion of the power that the i_{th} WPP should supply.

$$P_{del.,WT,i} = \frac{1}{k} P_{WPP,total} \frac{P_{del.,WPP,max,i}}{\sum_{i=1}^{n} P_{del.,WPP,max,i}} \tag{5.6}$$

with n being a total number of the participating WPPs, k is the number of WTs in that plant. Following system disturbance, the WPP frequency support controller is being activated if any of the ac frequencies exceed pre-specified dead-band. As mentioned earlier, the functioning of the proposed algorithm is not dependent on the frequency support provided by the WPPs. However, as it will be seen in the results section, the implemented controller enhances the distribution of the active power provided by the WPPs for frequency response.

5.2.2 Modal analysis of the developed selective mutual frequency support strategy

The effect of the parameter variation of the proposed controller on the stability of the considered test system is investigated in this section. To this end, the CIGRE benchmark

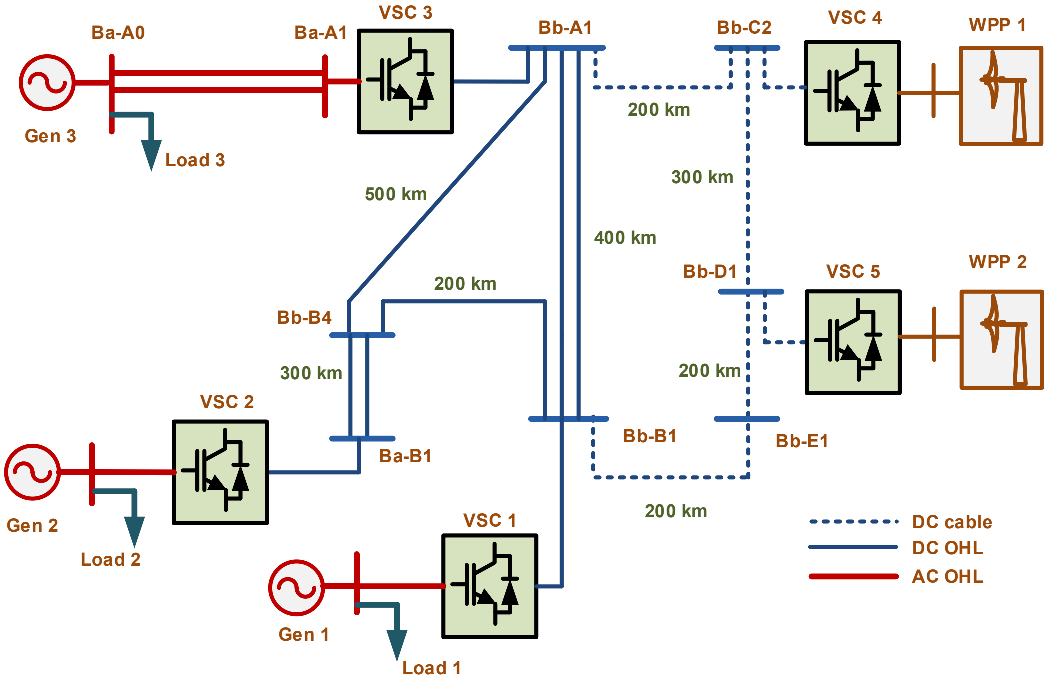

Figure 5.9. MT-HVDC test systems used in this study (part of CIGRE B4 benchmark system).

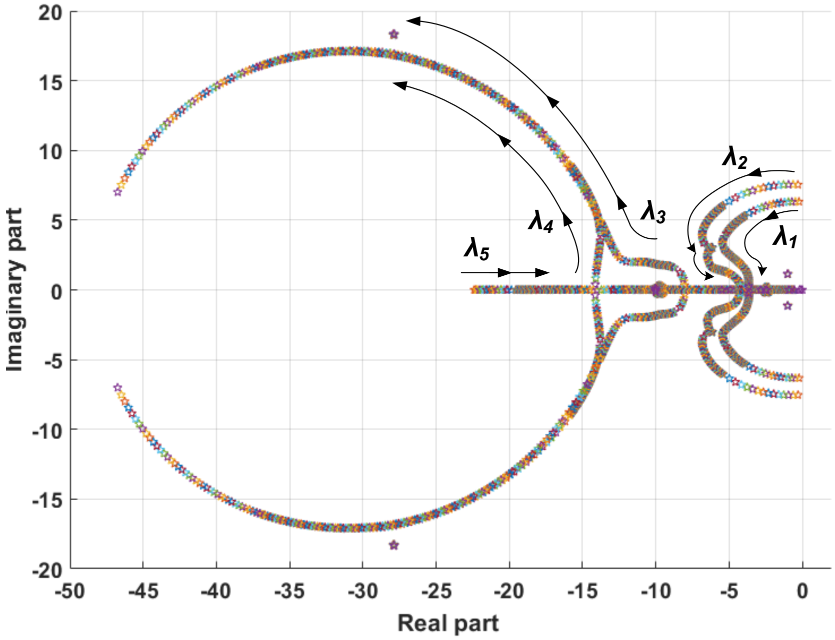

Figure 5.10. The effect of the change of the proportional gain $k_{P,FS}$ on system eigenvalues.

MT-HVDC test system, which was considered in Chapter 4 and is depicted in Fig. 5.9 for the readers reference, is used for the verification of the proposed selective mutual frequency support strategy. The generations of Areas 1 and Area 3 are assumed to be dominated by thermal units, whereas the generation of Area 2 is assumed to be dominated by gas-fired power plants. The selection of systems with different frequency response characteristics is meant to make it more challenging for achieving precise mutual frequency support. The same test system is used for time-domain simulations of the proposed strategy in Subsection 5.2.3.

The right-most eigenvalues of the combined system experiencing relatively larger movement during the variation of the proposed controller's parameters are shown in Fig. 5.10-Fig. 5.12. Specifically, the proportional and integral gain variation effect is depicted in Fig.5.10 and Fig.5.11, respectively, whereas Fig.5.12 demonstrates the effect of the variation of the AFs of the proposed controller. In all three figures four pair of oscillatory eigenvalues ($\lambda_1 - \lambda_4$) have been identified as the ones with relatively more movement during the variation of the considered parameters of interest. Another fast moving eigenvalue (λ_5) was located in the stable region for the considered variation and had no imaginary

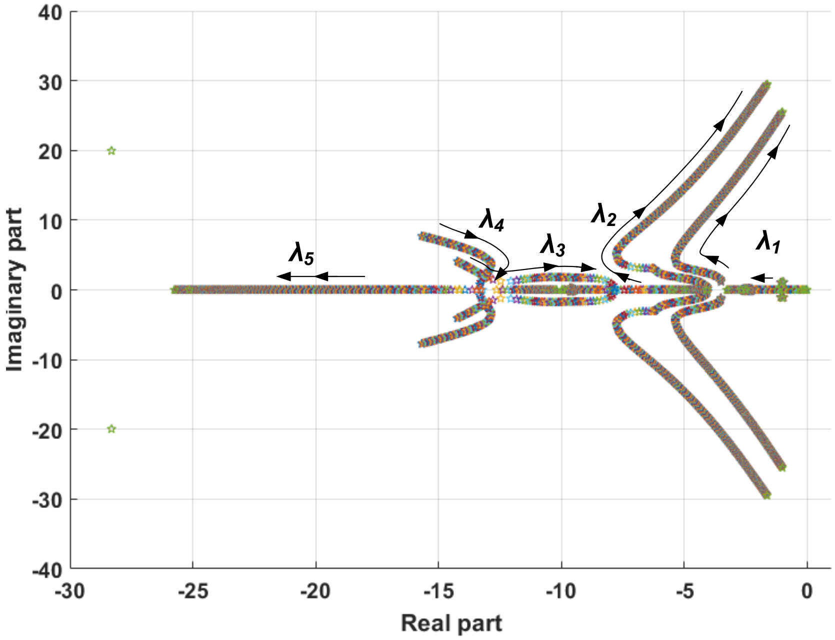

Figure 5.11. The effect of the change of the integral gain $k_{I,FS}$ on system eigenvalues.

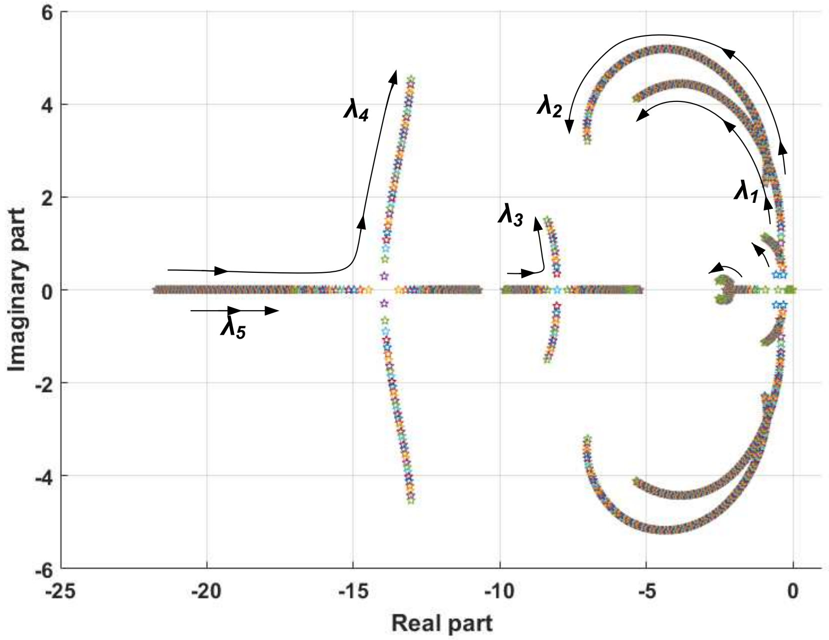

Figure 5.12. The effect of the change of AF on system eigenvalues.

component. The black arrows indicate the direction of the eigenvalue movement as the parameter is varied in the specified range. Please notice that the numbering of eigenvalues shown in Fig.5.10-Fig.5.12 is for convenience only and is not according to the order they appear in after they are extracted from the state matrix. Fig.5.13 presents the section of the results of participation factor analysis that associates the critical oscillatory modes to the states of the system. Only the states making a major contribution to the considered modes are depicted in Fig.5.13. It can be seen that the major contributing states are those associated with the dc voltage-droop controller (Vdc-cont), the turbine governors of the three areas (G-TG, combined participation of all relevant states), generator speeds of three areas (G-w), the dc side currents (Idc, combined participation of all relevant states) and the states associated with the proposed controller (FS). Specifically, the states associated with the proposed controller have relatively greater participation on modes λ_1 and λ_2, and lesser participation on the other two modes.

Following a closer look is given to the Fig.5.10-Fig.5.12. In Fig.5.10, the proportional gain is varied in the range from 2pu to 150 pu, by the step of 0.1-1 pu depending on the section of interest to accurately capture the trajectories of interest. During low values of the proportional gains, the eigenvalues with lowest damping are λ_1 and λ_2. With an increase of the parameter, the λ_1 and λ_2 start moving to the left hand side of the complex plane and increase the damping of the system, verifying the results of the participation factor analysis. At an inflection point that happens at the gains of 18 pu, the eigenvalues λ_1 and λ_2 start moving downwards with a greater speed. However, the eigenvalues λ_3 and λ_4 demonstrate an opposite trend, as the imaginary part of those eigenvalues is increased with an increase of the proportional gain. Specifically, the eigenvalue λ_3 experiences an inflection point at a gain of 23 pu and starts fast upward movement. For a large range of the parameter variation the system eigenvalues are well within the left hand plain. However, the proportional gain of 20 pu is selected in this study to ensure the maximum damping. Furthermore, Fig.5.11 demonstrates the effect of the variation of the integral gain in the range of 1pu- 1400 pu, by the step of 1-16 pu depending on the section of interest. Opposite to the previous case, the λ_3 and λ_4 are the ones with lower damping during the initial values of integral gains. The increase of the gain causes a decrease of the imaginary parts of λ_3 and λ_4 and increase of the respective parameter for λ_1 and λ_2. At the gain of around 80 pu, an inflection point occurs, and the modes λ_1 and λ_2 start upper-right movement towards the unstable region, implying an upper limit for the selection of the integral gains. Finally, the Fig.5.12 presents the effect of the change of AF on system eigenvalue movement. The whole range of the AF variation, from 0-1 pu (0-100%) is considered by increasing the AF by the steps of 0.1 pu. The increase of the AF results in an increased system damping as suggested by the trajectories of λ_1 and λ_2. Although the other two oscillatory modes experience an increase in their imaginary components, even for the largest values of AF those modes remain better damped than λ_1 and λ_2. The modal analysis results imply the effectiveness of the proposed controller to enhance the damping and the stability of the system.

5.2.3 Time-domain simulations of the developed selective mutual frequency support strategy

The effectiveness of the proposed algorithm is evaluated using time-domain simulation conducted in Matlab/ Simulink environment. Several operational cases are considered for the comprehensive evaluation. Identical frequency regulation grid codes are considered for the ac networks for the clarity of illustration. P-V droop-controlled converters VSC1 and VSC3 work in the inverter mode and transfer power from dc grid to the respective ac systems. The third droop-controlled converter VSC2, together with the VSC4 and VSC5 interfaced to the WPPs, operate in the rectifier mode and inject power to the dc system. The positive direction of the current is from the ac side of the VSC to the dc side.

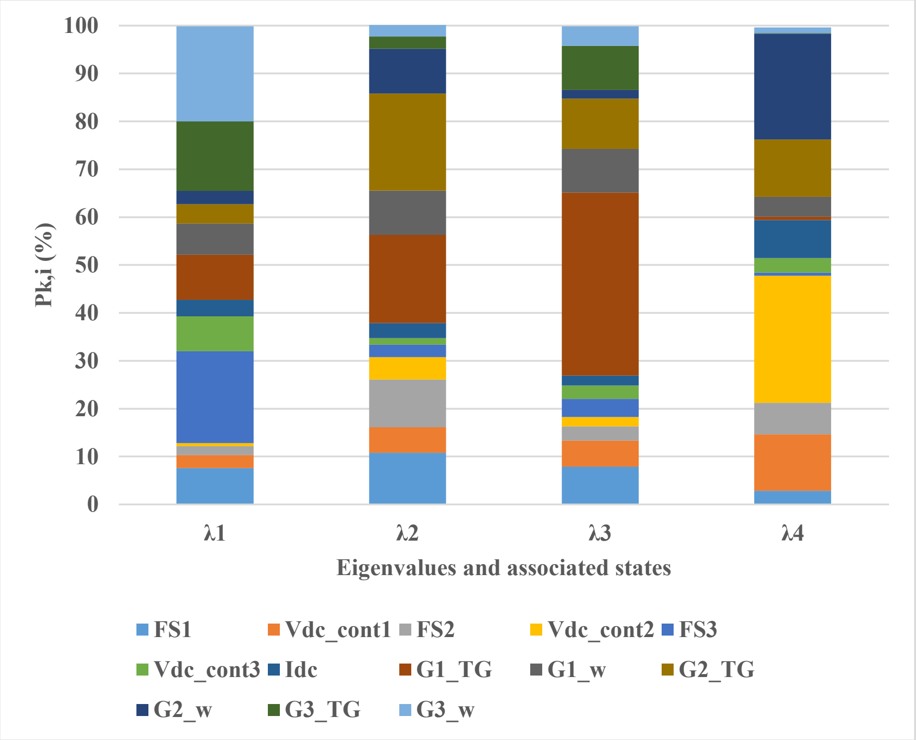

Figure 5.13. The percent participation of the color coded states to the critical oscillatory eigenvalues $\lambda_1 - \lambda_4$.

5.2.3.1 System response during ac side disturbances.

In this scenario, the effect of the proposed controller for frequency response sharing is evaluated during the ac side disturbances. Fig.5.14 - Fig.5.16 demonstrate the system response during subsequent load increases in the area 3 and area 2. The AF for the affected grids is set to 50% in this scenario, aiming to achieve twice more effort from the disturbed grid(s) compared to the supporting grid(s). When the load in area 3 is increased by 0.4 pu at time t=5s, the power unbalance in area 3 causes the frequency decrease in that area. Due to the provided active power support, the other two ac systems also experience a decline in their frequencies (positive frequency deviation shown in Fig. 5.14a). As the frequency deviations of all ac systems exceed the specified threshold (η_{min}-η_{max}) in Fig. 5.14a, detection of the area causing the disturbance would not be possible by observing the frequency change only. Therefore, the proposed controller of Fig. 5.8 utilizes the power deviation ΔP to continuously detect the area under the disturbance. As can be seen from Fig. 5.14b, after the disturbance at t=5s, only the affected area 3 experiences positive power deviation ΔP_3. As the product of the frequency deviation Δf_3 and ΔP_3 is positive, the disturbance is detected in area 3 (Fig. 5.14c). Please notice that the disturbance state γ in the other two areas remains zero. The detection of the affected grid modifies the respective frequency contribution factor of area 3 (equation (5.4)) to achieve desired ratio-based frequency regulation. Fig.5.15 depicts the frequency trajectories of the three ac systems in response to the system disturbances. When the load in area 3 is increased, both area 1 and area 2 become supporting grids by injecting extra power to the dc grid. At this situation, as the first two areas have identical operational status and grid codes, the proposed algorithm achieves uniform frequency regulation between those areas. As such, the frequency deviations at the nadir points are $\Delta f_{1,nadir} = \Delta f_{2,nadir} = 0.4Hz$, and frequency deviations at the quasi-steady-state conditions are $\Delta f_{1,qss} = \Delta f_{2,qss} = 0.21Hz$. As per the ratio pre-specified by the system operators, the affected area experiences twice the frequency deviation of the supporting areas with $\Delta f_{3,nadir} = 0.8Hz$ and $\Delta f_{3,qss} = 0.42Hz$, ensuring the selective participation of the ac grids into frequency response precisely determined by the desired ratios.

Furthermore, gas turbine dominated area 2 experiences 0.4 pu load increase at time t=35s. As can be seen from Fig. 5.14b, the ΔP_2 becomes a positive quantity, and, because of having identical sign with the frequency deviation Δf_2 in Fig. 5.14a, the disturbance in area 2 is also detected (Fig. 5.14c). After detection of the state of the area 2, the respective weight factor is modified according to its predefined AF. The desired ratio-based frequency support is precisely achieved throughout the disturbance period as seen in Fig. 5.15. The dc system voltages and converter power injections for the considered two disturbances are

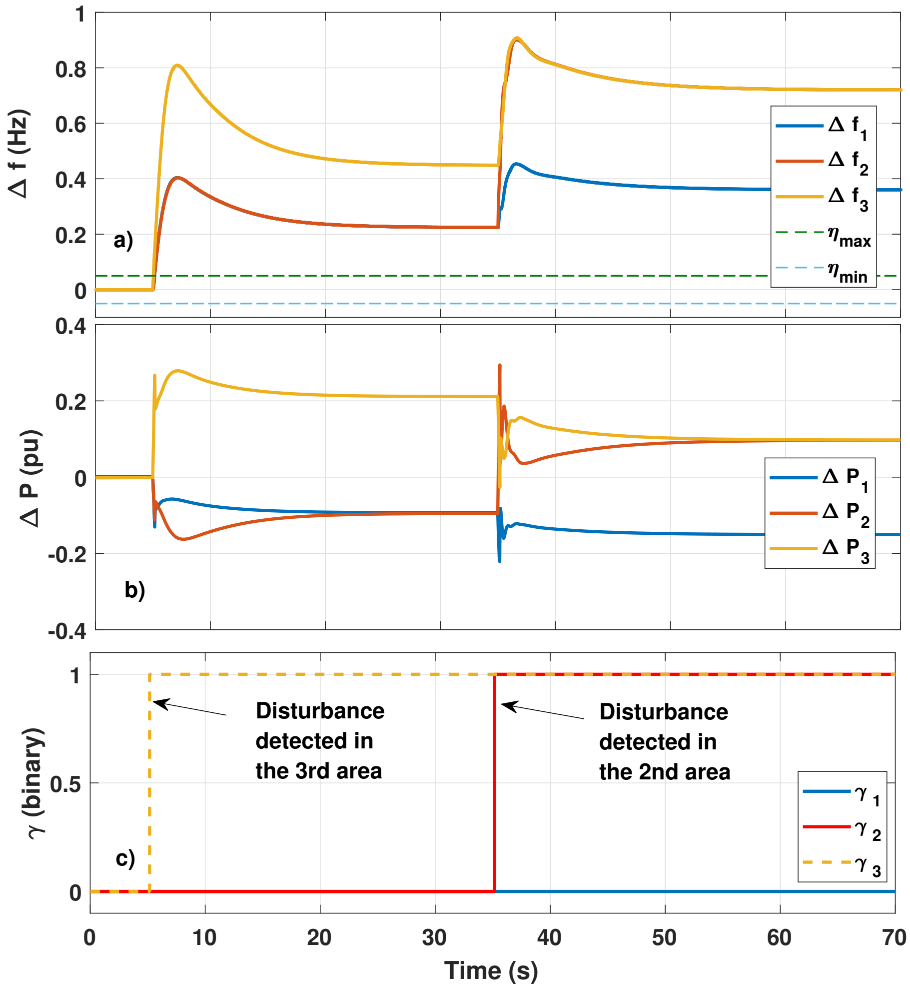

Figure 5.14. a) System frequency deviations, b) converter power deviations, c) the detection of the grid state.

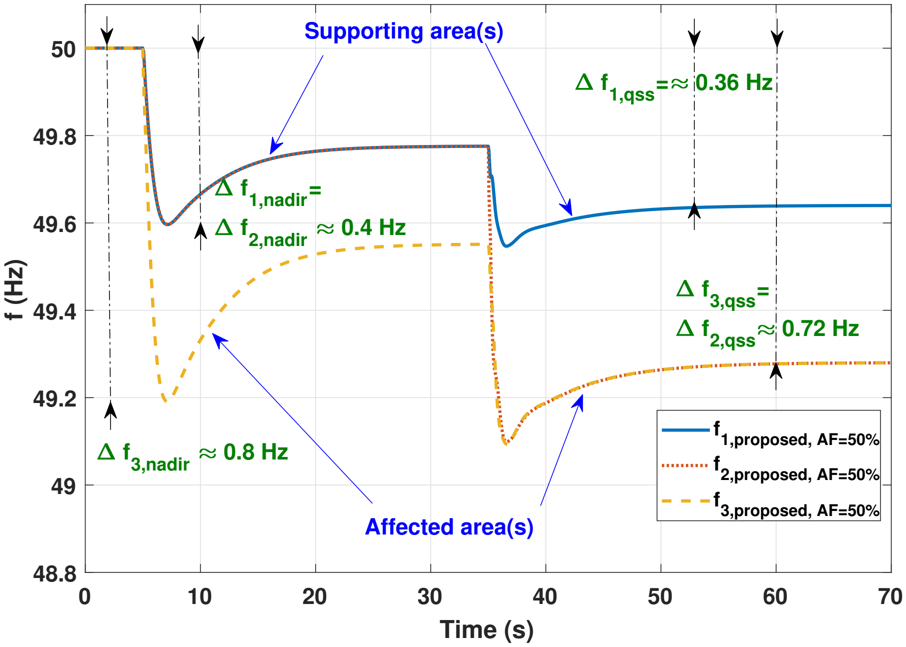

Figure 5.15. Frequency trajectories at the MT-HVDC interconnected ac grids.

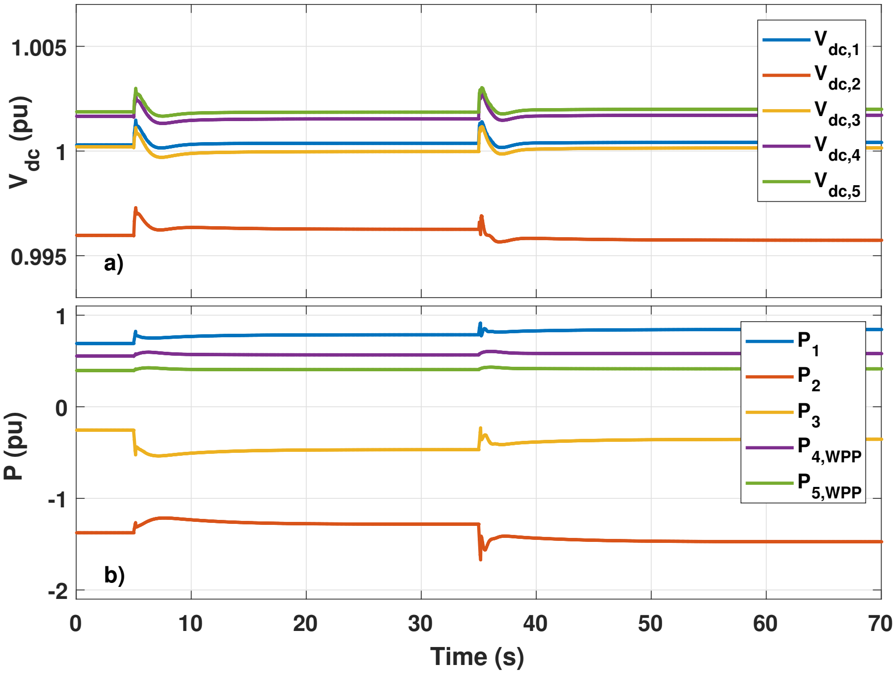

Figure 5.16. a) Dc system voltage profiles, b) converter power injections.

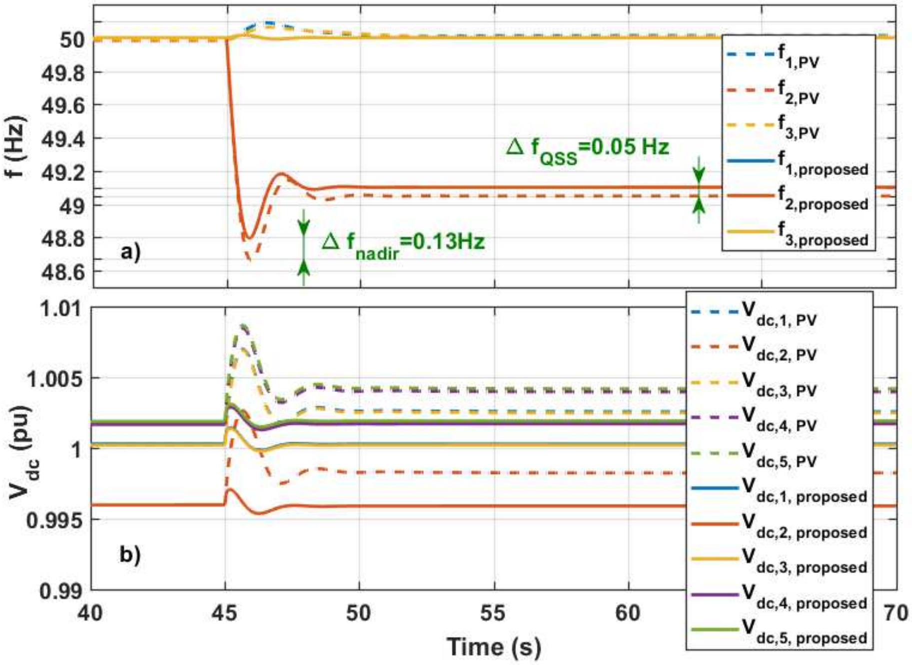

Figure 5.17. Comparison of a) system frequencies and b) voltage profiles between the proposed strategy (AF=0%) and P-V strategy.

depicted in Fig. 5.16, where shown in Fig. 5.16a the dc system average voltage is adjusted around nominal value as a result of the action of the voltage regulation loop. The wind farm active power increase during the frequency events in main ac systems can be observed from the respective power trajectories in Fig. 5.16b.

5.2.3.2 Comparison with other methods.

The proposed strategy is compared with several recently-reported control approaches as follows: with power-voltage (P-V) droop control of [156] (which is also part of the controller developed in Chapter 4), with the conventional FD algorithm (C-FD) presented in [26], with Adaptive Droop Control (ADC) reported in [97], with Adaptive Virtual Synchronous Generator (A-VSG) method of [131], and with the FC algorithm. The results of the comparison for the five considered cases are shown in Fig. 5.17- Fig. 5.21. In all considered scenarios of this subsection 0.4 pu demand increase is initiated in area 2 at time t=45 s.

When using P-V droop controllers, including the one proposed in [156], asynchronous ac grids interconnected through MT-HVDC systems do not provide any mutual frequency support. Assuming that in this case it is desired by the system operators to achieve no frequency support between ac systems, the AF of the affected grid with the proposed strategy is set to zero to allow a fair comparison. As can be seen from the dotted frequency trajectories of Fig. 5.17 a, area 1 and area 3 do not assist area 2 in overcoming the disturbance. Meanwhile, the WPPs inject more power to dc grid during the frequency event, and the P-V droop controllers distribute this additional power between all three areas. This distribution of P-V controller results in an unnecessary allocation of power to area 1 and area 3, which causes an increase of the frequencies of those areas. The solid frequency trajectories of Fig. 5.17 a demonstrate the response of the system with the proposed strategy. With the AF set to zero, the proposed controller quickly regulates the summation of the weighted frequency deviation of area 1 and area 3 to zero (Fig. 5.8). Therefore, the frequencies of both area 1 and area 3 are controlled to their nominal values, not allowing any unnecessary power being allocated to those areas. This control action results in redirection of all additional power to the affected area 2 and increase of its frequency profile compared to the case when P-V control is used. In particular, the frequency nadir is improved by 0.13 Hz and quasi steady-state (QSS) frequency is improved by 0.05 Hz. This improvement verifies the advantage of the proposed controller considering the specific operation objective when no mutual frequency support is required.

The strategies of [26,97,131,155], on the other hand, would try to equalize the frequency deviations of asynchronous ac systems given an equal droop gain settings for [26, 97, 131] methods or equal weight factors for [155] approach. Therefore, the AF of the affected area is set 100% to achieve full support between asynchronous ac systems when compared to those methods. It can be observed from Fig. 5.18a that with C-FD approaches the relative frequency deviations are poorly defined with the supporting grids' frequencies ($f_{1,C-FD}$ and $f_{3,C-FD}$) being much higher than the identical parameter of the affected grid ($f_{2,C-FD}$). With the proposed strategies, on the other hand, equal frequency deviations is achieved for all three areas as per the system operator requirement. As a result, the proposed strategy increases the frequency nadir by 0.355 Hz and QSS frequency by 0.39 Hz.

Shown in Fig. 5.19a and Fig. 5.20a, the controllers of [97] and [131] have both demonstrated an improved performance in achieving full mutual frequency support compared to the C-FD approach. However, the proposed strategy still outperforms those approaches in achieving full mutual frequency support. Specifically, when compared to the ADC approach, the proposed approach achieves 0.125 Hz and 0.25 Hz improvement at the nadir and QSS points, respectively. The A-VSG approaches achieves further improvement compared to ADC approach by falling behind the proposed strategy by only 0.085 Hz and 0.19

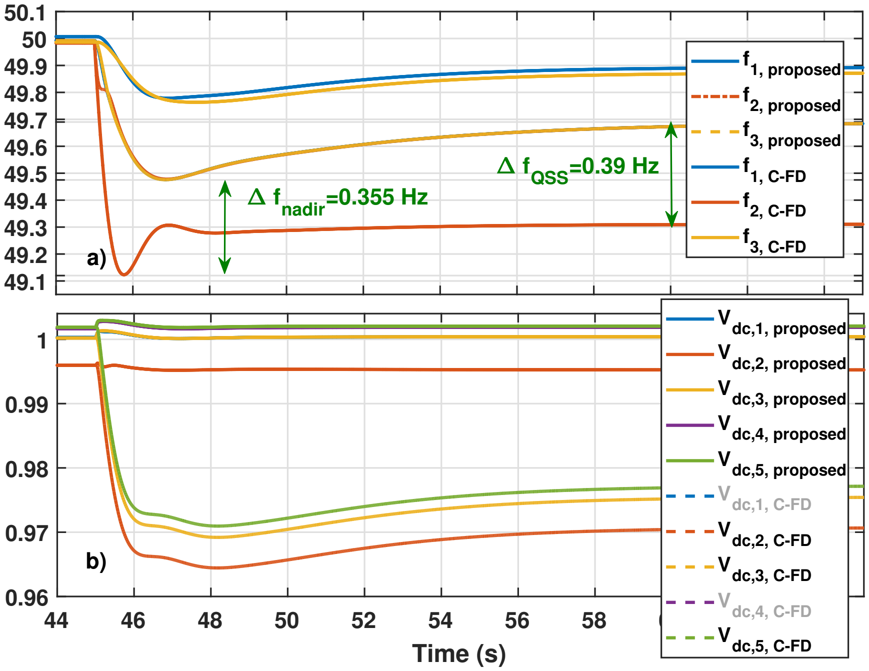

Figure 5.18. Comparison of a) system frequencies and b) voltage profiles between the proposed strategy (AF=100%) and C-FD strategy.

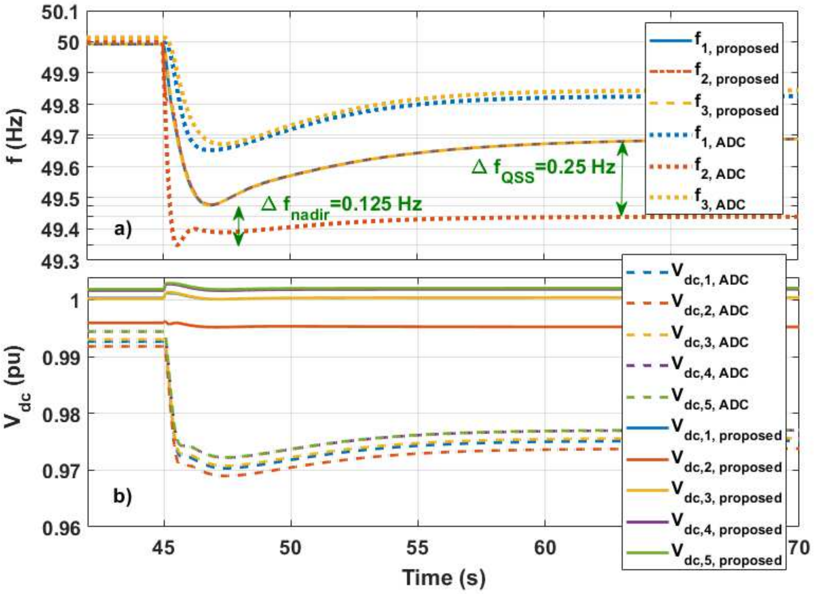

Figure 5.19. Comparison of a) system frequencies and b) voltage profiles between the proposed strategy (AF=100%) and ADC strategy.

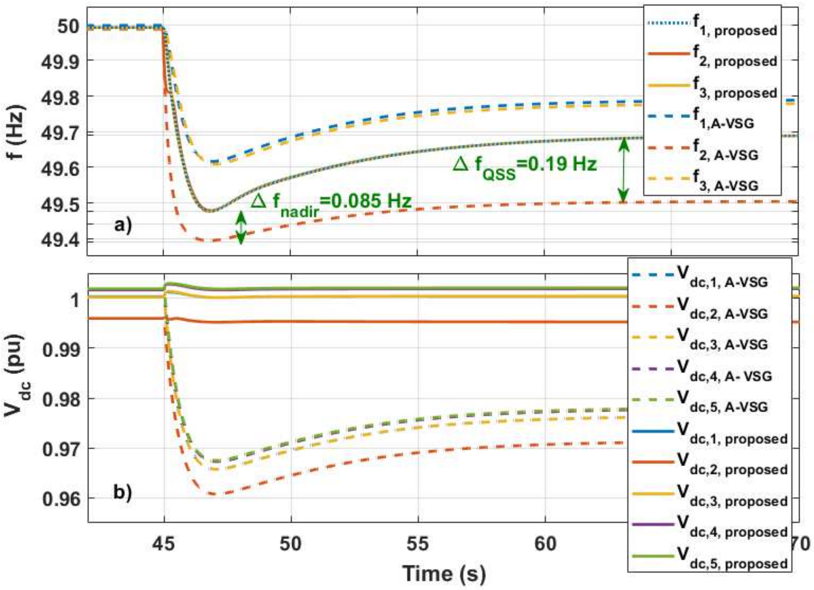

Figure 5.20. Comparison of a) system frequencies and b) voltage profiles between the proposed strategy (AF=100%) and A-VSG strategy.

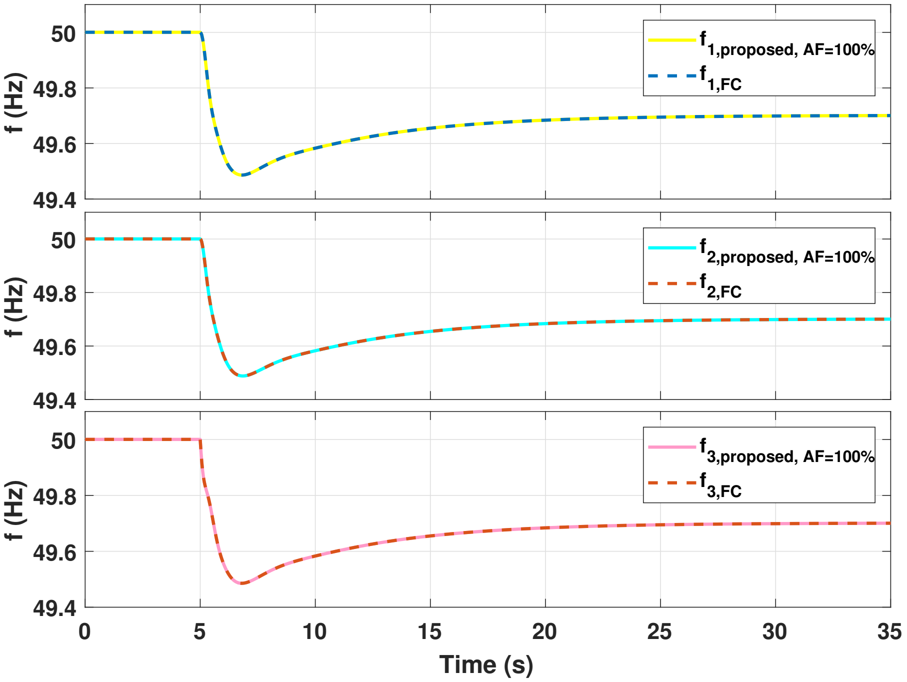

Figure 5.21. Comparison of the system frequencies between the proposed strategy with AF=100% and FC strategy.

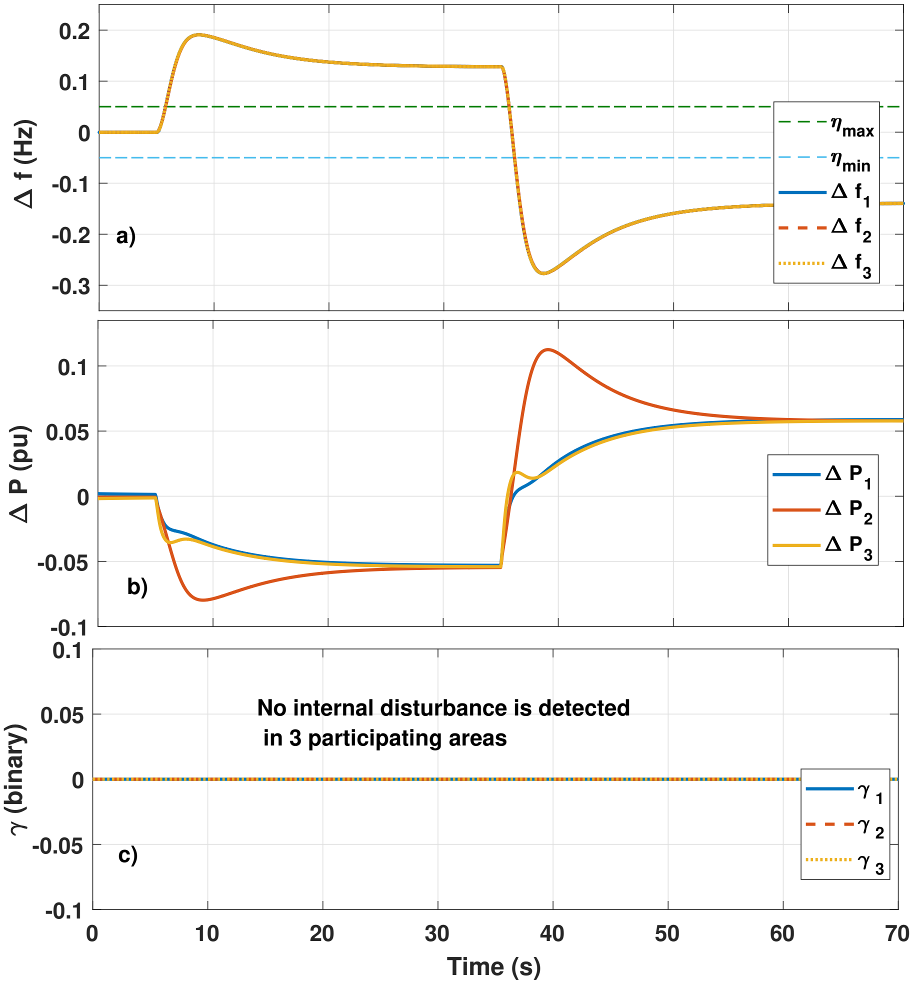

Figure 5.22. a) System frequency deviations, b) converter power deviations, c) the detection of the grid state during wind speed changes.

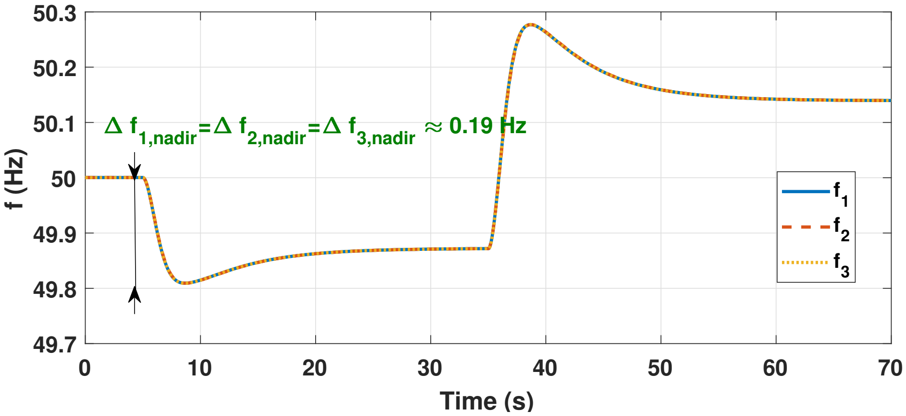

Figure 5.23. Frequency trajectories during wind speed changes.

Hz at the frequency nadir and QSS frequency, respectively. The droop approaches also cause significant deviation of the dc voltages (Fig. 5.18b, Fig. 5.19b and Fig. 5.20b). This deviation is highly dependent on the selected droop gains and extent of the disturbance. Selection of higher droop gains might result in further improvement of their frequency support objectives which would come at the cost of larger voltage deviations. Finally, Fig. 5.21 demonstrates that for this case the proposed strategy acts like FC algorithm: it ensures identical frequency deviations for all interconnected areas independent of which grid is causing the disturbance. The results presented in Fig. 5.18-Fig. 5.21 reveal operation of the proposed strategy at only one operation mode (full mutual frequency support) as the studies used for comparison are limited to those modes only. The main advantage of the proposed controller, on the other hand, is the capability to precisely achieve any extent of mutual frequency support considering the operational state of the participating area.

5.2.3.3 System response during changes in the wind speed.

The performance of the proposed strategy was also tested in the situation when the disturbance is not caused by any of the participating ac grids. As such, the wind speed is varied from 12m/s to 11m/s and from 11 m/s to 13 m/s at times t=5s and t=35 s, respectively. As depicted in Fig. 5.22a and Fig. 5.22b, all of the ac systems demonstrate similar trend in terms of frequency deviations Δf and power mismatches ΔP. Therefore, no disturbance is detected in those three areas (Fig. 5.22c), and the proposed controller redirects the active power to share the burden on all three ac areas equally by achieving identical frequency deviations as shown in Fig. 5.23. The dc voltages and active power injections for this scenario are depicted in Fig. 5.24a and Fig. 5.24b, respectively.

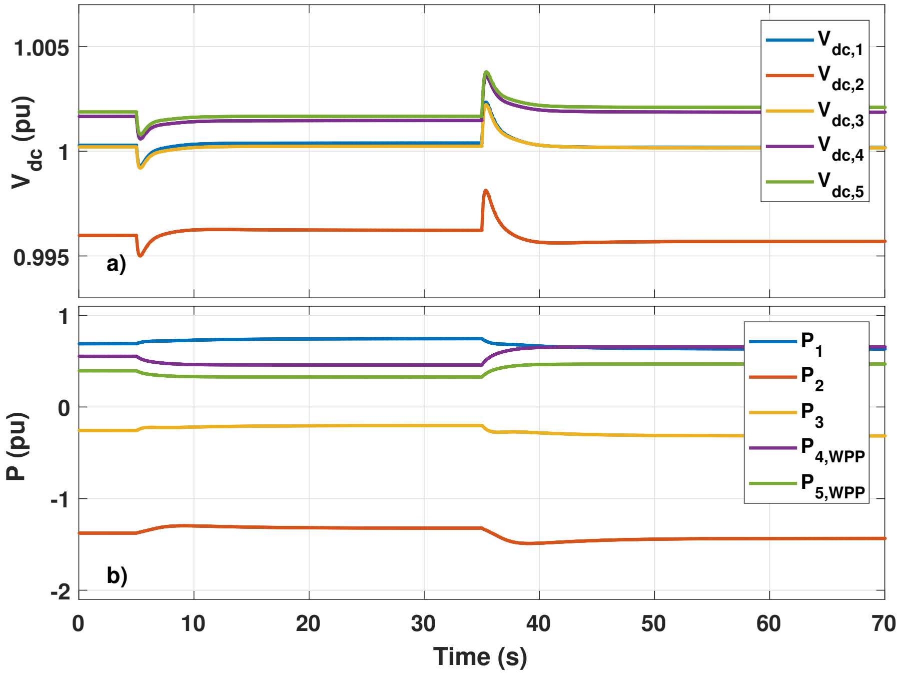

Figure 5.24. a) Dc system voltage profiles b) converter power injections during wind speed changes.

5.2.3.4 System response with no frequency support from WPPs.

As mentioned previously, the proposed strategy achieves proper allocation of the power reserves between asynchronous ac systems even if there is no extra support from WPPs. The simulation scenario is therefore conducted to compare a case when WPPs provide the frequency support with a case when WPPs do not provide any extra support during the frequency event. For the latter case, the WPPs operate at MPPT mode during the normal condition (e.g., $\Delta P_{del.,WT} = 0$). The previous scenario of a 0.4 pu load increase in area 3 is repeated here. The assistance factor of the affected area is pre-set to 50 %. As can be seen from Fig. 5.25, for both cases the proposed controller achieves twice the frequency deviation of the affected area compared to the identical parameter of the healthy grids (area 1 and area 2 in this case). Therefore, accurate allocation of the power reserves between asynchronous ac grids based on the operator's pre-specified ratios is achieved throughout the frequency event. It can also be noticed that the extraction of additional power from WPP results in less frequency deviation in all three grids, which, however, is at the cost of operation WPPs at off-MPPT during normal conditions.

Apart from WPPsâĂŹ frequency response controller, other strategies can also be seamlessly integrated with the proposed approach to provide extra power support during frequency events and so to enhance the frequency response of the interconnected system. Such methods include but are not limited to the extraction of additional power from converter capacitors [171] or storage devices [172], and modulation of the converters' reactive power output as in [173]. The development of a strategy combining different techniques for boosting the frequency response will be a subject matter of our future research.

5.2.3.5 Effect of the proposed controller when two ac systems are interconnected by a tie line.

In all previously discussed scenarios, the ac systems connected to the MT-HVDC systems were operating asynchronously. This scenario considers a case when some of the ac systems are connected by both direct connection (synchronous connection) as well as through MT-HVDC system. Specifically, area 1 and area 2 of Fig. 5.9 have a tie-line connection. In this scenario, the regulation of the tie-line power to the nominal value is achieved by means of Automatic Generation Control (AGC) [45] (investigation of the system performance in the secondary frequency response time-scale is out of the scope of this thesis). Before going into the time-domain simulations, the stability of the entire network with and without the implemented frequency regulation controller is investigated. To this end, the eigenvalues of the system are shown in Fig. 5.26, where it can be seen that the damping of the

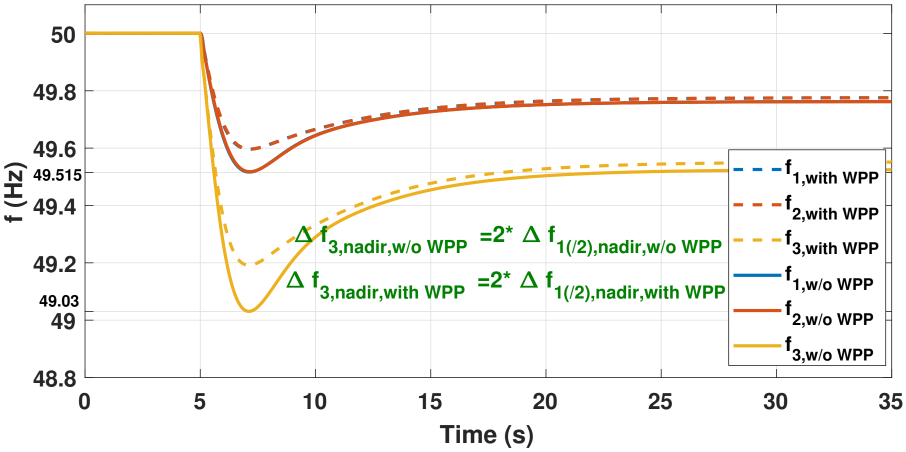

Figure 5.25. The frequency response of the system during increase of the load in area 3 with AF=50% for the affected system. The cases with (dotted trajectories) and without (solid trajectories) participation of WPPs into frequency response are presented.

critical eigenvalues significantly increases with the application of the proposed algorithm, changing from around 7% to 40%. Furthermore, Fig. 5.27 depicts the system response when the power demand in area 1 is reduced by 0.2 pu at time t=30s. With an AF for the affected area set as 100%, the other two grids fully participate in the disturbance mitigation, therefore they also experience increase in their frequencies as a result of excess power available in the system. It can be seen that the tieline interconnection does not affect the expected operation of the proposed controller. In fact, the tieline power sees little variation from its reference value during the disturbance. Both the frequency and tieline power are then slowly being restored to the reference values with the help of AGC controller.

5.3 Discussion

This chapter presented the developed converter-control strategies for ensuring enhanced reciprocal frequency support between MT-HVDC interlinked ac systems. The modifications are carried out in the outer power-voltage droop loop by adding frequency-dependent term to the original power reference. The proposed control strategy demonstrated an enhanced frequency response of the affected ac grid achieved by the provided support from

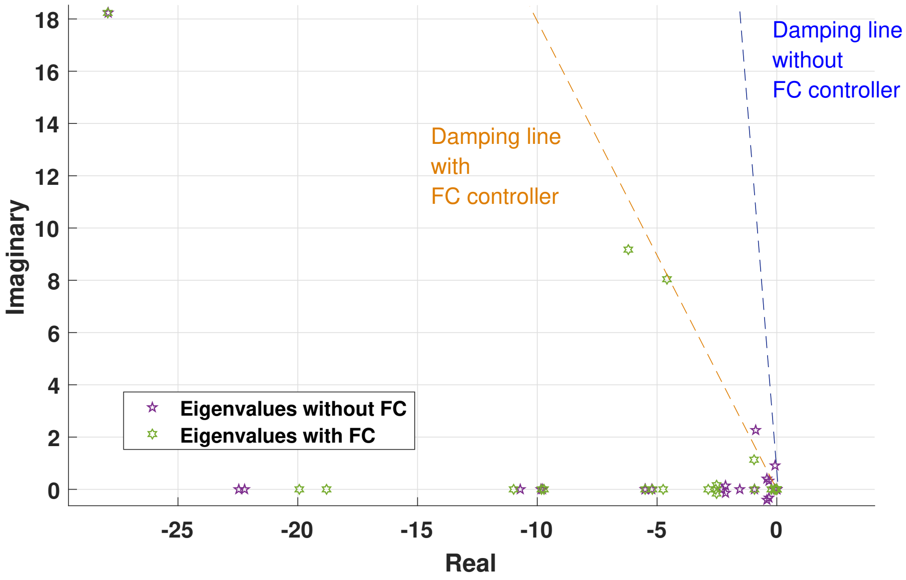

Figure 5.26. Critical eigenvalues of the system with and without the FC algorithm.

the other grids. Then the controller was augmented to enable the capability of achieving equitable mutual frequency response; that is, to achieve pre-specified ratios between the frequency deviations of participating ac grids based on their operational status. To this end, the controller of the first part of this chapter was modified to continously detect the affected grid and to enable achieving the desired ratio-based frequency deviation sharing. The conducted modal analysis verified the capability of the proposed controller to enhance the damping of the interlinked system. Comprehensive time-domain simulation have then been used to verify the comparative advantage of the proposed control algorithm with respect to other recently-reported control approaches.

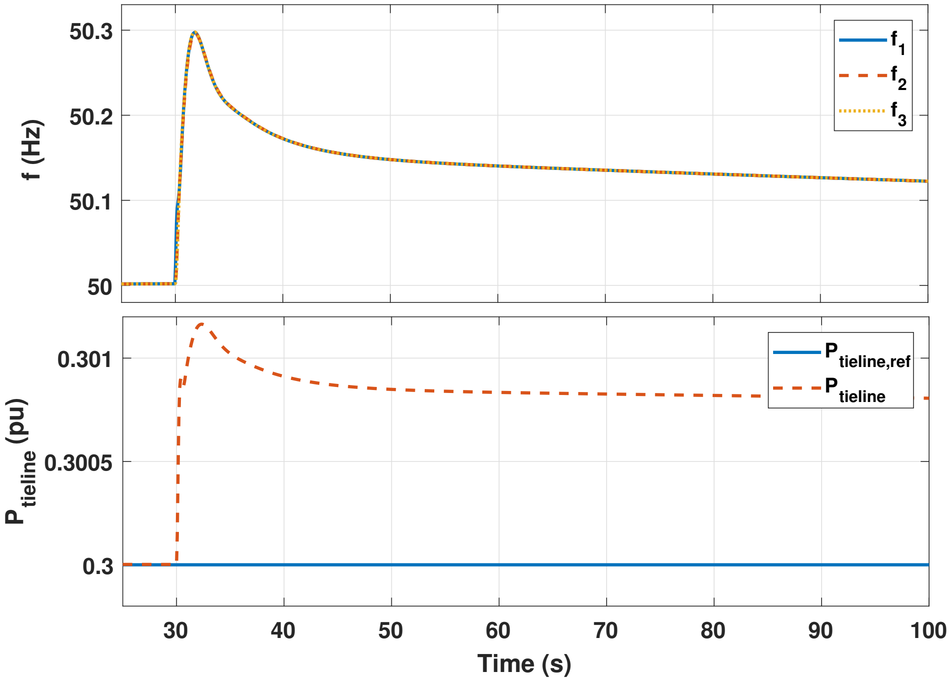

Figure 5.27. The frequency response and tieline power flow during the reduction of power demand in area 1 by 0.2 pu.

Chapter 6

Decentralized control strategy for MT-DCμGrids

The load sharing in the MT-DCμGrids is affected by the practical factors such as the cable resistances and changes in the system topology. It was shown in the Literature Review chapter that the signal injection based techniques have recently become popular for the control of MT-DCμGrids as they provide decentralized control of such grids without relying on the system information and parameters. The drawbacks of existing signal-injection based techniques have been also discussed, including the fact that those controllers rely on the synchronization between the injected signals and they modify the existing control structures significantly.

This chapter presents a new signal-injection based control algorithm for the application in MT-DCμGrids to achieve accurate load distribution between droop-controlled converters. An identical steady state voltage feedback is used for all droop-controlled converters to ensure accurate current sharing. The information about the common voltage is obtained by means of the proposed communication-less control strategy. The proposed strategy does not require prior information about the grid topology and parameters. Therefore, it is applicable to general-structure MT-DCμGrids. The conducted stability analysis demonstrates that the proposed approach and the conventional droop control of MT-DCμGrids exhibit similar dynamic performance. Compared to the other signal injection based techniques, on the other hand, the proposed strategy does not require synchronization between superimposed ac voltages, which makes the proposed strategy more appealing from the system's stable operation perspective. Additionally, unlike other similar techniques, the proposed strategy does not modify the conventional structure of the outer control layer significantly, therefore it is easy to integrate with the conventional droop controllers. Furthermore, the proposed algorithm has a potential to enhance the operation of the Interlinking Converters in the hybrid ac/MT-DCμGrid systems. A comprehensive nonlinear simulation study is conducted in the Matlab/Simulink environment. The simulation results verify the effectiveness of the proposed communication-free control scheme to enable proper load distribution between droop-controlled converters of MT-DCμGrids as well as enhance the load sharing between ac and MT-DCμGrids. Finally, the proposed control approach is verified using an

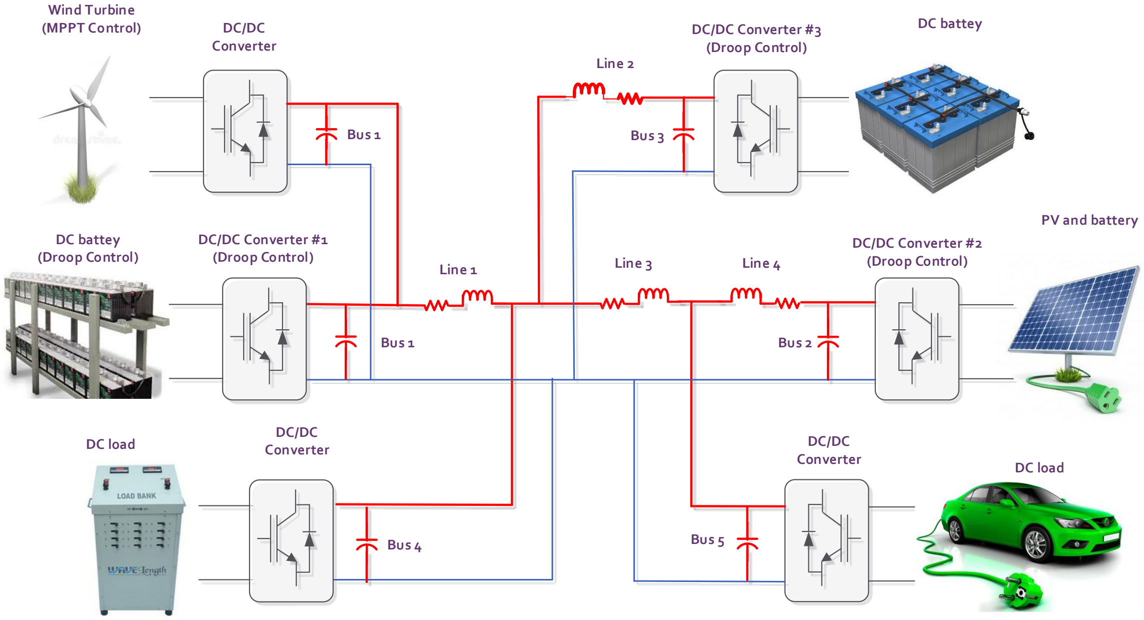

Figure 6.1. The layout of the considered MT-DCμGrid system

OPAL-RT setup. The work of this chapter has been published in IEEE Transactions on Power Systems [174].

6.1 The description of the developed controller for MT-DCμGrids

6.1.1 The considered study system and the current sharing issue with the conventional droop control

Fig.6.1 represents a typical layout of a MT-DCμGrid, which is also considered in this study as a test system. The system presents a multi-bus microgrid, where the loads are connected to more than one bus. The dc/dc converters are used to interface both Distributed Generation (DG) and the loads to the respective dc buses. The system parameters are provided in Table A8 in the Appendix.

The converters interfacing three DGs are utilized to control the dc system voltage through I-V droop control, as those sources are assumed to have a dispatchable active power output. As shown in the Literature Review chapter, several recent studies aim addressing the current sharing issue between droop-controlled converters. The signal injection based technique become a promising candidate among the existing communication-free controllers developed for addressing the current-sharing issue. In the latter approach, a small ac signal is superimposed on dc grid voltage, and the usage of this ac signal allows achieving proper current-sharing between the converters. However, as discussed in the Literature Review chapter, and as will be demonstrated by the simulation studies conducted in this chapter, the existing signal-injection based techniques might not ensure proper operation of MT-DCμGrids. Particularly, those strategies modify the conventional I-V droop control significantly. Therefore in case those strategies fail the intended synchronization-based operation, not only their accurate current sharing capability might be lost, but the entire microgrid operation might be discontinued due to inability of ensuring even basic operation of the system using conventional droop control.

To overcome the mentioned drawbacks of the controllers available in the literature, a new signal injection based technique is developed for MT-DCμGrids and is presented in the current chapter. As discussed in Chapter 3, the issue of inaccurate load distribution in MT-DCμGrids is caused by non-uniform voltage profile throughout dc microgrid. Therefore, the developed controller aims using a common voltage as a feedback signal in all droop-controlled converters [155, 156]. The voltage measured at any converter can serve as such signal. In case of using such feedback signal the current output at the i_{th} converter would be as per (6.1).

$$I_{i,out} = \frac{V_{dc,ref} - V_{dc,common}}{k_{droop,i}} \tag{6.1}$$

where V_{common} is the terminal voltage at any predetermined converter. Considering the identical reference voltage signals V_{ref} at all converters, (6.1) demonstrates that the quantity $I_{i,out} * k_{droop,i}$ is equal for all droop-controlled converters. Therefore, the usage of the common feedback signal would result in accurate load sharing independent of the system topology and parameters. Important to note that the terminal voltage of any converter can be used as a common signal.

The challenge, however, is to acquire the information of the common bus voltage $V_{dc,common}$ at different converters. In the case of existence of the communication links (like in MT-HVDC systems), the common voltage could have been measured at the output of any pre-selected converter and communicated to all other converters to be used as a feedback signal. Therefore, a single converter would use the locally measured voltage and the same voltage would be communicated and used in all other converters. This chapter, on the other hand, proposes a communication-free power-sharing control strategy suitable for MT-DCμGrids, where the communication infrastructure might not be available. To transfer the voltage information in the communication-free manner, the signal injection based technique is developed in this study.

In the developed strategy, the common voltage information is embedded in the frequency of an ac signal superimposed on the dc voltage at the pre-specified converter. The frequency of the imposed signal varies around the nominal frequency according to the variation of the measured dc voltage at that converter, therefore, it contains information about the magnitude of the common voltage. Considering that the frequency is a global variable in the system, this frequency can be detected at each converter with the help of proper frequency detection technique. The estimation of the frequency allows estimation of the magnitude of the common voltage at all converters without using any communication infrastructure. Furthermore, unlike other signal-injection techniques (e.g. [151, 152]), the proposed strategy uses only one converter at which the frequency of the superimposed signal is determined, and the rest of the system ac voltages follow this frequency, eliminating the need for the synchronization between the frequencies at different converters.

6.1.2 The implementation of the proposed algorithm

The general steps to implement the proposed control strategy can be described as follows

1. Inject ac signal at one preselected converter with the frequency containing information about the dc voltage magnitude at that converter.
2. Detect the frequency of the injected ac signal at all other converters (this frequency is a global variable in the whole system).
3. Extract the value of the common voltage $V_{dc,common,est}$ from the frequency information.
4. Use the estimated information to generate the correction term and add to the local voltage feedback.

In the first step, the information of the common voltage magnitude is embedded in the frequency of the small ac voltage, which is superimposed on the dc voltage. This is done

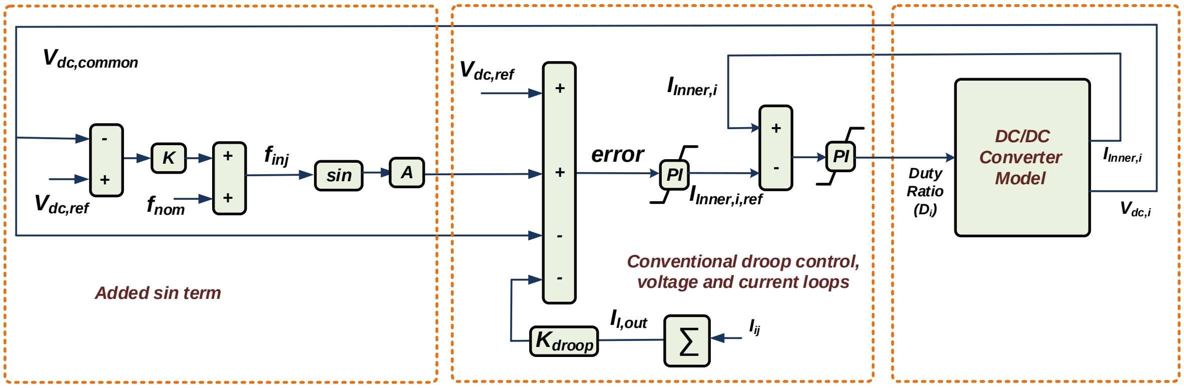

Figure 6.2. The control of the ac superimposing converter (based on local measurements only).

by adding the required sinusoidal voltage to the reference of common converter as shown in Fig.6.2. The converter superimposing the ac signal should have a voltage regulation loop so that the ac signal added to the converter reference voltage can be followed in the terminal voltage. Therefore, any of the droop-controlled converters can be selected for superimposing the ac signal. The frequency of the injected voltage f_{inj} is determined by equation (6.2)

$$f_{inj} = (V_{dc,ref} - V_{dc,common}) * K + f_{nom} \tag{6.2}$$

where $V_{dc,ref}$ and $V_{dc,common}$ are the reference and locally measured voltages at the common converter, respectively, K is the normalization constant and f_{nom} is the nominal frequency around which the frequency of the injected signal will be varied. Similar to other signal-injection based techniques, the nominal injected frequency is selected to be 50 Hz in this study. Such selection allows relatively easier detection of the frequency of the superimposed ac signal. The linear relationship between the frequency of the injected ac signal and the dc terminal voltage measured at the common converter is demonstrated in Fig.6.3, where the injected frequency is varied as a function of the common voltage magnitude $V_{dc,common}$. The nominal frequency f_{nom} is upper limited by the bandwidth of the voltage control loop, which should allow sufficient tracking capability for the added ac reference signal. The magnitude of the injected voltage is determined by the parameter A (Fig. 6.2) and is selected as 0.6% of the nominal dc voltage to allow proper frequency detection while remaining within the acceptable dc voltage limits [152]. After forming the sinusoidal ac term, it is added to the dc voltage reference as shown in Fig. 6.2. The volt-

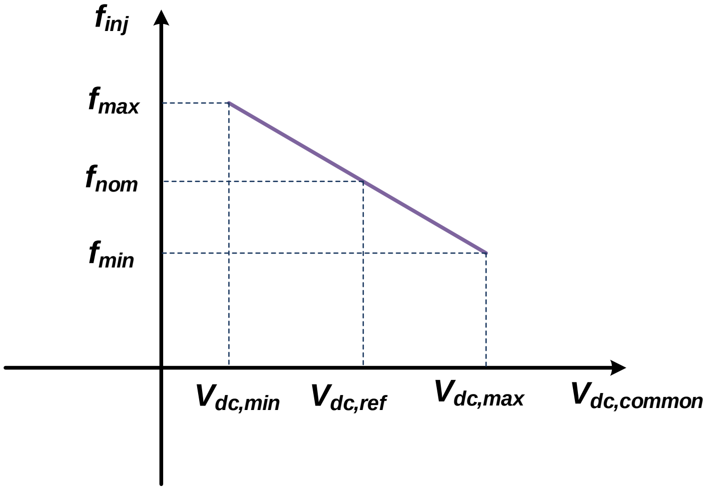

Figure 6.3. The relationship between the frequency of the injected voltage and the magnitude of the common voltage

age controller then forces the local voltage to follow the modified reference voltage. Please note that to achieve zero steady-state error (to exactly track the ordered reference sin wave), PR controllers can be added to the conventional PI controllers of I-V loops. However, with the relatively low range of the injected frequencies, the conventional PI-based controller structure allows sufficient tracking of the generated reference signal; therefore no relatively complex controller structures need to be used. The superimposed voltage propagates throughout the system, which causes the dc grid currents to also experience a sinusoidal component at the same frequency as the injected voltage signal. The propagation of the injected ac voltage signal thought dc grid together with the contribution from the ac component of the converter currents makes the voltages at the terminals of the other converters to experience an ac component.

The control of the converters other than the injecting converter is shown in Fig. 6.4. The main aim of the added part is to calculate the common voltage magnitude from the estimated frequency information and use it as a steady-state feedback signal instead of the local measured voltage. The locally measured voltage $V_{dc,i}$ contains a dc term and an ac component. To extract the frequency of the ac component, the dc term is minimized by the subtraction of the $V_{dc,i}$ from the dc voltage reference $V_{dc,ref}$ (Fig. 6.4a). Afterward, the Second Order Generalized Integrator (SOGI) block is added in the current work in series to the single-phase FLL to remove the dc offset signal and enable the frequency detection.

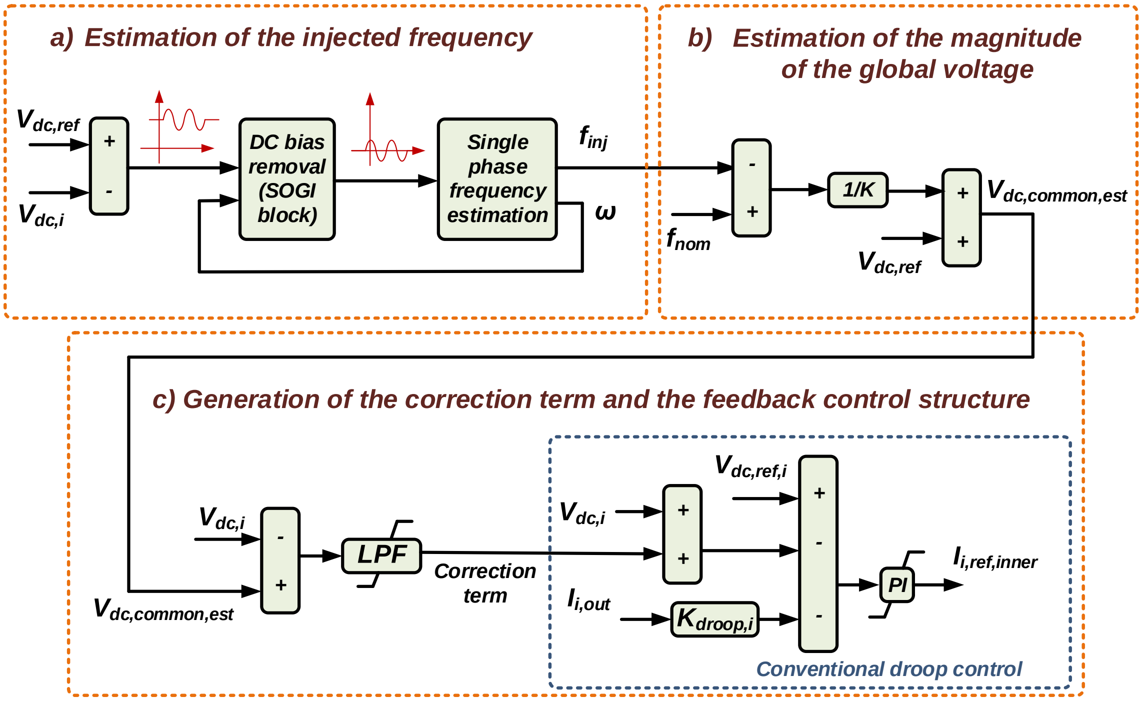

Figure 6.4. The control of the converters other tha n the ac injecting converter (based on local measurements only).

After the removal of the dc term, the single-phase FLL, which was presented in Chapter 2, estimates the frequency of the superimposed signal. It is worth mentioning that there is no specific requirement on the selection of the type of the frequency estimation technique, therefore any of the single-phase grid synchronization and frequency detection techniques with its respective design guidelines can be used to extract the frequency of the injected signal.

After acquiring the frequency of the sinusoidal component, the magnitude of the common voltage can be determined from equation (6.2) as per equation (6.3)

$$V_{dc,common,est} = V_{dc,ref} + \frac{f_{nom} - f_{inj}}{k} \tag{6.3}$$

The realization of equation (6.3) is shown in Fig.6.4b. The estimated voltage could be directly used as a feedback voltage signal, which would ensure accurate current sharing in steady state. However, the direct usage of the estimated global voltage, as will be shown in the stability analysis subsection, might result in missing the fast dynamics associated with the changes of local dc voltages and result in less system damping. Therefore, in this thesis, the feedback signal at the i_{th} converter $V_{dc,feedback,i}$ is determined according to (6.4) to capture the fast dynamics associated with the local voltage and to ensure steady state accurate current sharing with the estimated global voltage.

$$V_{dc,feedback,i} = (V_{dc,common,est} - V_{dc,i}) * G_{s,LPF} + V_{dc,i} \tag{6.4}$$

where the $G_{s,LPF} = \dfrac{\omega_c}{\omega_c + s}$ is the transfer function of the first order low pass filter (LPF) used in this study. The effect of the parameter ω_c on the system performance will be demonstrated in the stability analysis presented in the next subsection. This filter allows slowing the effect of the dynamics associated with the common voltage estimation on the feedback loop. On the other hand, it can be noticed from (6.4) that in steady state, when the LPF has no effect on the dc quantities, the feedback signal is determined by

$$\begin{aligned} V_{dc,feedback,SS} = {} & (V_{dc,common,est} - V_{dc,i}) \\ & + V_{dc,i} = V_{dc,common,est} \end{aligned} \tag{6.5}$$

where $V_{dc,feedback,SS}$ is the steady-state feedback signal and is equal to the $V_{dc,common,est}$. As can be noticed from Fig.6.4, the modified controller simply adds a correction term to the conventional control with local voltage feedback. This term is responsible for modifying the steady-state feedback signal to ensure the accurate current sharing in the MT-DCμGrid.

Also, if the input to FLL is below 3% of the nominal injected voltage, it is advised to freeze FLL for several cycles to mitigate the effect of the large dc voltage changes on the operation of FLL. The freezing of the FLL can be accomplished by sampling and holding the d/q components of the FLL voltage. By doing this, the detected frequency will maintain constant value during the voltage transient, hence the correction term will not change its value for the initial several cycles of the transient. Thus, the FLL does not experience the harsh dynamics associated with the dc link voltages. After the FLL is activated, the detected frequency will contain information about the changed voltage of the common converter, and hence the equal current sharing will be achieved subsequently.

It is worthy to note that the conventional droop control requires larger droop gains to provide sufficient responsiveness for achieving desired load distribution. This causes the dc voltage references to be penalized with larger voltage shifting term, the latter being equal to the product of the output current and the droop gain. The proposed strategy, on the other hand, does not require large droop constants for achieving exact current sharing, as the latter is ensured by using the common steady-state feedback signal in all converters.

Although the proposed strategy employs one converter to inject the ac signal to the grid, the system can continue reliable operation even after the injection of that signal is stopped (e.g. due to the failure of the common converter). The lack of the ac signal will be locally detected at the other converters and the estimated frequency and the correction term will be frozen (similar to the freezing of grid synchronization techniques in ac systems during grid fault conditions). The constant correction terms would result in improving the current sharing, but it will not guarantee the exact current sharing. By having the predefined sequence of the converters which should inject the ac signal, the next converter after the failed converter can pick-up and start the superimposition of the ac signal. Please note that there is no difference which voltage is global: as long as all droop-controlled converters use identical steady state voltage feedback, the proper current sharing will be achieved. The sequence of the selection of the injecting converters can be guaranteed by various waiting time after the detection of the lack of the superimposed ac signal. The mentioned operation logic is summarized in Fig. 6.5.

6.2 The stability analysis of the proposed controller

In order to understand the effect of the proposed controller on the stability of the system, an eigenvalue analysis is conducted considering the following controller alternatives: conventional droop control with the direct feedback from the terminal voltage (Fig. 6.6a), the strategy where an estimated global voltage is directly used as a feedback signal (Fig.

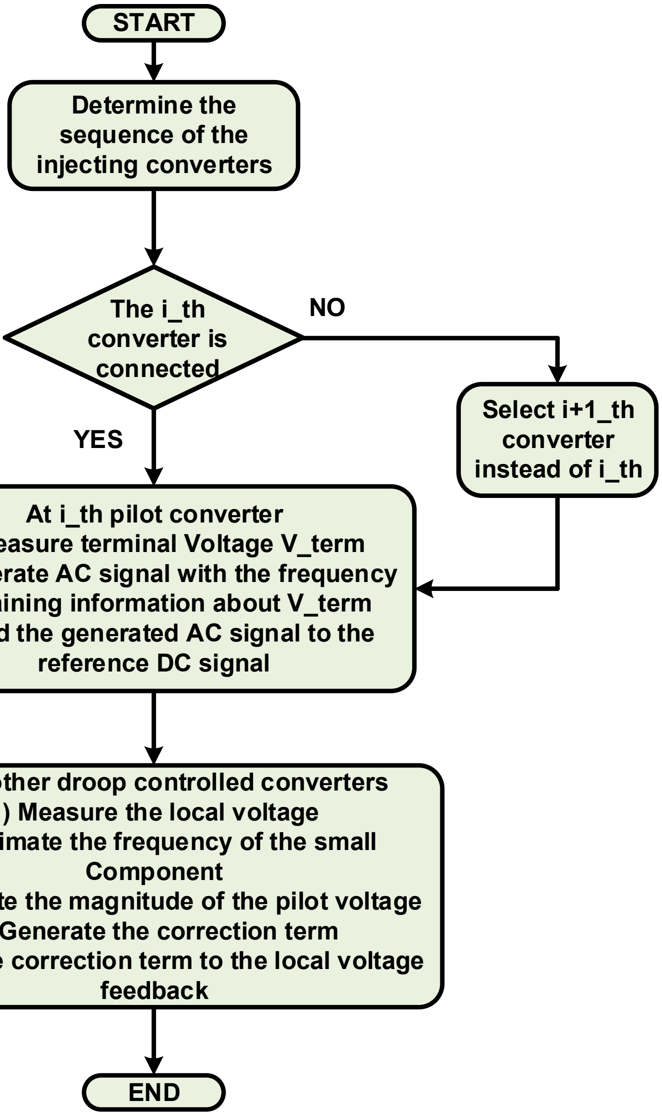

Figure 6.5. The operation flowchart of the proposed algorithm

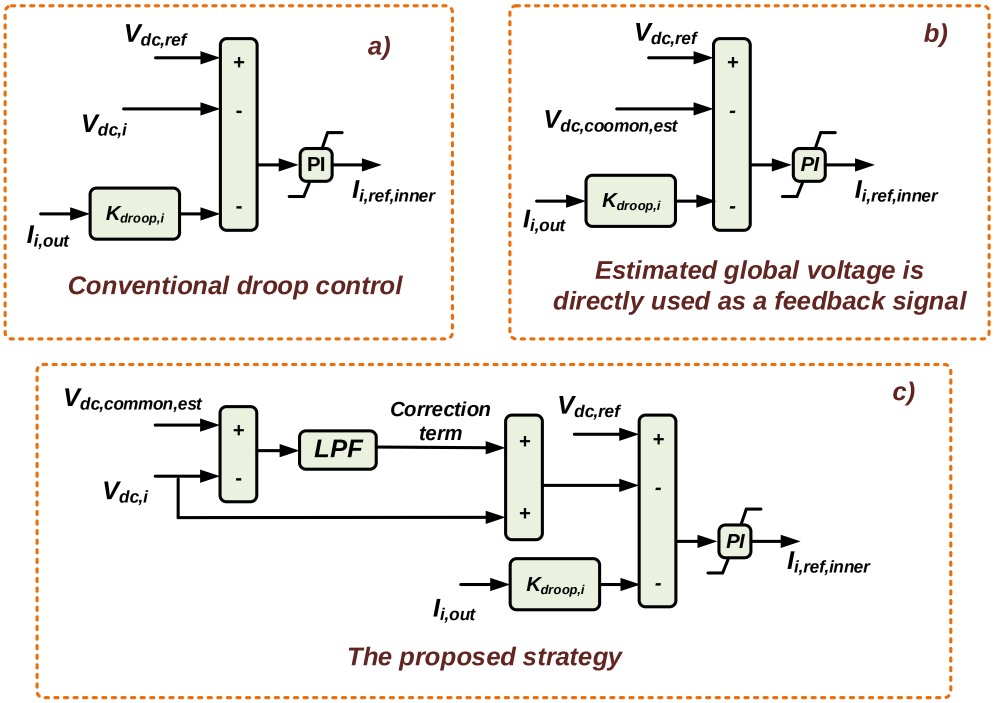

Figure 6.6. The control structures considered for the stability analysis.

6.6b), and the proposed strategy where an estimated global voltage is used to generate the correction term with the help of the LPF (Fig. 6.6c). After constructing the system model based on the algebraic-differential equations, the Matlab/ Simulink linearization toolbox is utilized to obtain the system eigenvalues.

Fig. 6.7a demonstrates the positioning of all system eigenvalues with the abovementioned three controller alternatives, and Fig. 6.7b elaborates on the positioning of the critical eigenvalues. For the proposed strategy, the LPF cutoff frequency ω_c is varied from 1 rad/s to 1000 rad/s (with the step size of 10 rad/s before ω_c =100 rad/s and then with the step size of 100 rad/s before ω_c =1000 rad/s) and the resultant system eigenvalues are plotted in Fig. 6.7b as cross points. With the conventional droop control (pentagram points), the critical oscillatory eigenvalues are located more left than the identical eigenvalues when the estimated global voltage is directly used as a feedback signal (square points). It can be thus stated that by using the locally measured converter terminal voltage (conventional droop control) the system has better damping. To overcome this issue, the proposed strategy uses the estimation of the common voltage magnitude to generate a correction term with the LPF and not as a direct feedback for the controller. With relatively small values of the ω_c (below around 25rad/s) the proposed controller demonstrates similar damping characteristics as the conventional droop control. With an increase of the cutoff frequency the critical oscilatory eigenvalues start moving to the right. Eventually, with large values of the cutoff frequency (above 300 rad/s), the eigenvalues are approaching those obtained with the direct usage of the estimated global voltage signal. Although with the latter strategy the critical eigenvalues appear to be the rightmost, however, the system remains in a safe operating zone and all eigenvalues are located in the left half plane. The conducted stability analysis demosntrates that with the proper selection of ω_c (20 rad/s in this study) the proposed strategy achieves an enhanced dynamic performance similiar to the conventional droop control and superior steady state current sharing capability similar to the controller that uses the estimated global voltage directly as a feedback signal. It was also observed that there is only a slight variation in the location of the system eigenvalues when different converters are considered for superimposing the ac signal. Therefore, the change of the superimposing converter has negligible impact on the steady-state and dynamic performance of the system.

6.2.1 Proposed strategy for the Hybrid ac/ MT-DCμGrids

The proposed strategy is applicable for the control of the ICs in the hybrid ac/ MT-DCμGrids. The typical structure of such a hybrid system is shown in Fig. 6.8, which is an extended version of the MT-DCμGrid shown in Fig. 6.1 with two added ICs and an

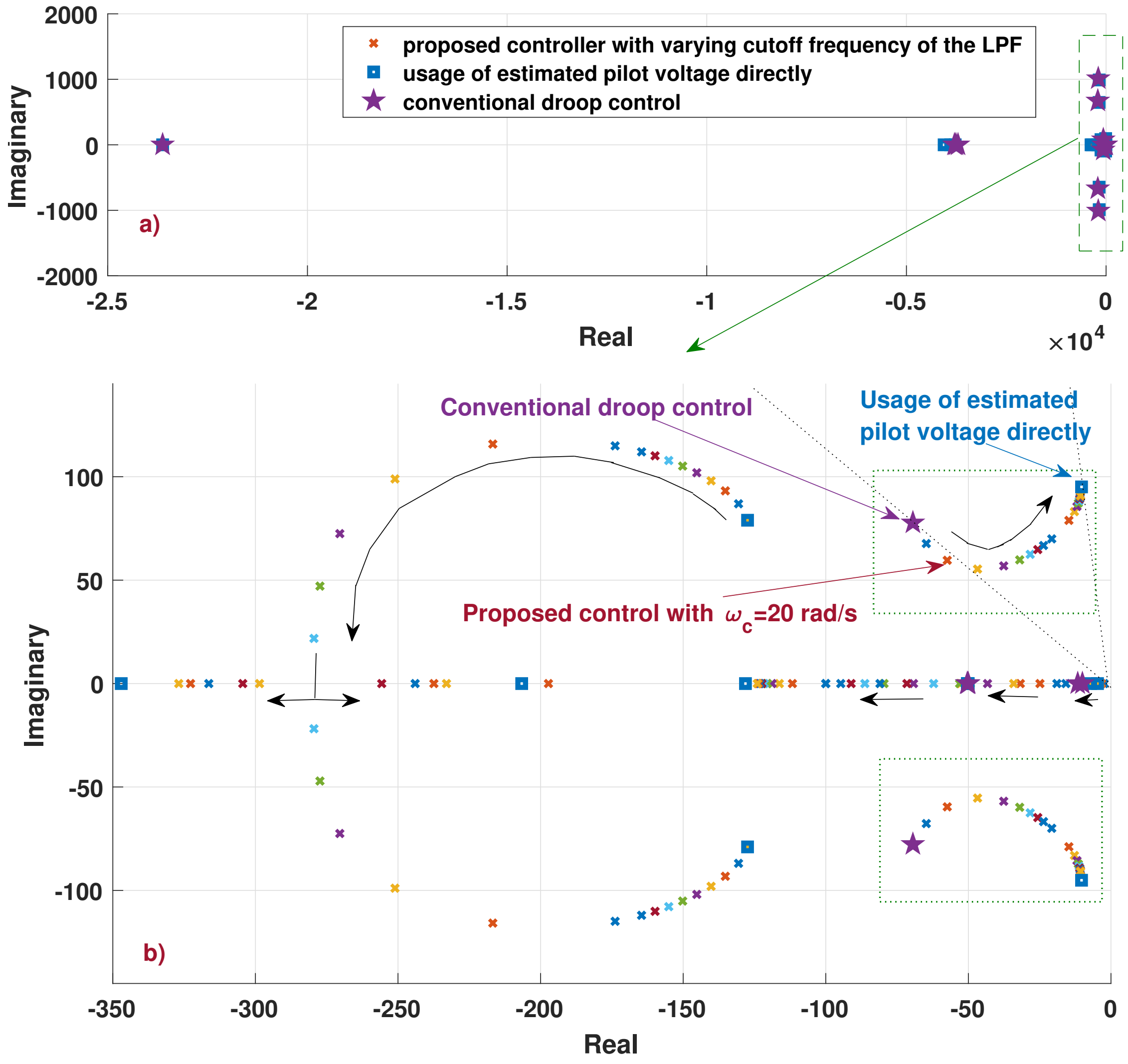

Figure 6.7. The system eigenvalues considering the conventional droop control (pentagram), the strategy where an estimated global voltage is directly used as a feedback signal (square) and the proposed strategy where an estimated global voltage is used to generate the correction term with the help of LPF (cross).

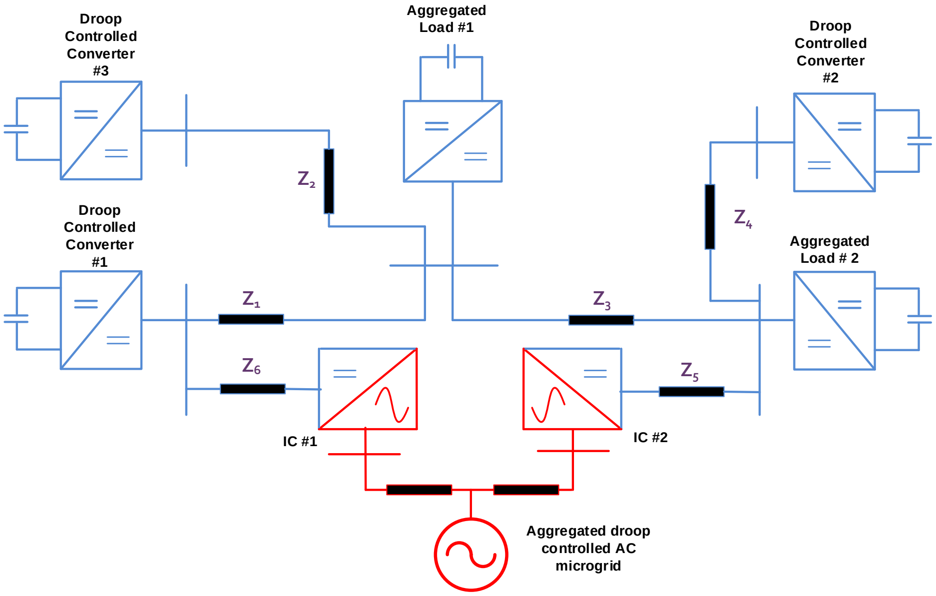

Figure 6.8. The structure of the considered hybrid ac/MT-DCμGrid

aggregated ac subgrid. The ac microgrids are modeled as an aggregated droop-controlled system and their detailed investigation is a subject matter of future research. The ICs aim to distribute the loading between the ac and dc subgrids by employing the droop control, which determines the direction and the amount of the active power transferred through the ICs. The ac and dc loading is calculated at each IC using the local measurements of the ac frequency and the local dc voltage, respectively. The respective normalized values are used for those calculations as determined per (6.6),(6.7) to limit the error variation in the range of [-1,1].

$$\omega_{pu} = \frac{\omega - (\omega_{max} + \omega_{min})/2}{(\omega_{max} - \omega_{min})/2} \tag{6.6}$$

$$V_{dc,pu} = \frac{V_{dc} - (V_{dc,max} + V_{dc,min})/2}{(V_{dc,max} - V_{dc,min})/2} \tag{6.7}$$

In (6.6),(6.7), the ω and V_{dc} are locally measured frequency and the dc voltage, respectively, while their minimum and maximum values are pre-specified quantities. The current reference of the IC is then determined as follows

$$I_{d,ref,IC} = \frac{1}{\gamma} * e_{\omega,V} \tag{6.8}$$

where the γ is the droop gain of the particular converter determined by its rating, $e_{\omega,V}$ is the error signal defined as the difference of the normalized frequency ω_{pu} and the normalized dc voltage $V_{dc,pu}$. The positive error refers to the active power transfer from the dc grid to the ac grid, and vice-versa for the negative error. The usage of the frequency in (6.6) as an indicator of the ac system loading is justified by the fact that this parameter is a global variable in the whole ac microgrid. In contrary, the dc bus voltage is not a global parameter in the dc grid due to voltage drops across the lines. Therefore, the feedback dc voltage in (6.7) at each IC can be different, causing a difference in the error term calculated at each IC. Thus, at different ICs the detected dc loading would be different. Moreover, the power/current reference of the ICs might not be according to their rating, resulting in the sharing error between those ICs.

To overcome the above-mentioned issues, in the current work it is proposed to utilize the steady-state magnitude of the common dc voltage as a feedback in all ICs which are connected to the same MT-DCμGrid at different locations. Similar to the proposed strategy for the power-sharing between dc/dc converters, the ICs would also detect the frequency of the superimposed ac signal, estimate the magnitude of the common voltage, generate the correction term and add to the local measured feedback voltage. Therefore, the steady state current reference of the i_{th} IC would be determined as per

$$\begin{aligned} I_{d,ref,IC,i} = \frac{1}{\gamma_i} * (&\frac{\omega - (\omega_{max} + \omega_{min})/2}{(\omega_{max} - \omega_{min})/2} - \\ &\frac{V_{dc,common,ss} - (V_{dc,max} + V_{dc,min})/2}{(V_{dc,max} - V_{dc,min})/2}) \end{aligned} \tag{6.9}$$

where $V_{dc,common,ss}$ is the steady state voltage feedback acquired by the proposed method. Except the parameter γ_i, the right-hand side of the (6.9) is identical for all ICs. Therefore, accurate current sharing is achieved between ICs independent from their connection points.

It was shown that the application of the proposed control strategy to hybrid ac/MT-DCμGrid results in an improved performance of ICs. However, it is worth noting that the detailed investigation of ac microgrids is out of the scope of this thesis.

6.3 Simulation Results

To test the effectiveness of the proposed method, a simulation model of the system shown in Fig. 6.1 is developed in the Matlab/Simulink environment using the SimPowerSystem toolbox. Furthermore, the system is extended to hybrid ac/MT-DCμGrid of Fig. 6.8 to demonstrate the application of the proposed algorithm to hybrid ac/ MT-DCμGrids. The system parameters can be found in the Table A8 in the Appendix. In the Subsection A, the comparison between the conventional droop and the proposed approach is demonstrated by switching from the former to the latter strategy. The advantage of the proposed strategy in terms of accuracy of the load sharing is clearly demonstrated in the presence of both equaly and unequally rated converters. Moreover, the performance of the proposed controller is evaluated in Subsection B in the presence of the renewable sources having Maximum Power Point Tracking (MPPT) control algorithm. Furthermore, Subsection C presents the application of the proposed controller to enhance the performance of the ICs interfacing ac and MT-DCμGrids. Enhanced load sharing between dc and ac subgrids is achieved.

6.3.1 The performance evaluation during the activation of the proposed controller and the load step change

In this scenario the current sharing between droop-controlled converters is investigated with both conventional and the proposed strategy. Both identical as well as unequally rated dc/dc converters are considered. The converter #2 has twice higher rating than converters #1 and #3, therefore the droop gain of the converter #2 is selected to be twice lower than the equivalent gain of the other two converters. The mentioned selection of the droop gains should ideally result in twice higher current output from the converter #2 than from the other two converters during all steady state operational points. In the beginning of the simulation the system performance with the conventional droop control is demonstrated by deactivation of the proposed correction term. As it can be observed from the subfigure (a) of Fig. 6.9, the output currents from the first, second and the third converters are approximately 3.55A, 2.8A, 6A, respectively. This contradicts with the desired current sharing, might result in the converter overloading (especially for the third converter) and does not utilize the large current headroom of the second converter. Starting from time t=5 s, when the proposed correction term is activated, the current sharing changes significantly, resulting in the 3.1A, 6.2A and 3.1A, output currents from the first, second and the third converters, respectively. The zoomed version of the current injections verifies that the first and third converters share identical current, as it was desired by identically predetermined

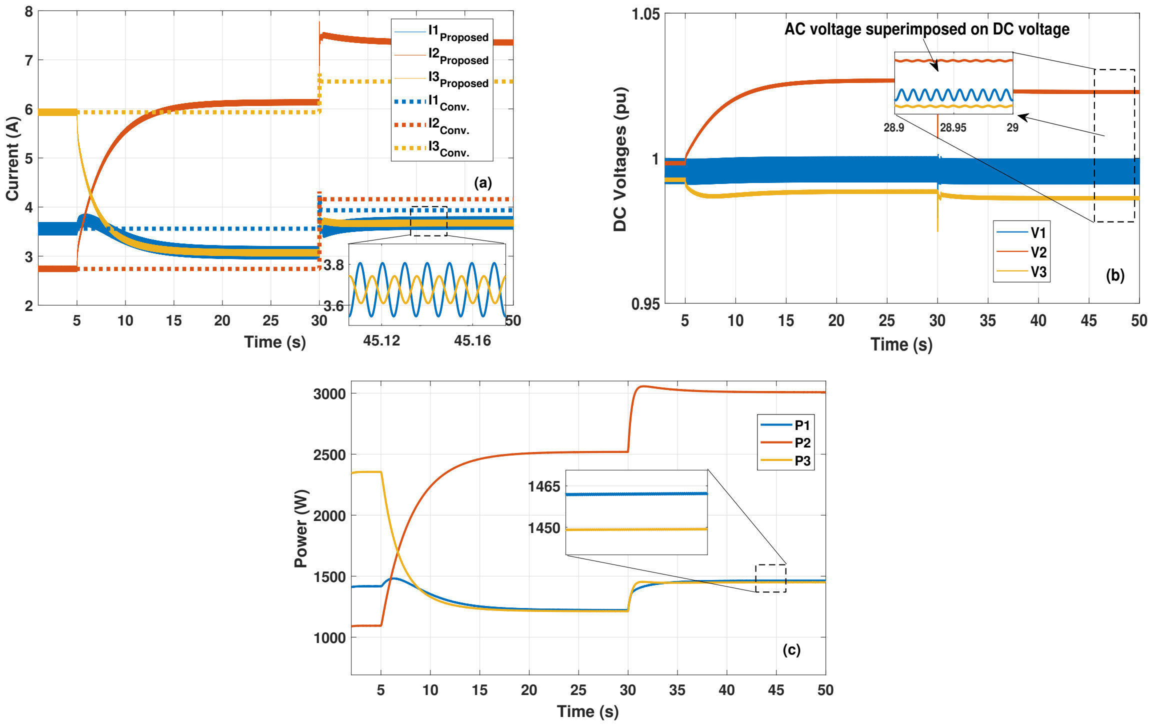

Figure 6.9. The system response during the activation of the proposed strategy and step change in the load current. The current output (a), the actual voltages at the terminals (b) and the power injections from the droop-controlled converters (c).

droop gains. The twice larger current from the second converter ($6.2A$) also validates the proper controller action. The subsequent 20% load increase is initiated at the time t=30s, which results in the accurate current sharing determined solely by the predefined droop gains. Specifically, the current injections in the numerical order are $3.75A$, $7.5A$ and $3.75A$. The terminal voltages of the droop-controlled converters are depicted in the subfigure (b) of Fig.6.9, which validate the proper voltage regulation during whole operation. The zoomed version of the actual voltage profile clearly illustrates the small superimposed ac voltage. The subfigure (c) of Fig.6.9 shows the converter power injections. It can be observed that unlike for the case of the current injections, the power injections does not accurately follow the desired sharing logic. For example, the power injection of the second converter is not exactly twice as large as for the other two converter even after the activation of the correction term. The small mismatch between output power injections is the natural result caused by the unequal terminal voltages at different dc/dc converters.

6.3.2 The performance in the presence of the MPPT controlled renewable sources

This scenario considers the presence of the MPPT controlled renewable sources connected at the Bus 1 in the dc grid. Several current step changes are considered and the system response is investigated thereof. As shown in Fig.6.10a, at time t=25s the current injected by the MPPT controlled renewable source is decreased by $2A$, which results in an increased generation from all three DGs to satisfy the present load. As can be seen in Fig.6.10b, decrease in the total current injected to the dc system results in slight decrease in the common voltage magnitude. According to the relationship of the common voltage and the frequency of the injected ac signal illustrated in Fig. 6.3, the latter parameter increases with the decrease of the common voltage (Fig.6.10b). This change in the frequency modifies the correction term at each converter, which results in $4.05A, 8.1A$ and $4.05A$ current outputs from the first, second and the third converters, respectively, accurately satisfying the predetermined current sharing goal. Furthermore, at time t=40s, the MPPT controlled source is deactivated ($I_{MPPT} = 0$), which initiate current increase in the droop-controlled converters, resulting in $4.55A, 9.1A$ and $4.55A$ current output from the first, second and the third converters, respectively. Finally, at time t=55 s the MPPT controlled source is suddenly connected to inject $3A$ current to the dc grid. This scenario again validates the effectiveness of the proposed controller in achieving accurate current sharing between droop-controlled converters. The Fig.6.10c proves the acceptable dc grid voltage profile throughout the operation. The power injections from the droop-controlled converters are shown in Fig.6.10d.

6.3.3 The comparative current-sharing analysis

In this scenario, the converter current sharing capability and the performance of the system depicted in the Fig. 6.1 is evaluated below considering the conventional droop control strategy, the proposed strategy and the current-sharing method proposed in [152]. Similar to the proposed approach, the method presented in [152] neither rely on the communication network nor require the complete information of the system topology and line parameters to achieve an accurate current sharing. Furthermore, the controller presented in [152] also relies on the signal injection technique, where all the droop-controlled converters superimpose an ac signal into dc grid voltage. As elaborated in the Literature Review section, the change in the converter output current changes the frequency of the injected signal, which, assuming a strong relationship between the phase angle and the reactive power, in turn, results in a change of the reactive power associated with the injected signal. The

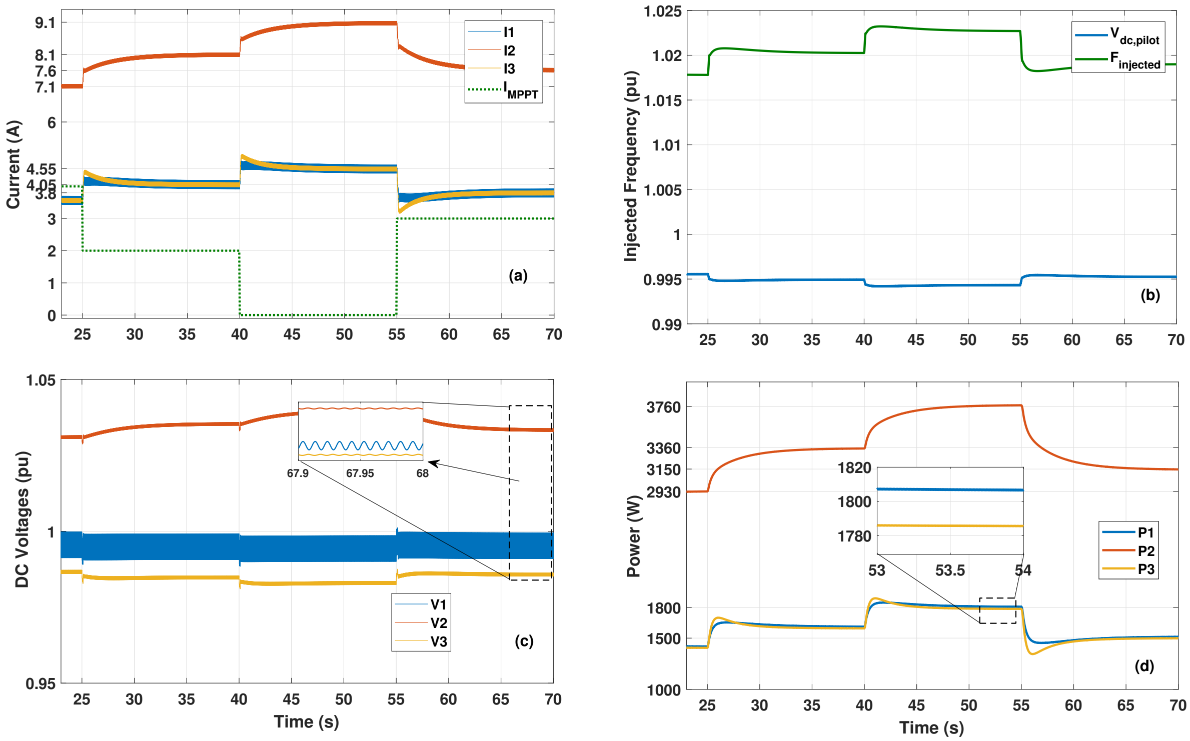

Figure 6.10. The system response during step changes in the current injected to the dc grid. The current output of the droop-controlled converters (a), the magnitude of the common bus voltage and the frequency of the superimposed ac signal (b), the actual voltages at the terminals of the droop-controlled converters (c), the converter power injections (d).

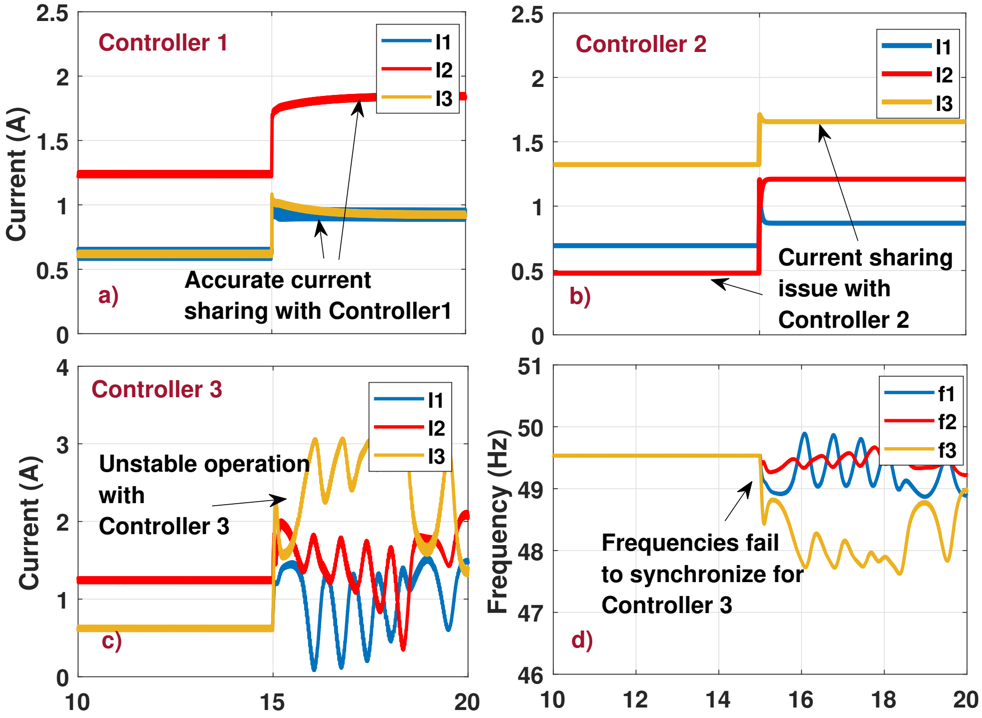

Figure 6.11. The results of the current sharing acquired with different controller alternatives: Controller 1-proposed method, Controller 2-conventional droop control and Controller 3-the existing SBDC method.

measured reactive power is subtracted from the dc voltage reference, therefore, change in the frequency results in the variation of the dc voltage. The latter adjustment of the dc voltages aims the regulation of the converter output currents. Once the frequencies of the injected signals at different converters are synchronized, the current sharing between the droop-controlled converters will be determined only based on the droop gains.

Fig. 6.11 depicts the current sharing for the considered three scenarios. As can be seen in Fig. 6.11, before the time t=15 s, the proper current sharing based on prespecified droop gains, is achieved when the proposed controller (Fig. 6.11 a) is used. The conventional droop control, in contrary, results in a current sharing being affected by the system topology and parameters (Fig. 6.11 b). Similar to the proposed controller, the strategy presented in [152] (Fig. 6.11 c) also achieves a proper load distribution between the droop-controlled converters, which is a result of the frequencies of the injected ac signals being synchronized before t=15s (Fig. 6.11 d). At time t=15s, approximately 500 W load increase is initiated in the system. Unlike the proposed controller, which results in a proper current sharing, the frequencies of the injected signals of [152] fail to synchronize and the system loses its stability. The failure in synchronization can be explained by the fact that the relationship between the frequency (phase angle) of the injected signal and the reactive power resulted from the same signal is not very strong when the line inductances are not sufficiently smaller than the line resistances [175].

6.3.4 The performance of the proposed approach on the operation of the Interlinking Converters

This scenario demonstrates the potential of the proposed algorithm to enhance the operation of the ICs connected to the same ac and MT-DCμGrids at various locations of those systems. As it was discussed in the previous section, the difference in the measured dc voltages at each IC results in different calculated error terms and causes non-identical current reference even for identically rated ICs. The system depicted on Fig. 6.8 is considered for this scenario. Fig. 6.12 presents the effect of the activation of the proposed correction term on the operation of the two ICs. Before the time t=7s, the ICs use the local voltage measurement as a feedback signal to generate the error term. This results in significant deviation of the currents through two ICs as presented in Fig.6.12 (a). As can be observed, while one of the ICs gives power to the dc subgrid, the other IC provides power back to the ac subgrid, resulting in the circulating current between the ICs. At time t=7s, the activation of the correction term results in significant reduction of the current flowing through both ICs, as well as both currents become unidirectional. Fig. 6.12 (b) clearly

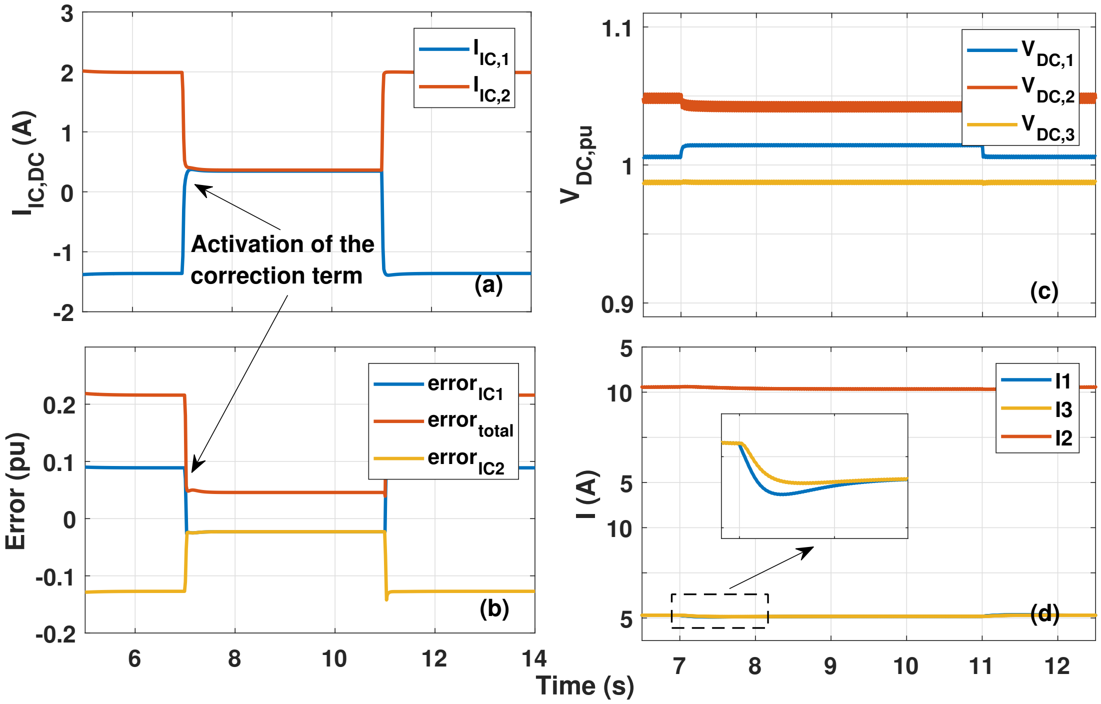

Figure 6.12. The response of the hybrid ac/MT-DCμGrid during the activation/deactivation of the proposed strategy. The current transferred trough the ICs (a), the error term at each IC (b), the dc/dc terminal voltages (c) and current injections (d).

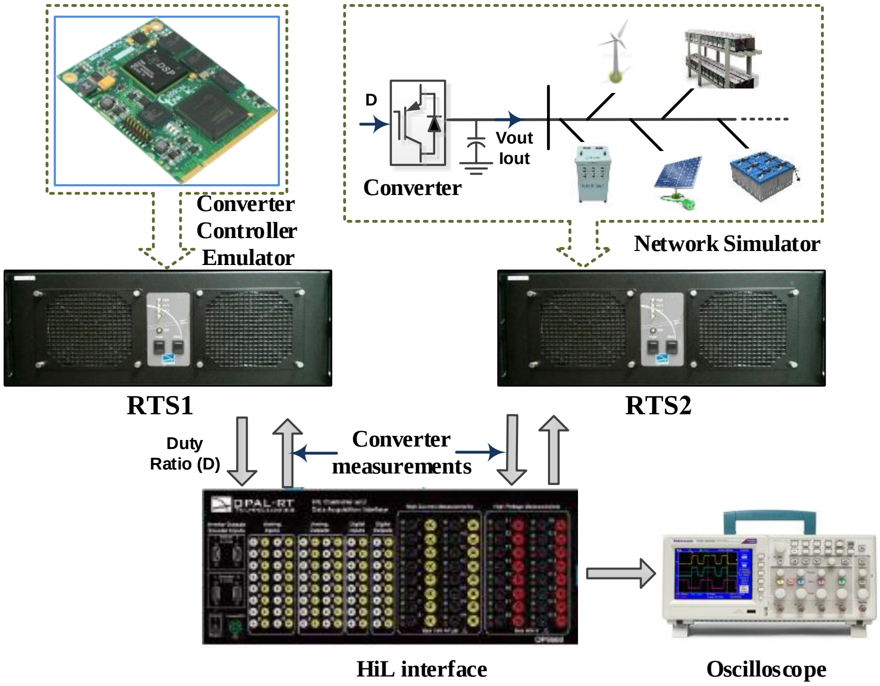

Figure 6.13. The implemented Hardware-in-the-Loop setup

demonstrates that the error terms in both ICs are also reduced. Apart from the individual error terms, the total error ($error_{total}$), defined as the summation of the absolute values of individual errors, is also reduced from 0.22 pu to 0.05 pu. This decrease in total error term refers to the achievement of better load sharing between ac and dc subgrids, which is the end goal of connecting the subgrids though the ICs. Fig.6.12 (c), (d), (e) illustrate the output currents of the droop-controlled dc/dc converters as well as their terminal voltages, validating the proper current sharing between the droop-controlled dc/dc converters as well.

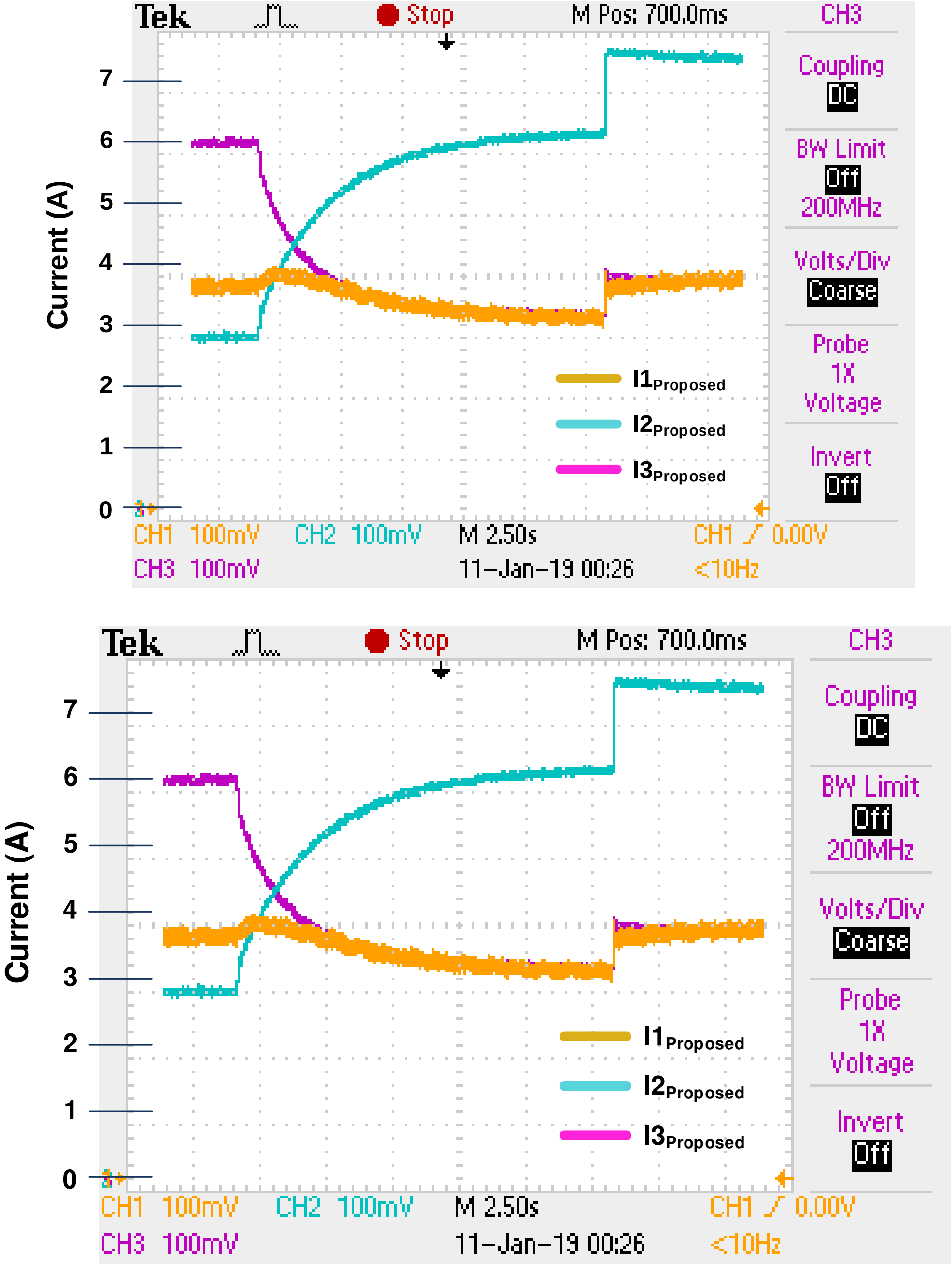

Figure 6.14. The current-sharing obtained with the HiL implementation during the activation of the proposed strategy and step change in the load current.

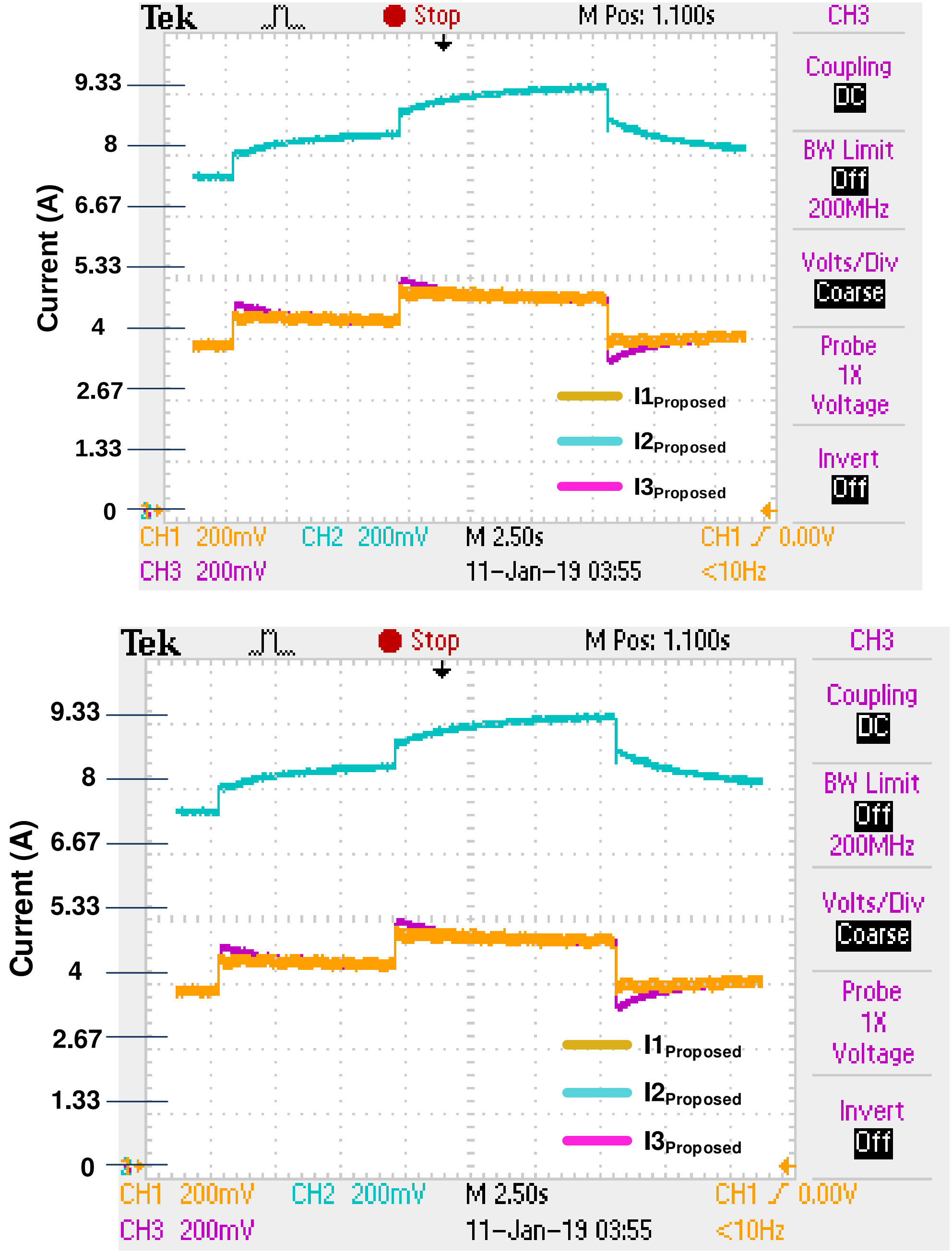

Figure 6.15. The current-sharing obtained with the HiL implementation during step changes in the current injected to the dc grid.

6.4 Real-time implementation of the proposed control structure

The validation of the proposed algorithm including its ability to properly modulate and demodulate an ac signal has been also done through hardware-in-the-loop (HiL) implementation, which has been realized by an OPAL-RT real-time simulator (RTS). Utilizing an RTS to validate microgrid control methods is a well-established practice [176–178]. In the implemented setup, two RTS (RTS1 and RTS2) of OPAL-RT were utilized as shown in Fig. 6.13. RTS1 is used to emulate the controller and exchange the real-time data with the MT-DCμGrid modeled in RTS2. This approach, also reported in other recent studies (e.g. [179, 180]), allows us to consider important features of practical implementations, including the delays existing in analog/digital conversions, and the noises that are present in the acquisitions of feedback signals. The fixed-step sampling time of $10\mu s$ was selected for running the RTS models. Farther details about the OPAL-RTS and HiL can be found in [181, 182]. The case studies presented in Subsection 6.3.1 and Subsection 6.3.2 are repeated for the evaluation of the HiL performance of the proposed algorithm. The signals plotted in Fig.6.14 and Fig.6.15 are extracted through input/output (IO) ports of OPAL-RT and are sent to 4-channel TBS1064 Tektronix digital oscilloscope. It is worth noting that the results obtained with both HiL implementation (Fig.6.14 and Fig.6.15) and the simulation study (Fig. 6.9 and Fig. 6.10, respectivelly) demonstrate similar transient and steady state response of the system during the considered system disturbances. The presented scenarios of the activation of the proposed strategy, the change of the system load and the variation of the current injected to the system prove the effectiveness of the proposed strategy in achieving proper current sharing between the droop-controlled converters of MT-DCμGrids.

6.5 Discussion

This chapter proposed a communication-free control algorithm for droop-controlled MT-DCμGrids to achieve precise current sharing. The steady-state voltage feedback is common for all droop-controlled converters, which allows overcoming the inaccurate current sharing resulted from the difference between converter terminal voltages. The information about the common voltage is acquired in a communication-free manner by embedding it in the frequency of the small ac signal superimposed on the dc voltage. Therefore, the algorithm does not rely on the information of the grid structure and line parameters and is applicable for general structure multibus microgrids. Furthermore, the proposed strategy improves the operation of the Interlinking Converters interfacing the ac and MT-DCμGrids by enabling precise current sharing between the converters and reduced error between the subgrids. The effectiveness of the proposed algorithm is verified by both Matlab/ Simulink simulation and OPAL-RT based Hardware-in-the-loop implementation.

Chapter 7

Conclusion, Research Outcomes and Future Work

7.1 Conclusion

Dc grids are increasingly viewed as promising alternatives to the conventional ac grids in certain power-system applications. The formation of such dc networks became practical with recent advances in power electronic technology. The development of dc grids, in particular, Multi Terminal High Voltage Direct Current (MT-HVDC) systems and Multi Terminal DC MicroGrids (MT-DCμGrids), has gained significant attention in recent years as they can facilitate larger integration of renewable energy sources. The research presented in this thesis was undertaken to assist the advancement of such dc systems by proposing improved control strategies for the converters interfacing with these grids. For this purpose, the outer levels of the converters' controllers have been modified to ensure proper functioning of the system. Specifically, Chapter 4 demonstrated an enhanced voltage regulation and power sharing strategy for MT-HVDC systems. This strategy regulates the average dc system voltage, overcoming the voltage regulation issue present in power-voltage droop controlled MT-HVDC systems. Further augmentation of the power-sharing loop ensures that the developed controller performs satisfactorily when large delays are present in communication networks. Chapter 5 has extended the functionality of the controller developed in the previous chapter to enhance mutual frequency support between MT-HVDC interconnected asynchronous ac systems. It has been shown that during a disturbance in any of the participating ac grids, the controller is capable of equalizing the effect of a disturbance on all participating ac grids. The result is less stress on the affected ac system. Furthermore, the controller has been enhanced to allow equitable resource sharing between ac systems, considering the fact that a specific system might be causing the disturbance itself or might be assisting in overcoming the disturbance caused by any other grid. Finally, a decentralized controller has been developed for the converters of MT-DCμGrids. The proposed controller, which belongs to the family of signal-injection based technique, provides plug-and-play capability for the converters in general-structure dc microgrids. The proposed strategy offers decentralized control of the converters and does not rely on prior information about the network parameters and topology. The drawbacks of the existing signal-injection based techniques have been addressed in the proposed strategy. To verify the effectiveness of all developed controllers, several test systems and many case studies have been conducted. The verification was done based on modal analysis, time-domain simulations, as well as OPAL-RT based real-time implementations of the proposed controllers. Comparative analysis with recent similar control approaches has demonstrated the advantage of the proposed controllers for facilitating the formation of dc systems for a variety of applications.

7.2 Research outcome

The following papers have been published as an outcome of the research presented in this thesis.

- A. Kirakosyan, E. F. El-Saadany, M. S. El Moursi and M. Salama, (2020) "Selective Frequency Support Approach for MTDC Systems Integrating Wind Generation," in IEEE Transactions on Power Systems, doi: 10.1109/TPWRS.2020.3006832.
- A. Kirakosyan, E. F. El-Saadany, M. S. E. Moursi, A. H. Yazdavar and A. Al-Durra, (2020) "Communication-Free Current Sharing Control Strategy for DC Microgrids and Its Application for AC/DC Hybrid Microgrids," in IEEE Transactions on Power Systems, vol. 35, no. 1, pp. 140-151.
- A. Kirakosyan, E. F. El-Saadany, M. S. E. Moursi, S. Acharya and K. A. Hosani, (2018) "Control Approach for the Multi-Terminal HVDC System for the Accurate Power Sharing" in IEEE Transactions on Power Systems, vol. 33, no. 4, pp. 4323-4334.
- A. Kirakosyan, E. F. El-Saadany, M. S. E. Moursi and K. Al Hosani, (2018) "DC Voltage Regulation and Frequency Support in Pilot Voltage Droop-Controlled Multiterminal HVdc Systems" in IEEE Transactions on Power Delivery, vol. 33, no. 3, pp. 1153-1164.
- A. Kirakosyan, E. F. El-Saadany, M. S. E. Moursi, M. Salama, (2020) âĂIJDecentralized current sharing in dc microgrids considering normal and disturbed operation modesâĂİ in International Conference on Renewable Energies and Power Quality (ICREPQ'20), Granada, Spain. Paper ID: 378-20-kirakosyan.

- A. Kirakosyan, E. F. El-Saadany, M. S. E. Moursi, A. Yazdavar and M. Salama, (2020) âĂIJSharing of the loading of asynchronous ac microgrids connected through dc microgridsâĂİ Accepted in IEEE PES General Meeting, Montreal, Quebec, Canada. Submission ID 20PESGM1101.
- A.Kirakosyan, E. F. El-Saadany, M. S. E. Moursi, M. Salama, (2019) âĂIJAverage voltage regulation in droop-controlled MTDC gridsâĂİ IEEE Electrical Power and Energy Conference (EPEC). Paper 1570557740.
- A. Kirakosyan, E. F. El-Saadany and M. S. El-Moursi, (2018) "Simultaneous voltage regulation and power sharing control algorithm for MTDC grids," IEEE Electrical Power and Energy Conference (EPEC), pp. 1-6.

7.3 Future work

To further promote the development of dc grids with an aim of enhancing the performance of power systems in general, several research topics are suggested below. The authors believe that these studies and research directions can help to improve the content of the current thesis and constitute new research directions.

- The cyber security of the proposed communication-based approaches for MT-HVDC applications will be investigated in the future research. Specifically, state-estimation based techniques needs to be developed to determine the communicated signals that have been altered by attackers and to modify the control structure to overcome the detrimental effect of such attacks.
- The interaction between the turbines of the wind power plant should be investigated during the period when those generating units participate into the frequency regulation of the main ac system. The dynamic interactions of the turbines with other turbines and with other components of the wind farm need to be investigated.
- New control strategy should be designed for the converters of wind turbines for extracting maximum power from those units during normal operation and avoiding second frequency deep when the turbines participate into frequency regulation.
- Economic aspect should be considered for developing controllers for sharing the frequency support reserves between ac systems. Specifically, the systems that produce less-expensive power could be set to participate more in the mutual frequency support.

- The selection and placement of dc choppers in MT-HVDC systems should be conducted. The coordinated operation of dc choppers installed in dc grids should be organized for avoiding overvoltages and ensuring continuous system operation. Detailed investigation of the Fault Ride Through capabilities of MT-HVDC systems is then to be conducted.
- The benefits of integration of storage systems into dc grids should be analyzed. Respective control strategies should be developed for providing frequency support from those storage units to the neighboring ac systems. Comparative technical and economic analysis should be conducted to compare operation of storage devices with alternative technologies, e.g., with the deloaded operation of wind turbines.
- The considered MT-HVDC systems were based on paralleled VSCs. The operation of possible MT-HVDC configuration, in which some of the paralleled converters are of LCC type, should be investigated. The latter converters are expected to operate in a unidirectional power flow mode, and thus the voltage regulation and frequency support through those LCCs should be researched.
- In the light of the proposed signal-injection based technique for MT-DCμGrids, consideration should be given to the system operation in case of multi-microgrid system including both ac and dc grids. Detailed investigation of the ac system dynamics and their affect on the proposed signal-injection based strategy should be analyzed. Appropriate methods should be developed for clustering those microgrids and enhancing load-sharing in the subgrid level.

References

[1] "Access to energy," 2019 (accessed June 15, 2020). [Online]. Available: https://ourworldindata.org/energy-access

[2] "The strategic importance of electrification," 2020 (accessed June 15, 2020). [Online]. Available: https://www.iec.ch/smartenergy/importance/

[3] "Electrification," 2020 (accessed June 15, 2020). [Online]. Available: https://www.britannica.com/art/stagecraft/Electrification

[4] "History of electricity," 2020 (accessed June 11, 2020). [Online]. Available: https://www.instituteforenergyresearch.org/history-electricity/

[5] "The war of the currents: Ac vs. dc power," 2014 (accessed June 11, 2020). [Online]. Available: https://www.energy.gov/articles/war-currents-ac-vs-dc-power

[6] "Chicago's world's fair 1893," 2019 (accessed July 7, 2020). [Online]. Available: http://projects.leadr.msu.edu/makingmodernus/exhibits/show/electrifying-america/chicago-s-world-s-fair-1893

[7] "The gotland hvdc link," 2020 (accessed June 11, 2020). [Online]. Available: https://new.abb.com/systems/hvdc/references/the-gotland-hvdc-link

[8] J. Arrillaga, *High voltage direct current transmission.* Iet, 1998, no. 29.

[9] M. A. Hannan, I. Hussin, P. J. Ker, M. M. Hoque, M. S. Hossain Lipu, A. Hussain, M. S. A. Rahman, C. W. M. Faizal, and F. Blaabjerg, "Advanced control strategies of vsc based hvdc transmission system: Issues and potential recommendations," *IEEE Access*, vol. 6, pp. 78 352–78 369, 2018.

[10] "Making light of hvdc transmission in gotland," (accessed July 12, 2020). [Online]. Available: https://www.nsenergybusiness.com/features/featuremaking-light-of-hvdc-transmission-in-gotland/

[11] T. K. Vrana and S. Energi, "Review of hvdc component ratings: Xlpe cables and vsc converters," in *2016 IEEE International Energy Conference (ENERGYCON)*, 2016, pp. 1–6.

[12] G. Bathurst and P. Bordignan, “Delivery of the nan’ao multi-terminal vsc-hvdc system,” in *11th IET Int. Conf. on AC and DC Power Trans.*, Feb 2015, pp. 1–6.

[13] G. Tang, Z. He, H. Pang, X. Huang, and X. p. Zhang, “Basic topology and key devices of the five-terminal dc grid,” *CSEE Jour. of Pow. and En. Sys.*, vol. 1, no. 2, pp. 22–35, June 2015.

[14] “The worlds first dc-grid with hvdc light technology,” 2019 (accessed November 21, 2019). [Online]. Available: https://new.abb.com/systems/hvdc/references/zhangbei

[15] “National offshore wind energy grid interconnection studyexecutive summary,” 2014 (accessed October 4, 2019). [Online]. Available: https://www.energy.gov

[16] S. K. Chaudhary, R. Teodorescu, and P. Rodriguez, “Wind farm grid integration using vsc based hvdc transmission-an overview,” in *Energy 2030 Conference, 2008. ENERGY 2008. IEEE.* IEEE, 2008, pp. 1–7.

[17] E. Bompard, G. Fulli, M. Ardelean, and M. Masera, “It’s a bird, it’s a plane, it’s a...supergrid: Evolution, opportunities, and critical issues for pan-european transmission,” *IEEE Power and Energy Magazine*, vol. 12, no. 2, pp. 40–50, March 2014.

[18] “National offshore wind energy grid interconnection studyexecutive summary,” 2020 (accessed March 24, 2019). [Online]. Available: https://energyfutureslab.blog/2015/08/07/what-will-european-electricity-look-like-in-2050-changes-in-2050-electricity-use/

[19] F. Gao, S. Bozhko, A. Costabeber, C. Patel, P. Wheeler, C. I. Hill, and G. Asher, “Comparative stability analysis of droop control approaches in voltage-source-converter-based dc microgrids,” *IEEE Trans. on Power Electronics*, vol. 32, no. 3, pp. 2395–2415, 2017.

[20] “Philips shines light on opening of the office of the future âĂŞ the edge in amsterdam,” 2015 (accessed March 29, 2020). [Online]. Available: https://www.philips.com/aw/about/news/archive/standard/news/press/2015/20150625-Philips-shines-light-on-opening-of-the-office-of-the-future-the-Edge-in-Amsterdam.html

[21] F. Zhang, C. Meng, Y. Yang, C. Sun, C. Ji, Y. Chen, W. Wei, H. Qiu, and G. Yang, “Advantages and challenges of dc microgrid for commercial building a case study from xiamen university dc microgrid,” in *2015 IEEE First International Conference on DC Microgrids (ICDCM)*, 2015, pp. 355–358.

[22] "Dc microgrids in buildings," 2019 (accessed June 9, 2020). [Online]. Available: https://www.csagroup.org/wp-content/uploads/CSA-Group-Research-DC-Microgrids-In-Buildings.pdf

[23] "The sendai microgrid," 2019 (accessed June 9, 2020). [Online]. Available: https://building-microgrid.lbl.gov/sendai-microgrid

[24] "State of the art in microgrid technology," 2020 (accessed June 9, 2020). [Online]. Available: https://www.ufjf.br/cobep2017/files/2017/08/Guerrero-AAU-PRESENTATION.pdf

[25] "Growing dc power," 2015 (accessed July 3, 2020). [Online]. Available: https://www.tdworld.com/grid-innovations/smart-grid/article/20965099/growing-dc-power

[26] N. R. Chaudhuri, R. Majumder, and B. Chaudhuri, "System frequency support through multi-terminal dc (mtdc) grids," *IEEE Trans. Power Syst.*, vol. 28, pp. 347–356, Feb 2013.

[27] S. G. Vennelaganti and N. R. Chaudhuri, "Ratio-based selective inertial and primary frequency support through mtdc grids with offshore wind farms," *IEEE Trans. on Power Syst.*, vol. 33, no. 6, Nov 2018.

[28] H. Ye, W. Pei, L. Kong, and T. An, "Low-order response modeling for wind farm-mtdc participating in primary frequency controls," *IEEE Trans. on Power Syst.*, vol. 34, no. 2, pp. 942–952, March 2019.

[29] A. Junyent-Ferr, Y. Pipelzadeh, and T. C. Green, "Blending hvdc-link energy storage and offshore wind turbine inertia for fast frequency response," *IEEE Trans. on Sustain. Energy*, vol. 6, no. 3, pp. 1059–1066, July 2015.

[30] N. R. Chaudhuri, R. Majumder, B. Chaudhuri, J. Pan, and R. Nuqui, "Modeling and stability analysis of mtdc grids for offshore wind farms: A case study on the north sea benchmark system," in *2011 IEEE Power and Energy Society General Meeting*, July 2011, pp. 1–7.

[31] J. Renedo, A. G. Cerrada, and L. Rouco, "Active power control strategies for transient stability enhancement of ac/dc grids with vsc-hvdc multi-terminal systems," *IEEE Trans. Power Syst.*, vol. 31, no. 6, pp. 4595–4604, Nov 2016.

[32] N. R. Chaudhuri, R. Majumder, B. Chaudhuri, and J. Pan, "Stability analysis of vsc mtdc grids connected to multimachine ac systems," *IEEE Trans. on Power Del.*, vol. 26, no. 4, pp. 2774–2784, 2011.

[33] E. Prieto-Araujo, A. Egea-Alvarez, S. Fekriasl, and O. Gomis-Bellmunt, "Dc voltage droop control design for multiterminal hvdc systems considering ac and dc grid dynamics," *IEEE Trans. Power Del.*, vol. 31, no. 2, pp. 575–585, April 2016.

[34] H. Awad, J. Svensson, and M. J. Bollen, "Tuning software phase-locked loop for series-connected converters," *IEEE Trans. Power Del.*, vol. 20, no. 1, pp. 300–308, Jan 2005.

[35] Y. Xia, S. C. Douglas, and D. P. Mandic, "Adaptive frequency estimation in smart grid applications: Exploiting noncircularity and widely linear adaptive estimators," *IEEE Signal Process. Mag.*, vol. 29, no. 5, pp. 44–54, Sept 2012.

[36] J. Beerten, S. Cole, and R. Belmans, "Modeling of multi-terminal vsc hvdc systems with distributed dc voltage control," *IEEE Trans. Power Sys.*, vol. 29, no. 1, pp. 34–42, Jan 2014.

[37] P. Kanjiya, V. Khadkikar, and M. S. E. Moursi, "A novel type-1 frequency-locked loop for fast detection of frequency and phase with improved stability margins," *IEEE Tran. Power Electron.*, vol. 31, no. 3, pp. 2550–2561, March 2016.

[38] S. Golestan, M. Monfared, and F. D. Freijedo, "Design-oriented study of advanced synchronous reference frame phase-locked loops," *IEEE Trans. Power Electron.*, no. 2, Feb 2013.

[39] H. Karimi, M. Karimi-Ghartemani, and M. R. Iravani, "Estimation of frequency and its rate of change for applications in power systems," *IEEE Trans. Power Del.*, vol. 19, no. 2, pp. 472–480, April 2004.

[40] M. Mojiri, M. Karimi-Ghartemani, and A. Bakhshai, "Estimation of power system frequency using an adaptive notch filter," *IEEE Trans. Instrum. Meas.*, vol. 56, no. 6, pp. 2470–2477, Dec 2007.

[41] O. Venjakob, S. Kubera, R. Hibberts-Caswell, P. Forsyth, and T. Maguire, "Setup and performance of the real-time simulator used for hardware-in-loop-tests of a vsc-based hvdc scheme for offshore applications," in *Proc. Int. Conf. Power Syst. Trans.*, 2013, pp. 18–20.

[42] W. Li and J. BÃĺlanger, "An equivalent circuit method for modelling and simulation of modular multilevel converters in real-time hil test bench," *IEEE Trans. on Power Del.*, vol. 31, no. 5, pp. 2401–2409, Oct 2016.

[43] G. P. Adam and B. W. Williams, “Half- and full-bridge modular multilevel converter models for simulations of full-scale hvdc links and multiterminal dc grids,” *IEEE J. Emerg. Sel. Topics Power Electron.*, vol. 2, no. 4, pp. 1089–1108, Dec 2014.

[44] “Half-bridge mmc,” 2020 (accessed June 15, 2020). [Online]. Available: https://www.mathworks.com/help/physmod/sps/powersys/ref/halfbridgemmc.html

[45] P. Kundur, N. J. Balu, and M. G. Lauby, *Power system stability and control.* McGraw-hill New York, 1994, vol. 7.

[46] P. Pourbeik *et al.*, “Dynamic models for turbine-governors in power system studies,” *IEEE Task Force on Turbine-Governor Modeling*, no. 2013, 2013.

[47] M. Kang, K. Kim, E. Muljadi, J. Park, and Y. C. Kang, “Frequency control support of a doubly-fed induction generator based on the torque limit,” *IEEE Trans. Power Syst.*, vol. 31, no. 6, pp. 4575–4583, Nov 2016.

[48] “Gmb dynamic models for pss software product suite,” 2012 (accessed December 24, 2019). [Online]. Available: https://new.siemens.com

[49] W. G. on Prime Mover and E. S. M. for System Dynamic Performance Studies, “Hydraulic turbine and turbine control models for system dynamic studies,” *IEEE Trans. Power Syst.*, vol. 7, no. 1, pp. 167–179, Feb 1992.

[50] “Hydraulic turbine and governor,” 2016 (accessed August 25, 2020). [Online]. Available: https://www.mathworks.com/help/physmod/sps/powersys/ref/hydraulicturbineandgovernor.html

[51] S. K. Kim, E. S. Kim, J. Y. Yoon, and H. Y. Kim, “Pscad/emtdc based modeling of a wind energy conversion scheme for grid-connection,” *IFAC Proceedings Volumes*, vol. 36, no. 20, pp. 647–651, 2003.

[52] A. B. T. Attya and J. L. Dominguez-GarcÃŋa, “Insights on the provision of frequency support by wind power and the impact on energy systems,” *IEEE Trans. Sustain. Energy*, vol. 9, no. 2, pp. 719–728, April 2018.

[53] F. Díaz-González, M. Hau, A. Sumper, and O. Gomis-Bellmunt, “Participation of wind power plants in system frequency control: Review of grid code requirements and control methods,” *Renewable and Sustainable Energy Reviews*, vol. 34, pp. 551–564, 2014.

[54] K. V. Vidyanandan and N. Senroy, "Primary frequency regulation by deloaded wind turbines using variable droop," *IEEE Trans. on Power Syst.*, vol. 28, no. 2, pp. 837–846, May 2013.

[55] E. Robles, M. Haro-Larrode, M. Santos-Mugica, A. Etxegarai, and E. Tedeschi, "Comparative analysis of european grid codes relevant to offshore renewable energy installations," *Renewable and Sustainable Energy Reviews*, vol. 102, pp. 171–185, 2019.

[56] E. Nycander and L. Söder, "Review of european grid codes for wind farms and their implications for wind power curtailments," in *17th International Wind Integration Workshop Stockholm, Sweden| 17–19 October 2018*, 2018.

[57] "Parameters related to frequency stability: Entso-e guidance document for national implementation for network codes on grid connection," (accessed December 21, 2019). [Online]. Available: https://eepublicdownloads.blob.core.windows.net

[58] B. Mohandes, M. S. E. Moursi, N. Hatziargyriou, and S. E. Khatib, "A review of power system flexibility with high penetration of renewables," *IEEE Trans. on Power Syst.*, vol. 34, no. 4, pp. 3140–3155, 2019.

[59] Q. Xu, X. Hu, P. Wang, J. Xiao, P. Tu, C. Wen, and M. Y. Lee, "A decentralized dynamic power sharing strategy for hybrid energy storage system in autonomous dc microgrid," *IEEE Trans. on Industrial Electron.*, vol. 64, no. 7, pp. 5930–5941, July 2017.

[60] A. Bamigbade, V. M. Khadkikar, and M. Al Hosani, "Single-phase type-1 frequency-fixed fll for distorted voltage condition," *IEEE Trans. on Industrial Electron.*, pp. 1–1, 2020.

[61] S. M. Silva, B. M. Lopes, B. J. C. Filho, R. P. Campana, and W. C. Bosventura, "Performance evaluation of pll algorithms for single-phase grid-connected systems," in *Conference Record of the 2004 IEEE Industry Applications Conference, 2004. 39th IAS Annual Meeting.*, vol. 4, 2004, pp. 2259–2263 vol.4.

[62] "Linearizing models," (accessed June 9, 2020). [Online]. Available: https://www.mathworks.com/help/simulink/ug/linearizing-models.html

[63] P. W. Sauer and M. A. Pai, *Power system dynamics and stability.* Prentice hall Upper Saddle River, NJ, 1998, vol. 101.

[64] B. Pal and B. Chaudhuri, *Robust control in power systems.* Springer Science & Business Media, 2006.

[65] G. Li, Z. Du, C. Shen, Z. Yuan, and G. Wu, "Coordinated design of droop control in mtdc grid based on model predictive control," *IEEE Trans. on Power Syst.*, vol. 33, no. 3, pp. 2816–2828, May 2018.

[66] G. O. Kalcon, G. P. Adam, O. Anaya-Lara, S. Lo, and K. Uhlen, "Small-signal stability analysis of multi-terminal vsc-based dc transmission systems," *IEEE Trans. Power Syst.*, vol. 27, pp. 1818–1830, Nov 2012.

[67] J. Lei, T. An, Z. Du, and Z. Yuan, "A general unified ac dc power flow algorithm with mtdc," *IEEE Trans. Power Sys.*, vol. 32, no. 4, pp. 2837–2846, July 2017.

[68] S. Peng, J. Tang, and W. Li, "Probabilistic power flow for ac vsc-mtdc hybrid grids considering rank correlation among diverse uncertainty sources," *IEEE Trans. Power Sys.*, vol. 32, no. 5, Sept 2017.

[69] K. Meng, W. Zhang, y. li, Z. Y. Dong, Z. Xu, K. P. Wong, and Y. Zheng, "Hierarchical scopf considering wind energy integration through multi-terminal vsc-hvdc grids," *IEEE Trans. Power Sys.*, vol. PP, no. 99, pp. 1–1, 2017.

[70] J. Cao, W. Du, and H. F. Wang, "An improved corrective security constrained opf for meshed ac/dc grids with multi-terminal vsc-hvdc," *IEEE Trans. Power Sys.*, vol. 31, no. 1, pp. 485–495, Jan 2016.

[71] A. Raza, Y. Liu, K. Rouzbehi, M. Jamil, S. O. Gilani, X. Dianguo, and B. W. Williams, "Power dispatch and voltage control in multiterminal hvdc systems: A flexible approach," *IEEE Access*, vol. 5, pp. 24 608–24 616, 2017.

[72] W. Sanusi, M. A. Hosani, and M. E. Moursi, "A novel dc fault ride-through scheme for mtdc networks connecting large-scale wind parks," *IEEE Trans. Sustain. Energy*, vol. PP, no. 99, pp. 1–1, 2017.

[73] R. Li, L. Xu, L. Yao, and B. W. Williams, "Active control of dc fault currents in dc solid-state transformers during ride-through operation of multi-terminal hvdc systems," *IEEE Trans. on Energy Conv.*, vol. 31, no. 4, pp. 1336–1346, Dec 2016.

[74] B. Silva, C. L. Moreira, H. Leite, and J. A. P. Lopes, "Control strategies for ac fault ride through in multiterminal hvdc grids," *IEEE Trans. Power Del.*, vol. 29, no. 1, pp. 395–405, Feb 2014.

[75] J. Renedo, A. GarcÃŋa-Cerrada, and L. Rouco, "Reactive-power coordination in vsc-hvdc multi-terminal systems for transient stability improvement," *IEEE Trans. Power Sys.*, vol. 32, no. 5, pp. 3758–3767, Sept 2017.

[76] G. Tang, Z. Xu, H. Dong, and Q. Xu, "Sliding mode robust control based active-power modulation of multi-terminal hvdc transmissions," *IEEE Trans. Power Sys.*, vol. 31, no. 2, pp. 1614–1623, March 2016.

[77] L. Harnefors, N. Johansson, L. Zhang, and B. Berggren, "Interarea oscillation damping using active-power modulation of multiterminal hvdc transmissions," *IEEE Trans. Power Sys.*, vol. 29, no. 5, pp. 2529–2538, Sept 2014.

[78] Y. Liu, A. Raza, K. Rouzbehi, B. Li, D. Xu, and B. W. Williams, "Dynamic resonance analysis and oscillation damping of multiterminal dc grids," *IEEE Access*, vol. 5, pp. 16 974–16 984, 2017.

[79] F. D. Bianchi and J. L. Domnguez-Garca, "Coordinated frequency control using mt-hvdc grids with wind power plants," *IEEE Trans. Sustain. Energy*, vol. 7, no. 1, pp. 213–220, Jan 2016.

[80] F. Longatt and J. Roldan, "Effects of dc voltage control strategy on voltage response on multi-terminal hvdc following loss of a converter station," in *2013 IEEE PES Gen. Meet.*, July 2013, pp. 1–5.

[81] E. Prieto-Araujo, F. D. Bianchi, A. Junyent-Ferre, and O. Gomis-Bellmunt, "Methodology for droop control dynamic analysis of multiterminal vsc-hvdc grids for offshore wind farms," *IEEE Trans. Power Del.*, vol. 26, no. 4, pp. 2476–2485, Oct 2011.

[82] K. Rouzbehi, J. I. Candela, A. Luna, G. B. Gharehpetian, and P. Rodriguez, "Flexible control of power flow in multiterminal dc grids using dc x2013;dc converter," *IEEE J. Emerg. Sel. Topics Power Electron.*, vol. 4, no. 3, pp. 1135–1144, Sept 2016.

[83] K. Rouzbehi, A. Miranian, A. Luna, and P. Rodriguez, "Dc voltage control and power sharing in multiterminal dc grids based on optimal dc power flow and voltage-droop strategy," *IEEE Jour. of Emerg. and Sel. Top. in Power Electron.*, vol. 2, no. 4, pp. 1171–1180, Dec 2014.

[84] K. Rouzbehi, W. Zhang, J. I. Candela, A. Luna, and P. Rodriguez, "Unified reference controller for flexible primary control and inertia sharing in multi-terminal voltage source converter-hvdc grids," *IET Gen., Trans. Distribution*, vol. 11, no. 3, pp. 750–758, 2017.

[85] A. E. Leon, “Short-term frequency regulation and inertia emulation using an mmc-based mtdc system,” *IEEE Trans. Power Sys.*, vol. PP, no. 99, pp. 1–1, 2017.

[86] J. N. Sakamuri, M. Altin, A. D. Hansen, and N. A. Cutululis, “Coordinated frequency control from offshore wind power plants connected to multi terminal dc system considering wind speed variation,” *IET Renewable Power Generation*, vol. 11, no. 8, pp. 1226–1236, 2017.

[87] J. N. Sakamuri, M. Altin, A. D. Hansen, N. A. Cutululis, and Z. H. Rather, “Coordinated control scheme for ancillary services from offshore wind power plants to ac and dc grids,” in *2016 IEEE Power and Energy Soc. Gen. Meeting (PESGM)*, July 2016, pp. 1–5.

[88] O. D. Adeuyi, M. Cheah-Mane, J. Liang, and N. Jenkins, “Fast frequency response from offshore multi-terminal vsc-hvdc schemes,” *IEEE Trans. Power Del.*, vol. PP, no. 99, pp. 1–1, 2017.

[89] F. Teng and G. Strbac, “Assessment of the role and value of frequency response support from wind plants,” *IEEE Trans. Sustain. Energy,*, vol. 7, no. 2, pp. 586–595, April 2016.

[90] J. Rafferty, L. Xu, Y. Wang, G. Xu, and F. Alsokhiry, “Frequency support using multi-terminal hvdc systems based on dc voltage manipulation,” *IET Ren. Power Gen.*, vol. 10, no. 9, pp. 1393–1401, 2016.

[91] L. Xu and L. Yao, “Dc voltage control and power dispatch of a multi-terminal hvdc system for integrating large offshore wind farms,” *IET Renewable Power Generation*, vol. 5, no. 3, pp. 223–233, May 2011.

[92] T. M. L. Assis, S. Kuenzel, and B. C. Pal, “Impact of multi-terminal hvdc grids on enhancing dynamic power transfer capability,” *IEEE Trans. Power Sys.*, vol. 32, no. 4, pp. 2652–2662, July 2017.

[93] L. Papangelis, M. S. Debry, P. Panciatici, and T. V. Cutsem, “Coordinated supervisory control of multi-terminal hvdc grids: A model predictive control approach,” *IEEE Trans. on Power Syst.*, vol. 32, no. 6, pp. 4673–4683, Nov 2017.

[94] K. Rouzbehi, A. Miranian, J. I. Candela, A. Luna, and P. Rodriguez, “A generalized voltage droop strategy for control of multiterminal dc grids,” *IEEE Trans. Ind. Appl.*, vol. 51, no. 1, pp. 607–618, Jan 2015.

[95] C. Gavriluta, I. Candela, A. Luna, A. Gomez-Exposito, and P. Rodriguez, “Hierarchical control of hv-mtdc systems with droop-based primary and opf-based secondary,” *IEEE Trans. Smart Grid*, vol. 6, no. 3, pp. 1502–1510, May 2015.

[96] T. M. Haileselassie and K. Uhlen, “Primary frequency control of remote grids connected by multi-terminal hvdc,” in *IEEE PES Gen. Meet.*, July 2010, pp. 1–6.

[97] W. Wang, Y. Li, Y. Cao, U. Haeger, and C. Rehtanz, “Adaptive droop control of mtdc system for frequency support and power sharing,” *IEEE Trans. Power Sys.*, vol. PP, no. 99, pp. 1–1, 2017.

[98] R. Eriksson, J. Beerten, M. Ghandhari, and R. Belmans, “Optimizing dc voltage droop settings for ac/dc system interactions,” *IEEE Trans. Power Del.*, vol. 29, no. 1, pp. 362–369, Feb 2014.

[99] X. Zhao and K. Li, “Droop setting design for multi terminal hvdc grids considering voltage deviation impacts,” *Elec. Pow. Sys. Research*, vol. 123, pp. 67–75, 2015.

[100] J. Beerten and R. Belmans, “Analysis of power sharing and voltage deviations in droop-controlled dc grids,” *IEEE Trans. Power Syst.*, vol. 28, no. 4, pp. 4588–4597, Nov 2013.

[101] B. Berggren, K. LindÃl’n, and R. Majumder, “Dc grid control through the pilot voltage droop concept 2014 methodology for establishing droop constants,” *IEEE Trans. Power Syst.*, vol. 30, pp. 2312–2320, Sept 2015.

[102] B. Berggren, R. Majumder, and K. LindÃl’n, “Dc grid control through the pilot voltage droop concept: Mitigating consequences of time delays,” in *2015 IEEE 5th Int. Conf. POWERENG*, May 2015, pp. 134–141.

[103] Y. Wang, W. Wen, C. Wang, H. Liu, X. Zhan, and X. Xiao, “Adaptive voltage droop method of multiterminal vsc-hvdc systems for dc voltage deviation and power sharing,” *IEEE Trans. on Power Del.*, vol. 34, no. 1, pp. 169–176, Feb 2019.

[104] N. R. Chaudhuri and B. Chaudhuri, “Adaptive droop control for effective power sharing in multi-terminal dc (mtdc) grids,” *IEEE Trans. Power Syst.*, vol. 28, no. 1, pp. 21–29, Feb 2013.

[105] P. Rault, J. Freytes, X. Guillaud, F. Colas, H. Saad, O. Despouys, and S. Nguefeu, “Coordinated control for multi terminal dc grids connected to offshore wind farms,” in *2016 IEEE 17th Workshop on Control and Modeling for Power Electronics (COMPEL)*, June 2016, pp. 1–8.

[106] J. Beerten, R. Eriksson, and D. V. Hertem, “A new approach to hvdc grid voltage control based on generalized state feedback,” in *2014 IEEE PES Gen. Meet.*, July 2014, pp. 1–5.

[107] R. Teixeira Pinto, P. Bauer, S. F. Rodrigues, E. J. Wiggelinkhuizen, J. Pierik, and B. Ferreira, “A novel distributed direct-voltage control strategy for grid integration of offshore wind energy systems through mtdc network,” *IEEE Trans. on Industrial Electron.*, vol. 60, no. 6, pp. 2429–2441, June 2013.

[108] M. A. Abdelwahed and E. F. El-Saadany, “Power sharing control strategy of multiterminal vsc-hvdc transmission systems utilizing adaptive voltage droop,” *IEEE Tran. Sustain Energy*, vol. 8, no. 2, pp. 605–615, April 2017.

[109] L. Xu, L. Yao, and M. Bazargan, “Dc grid management of a multi-terminal hvdc transmission system for large offshore wind farms,” in *2009 International Conference on Sustainable Power Generation and Supply*, April 2009, pp. 1–7.

[110] L. Xu, B. W. Williams, and L. Yao, “Multi-terminal dc transmission systems for connecting large offshore wind farms,” in *2008 IEEE Power and Energy Society General Meeting - Conversion and Delivery of Electrical Energy in the 21st Century*, July 2008, pp. 1–7.

[111] J. Liang, O. Gomis-Bellmunt, J. Ekanayake, and N. Jenkins, “Control of multiterminal vsc-hvdc transmission for offshore wind power,” in *2009 13th European Conference on Power Electronics and Applications.* IEEE, 2009, pp. 1–10.

[112] J. He and Y. W. Li, “Analysis, design, and implementation of virtual impedance for power electronics interfaced distributed generation,” *IEEE Trans. on Industry Applications*, vol. 47, no. 6, pp. 2525–2538, Nov 2011.

[113] B. Berggren, R. Majumder, S. Charles, and K. Linden, “Method and control device for controlling power flow within a dc power transmission network,” Oct. 2013, uS Patent 8,553,437.

[114] A. Sarlette, J. Dai, Y. Phulpin, and D. Ernst, “Cooperative frequency control with a multi-terminal high-voltage dc network,” *Automatica*, vol. 48, no. 12, pp. 3128–3134, 2012.

[115] I. MartÃŋnez Sanz, B. Chaudhuri, and G. Strbac, “Inertial response from offshore wind farms connected through dc grids,” *IEEE Trans. on Power Syst.*, vol. 30, no. 3, pp. 1518–1527, May 2015.

[116] G. L. Yu, B. H. Zhang, H. Xie, and C. G. Wang, "Wide-area measurement-based non-linear robust control of power system considering signals' delay and incompleteness," in *2007 IEEE Power Eng. Soc. Gen. Meet.*, June 2007, pp. 1–8.

[117] Y. Pipelzadeh, B. Chaudhuri, and T. C. Green, "Inertial response from remote offshore wind farms connected through vsc-hvdc links: A communication-less scheme," in *2012 IEEE Power and Energy Society General Meeting*, July 2012, pp. 1–6.

[118] J. H. Eto, "Use of frequency response metrics to assess the planning and operating requirements for reliable integration of variable renewable generation," 2011.

[119] Y. Mu, J. Wu, J. Ekanayake, N. Jenkins, and H. Jia, "Primary frequency response from electric vehicles in the great britain power system," *IEEE Trans. on Smart Grid*, vol. 4, no. 2, pp. 1142–1150, June 2013.

[120] "Reliability guideline: North american electric reliability corporation," 2019 (accessed October 2, 2019). [Online]. Available: https://www.nerc.com

[121] Z. Lu, Y. Ye, and Y. Qiao, "An adaptive frequency regulation method with grid-friendly restoration for vsc-hvdc integrated offshore wind farms," *IEEE Trans. on Power Syst.*, pp. 1–1, 2019.

[122] S. I. Abouzeid, Y. Guo, H. Zhang, and X. Ma, "Improvements in primary frequency regulation of the grid-connected variable speed wind turbine," *IET Renewable Power Generation*, vol. 13, no. 3, pp. 491–499, 2019.

[123] A. Bucurenciu, M. Ndreko, M. Popov, and M. A. M. M. van der Meijden, "Frequency response using mtdc grids: A comparative study of common methods," in *2015 IEEE Eindhoven PowerTech*, June 2015, pp. 1–6.

[124] S. G. Vennelaganti and N. R. Chaudhuri, "Selective power routing in mtdc grids for inertial and primary frequency support," *IEEE Trans. on Power Syst.*, vol. 33, no. 6, pp. 7020–7030, Nov 2018.

[125] S. Akkari, J. Dai, M. Petit, and X. Guillaud, "Interaction between the voltage-droop and the frequency-droop control for multi-terminal hvdc systems," *IET Generation, Transmission Distribution*, vol. 10, no. 6, pp. 1345–1352, 2016.

[126] Y. Wen, J. Zhan, C. Y. Chung, and W. Li, "Frequency stability enhancement of integrated ac/vsc-mtdc systems with massive infeed of offshore wind generation," *IEEE Trans. Power Syst.*, vol. 33, no. 5, pp. 5135–5146, Sep. 2018.

[127] B. Silva, C. L. Moreira, L. Seca, Y. Phulpin, and J. A. Pecas Lopes, “Provision of inertial and primary frequency control services using offshore multiterminal hvdc networks,” *IEEE Trans. on Sustain. Energy*, vol. 3, no. 4, pp. 800–808, Oct 2012.

[128] I. Egido, F. Fernandez-Bernal, P. Centeno, and L. Rouco, “Maximum frequency deviation calculation in small isolated power systems,” *IEEE Trans. Power Syst.*, vol. 24, no. 4, pp. 1731–1738, Nov 2009.

[129] I. M. Sanz, B. Chaudhuri, and G. Strbac, “Frequency changes in ac systems connected to dc grids: Impact of ac vs. dc side events,” in *2014 IEEE PES Gen. Meeting*, July 2014, pp. 1–5.

[130] A. Ulbig, T. S. Borsche, and G. Andersson, “Impact of low rotational inertia on power system stability and operation,” *IFAC Proc. Vol.*, vol. 47, no. 3, pp. 7290–7297, 2014.

[131] R. Wang, L. Chen, T. Zheng, and S. Mei, “Vsg-based adaptive droop control for frequency and active power regulation in the mtdc system,” *CSEE Journal of Power and Energy Systems*, vol. 3, no. 3, pp. 260–268, Sept 2017.

[132] S.-W. Lee and B.-H. Cho, “MasterâĂŞslave based hierarchical control for a small power dc-distributed microgrid system with a storage device,” *Energies*, vol. 9, p. 880, 10 2016.

[133] L. Guo, Y. Feng, X. Li, C. Wang, and Y. Li, “Stability analysis of a dc microgrid with master-slave control structure,” in *2014 IEEE Energy Conversion Congress and Exposition (ECCE)*, 2014, pp. 5682–5689.

[134] P. H. Huang, P. C. Liu, W. Xiao, and M. S. E. Moursi, “A novel droop-based average voltage sharing control strategy for dc microgrids,” *IEEE Tran. Smart Grid*, vol. 6, no. 3, pp. 1096–1106, May 2015.

[135] B. Wang, M. Sechilariu, and F. Locment, “Intelligent dc microgrid with smart grid communications: Control strategy consideration and design,” *IEEE Tran. Smart Grid*, vol. 3, no. 4, pp. 2148–2156, Dec 2012.

[136] Y. Ito, Y. Zhongqing, and H. Akagi, “Dc microgrid based distribution power generation system,” in *IPEMC 2004.*, vol. 3, Aug 2004, pp. 1740–1745 Vol.3.

[137] D. Chen, L. Xu, and L. Yao, “Dc voltage variation based autonomous control of dc microgrids,” *IEEE Tran. Power Del.*, vol. 28, no. 2, pp. 637–648, April 2013.

[138] P. Wang, X. Lu, X. Yang, W. Wang, and D. Xu, "An improved distributed secondary control method for dc microgrids with enhanced dynamic current sharing performance," *IEEE Tran. Power Electron.*, vol. 31, no. 9, pp. 6658–6673, Sept 2016.

[139] J. M. Guerrero, J. C. Vasquez, J. Matas, L. G. de Vicuna, and M. Castilla, "Hierarchical control of droop-controlled ac and dc microgrids x2014;a general approach toward standardization," *IEEE Trans. on Industrial Electron.*, vol. 58, no. 1, pp. 158–172, Jan 2011.

[140] S. Anand, B. G. Fernandes, and J. Guerrero, "Distributed control to ensure proportional load sharing and improve voltage regulation in low-voltage dc microgrids," *IEEE Tran. Power Electron.*, vol. 28, no. 4, pp. 1900–1913, April 2013.

[141] X. Lu, J. M. Guerrero, K. Sun, and J. C. Vasquez, "An improved droop control method for dc microgrids based on low bandwidth communication with dc bus voltage restoration and enhanced current sharing accuracy," *IEEE Tran. Power Electron.*, vol. 29, no. 4, pp. 1800–1812, April 2014.

[142] S. Augustine, M. K. Mishra, and N. Lakshminarasamma, "Adaptive droop control strategy for load sharing and circulating current minimization in low-voltage standalone dc microgrid," *IEEE Tran. Sustain Energy*, vol. 6, no. 1, pp. 132–141, Jan 2015.

[143] V. Nasirian, S. Moayedi, A. Davoudi, and F. L. Lewis, "Distributed cooperative control of dc microgrids," *IEEE Tran. Power Electron.*, vol. 30, no. 4, pp. 2288–2303, April 2015.

[144] L. Yang, Y. Chen, A. Luo, W. Wu, K. Huai, X. Zhou, L. Zhou, Q. Xu, and J. M. Guerrero, "Second ripple current suppression by two bandpass filters and current sharing method for energy storage converters in dc microgrid," *IEEE Jour. of Emerg. and Select. Top. in Power Electron.*, vol. 5, no. 3, pp. 1031–1044, Sept 2017.

[145] V. Nasirian, A. Davoudi, F. L. Lewis, and J. M. Guerrero, "Distributed adaptive droop control for dc distribution systems," *IEEE Tran. Energy Conv.*, vol. 29, no. 4, pp. 944–956, Dec 2014.

[146] Q. C. Zhong, "Robust droop controller for accurate proportional load sharing among inverters operated in parallel," *IEEE Trans. Indust. Electron.*, vol. 60, no. 4, pp. 1281–1290, April 2013.

[147] A. Khorsandi, M. Ashourloo, H. Mokhtari, and R. Iravani, “Automatic droop control for a low voltage dc microgrid,” *IET Gen., Trans. Distrib.*, vol. 10, no. 1, pp. 41–47, 2016.

[148] A. Tah and D. Das, “An enhanced droop control method for accurate load sharing and voltage improvement of isolated and interconnected dc microgrids,” *IEEE Tran. Sustain Energy*, vol. 7, no. 3, pp. 1194–1204, July 2016.

[149] C. Liu, J. Zhao, S. Wang, W. Lu, and K. Qu, “Active identification method for line resistance in dc microgrid based on single pulse injection,” *IEEE Tran. Power Electron.*, vol. 33, no. 7, pp. 5561–5564, July 2018.

[150] J. Yang, X. Jin, X. Wu, P. Acuna, R. P. Aguilera, T. Morstyn, and V. G. Agelidis, “Decentralised control method for dc microgrids with improved current sharing accuracy,” *IET Generation, Transmission Distribution*, vol. 11, no. 3, pp. 696–706, 2017.

[151] A. Tuladhar and H. Jin, “A novel control technique to operate dc/dc converters in parallel with no control interconnections,” in *PESC 98 Record. 29th Annual IEEE Power Electronics Specialists Conference (Cat. No.98CH36196)*, vol. 1, May 1998, pp. 892–898 vol.1.

[152] S. Peyghami, P. Davari, H. Mokhtari, P. C. Loh, and F. Blaabjerg, “Synchronverter-enabled dc power sharing approach for lvdc microgrids,” *IEEE Tran. Power Electron.*, vol. 32, no. 10, pp. 8089–8099, Oct 2017.

[153] “Continuous monitoring of hvdc power cables with integrated fibre optic cables,” 2019 (accessed June 19, 2020). [Online]. Available: http://www.jicable.org/TOUT_JICABLE_FIRST_PAGE/2019/2019-A6-5_page1.pdf

[154] H. Wang, M. Han, R. Han, J. M. Guerrero, and J. C. Vasquez, “A decentralized current-sharing controller endows fast transient response to parallel dc 8211;dc converters,” *IEEE Tran. Power Electron.*, vol. 33, no. 5, pp. 4362–4372, May 2018.

[155] A. Kirakosyan, E. F. El-Saadany, M. S. E. Moursi, and K. A. Hosani, “Dc voltage regulation and frequency support in pilot voltage droop-controlled multiterminal hvdc systems,” *IEEE Trans. on Power Del.*, vol. 33, no. 3, pp. 1153–1164, June 2018.

[156] A. Kirakosyan, E. F. El-Saadany, M. S. E. Moursi, S. Acharya, and K. A. Hosani, “Control approach for the multi-terminal hvdc system for the accurate power sharing,” *IEEE Trans. Power Syst.*, vol. 33, no. 4, pp. 4323–4334, July 2018.

[157] M. Guan and Z. Xu, "Modeling and control of a modular multilevel converter-based hvdc system under unbalanced grid conditions," *IEEE Trans. Power Electron.*, vol. 27, no. 12, pp. 4858–4867, Dec 2012.

[158] M. Saeedifard and R. Iravani, "Dynamic performance of a modular multilevel back-to-back hvdc system," *IEEE Trans. Power Del.*, vol. 25, no. 4, pp. 2903–2912, Oct 2010.

[159] A. Raza, X. Dianguo, L. Yuchao, S. Xunwen, B. W. Williams, and C. Cecati, "Coordinated operation and control of vsc based multiterminal high voltage dc transmission systems," *IEEE Trans. Sustain. Energy*, vol. 7, no. 1, pp. 364–373, Jan 2016.

[160] A. A. van der Meer, M. Ndreko, M. Gibescu, and M. A. M. M. van der Meijden, "The effect of frt behavior of vsc-hvdc-connected offshore wind power plants on ac/dc system dynamics," *IEEE Trans. Power Del.*, vol. 31, no. 2, pp. 878–887, April 2016.

[161] "Vsc-based hvdc link," 2016 (accessed December 20, 2016). [Online]. Available: https://www.mathworks.com

[162] J. Beerten, G. B. Diaz, S. D'Arco, and J. A. Suul, "Comparison of small-signal dynamics in mmc and two-level vsc hvdc transmission schemes," in *2016 IEEE Int. Energy Conf. (ENERGYCON)*, April 2016, pp. 1–6.

[163] J. Zhu, C. D. Booth, G. P. Adam, and A. J. Roscoe, "Coordinated direct current matching control strategy for multi-terminal dc transmission systems with integrated wind farms," *Electric Power Systems Research*, vol. 124, pp. 55–64, 2015.

[164] "Cigre b4 working group," (accessed Sep. 3, 2017). [Online]. Available: http://b4.cigre.org/publications

[165] J.-N. Paquin, C. Dufour, and J. Bélanger, "A hardware-in-the-loop simulation platform for prototyping and testing of wind generator controllers," in *CIGRÉ Canada Conference on Power Syst. Winnipeg*, 2008.

[166] A. Ameli, A. Hooshyar, A. H. Yazdavar, E. F. El-Saadany, and A. Youssef, "Attack detection for load frequency control systems using stochastic unknown input estimators," *IEEE Trans. on Information Forensics and Security*, vol. 13, no. 10, pp. 2575–2590, Oct 2018.

[167] A. Kirakosyan, E. F. El-Saadany, M. S. El Moursi, and M. Salama, "Selective frequency support approach for mtdc systems integrating wind generation," *IEEE Trans. on Power Syst.*, pp. 1–1, 2020.

[168] "Entso frequency analysis," 2016 (accessed January 5, 2017). [Online]. Available: www.entsoe.eu/Documents/SOC20documents/RGCE_SPD_frequency_stability_criteria_v10.pdf

[169] "Rocof definitions," 2012 (accessed June 25, 2015). [Online]. Available: http://www.soni.ltd.uk

[170] "Fullfilement of grid code requirements in the area served by ucte by combined cycle power plants," 2016 (accessed November 30, 2016). [Online]. Available: http://www.energy.siemens.com

[171] J. Zhu, C. D. Booth, G. P. Adam, A. J. Roscoe, and C. G. Bright, "Inertia emulation control strategy for vsc-hvdc transmission systems," *IEEE Trans. Power Syst.*, vol. 28, no. 2, pp. 1277–1287, 2013.

[172] C. Gavriluta, J. I. Candela, C. Citro, J. Rocabert, A. Luna, and P. RodrÃŋguez, "Decentralized primary control of mtdc networks with energy storage and distributed generation," *IEEE Trans. Industry Applic.*, vol. 50, no. 6, pp. 4122–4131, 2014.

[173] A. Moeini and I. Kamwa, "Analytical concepts for reactive power based primary frequency control in power systems," *IEEE Trans. Power Syst.*, vol. 31, no. 6, pp. 4217–4230, 2016.

[174] A. Kirakosyan, E. F. El-Saadany, M. S. E. Moursi, A. H. Yazdavar, and A. Al-Durra, "Communication-free current sharing control strategy for dc microgrids and its application for ac/dc hybrid microgrids," *IEEE Trans. on Power Syst.*, vol. 35, no. 1, pp. 140–151, 2020.

[175] "Lv power cable data," 2016 (accessed January 04, 2019). [Online]. Available: www.ffcpg.com.my

[176] T. Nguyen, H. Yoo, and H. Kim, "A droop frequency control for maintaining different frequency qualities in a stand-alone multimicrogrid system," *IEEE Trans. on Sustain. Energy*, vol. 9, no. 2, pp. 599–609, April 2018.

[177] M. Hamzeh, M. Ghafouri, H. Karimi, K. Sheshyekani, and J. M. Guerrero, "Power oscillations damping in dc microgrids," *IEEE Trans. on Energy Conv.*, vol. 31, no. 3, pp. 970–980, Sep. 2016.

[178] A. H. Yazdavar, M. A. Azzouz, and E. F. El-Saadany, "A novel decentralized control scheme for enhanced nonlinear load sharing and power quality in islanded microgrids," *IEEE Trans. on Smart Grid*, vol. 10, no. 1, pp. 29–39, Jan 2019.

[179] O. Khan, S. Acharya, M. A. Hosani, and M. S. E. Moursi, “Hill climbing power flow algorithm for hybrid dc/ac microgrids,” *IEEE Trans. on Power Electronics*, vol. 33, no. 7, pp. 5532–5537, July 2018.

[180] H. R. Baghaee, M. Mirsalim, G. B. Gharehpetan, and H. A. Talebi, “Nonlinear load sharing and voltage compensation of microgrids based on harmonic power-flow calculations using radial basis function neural networks,” *IEEE Systems Journal*, vol. 12, no. 3, pp. 2749–2759, Sep. 2018.

[181] O. Crăciun, A. Florescu, I. Munteanu, A. I. Bratcu, S. Bacha, and D. Radu, “Hardware-in-the-loop simulation applied to protection devices testing,” *International Journal of Electrical Power & Energy Systems*, vol. 54, pp. 55–64, 2014.

[182] C. Dufour and J. BÃľlanger, “On the use of real-time simulation technology in smart grid research and development,” *IEEE Trans. on Industry Applications*, vol. 50, no. 6, pp. 3963–3970, Nov 2014.

[183] G. Adam, O. Anaya-Lara, G. Burt, S. Finney, and B. Williams, “Comparison between two vsc-hvdc transmission technologies: Modular and neutral point clamped multilevel converter,” 11 2009, pp. 277–282.

[184] “Tune pid controllers by using field-oriented control autotuner,” 2020 (accessed March 15, 2020). [Online]. Available: https://www.mathworks.com/help/mcb/ug/how-to-use-field-oriented-control-autotuner.html

[185] “Inside current-mode control,” (accessed July 19, 2020). [Online]. Available: https://application-notes.digchip.com/006/6-8586.pdf

[186] M. Raza, E. Prieto-Araujo, and O. Gomis-Bellmunt, “Small-signal stability analysis of offshore ac network having multiple vsc-hvdc systems,” *IEEE Transactions on Power Delivery*, vol. 33, no. 2, pp. 830–839, 2018.

[187] J. Qi, Y. Gangui, C. Yuru, L. Yonglin, and J. Zhang, “Small-signal stability analysis of photovoltaic generation connected to weak ac grid,” *Journal of Modern Power Systems and Clean Energy*, vol. 7, no. 2, pp. 254–267, 2019.

Appendix

A1 Park (or direct-quadrature-zero) transformation

The direct-quadrature-zero $dq0$ transformation is mathematical transformation that projects the three-phase ac signals (voltages, currents) from stationary abc reference frame into rotating $dq0$ reference frame. As a result, three phase ac quantities are being represented by dc quantities without loosing information, which largely simplifies the analysis of three-phase ac circuits. What is more, in the balanced three-phase systems the 0 component of the $abc - dq0$ transformation is zero, which eventually presents the three-phase quantities by their d and q components, which are then used for performing simplified calculations and control of the circuit. The transformation consists originally evolved as a result of using Clarke and Park transformation matrices. Specifically, the Clark transformation projects the original three-phase ac quantities (e.g. V_a, V_b, V_c) from stationary abc reference frame into another stationary frame, namely $\alpha\beta0$ frame, as per (A.1)

$$\begin{bmatrix} x_\alpha \\ x_\beta \\ x_0 \end{bmatrix} = \frac{2}{3} \begin{bmatrix} 1 & -\frac{1}{2} & -\frac{1}{2} \\ 1 & \frac{\sqrt{3}}{2} & -\frac{\sqrt{3}}{2} \\ \frac{1}{2} & \frac{1}{2} & \frac{1}{2} \end{bmatrix} \begin{bmatrix} x_a \\ x_b \\ x_c \end{bmatrix} \tag{A.1}$$

where x_α, x_β and x_0 are the corresponding voltage quantities in $\alpha\beta0$ frame. Please note that the latter quantities are ac in nature, however, the quantity V_0 is zero for the balanced ac systems. Thus the Clark transformation reduces the original three ac signals into corresponding two ac signals. The Park transformation is then applied by transforming the quantities from stationary $\alpha\beta0$ frame into rotating $dq0$ frame as per

$$\begin{bmatrix} x_d \\ x_q \\ x_0 \end{bmatrix} = \frac{2}{3} \begin{bmatrix} cos(\theta) & sin(\theta) & 0 \\ sin(\theta) & -cos(\theta) & 0 \\ 0 & 0 & 0 \end{bmatrix} \begin{bmatrix} x_\alpha \\ x_\beta \\ x_0 \end{bmatrix} \tag{A.2}$$

where θ is the angle between the rotating $dq0$ reference frame and the stationary $\alpha\beta0$ frame, and is related to the speed of rotation of the $dq0$ as per

$$\omega_{dq} = \frac{d\theta}{dt} \tag{A.3}$$

Combining the steps of equation (A.1) and (A.2), the transformation of three-phase ac quantities their corresponding $dq0$ components can be done using the transformation matrix T as per

$$\begin{bmatrix} x_d \\ x_q \\ x_0 \end{bmatrix} = T \begin{bmatrix} x_a \\ x_b \\ x_c \end{bmatrix} = \frac{2}{3} \begin{bmatrix} cos(\theta) & cos(\theta - \frac{2\pi}{3}) & cos(\theta + \frac{2\pi}{3}) \\ sin(\theta) & sin(\theta - \frac{2\pi}{3}) & sin(\theta + \frac{2\pi}{3}) \\ \frac{1}{2} & \frac{1}{2} & \frac{1}{2} \end{bmatrix} \begin{bmatrix} x_a \\ x_b \\ x_c \end{bmatrix} \tag{A.4}$$

After using the input dc quantities resultant from the above transformations (e.g., for the controller implementation), the output dc variables are transformed back to the original abc frame using the inverse transformation matrix T^{-1} as per

$$\begin{bmatrix} x_a \\ x_b \\ x_c \end{bmatrix} = T^{-1} \begin{bmatrix} x_d \\ x_q \\ x_0 \end{bmatrix} = \frac{2}{3} \begin{bmatrix} cos(\theta) & sin(\theta) & 1 \\ cos(\theta - \frac{2\pi}{3}) & sin(\theta - \frac{2\pi}{3}) & 1 \\ cos(\theta + \frac{2\pi}{3}) & sin(\theta + \frac{2\pi}{3}) & 1 \end{bmatrix} \begin{bmatrix} x_d \\ x_q \\ x_0 \end{bmatrix} \tag{A.5}$$

Identical transformation matrices can be used for transforming three-phase ac currents to their $dq0$ components and back to three-phase quantities. Please notice that the implemented transformation is magnitude invariant, so that the magnitude of the transformed variable is the same in both systems. Alternatively, the power invariant transformation could be adopted by using the scaling factor of $\sqrt{2/3}$ instead of $2/3$ in the transformation matrix T. Also, the implemented transformation the a axis of three-phase signals and the d axis of the rotating $dq0$ frame are initially aligned, and the alignment during the sudden shifts of the respective vectors is done with the help of grid synchronization techniques. Alternatively, q axis of $dq0$ frame could have been initially aligned with the a axis of three-phase frame.

A2 Selection of the parameters for Inner Current Controllers

It is worth noting that although the average model is used to represent the converters, the design of the converter control parameters considers the limitations induced by the actual operation as well. Specifically, in the detailed converter model, the controller's output is supplied to the Pulse Width Modulation (PWM) block to generate the pulses required for turning on and off the IGBT switches. Inside the PWM block, the triangular reference is compared with the modulation voltage to generate those pulses. The speed of operation of PWM block is determined by the frequency of the triangular waveform, the latter is called switching frequency as it determines how often IGBT switches are turning on and off. Selection of the proper switching frequency is of prime importance for the operation of VSCs. Higher switching frequencies are desired from the control and filtering perspective, whereas selection of too high switching is restricted by the capabilities of the IGBT switches and by the excessive losses occurring as a result of too fast switching. The switching frequency f_{sw} of IGBT devices for MT-HVDC applications is usually below 3 kHZ, whereas higher switching frequencies are employed for low voltage-low power applications such as MT-DCμGrids [183]. This upper limit on the speed of PWM restricts the speed of operation of inner current control loop. Particularly, it is recommended that the bandwidth of the current controller is at least ten times less than that of the PWM block [184]. The controller parameters for the inner current loop (proportional and integral gains of PI controller) are selected accordingly to ensure ten times difference between the bandwidths of the respective blocks. Additionally, for the VSCs in MT-HVDC applications, the structure of ICC is designed in such a way as to decouple the d and q axis controllers by substituting the coupling terms from each loop, as well as to minimize the effect of the grid voltage by providing a feedforward voltage compensation. As a result, the pu parameters of the ICC are calculated according to equations (A.6) to mimic the response of the first order system [185].

$$\begin{cases} K_{p,inner} = BW_{ICC} L_f I_{base}/(\sqrt(2/3)V_{base}) \\ K_{i,inner} = BW_{ICC} R_f I_{base}/(\sqrt(2/3)V_{base}) \\ BW_{ICC} = \dfrac{f_{sw} * 2 * \pi}{10} \end{cases} \tag{A.6}$$

where $K_{p,inner}$ and $K_{i,inner}$ are the proportional and integral gains of the ICC, L_f and R_f

are the inductance and resistance of the phase reactor, I_{base} and V_{base} are the current and voltage base values, and the BW_{ICC} and f_{sw} are the bandwidth of ICC and the switching frequency of the converter, respectively. Further fine-tuning is done to adjust the response of the combined system.

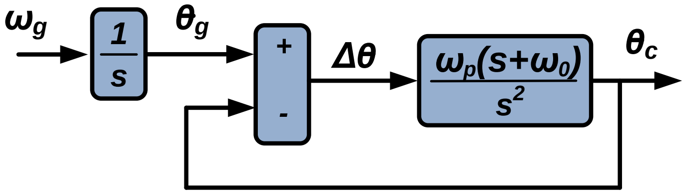

Figure A1. The model of the phase angle estimation loop of the considered grid synchronization technique.

A3 Common Reference Frame

As it was previously discussed, the modeling of three-phase ac circuits in rotating $dq0$ reference frame is common practice as it simplifies the analysis of the system and is especially suitable for stability studies. However, different components of ac systems might be modeled in distinct $dq0$ reference frames. To integrate these models together, the transformation of the dq components of the respective variables between different frames can be done as per equation (A.7) [186, 187].

$$\begin{bmatrix} x_d^{'} \\ x_q^{'} \end{bmatrix} = \begin{bmatrix} cos(\Delta\theta) & sin(\Delta\theta) \\ -sin(\Delta\theta) & cos(\Delta\theta) \end{bmatrix} \begin{bmatrix} x_d \\ x_q \end{bmatrix} \tag{A.7}$$

In equation (A.7), $\Delta\theta$ is the phase angle difference between the two considered frames. This dynamic behavior of this angle is dependent on the grid synchronization technique used. For the FLL employed in this study, this angle can be derived from the mathematical model of the phase angle estimation loop shown in Fig. A1 [37].

In the latter figure, θ_g is the grid voltage angle, θ_c is the converter reference frame angle, and $\Delta\theta$ is the angle difference between two reference frames. Thus, the closed loop dynamics of $\Delta\theta$ are given by

$$\Delta\theta(1 + \frac{\omega_p(s+\omega_0)}{s^2}) = \theta_g \tag{A.8}$$

From which

$$\Delta\theta = \omega_g \frac{s}{s^2 + \omega_p(s+\omega_0)} \tag{A.9}$$

where $\omega_p = 2\pi 40$ rad/s and $\omega_0 = 2\pi 15$ rad/s are parameters of FLL. The phase angle of equation (A.9) can be then used in (A.7) to establish the relationship between dynamics of the grid voltage reference frame and the converter reference frame.

A4 The parameters of the test systems used throughout the thesis

Table A1. The parameters of the four terminal MT-HVDC system shown in Fig. 4.15.

Base power	800 MVA	Ac voltage	150 kV
Dc voltage	300 kV	Ac frequency	50 Hz
Dc link capacitance	350 μF	Dc cable inductance	0.16 mH/km
Dc cable resistance	14 mΩ/km	Dc cable capacitance	0.23 μF/km
Filter inductance	0.014 H	Filter resistance	0.04 Ω
ICC P gain	0.6 pu	$\text{Length}_{\text{VSC1 to VSC2}}$	20 km
ICC I gain	18 pu	$\text{Length}_{\text{VSC1 to VSC3}}$	100 km
ODCVC P gain	8 pu	$\text{Length}_{\text{VSC2 to VSC3}}$	100 km
ODCVC I gain	200 pu	$\text{Length}_{\text{VSC3 to VSC4}}$	50 km
PSI P gain	2 pu	Short Circuit Ratio	10
PSI I gain	30 pu	X over R ratio	7

Table A2. The parameters of the five terminal MT-HVDC system shown in Fig. 4.2.

Base power	900 MVA	Ac voltage	230 kV
Dc voltage	400 kV	Ac frequency	50 Hz
Dc link capacitance	225 μF	Dc cable inductance	0.16 mH/km
Dc cable resistance	14 mΩ/km	Dc cable capacitance	0.23 μF/km
Filter inductance	0.028 H	Filter resistance	0.088 Ω
ICC P gain	0.6 pu	Inertia G2, G4	3 s
ICC I gain	18 pu	Inertia G3	6s
ODCVC P gain	8 pu	$\text{Length}_{\text{VSC2 to VSC3}}$	100 km
ODCVC I gain	200 pu	$\text{Length}_{\text{VSC3 to VSC4}}$	50 km
AVS P gain	0.2 pu	MMC arm inductance	0.15 pu
AVS I gain	50 pu	MMC arm resistance	0.0015 pu

Table A3. The parameters of the Cigre B4 MT-HVDC test system shown in Fig. 4.24.

Base power	1000 MVA	Ac voltage	220 kV
Dc voltage	400 kV	Ac frequency	50 Hz
Dc link capacitance	250 μF	Dc cable inductance	2.1 mH/km
Dc cable resistance	9.5 mΩ/km	Dc cable capacitance	0.19 μF/km
Filter inductance	0.023 H	Filter resistance	0.07 Ω
ICC P gain	0.6 pu	Inertia G1	5 s
ICC I gain	18 pu	Inertia G2	4s
ODCVC P gain	8 pu	Inertia G3	7s
ODCVC I gain	200 pu		

Table A4. The parameters of the IEEE Type1 turbine-governor model.

K	20	K1	0.3
K2	0	K3	0.4
K4	0	K5	0.3
K6	0	K7	0
K8	0	T7	0
T1	0.1	T2	0
T3	0.25	T4	0.3
T5	10	T6	0.4
Pmax	1	Pmin	0.33

Table A5. The parameters of the GAST gas turbine-governor model.

T1	0.4	T2	0.1
T3	3	KT	2
Dturb	0	AT	0.85
VmaxGAST	0.8	VminGAST	0

Table A6. The parameters of the hydraulic turbine-governor model.

$\mathrm{K_a}$	3.3	$\mathrm{T_a}$	0.07 s
$\mathrm{R_{droop}}$	0.05	PID P gain	1.163
PID I gain	0.105	PID D gain	0.001
$\mathrm{K_B}$	0	$\mathrm{T_W}$	2.67
$\mathrm{K_T}$	1.0361		

Table A7. The parameters of the PMSG-WT.

Air density ρ	1.12 kg/m^3	Radius R	33.05 m
Moment of inertia J	70000 kg/m^2	N_p	48

Table A8. The parameters of the considered MT-DCμGrid shown in Fig. 6.1

$\mathrm{V_{dc,Grid}}$	400 V	Line 1 and 6 Resistances	2 Ω
$\mathrm{V_{dc,Grid}}$	400 V	Line 2 and 5 Resistances	1 Ω
Filter Inductance	0.2 mH	Line 3 and 4 Resistances	1.5 Ω
Filter capacitance	500 μF	Line 1 and 6 Inductances	15 mH
Filter Resistance	0.05 Ω	Line 3 and 4 Inductances	11.25 mH
Nom. Inj. Frequency	50 Hz	Line 2 and 5 Inductances	7.5 mH
$k_{p,dc}$	0.1 A/V	$k_{i,dc}$ (voltage reg.)	20 A/V
$k_{p,inner}$	0.02 pu/A	$k_{i,inner}$ (current reg.)	1 pu/A
$k_{droop,1,3}$	0.5 Ω	$k_{droop,2}$	Ω
IC capacitance	1250 μF	ac voltage	220 V
$k_{droop,1}$ (IC #1)	1 pu	$k_{droop,2}$ (IC #2)	1 pu